2014-12-08

Subtropical Atlantic Climate Variability Record in Speleothems from the Bahamas

Monica Arienzo
University of Miami, m.arienzo@umiami.edu

UNIVERSITY OF MIAMI

SUBTROPICAL ATLANTIC CLIMATE VARIABILITY RECORD IN SPELEOTHEMS FROM THE BAHAMAS

By

Monica Arienzo

A DISSERTATION

Coral Gables, Florida

December 2014

UNIVERSITY OF MIAMI

A dissertation submitted in partial fulfillment of
the requirements for the degree of
Doctor of Philosophy

SUBTROPICAL ATLANTIC CLIMATE VARIABILITY RECORD IN SPELEOTHEMS FROM THE BAHAMAS

Monica Arienzo

Approved:

_____
Peter K. Swart, Ph.D.
Lewis G. Weeks Professor
of Marine Geology and Geophysics

_____
Kenneth Broad, Ph.D.
Professor of Marine Affairs
and Policy

_____
Amy Clement, Ph.D.
Associate Dean and Professor
of Marine Physical Oceanography

_____
Philip (Flip) Froelich, Ph.D.
Froelich Education Services
Tallahassee, Florida

_____
Larry C. Peterson, Ph.D.
Professor of Marine Geology
and Geophysics

_____
M. Brian Blake, Ph.D.
Dean of the Graduate School

_____
Ali Pourmand, Ph.D.
Assistant Professor of Marine
Geology and Geophysics

ARIENZO, MONICA (Ph.D., Marine Geology and Geophysics)
Subtropical Atlantic Climate Variability Record in Speleothems from the Bahamas (December 2014)

Abstract of a dissertation at the University of Miami.

Dissertation supervised by Professor Peter K. Swart.
No. of pages in text. (331)

The last 100,000 years of climate consist of numerous abrupt millennial scale climate variations. Of interest to this study are Heinrich stadials which are extreme cold events in the North Atlantic. While a comprehensive picture of climate across Heinrich events is emerging for the North Atlantic, very few studies have been conducted in the subtropical western Atlantic, which may be important for the global propagation of these events. This study is the first study to determine paleoclimate of the Bahamas across Heinrich stadials.

Cave deposits, in particular stalagmites, offer the opportunity to obtain high resolution records of past climate. Typically, stable oxygen and carbon isotopes of the calcite are analyzed. However, when interpreting the oxygen isotope record of carbonates there are several climatic factors which can lead to changes in the oxygen isotopes. The hydrogen and oxygen isotopic analysis (δ^2H and $\delta^{18}O$) of water trapped within speleothem carbonate (fluid inclusions) can shed light on the drivers of the carbonate oxygen isotopes. The application of cavity ring-down spectroscopy to the δ^2H and $\delta^{18}O$ analysis of water in fluid inclusions was investigated at the University of Miami (this study) as an alternative to traditional δ^2H and $\delta^{18}O$ methods and results demonstrate acceptable precision and good agreement with previous results.

In order to ascertain the climate expression across Heinrich events in the sub-tropical Atlantic, carbon and oxygen isotopes, fluid inclusion isotopes and minor elements have been measured on a series of U-Th dated speleothems from Dan's Cave, Abaco Island, Bahamas. The analyses suggest that during Heinrich stadials 1-6 temperatures decreased by ~3 °C. These findings support previous work in other areas of the North Atlantic and are consistent with the climate response to a weakening of the Atlantic meridional overturning circulation.

To support the findings in the ancient stalagmites, a monitoring study has been conducted. The goal of the monitoring study is to better understand the drivers of kinetic isotope fractionation. In particular, the focus of this study was the carbonate clumped isotope methodology which is a relatively recent geochemical development and therefore more calibration studies are necessary. Nearly 2 years of monitoring a currently active cave in the Bahamas has been conducted and results demonstrate that clumped isotope fractionation increases during periods of increased ventilation and growth rate.

Modern studies of atmospheric dust demonstrate that currently there is seasonal deposition to the Caribbean derived from Africa. Iron concentrations within the cave in the modern are found to be heterogeneous in drip waters and calcite both temporally and spatially. The temporal variation is thought to be due annual variations in dust delivery and the amount of precipitation. Additionally, two stalagmites collected from the Bahamas exhibit iron concentrations which increase concurrently with Heinrich stadials, suggesting increased dust deposition to the Bahamas during these events.

ACKNOWLEDGEMENT

First I would like to thank my advisor Dr. Peter K. Swart. I have been extremely luckily to work with Peter, who taught me how to ask scientifically relevant questions, to write scientifically, and who also taught me how to solder. I also am grateful for his advice, in particular his rule of threes. I am extremely luckily to have had a committee which has pushed me, and supported me. Ali Pourmand provided me with the opportunity to utilize the Neptune, which has become extremely helpful in my post-doctoral research. I would also like to thank Amy Clement, who has helped me to better understand the climate as a system and to think about my paleoclimate reconstructions in a global perspective. I would also like to than Kenneth Broad, who I had the opportunity to work with in the field and at RSMAS. I am greatly appreciative of all of the numerous dives which were required to create such a unique collection of stalagmite samples. I would also like to thank Larry Peterson, who helped me understand the paleoclimate of the last glacial period and link my records to other records from around the world. Finally I would like to thank Flip Froelich, for pushing me to better understand speleothem geochemistry.

This work could not have been conducted without the help from many others. In particular, I would like to thank Huber Vonhof, who allowed me to visit his laboratory, utilize his machine for fluid inclusion analysis and has provided insightful comments to our publications. I would also like to thank Brian Kakuk who acquired permits necessary for sampling in the Bahamas and who has also conducted numerous dives to collect samples as part of this project. The Cape Eleuthera Institute in particular I would like to thank Ron and Karen, who have provided me with help while I am in the Bahamas, allowed me to store materials in their house, and who made sure I returned after visiting

the cave. I am also grateful for Carol DeWet, my undergraduate advisor, who first showed me the incredible world of carbonate geochemistry and encouraged me to pursue a Ph. D. Carol has continued to provide me with advice and support over the last six years which I am greatly appreciative of.

Funding for this project was provided by numerous sources, including the Rosenstiel Fellowship, Cave Research Foundation Student Research Grant, Geological Society of America Student Research Grant, RSMAS Alumni Award Research Grant, a NSF P2C2 grant awarded to P. Swart and others, and the CSL.

I would also like to thank my family for their support over the last six year. My parents, who have emotionally supported me, my brother and his wife who have been an excellent voice of reason. I'd like to thank my fellow SILers (past and present) including (but not limited too) Corey, Amel, Chris K., Amanda O. and Quinn, who have helped me immensely in the lab and have listened to me talk through issues, as well as Sean Murray who helped solve the dark secrets of clumped isotopes and Sevag Mehterian who was critical to me finishing. I would also like to thank Greta and Karen for their help over the years, as well as Grey Horwitz, Sevag and Kimberly Chamales who traveled with me to Hatchet Bay Cave. I'd also like to thank the rest of my RSMAS family, my Miami family, my roommates, Frisbee team members and Chico, who make the days always better. Lastly, I am greatly indebted to Gareth Blakemore, who cooked many meals for me, listened to me, and told me when I was being unreasonable, thank you.

TABLE OF CONTENTS

List of Figures

List of Tables

Chapter 1

Introduction

Summary

The primary objective of this dissertation is to determine the climatic response to millennial scale changes in the Bahamas using the geochemical records contained in stalagmites. The last 100,000 years have been characterized by millennial scale climate events, which are well expressed in the high latitudes, however little work has been conducted on the western subtropical Atlantic. To fill this gap, this study will elucidate the climatic responses to these events. The geochemical tools utilized for this study will aid in the reconstruction of both temperature and amount of precipitation. Below follows a brief overview of the background of the millennial scale climate events and the geochemical tools utilized during this study.

1.1 Background of Millennial Scale Climate Variability

Millennial scale climate variability as supported by marine, sediment, ice core, speleothem and lake records is a pervasive feature of climate during the last million years (Blunier and Brook, 2001; Bond et al., 1993; Bond et al., 1992). The last 70,000 years are characterized by 25 abrupt temperature changes known as Dansgaard/Oeschger (D/O) cycles and 6 cold (stadial) event known as Heinrich events (Dansgaard et al., 1984; Dansgaard et al., 1993). These cycles are alternations between warm interstadials and cold stadials, best expressed in the Greenland ice core record (Bond et al., 1997) and North Atlantic sediment records (Bond et al., 1993; Bond et al., 1992; Bond et al., 1997). Paleoclimate data support that D/O cycles and Heinrich stadials are global in their scale,

abrupt in their nature and a pervasive feature of climate (Clement and Peterson, 2008; McManus, 1999; Zhang and Delworth, 2005).

In order to understand the climatic expression of millennial scale climate change in the subtropical Atlantic, other paleoclimate proxies such as marine and lake sediments, and speleothems can be used (Keigwin and Jones, 1994; Peterson et al., 2000; Sachs and Lehman, 1999). A study conducted on a Florida sediment core from Lake Tulane indicates that stadials periods correlate with warm, wet periods (Grimm et al., 2006). The warm and wet Heinrich stadials in Florida are attributed to the reduction in northerly heat transport, creating warm and wet subtropics (Donders et al., 2009; Grimm et al., 2006). However, the Grimm et al. (2006) study was contrary to many other paleoclimate proxies, which supported a southerly shifted ITCZ and increased aridity in the Northern Hemisphere subtropics and tropics (Escobar et al., 2012; Hodell et al., 2012; Kanner et al., 2012; Peterson et al., 2000; Stager et al., 2011). By analyzing speleothems from the Bahamas, the aim of this study has been to continue to build upon the current knowledge of climate in the subtropical western Atlantic across Heinrich stadials and D/O interstadials. This was achieved through the geochemical analyses of speleothems from the Bahamas which formed over the last 70,000 years. Below follows a brief outline of the geochemical tools which were utilized, followed by a description of the samples available for this study.

1.2 Application of Speleothems to Paleoclimate Studies

Speleothems (cave calcites) have proven to be valuable archives for paleoclimate reconstructions. Speleothems can be accurately dated using U-Th techniques, easily analyzed for carbon and oxygen isotopes ($\delta^{13}C$ and $\delta^{18}O$) and elemental concentration,

and can be studied at a range of time scales from sub-annual to 100,000 years (Fairchild et al., 2006; Gordon et al., 1989). For paleoclimate studies, stalagmites, which form from the bottom of the cave, are typically used. Stalagmites form as a result of the precipitation of $CaCO_3$ in the form of aragonite or calcite (generally calcite). Cave drip waters become saturated with respect to low-Magnesium calcite (LMC) or aragonite through dissolution of the $CaCO_3$ overlying the cave (Figure 1.1). Aragonite forms when the Mg^{2+} content of the groundwater is high. When drip waters reach on open cave area, CO_2 degassing occurs leading to the precipitation of calcite (McDermott, 2004) (Figure 1.1):

$$Ca^{2+} + 2HCO_3^- \rightarrow CaCO_3(s) + H_2O + CO_2\,(g) \qquad (1)$$

Drip waters are elevated in dissolved CO_2 as a result of the high pCO_2 in the soil above the cave and karst and limestone dissolution. Carbonate precipitation occurs through thin (approximately 100 μm) layers of drip water (equation 1) (Fairchild et al., 2006).

Speleothem growth is dependent on the magnitude and duration of groundwater recharge, the calcium concentration of the drip water, the drip rate and cave ventilation (Fairchild et al., 2006; Richards et al., 1994). Layering is visible when organics, clay particles or fluid inclusions are incorporated in crystal formation. Crystal growth is generally not affected by these incorporations; however, growth hiatuses and large influxes of organic material can affect crystal growth (White, 1976). The cessation of growth can be driven by a significant decrease in the supply of water to the cave (Richards et al., 1994).

1.3 Oxygen and Carbon Isotopes

Carbon and oxygen isotopes are the most often used geochemical tool in paleoclimate studies. Oxygen and carbon isotope analyses rely on the determination of

the ratio of the less abundant isotope to the more plentiful one (i.e. $^{18}O/^{16}O$ and $^{13}C/^{12}C$) in the sample. Isotopic abundances are measured using mass spectrometer techniques and reported using the conventional delta notation as expressed for oxygen in equation 2:

$$\delta^{18}O = \left(\frac{^{18}O/^{16}O_{sample} - ^{18}O/^{16}O_{standard}}{^{18}O/^{16}O_{standard}} \right) \times 1000 \quad (2)$$

Oxygen isotopes in carbonates are reported relative to Vienna Pee Dee Belemnite (V-PDB), while in waters relative to Vienna Standard Ocean Mean Water (VSMOW) standards. Oxygen isotope analysis in carbonates is generally used to determine temperature at the time of formation (Craig, 1965; Epstein et al., 1953) as temperature is dependent on the calcite $\delta^{18}O$ value and the $\delta^{18}O$ value of the water at the time of formation. Paleotemperature reconstructions from $\delta^{18}O$ measurements of speleothem calcite have proven to be problematic. The issue lies in accurately determining $\delta^{18}O$ of the formation water. Variations in the $\delta^{18}O$ of the drip water is driven by the source water, evaporation and amount of rainfall (Dansgaard, 1964; Lachniet, 2009), making it difficult to make assumptions about the water from which the carbonate precipitated from. This requires either the monitoring of a currently active cave to determine the isotopic composition of the drip waters, or the isotopic analysis of water trapped within speleothem calcite, known as fluid inclusion isotopic analysis (Dublyansky and Spotl, 2009; Feng et al., 2012; Genty et al., 2014; Harmon et al., 1979; Matthews et al., 2000; Riechelmann et al., 2011; Schwarcz et al., 1976; Tremaine et al., 2011; Vonhof et al., 2006; Wainer et al., 2011). For many tropical speleothems, temperature is not thought to be the primary driver of the $\delta^{18}O$ of the calcite, rather $\delta^{18}O$ of the calcite is driven by changes in the amount of rainfall (Carolin et al., 2013; Kanner et al., 2012).

Carbon isotopes ($\delta^{13}C$) are also reported relative to VPDB, but are not as commonly used in speleothem studies because the environmental drivers are not as well understood (Lambert and Aharon, 2011). The $\delta^{13}C$ of the carbonate is dependent on the dissolved inorganic carbon of the drip waters. Carbon sources to the drip waters include atmospheric CO_2, soil biological components, overlying bedrock, cave atmosphere CO_2 and cave ventilation (Fairchild et al., 2006; Tremaine et al., 2011). These factors may vary with the seasons, temperature and rainfall amount (Fairchild et al., 2006). By combining multiple geochemical proxies a better interpretation of $\delta^{13}C$ in speleothems can be developed (Fairchild et al., 2006).

In order for the speleothems to accurately record environmental changes, the calcite must be precipitated in isotopic equilibrium (Hendy, 1971). Caves that precipitate stalagmites in equilibrium generally consist of a high relative humidity and a slow and constant drip rate (Lachniet, 2009).

1.4 Fluid Inclusion Isotopes

The analysis of microscopic water trapped in a mineral (or fluid inclusion) has been utilized as a method to understand the geologic history of the deposits (Goldstein, 1986, 2001; Lecuyer and Oneil, 1994; Schwarcz et al., 1976; Shepherd, 1977). This method has been successfully applied to speleothem studies for the reconstruction of paleotemperature and past oxygen isotope value of paleoprecipitation (Dublyansky and Spotl, 2009; van Breukelen et al., 2008; Vonhof et al., 2006; Wainer et al., 2011). The $\delta^{2}H$ and $\delta^{18}O$ analysis of water from fluid inclusions is a direct measurement of the oxygen isotopic value of the water the speleothem formed in. For example, determining

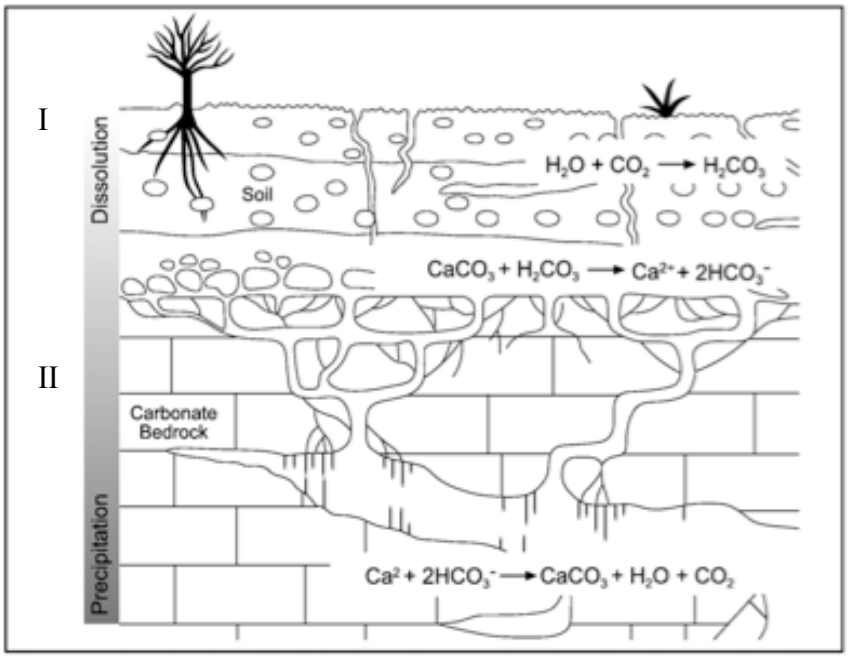

Figure 1.1: Dissolution and precipitation of the karst system. The dissolution zone (I) is where the drip water becomes saturated with Ca^{2+} and bicarbonate. When the drip water enters the cave environment (II), CO_2 degassing leads to the formation of $CaCO_3$. Figure from Fairchild et al. (2006)

the $\delta^{18}O$ values of both the trapped fluid and that of the accompanying mineral, and assuming that the $\delta^{18}O$ of the trapped water represents that of the fluids at the time of formation, allows the temperature of mineral formation to be determined. This method has been applied to stalagmites from Israel to determine changes in source water during the LGM versus the modern (Matthews et al., 2000) and to a speleothem from Oman which supports that modern day fluid inclusions are consistent with precipitation expectations (Fleitmann et al., 2003).

1.5 Minor and Trace Elements

Elemental concentration of speleothem carbonate may also provide paleoclimate information. Minor and trace elements are precipitated by substitution with Ca^{2+}, between lattice planes, at site defects or as adsorbed cations (Moore, 1989). Typically

Ca^{2+} is substituted by Mg^{2+}, Sr^{2+}, Ba^{2+}, Mn^{2+}, and Fe^{2+} (Fairchild and Treble, 2009). The distribution or partition coefficient (Doner and Hoskins, 1925) can be defined by equation 3 (Fairchild and Treble, 2009; Moore, 1989):

$$\left(\frac{Trace}{Ca_{CaCO3}}\right) = D_{Trace}\left(\frac{Trace}{Ca}\right)_{solution} \quad (3)$$

Where Trace is the concentration of the trace ion of interest and D_{trace} is the distribution coefficient for the element. The left side of the equation indicates the concentration of the element relative to calcium of the solid, while the right is the concentration in fluid phase (Moore, 1989). Of primary interest for cave studies is the incorporation of magnesium and strontium in the speleothem calcite.

The incorporation of trace and minor elements into the speleothem calcite is dependent on the elemental concentrations in the drip waters and temperature. Other factors that impact the incorporation of trace and minor elements into the calcite are the drip rate, type and amount of overlying bedrock, routing path of the water, and kinetic effects (Cruz et al., 2007). Coupling trace element concentrations with $\delta^{18}O$ and $\delta^{13}C$ analysis of speleothems can aid in the interpretation of the geochemical signature (Fairchild and Treble, 2009). For speleothems, the incorporation of Sr in stalagmites can be influenced by temperature, growth rate and bedrock type (Fairchild et al., 2000; Huang and Fairchild, 2001; Lorens, 1981). While enrichment in both Sr and Mg is thought to be driven by prior calcite precipitation (PCP) which is the precipitation of calcite prior to the drip water reaching the stalagmite (Fairchild and Treble, 2009). Increased PCP can occur during periods of increased residence times in the epikarst (Fairchild and Treble, 2009; Tremaine and Froelich, 2013).

1.6 Clumped Isotopes

Clumped isotope geochemistry is the study of multiply substituted isotopologues of CO_2, or CO_2 molecules that contain one or more rare isotope. The most abundant multiply substituted isotopologue (containing two or more rare isotopes) for CO_2 is $^{13}C^{18}O^{16}O$ (Table 1.1) and for CO_3^{2-} is $^{13}C^{18}O^{16}O_2^{2-}$ (Dennis, 2011).

The substitution of either heavy or light isotopes impacts the bond strength within the molecule. A bond between a heavy and light isotope is more stable than a bond between two light isotopes because the vibrational frequency decreases and the bond's zero point energy decreases (Bigeleisen and Mayer, 1947; Eiler, 2007, 2011; Urey, 1947). This is also true with two heavy isotopes (i.e. 2H-2H will have the lowest zero point energy, then 2H-1H followed by 1H-1H) (Eiler, 2007, 2011). Therefore, there is a thermodynamic preference for doubly substituted bonds (the bonding of two heavy bonds) and with decreasing temperatures the amount of doubly-substituted bonds increases. At high temperatures, entropy promotes a random distribution of bonds and a stochastic distribution is reached (Dennis, 2011). For CO_3^{2-} the exchange reaction is:

$$^{12}C^{18}O^{16}O_2^{2-} + {}^{13}C^{16}O_3^{2-} \leftrightarrow {}^{13}C^{18}O^{16}O_2^{2-} + {}^{12}C^{16}O_3^{2-} \quad (4)$$

And for CO_2:

$$^{12}C^{18}O^{16}O + {}^{13}C^{16}O_2 \leftrightarrow {}^{13}C^{18}O^{16}O + {}^{12}C^{16}O_2 \quad (5)$$

The equilibrium constants for these reactions are in fact temperature dependent and increased 'clumping' will be favored at lower temperatures (Ghosh et al., 2006; Wang et al., 2004b). Considering that clumping is an isotope exchange and is only a single phase, prior knowledge of the isotopic composition of the water or the dissolved inorganic

	Mass	Relative Abundance
$^{12}C^{16}O_2$	44	98.40%
$^{13}C^{16}O_2$	45	1.10%
$^{12}C^{16}O^{17}O$	45	761 ppm
$^{12}C^{16}O^{18}O$	46	0.40%
$^{13}C^{16}O^{17}O$	46	8.6 ppm
$^{12}C^{17}O_2$	46	147 ppb
$^{13}C^{16}O^{18}O$	**47**	**46.3 ppm**
$^{12}C^{17}O^{18}O$	47	1.6 ppm
$^{13}C^{17}O_2$	47	2 ppb
$^{12}C^{18}O_2$	48	4.2 ppm
$^{13}C^{17}O^{18}O$	48	18 ppb
$^{13}C^{18}O_2$	49	48 ppb

Table 1.1: Isotopologues of CO_2, their relative stochastic abundances and mass. Adapted from Dennis (2011). The most abundant multiply substituted isotopologue of CO_2 is $^{13}C^{16}O^{18}O$ with a relative abundance at the ppm level (shown in bold).

carbon is not necessary, which is a huge advantage over the oxygen isotope paleothermometer. This allows for paleotemperature reconstructions from carbonates which previously could not be studied due to a lack of knowledge of the oxygen isotopic composition of the formation water.

1.6.1 Analysis of Δ_{47}

Analysis of multiply substituted isotopologues in carbonates is not directly possible, however it is possible to analyze the evolved CO_2 from acid digestion. The Δ_{47} of the evolved CO_2 is calculated using equation 6 and represents the deviation of CO_2 from the stochastic distribution of isotopologues. Mass 47 is dominated by the $^{13}C^{18}O^{16}O$ species.

$$\Delta_{47} = \left[\left(\frac{R^{47}}{R^{47*}} - 1\right) - \left(\frac{R^{46}}{R^{46*}} - 1\right) - \left(\frac{R^{45}}{R^{45*}} - 1\right)\right] * 1000 \quad (6)$$

In equation 6, R^{47} is the ratio of mass 47 to 44, R^{46} is the ratio of mass 46 to 44 and R^{45} is the ratio of mass 45 to 44 from CO_2 of the sample while R^{47*} , R^{46*} and R^{45*} are the stochastic distribution of the ratios expected in the sample based on the sample's measured δ47, δ46 and δ45 values (Eiler, 2007; Huntington et al., 2009; Wang et al., 2004b).

1.6.2 Application of Δ_{47} to carbonates

Since the first theoretical proposal of the temperature dependence of Δ_{47} to temperature, there have been a series of studies which have attempted to calibrate this relationship in carbonates (Ghosh et al., 2006; Passey et al., 2010; Thiagarajan et al., 2011; Tripati et al., 2010; Wang et al., 2004b). The first Δ_{47} to temperature relationship for carbonates was developed by Ghosh et al. (2006):

$$\Delta_{47} = \frac{0.0059 * 10^6}{T^2} - 0.02 \qquad (7)$$

where T is the absolute temperature (kelvin) and Δ_{47} is the measured ratio of mass 47/44 of the sample relative to the stochastic distribution (equation 6). The application of the clumped isotope methodology for paleotemperature determination has been applied to a range of biogenic and inorganic calcites (Came et al., 2007; Dennis and Schrag, 2010; Ferry et al., 2011; Ghosh et al., 2006; Henkes et al., 2013; Hough et al., 2014; Passey et al., 2010; Thiagarajan et al., 2011; Tripati et al., 2010; Zaarur et al., 2011) and most carbonates appear to agree well with the Δ_{47} to temperature relationship found in Ghosh et al. (2006). Although clumped isotope geochemistry is still a relatively new area of study, it has been applied to the study of cave calcites (Affek et al., 2008; Daëron et al., 2011; Kluge and Affek, 2012; Kluge et al., 2012; Wainer et al., 2011) and cryogenic cave carbonates (Kluge et al., 2014). Studies of clumped isotopes in speleothems reveal a

deviation from the Δ_{47} to temperature relationship, with speleothem temperatures being warmer than expected (Affek et al., 2008; Daëron et al., 2011; Kluge and Affek, 2012; Kluge et al., 2012). Currently, this offset has been shown to be greatest among carbonates which have been studied. There is one important distinction between carbonate precipitated in speleothems and carbonate precipitation in other systems as carbonate precipitation in speleothems is a three phase system. During the process of carbonate precipitation in speleothems, the degassing of CO_2 from the dripwater (equation 1), is thought to lead to kinetic isotope fractionation depending on the rate of degassing and $CaCO_3$ precipitiation (Affek, 2013).

Clumped isotope studies demonstrate the potential of this methodology to determine paleotemperature, however there is still much to be learned about the kinetic fractionation of isotopes in particular for in speleothems. Further work is needed to accurately determine the calibration of absolute temperature reconstructions in speleothems (Affek et al., 2008; Wainer et al., 2011).

Not only does clumped isotope analysis allow for the determination of temperature at the time of formation, it additionally provides information of the $\delta^{18}O$ of the water from which the speleothem precipitated from. By analyzing samples from the same intervals for both fluid inclusion and clumped isotopes, paleotemperature can be independently determined using two different proxies, potentially aiding in calibration of the clumped isotope paleothermometer (Schauble et al., 2006; Wainer et al., 2011).

1.7 U-Th Dating

Age dating of speleothems is typically conducted by U-Th methods. This method relies on the decay of ^{238}U to ^{230}Th to determine the age of the sample. The decay

reaction for ^{238}U is shown in Figure 1.2. The half-lives for ^{234}Th and ^{234}Pa are relatively short compared to ^{238}U, ^{234}U and ^{230}Th and are therefore not included in the age calculations. There are certain assumptions which must be met in order for a sample to dated using U-Th methods. The sample must be within the dating limits of the methodology (i.e. less than 600,000 years) and changes in the isotope ratios must be driven by isotope decay (i.e. parent and daughter cannot be added and/or removed from the system).

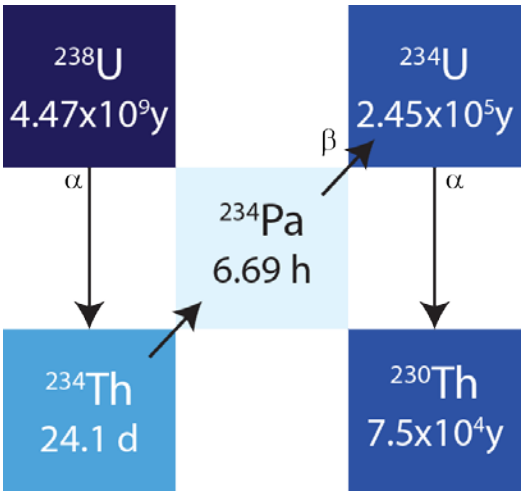

Figure 1.2: Decay chain for ^{238}U to ^{230}Th for the U-Th geochronometry. The isotopes of interest for U-Th dating are ^{238}U, ^{230}Th and ^{234}U. Also shown are the decay rates for each isotope, modified from Bourdon et al. (2003).

The equation utilized for age determination is:

$$\left\{\left[\frac{^{230}Th}{^{238}U}\right]-\left[\frac{^{232}Th}{^{238}U}\right]\left[\frac{^{230}Th}{^{232}Th}\right]_i\left(e^{-\lambda_{230}t}\right)\right\}-1=-e^{-\lambda_{230}t}+\left(\frac{\delta^{234}U_m}{1000}\right)\left(\frac{\lambda_{230}}{\lambda_{230}-\lambda_{234}}\right)\left(1-e^{-(\lambda_{230}-\lambda_{234})t}\right) \quad (8)$$

The ^{234}U is produced from alpha decay, and alpha emissions can damage bonds surrounding the nuclide. This causes ^{234}U to be susceptible to leaching and not in secular equilibrium (Edwards et al., 2003) and thus variation in the ^{234}U must be accounted for.

Therefore, in equation (8) the term $\delta^{234}U_m$ is utilized to account for variations in the ^{234}U, where:

$$\delta^{234}U_m = \left(\left[\frac{^{234}U}{^{238}U}\right] - 1\right) * 1000 \quad (9)$$

One of the primary hurdles to overcome with U-Th age dating in speleothems is the initial Thorium fraction which is deposited with the speleothem calcite as the sample is forming (Richards and Dorale, 2003). This thorium fraction is often referred to as initial or unsupported thorium and can be monitored through the measurement of ^{232}Th which is a long lived isotope of Th (1.401 X 10^{10} a) (Richards and Dorale, 2003). When ^{232}Th concentration is high, initial ^{230}Th is also high (Richards and Dorale, 2003). Considering that the unsupported Th fraction is deposited initially, it also decays with time and therefore must be accounted for. The calculation of the proportion of ^{230}Th which is unsupported is calculated from the initial ^{230}Th, measured $^{232}Th/^{238}U$, $^{230}Th/^{238}U$ and the decay of ^{230}Th as shown in equation (8).

Without accounting for the initial ^{230}Th fraction, ages would be older than the true age as it would appear that more Th has decayed from U. Typically for speleothems an initial $^{230}Th/^{232}Th$ activity ratio of 0.6 ±0.2 (2σ) is utilized as this value represents the average ratio in the upper crust (Richards and Dorale, 2003). For samples with low ^{232}Th, there is minimal initial ^{230}Th and therefore if the initial $^{230}Th/^{232}Th$ activity ratio is not accurately known, impacts on the error of the age is small (Edwards et al., 2003). Methods to account for initial Thorium include the measurement of actively forming samples (zero-age samples). By measuring an actively forming stalagmite sample, the age is assumed to be zero and therefore the Th present is derived from the detrital component and not from the decay of Uranium (Richards and Dorale, 2003). Also

measurement of drip water $^{230}Th/^{232}Th$ has been successfully used to account for initial Thorium (Richards and Dorale, 2003).

Issues with U-Th methods for dating speleothems can arise if the samples can be affected by post-depositional alteration or high detrital Th making dating difficult if not impossible to date (Richards and Dorale, 2003). For all speleothems, multiple ages are conducted to determine if there is the presence of age reversals which is indicative that isotope ratios are not solely due to decay. Additionally, it is common practice to utilize multiple U-Th ages per stalagmite to account for any variations in growth rate.

1.8 Samples for Study

To date, a suite of speleothem samples (n=53) have been collected from throughout the Bahamas platform from submerged caves ('Blue Holes') or from dry caves (Figure 1.3). Of the 53 samples, 32 have been dated using U-Th dating methods. The samples were collected by Brian Kakuk and Dr. Kenny Broad from submerged caves of Abaco Island, Andros Island, Grand Bahama, Eleuthera and Great Exuma, Bahamas using advanced diving technology (Figure 1.3). The age ranges for the dated stalagmites fall into three major categories: 13,000-100,000 yr BP, 200,000 to 250,000 yr BP and 300,000 to 375,000 yr BP (Figure 1.4). This includes the last four major sea level low stands. Samples chosen for this study are from Dan's Cave in Abaco Island, Bahamas and were forming over the last 100,000 years. A complete list of dated samples is provided in Appendix A.

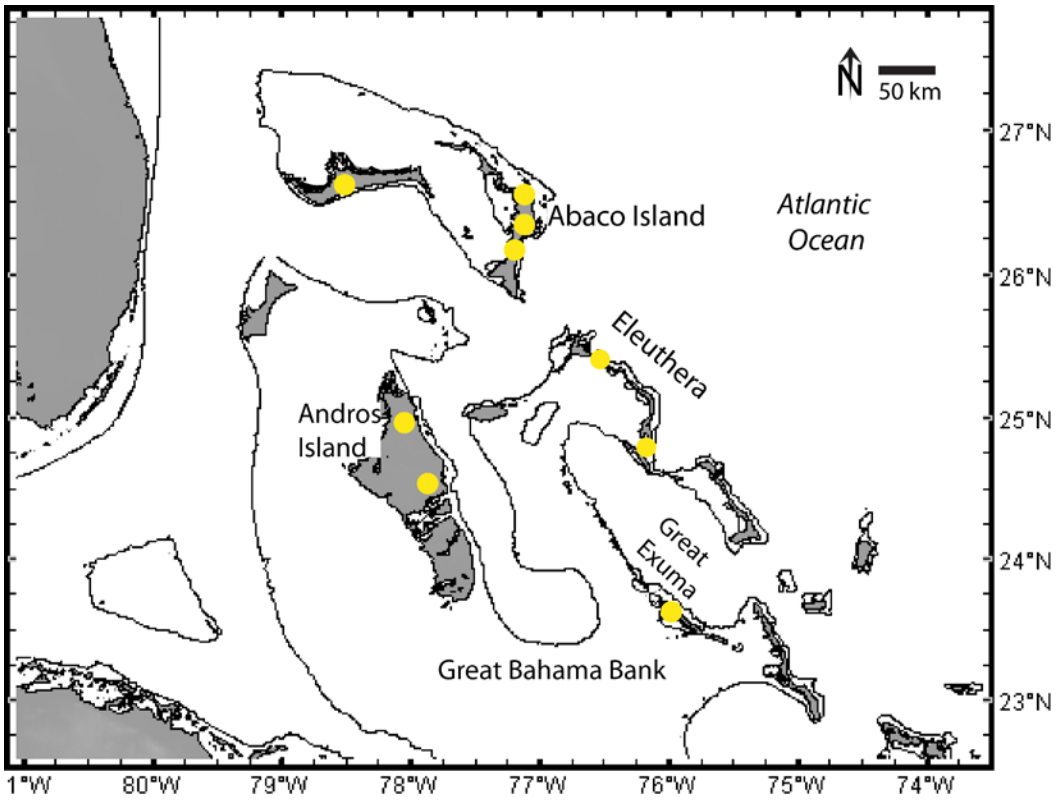

Figure 1.3: Map of the Bahamas showing the localities of samples collected for this study. Samples have been collected from Blue Holes and above ground caves from Grand Bahama, Abaco Island, Andros Island, Eleuthera, and the Exumas. Samples from Blue Holes are currently not forming, rather the samples were forming when sea level was low, and the cave was exposed to air. The bathymetric line is the 120 m water depth, which represents sea level during the Last Glacial Maximum. During sea level low stands, the bank top would have been exposed.

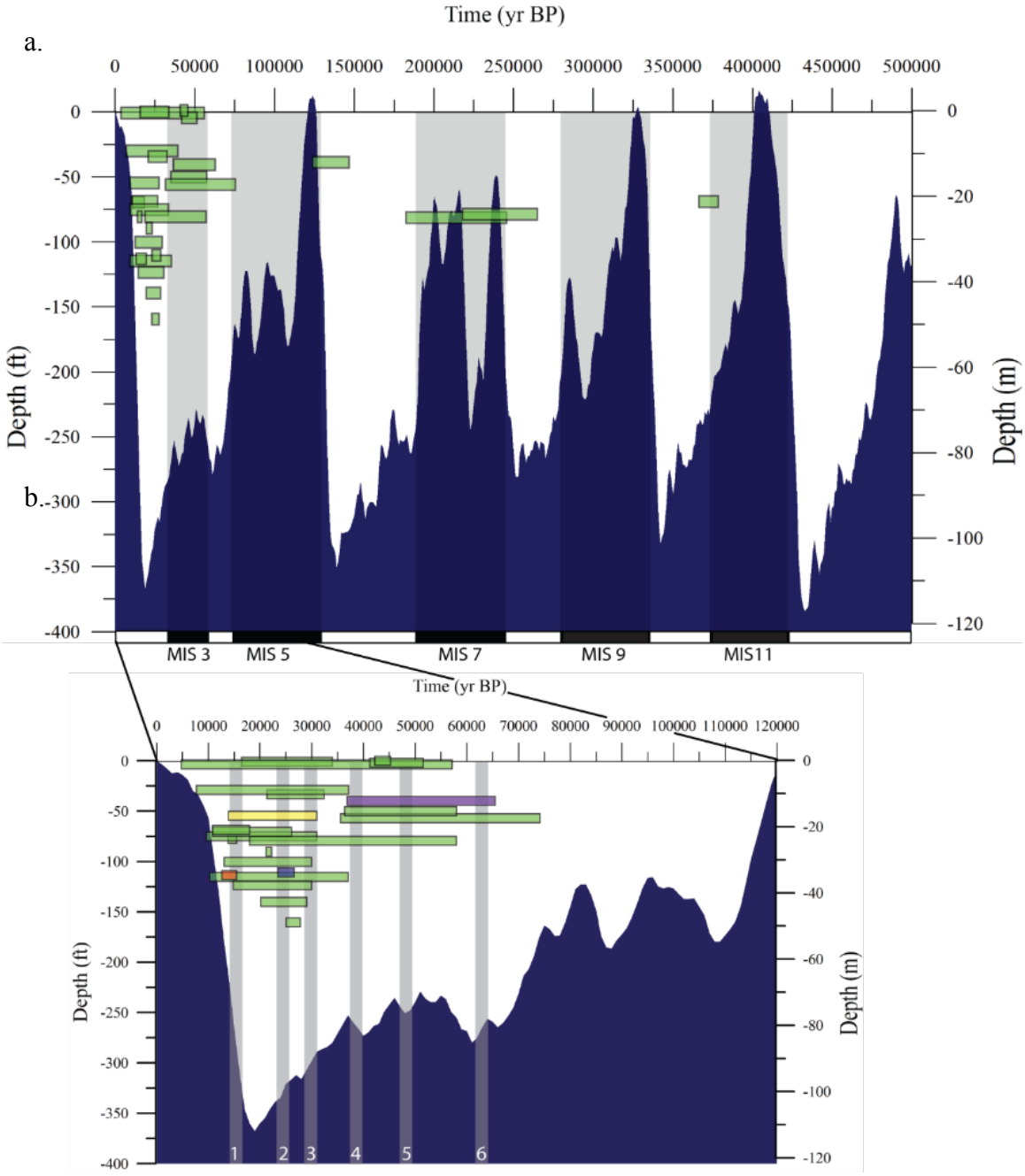

Figure 1.4: Samples which have been dated using U-Th methods from the Bahamas. a) Sea-level over the last 500,000 years shown in blue from Lisiecki (2005). Green bars represent the various stalagmite samples which have been dated, plotted at the depth the samples were collected. The length of bar is dependent on the time the stalagmite sample was forming over. Samples were forming over stage 2/3, 6/7 and stage 10/11. B) Close up of the last 120,000 years for the same samples in (a). The grey vertical bars represent the timing of Heinrich stadials 1-6. The colored bars represent the stalagmite samples which were focused on for this study. The samples include stalagmites AB-DC-09 (yellow), AB-DC-12 (purple), AB-DC-03 (red) and AB-DC-01 (blue).

To compare with the ancient stalagmites, since June of 2012, a cave monitoring project has been undertaken. This monitoring project has been conducted at Hatchet Bay Cave, on the island of Eleuthera, located on the eastern edge of the Bahamas platform (Figure 1.3). The goal of the cave monitoring project is to better characterize the modern drivers of speleothem geochemical variations through the analysis of the modern environment of the cave such as temperature, relative humidity, oxygen isotopes of the drip water and carbon isotopes of the dissolved inorganic carbon. These results are compared to results from calcite precipitated *in situ*. The precipitated calcite is analyzed for carbon, oxygen and clumped isotopes and elemental abundances. This project was based on the cave monitoring projects of Tremaine et al. (2011) and Banner et al. (2007).

1.9 Conclusion

Through the geochemical study of multiple stalagmites from the same cave, variations in climate conditions associated with millennial scale events can be ascertained. This dissertation will focus on climate reconstructions over the last 70,000 years from Dan's Cave, Abaco Island, Bahamas and additionally the relationship of the ancient to the modern through a cave monitoring study of Hatchet Bay Cave, Eleuthera, Bahamas.

Chapter 2

Measurement of $\delta^{18}O$ and $\delta^{2}H$ values of fluid inclusion water in speleothems using cavity ring-down spectroscopy compared to isotope ratio mass spectrometry [1]

Summary

The hydrogen and oxygen isotopic analyses ($\delta^{2}H$ and $\delta^{18}O$) of water trapped within speleothem carbonate (fluid inclusions) have traditionally been conducted utilizing dual-inlet isotope ratio mass spectrometry (IRMS) or continuous flow IRMS (CF-IRMS) methods. The application of cavity ring down spectroscopy (CRDS) to the $\delta^{2}H$ and $\delta^{18}O$ analysis of water in fluid inclusions was investigated at the University of Miami as an alternative method to CF-IRMS.

An extraction line was developed to recover water from the fluid inclusions consisting of a crusher, sample injection port and an expansion volume (either 100 or 50 cm^3) directly connected to the CRDS instrument (L2130-i Picarro). Tests were conducted to determine the reproducibility of standard water injections and crushes. In order to compare results with conventional analytical methods, samples were analyzed both at the University of Miami (CRDS method) and Vrije Universiteit Amsterdam (CF-IRMS method).

Analytical reproducibility of speleothem samples crushed on the Miami Device demonstrates an average external standard deviation of 0.5 and 2.0 ‰ for $\delta^{18}O$ and $\delta^{2}H$ respectively. Sample data are shown to fall near the global meteoric water line supporting the validity of the method. Three different samples were analyzed at Vrije Universiteit Amsterdam and the University of Miami in order to compare the

[1] Arienzo, M. M., Swart, P. K., Vonhof, H. B. 2013. Measurement of $\delta^{18}O$ and $\delta^{2}H$ of fluid inclusion water in speleothems using cavity ring-down spectroscopy compared with isotope ratio mass spectrometry*, Rapid Communications in Mass Spectrometry,* vol 27, 2616–2624, DOI: 10.1002/rcm.6723.

performance of each laboratory. The average offset between the two laboratories is 0.7 ‰ for $\delta^{18}O$ and 2.5 ‰ for $\delta^{2}H$.

The advantage of CRDS is that the system offers a low cost alternative to CF-IRMS for fluid inclusion isotope analysis. The CRDS method demonstrates acceptable precision and good agreement with results from the CF-IRMS method. These are promising results for the future application of CRDS to fluid inclusion isotope analysis.

2.1 Background

The $\delta^{2}H$ and $\delta^{18}O$ analyses of waters obtained from fluid inclusions are able to provide additional insights into the conditions prevalent at the time of mineral formation when combined with conventional $\delta^{18}O$ analysis of the solid phase. For example, determining the $\delta^{18}O$ values of both the trapped fluid and that of the accompanying mineral, and assuming that the $\delta^{18}O$ of the trapped water represents that of the fluids at the time of formation, allows the temperature of mineral formation to be determined (Schwarcz et al., 1976).

The $\delta^{2}H$ and $\delta^{18}O$ measurement of fluid inclusions is a two-step process, (i) the extraction of water from the sample, and (ii) the actual O and H isotopic analysis. The first step can be achieved either through thermal decrepitation or by crushing the sample. Thermal decrepitation releases trapped water by heating the fluid bearing sample to a high temperature (Dallai et al., 2004). While this method has proven to be effective in speleothem studies (Cisneros et al., 2011), there are limitations to this technique including inter laboratory offsets (Dallai et al., 2004; Matthews et al., 2000) arising from variations in the extraction temperature (Matthews et al., 2000), isotopic exchange at high temperature and fractionation during the thermal decrepitation process. Crushing of the

sample under vacuum or a flow of a carrier gas such as He also allows the H_2O to be released and is considered to be the preferred method, as it potentially avoids some of the problems associated with thermal decrepitation (Dennis et al., 2001; Harmon et al., 1979).

For the isotopic analysis of the released water, previous speleothem fluid inclusion isotopic studies relied first on dual inlet isotope ratio mass spectrometry (Dallai et al., 2004; Dennis et al., 2001; Matthews et al., 2000) and more recently on continuous flow isotope ratio mass spectrometry (CF-IRMS) (Dublyansky and Spotl, 2009; Vonhof et al., 2006; Wainer et al., 2011). Both methods require conversion of the water vapor to molecular species suitable for O and H isotopic analysis. The development of CF-IRMS allowed for faster analysis on smaller samples and a precision similar to that achieved using dual inlet methods (Dublyansky and Spotl, 2009; Sharp et al., 2001; Vonhof et al., 2006). One of the first successful systems which combines crushing with CF-IRMS was developed by Vonhof et al. (2006) at Vrije Univeristeit (VU) in Amsterdam. The Amsterdam Device consists of a crusher, cold trap and a flash heater to heat the trapped water, subsequently directed by the carrier gas to the inlet of the Finnigan TC-EA furnace (High Temperature Conversion-Elemental Analyzer, Thermo Scientific, Bremen, Germany). Within the TC-EA, the water vapor is converted to CO and H_2 by reaction with glassy carbon and the products then separated using a packed gas chromatographic column before analysis using an isotope ratio mass spectrometer (Sharp et al., 2001). A similar method was employed by Dublyansky and Spotl (2009) also using CF-IRMS and both laboratories are capable of analyzing small amounts of water (0.1-0.2 μL) with typical standard deviations of 0.5 ‰ for $\delta^{18}O$ and 1.5‰ for $\delta^{2}H$ (Wainer et al., 2011).

Although these systems have been applied to paleoclimate studies, (Dublyansky and Spotl, 2009; Griffiths et al., 2010; van Breukelen et al., 2008; Wainer et al., 2011) there is an observed inter laboratory offset of 1‰ for $\delta^{18}O$ and 3‰ for $\delta^{2}H$ (Wainer et al., 2011).

This paper describes the first application of cavity ring down spectroscopy (CRDS) to fluid inclusion isotopic analysis. We have constructed a fluid inclusion water extraction device (Miami Device) based on the Amsterdam Device and interfaced to a L2130-i Picarro water isotope analyzer. The important difference between the IRMS method and the CRDS method is that the latter does not require conversion of the water to other molecular species; rather the CRDS technique utilizes the absorption of a specific wavelength of laser light corresponding to the vibrational frequency of the $H_2{}^{16}O$, $H^2H^{16}O$ and $H_2{}^{18}O$ molecules. The precision of water isotopic analysis utilizing the CRDS systems has demonstrated to be superior to traditional IRMS systems (Brand et al., 2009). The motivation to conduct fluid inclusion isotopic analysis with CRDS is driven by the potential this system offers for faster analysis, less maintenance arising from simpler sample processing, and comparable precision.

2.2 Design of the System: The Miami Device

The Miami Device consists of a piston to crush the calcite and release the water from within the sample, a stainless steel line and a volume reservoir which is connected to the CRDS instrument (Figure 2.1). This design utilizes aspects of the Amsterdam Device as outlined in Vonhof et al. (2006) as well as the Picarro vaporizer unit (A0211, Picarro Inc., Santa Clara, CA, USA). The Picarro vaporizer unit consists of a heated 150 cm^3 volume reservoir through which N_2 gas has been flushed. The liquid water sample is

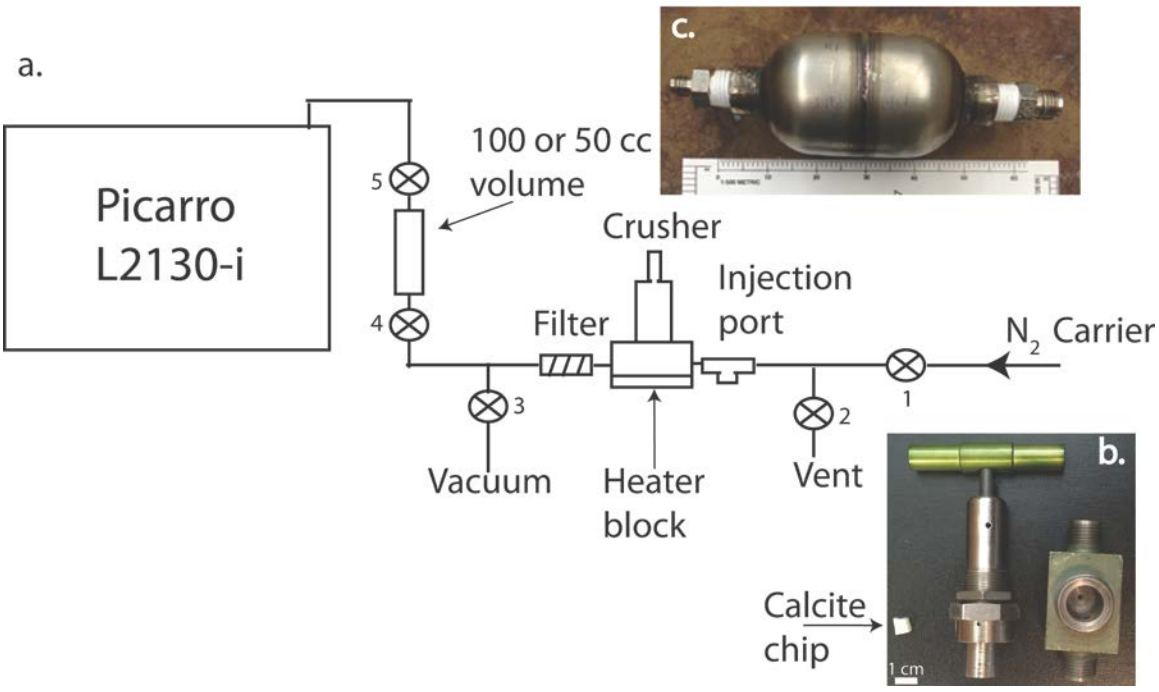

Figure 2.1: The design of the Miami Device. a) Schematic of the 'Miami Device'. The entire line is heated (~115ºC) to minimize absorption of water. Alternative designs which were tested are presented in Appendix B. b) Photograph of the modified valve unit showing the steel piston and the valve body which has been drilled to accommodate the piston. The piston is raised and lowered using the valve stem. Also shown is a typical calcite cube to be crushed, the sample weighed 0.4 grams. The crusher assembly can accommodate samples up to 1.3 cm^3 and can be disconnected for sample exchange. c) Photograph of the 100 cm^3 volume, made by Quality Float Works, Inc. The 50 cm^3 volume is similar in shape and length.

directly injected into the volume. After injection the volume is opened to the CRDS analyzer and the water enters the instrument. The large volume provides a continuous stable signal of water on which the $\delta^{18}O$ and $\delta^{2}H$ can be measured.

The Miami Device extraction line is constructed entirely of stainless steel (Swagelok SS-T2-S-6ME, Swagelok Florida Fluid System Technologies, Inc., Mulberry, Florida, USA), 1/8" external diameter tubing with the exception of ¼" stainless steel tubing (Swagelok SS-T4-S-6ME) connecting the volume to the crusher. The entire extraction line is heated with nickel-chromium resistance heating wire with fiberglass sleeving

(NI80-015, FBGS-N-22, OMEGA Engineering, Stamford, CT, USA) which ensures that there are no cold spots where water vapor can condense. Heating of the crusher unit is accomplished by a 100 W cartridge heater inserted into a base plate on which the crusher valve rests. Temperature is monitored throughout the line and at the crusher unit to ensure uniform heating throughout. The temperature is maintained at 115°C during analysis which represents the ideal temperature to limit adsorption of fluid inclusion water on calcite directly after crushing (Dublyansky and Spotl, 2009; Vonhof et al., 2006).

Crusher: The crusher consists of a modified 3/8" Nupro vacuum valve (Swagelok SS-6BG) (Figure 2.1 b) with the valve seat replaced by a steel piston which slides into a customized valve body milled to accommodate it. In order to crush the sample, the valve stem is turned to lower the piston to release the water within the calcite. A 0.5 μm pore size (Swagelok SS-2F-05) Swagelok in-line filter is located adjacent to the crusher to prevent particles of the crushed calcite sample from contaminating the downstream line and potentially entering the CRDS analyzer.

Water Injection Port: An injection port consisting of a septa (Swaglok SS-4-T) is fitted before the crusher and allows for the introduction of 0.1 to 1.2 μL standard water from a 5 μL syringe (Figure 2.1).

Expansion Volume: In order to mimic the design of the Picarro vaporizer, a 100 cm^3 or 50 cm^3 stainless steel expansion volume (Quality Float Works, Inc., Schaumburg, IL, USA) (Figure 2.1c) is placed downstream of the crusher. The volume can be isolated from the CRDS instrument and the crusher utilizing two Nupro SS-4H valves (Florida Fluid System Technologies, Inc., Mulberry, Florida, USA, valves 4 and 5).

Vacuum and Vent Connections: Between the crusher and the expansion volume a vacuum pump connection (KNF 84.4, KNF Neuberger, Inc., Trenton, NJ, USA) allows residual water vapor to be removed from the extraction line between crushed samples or injections of standard waters. The carrier gas can be isolated during line maintenance using a Swagelok SS-2P4T valve (valve 1, Figure 2.1) and the carrier gas can be vented to prevent excess pressure from entering the CRDS instrument (valve 2, Figure 2.1).

2.3 Protocol for Analysis

For a typical analysis, the sample (in the case of this paper, a stalagmite specimen) is subsampled utilizing a diamond band saw producing a calcite chip typically between 0.2 and 0.8 g, with the size dependent on the amount of water present in the sample (ideally between 0.3 to 1.0 μL). The calcite chip is then loaded and the crusher is connected to the N_2 supply. A crush is initiated once the temperature of the extraction line reaches 115°C and the background water concentration in the CRDS isotope analyzer is <150 ppm. The sample is then crushed to a fine powder. After the crush, water is carried to the expansion volume and into the analyzer (L2130-i, Picarro, Santa Clara, CA, USA). Once the concentration reaches 1,000 ppm H_2O as measured using the CRDS instrument, the valve between the volume and the crusher (valve 4, Figure 2.1) is closed. Water vapor continues to enter the analyzer from the expansion volume, and the concentration rises to values between 4,000 to 20,000 ppm depending upon the size of the sample crushed and its water concentration. If valve 4 is closed when the concentration of H_2O exceeds 1,000 ppm, the sample would flush through the CRDS water isotope analyzer too quickly and a stable measurement would not be attained. After at least 250 seconds of measurement, the valve closest to the CRDS analyzer is closed (valve 5, Figure 2.1), the

valve between the crusher and the volume (valve 4) is opened and the N_2 gas isolated (valve 1). This allows the crusher and volume to be evacuated to remove residual water vapor between samples. After pumping the line for approximately 60 seconds, the extraction line and the CRDS instrument is purged with the carrier gas. The next injection or crush can start once the background reaches <150 ppm H_2O, thereby allowing for five or six individual analyses per hour.

For standard water injections, water is injected through the water injection port (Swaglok SS-4-T) allowing for the introduction of 0.1 to 1.2 μL standard water through a septum (Figure 2.1). The procedure for a standard water injection is the same as the procedure described above for a sample crush.

For each individual rock sample analyzed there is a set protocol involving a series of standard injections before and after the rock is crushed. Prior to crushing the sample, the extraction line is first conditioned with 2 to 4 standard water injections (0.5 μL) with the isotopic compositions of the waters ideally not being too far from that expected in the crushed sample. The sample is then crushed, followed by two or more standard water injections in which the injection amount matches that released by the crush. This is because, as observed in other systems, the raw δ^2H and $\delta^{18}O$ values vary with the amount of water introduced, with a marked decrease in δ^2H and $\delta^{18}O$ values for smaller samples (Figure 2.2 a & b) (Dublyansky and Spotl, 2009) . In the case of oxygen and hydrogen, for both the 100 and 50 cm^3 volumes, a decrease in isotopic value is associated with

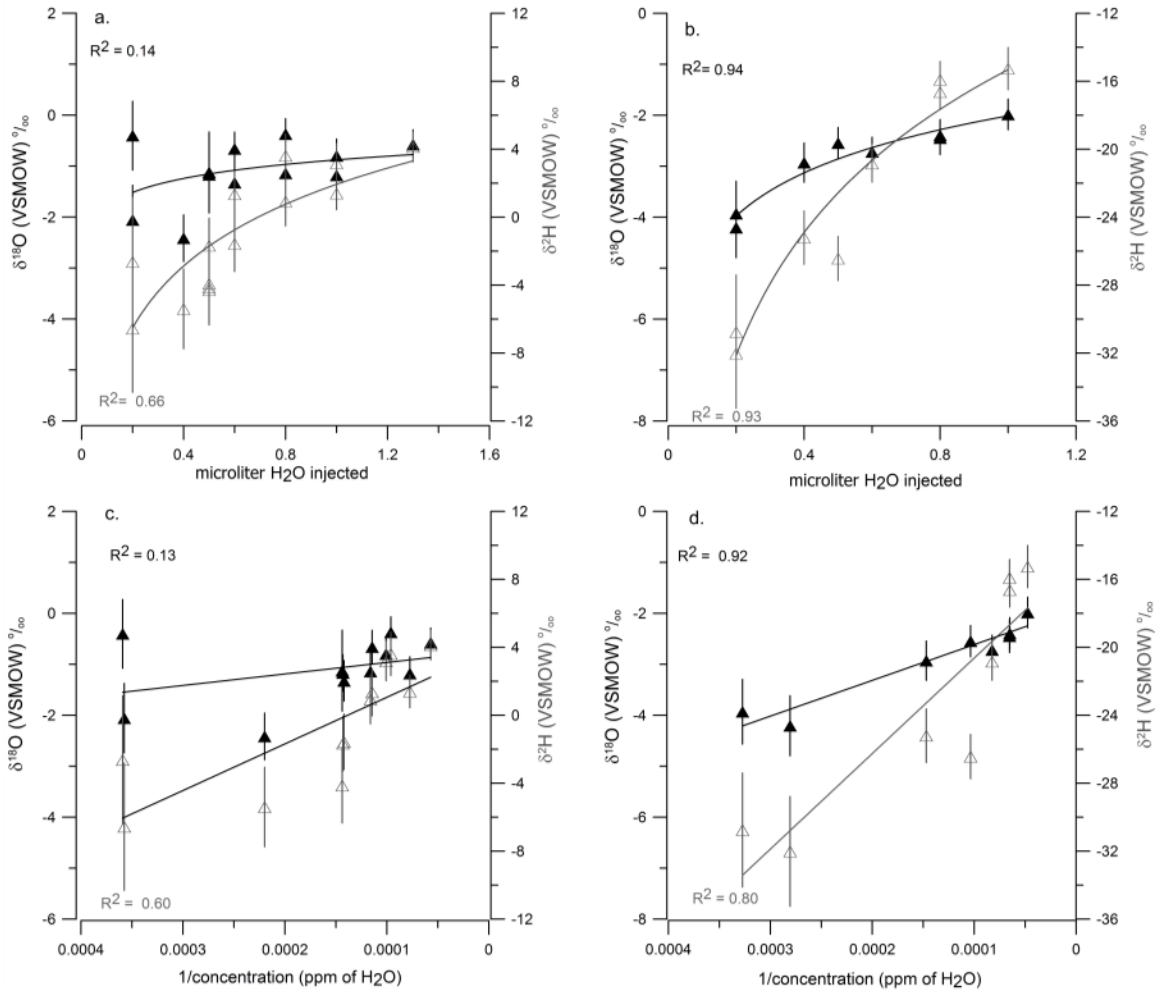

Figure 2.2: Standard water injections at variable injection amounts. For information on the standard waters, see Appendix B. a) Oxygen (filled black triangles) and hydrogen (grey open triangles) isotope values for standard water LS at variable water injection amounts using the 100 cm^3 volume. b) Oxygen (filled triangles) and hydrogen (grey open triangles) isotope values for standard water LS4 at variable water injection amounts using the 50 cm^3 volume. Regression lines are logarithmic fit to the data with r^2 values. Grey r^2 values correspond to hydrogen isotope data, black r^2 values correspond to oxygen isotope data. c) Oxygen (filled triangles) and hydrogen (grey open triangles) isotope values for standard water LS using the 100 cm^3 volume plotted versus 1/concentration of water in ppm. d) Oxygen (filled triangles) and hydrogen (grey open triangles) isotope values for standard water LS4 using the 50 cm^3 volume plotted versus 1/concentration of water in ppm. Regression lines are linear fit to the data with r^2 values. Grey r^2 values correspond to hydrogen isotope data, black r^2 values correspond to oxygen isotope data. All isotope ratios are relative to VSMOW. Vertical error bars represent standard deviation associated with the sample isotopic value.

smaller sample size (Figure 2.2), although the decrease is not as pronounced for $\delta^{18}O$. Plotting the $\delta^{2}H$ or $\delta^{18}O$ values versus 1/concentration, the data falls on a linear relationship (Figure 2.2 c & d), which has been observed for other CRDS instruments (Johnson et al., 2011). In order to correct for the size offset, directly after a crush, between two to four standard waters close in size to that of the crush are injected. The isotope crush data are then corrected for any offset as a result of size. In addition, this procedure allows us to assess whether any water adhered to the freshly crushed calcite (Vonhof et al., 2006). This correction method is similar to that followed at VU. In total, with two to four injections prior to the crush, followed by the crush and two or more injections after the crush, the entire process takes between one to two hours.

After the measurement cycle, the crusher is removed from the line and the contents exchanged for a new sample, and the crusher reconnected to the extraction line. The line is purged with dry N_2 for approximately 30 to 60 minutes to remove adhered water vapor before the next measurement cycle.

2.3.1 Calibration

Calibration is conducted utilizing a series of four laboratory standard waters, previously calibrated using the Vienna Standard Mean Ocean Water scale (VSMOW), Greenland Ice Sheet Precipitation (GISP), and Standard Light Antarctic Precipitation (SLAP). This injection size was chosen because smaller samples exhibit a larger standard deviation in their $\delta^{2}H$ and $\delta^{18}O$ values (Figure 2.2). Johnson et al. (2011) noted a significant increase in measurement errors below 2,500 ppm corresponding to approximately 0.1 μL for the Picarro water vapor analyzer, similar to what has been observed with the Miami Device.

2.3.2 Data reduction

The Picarro software continually collects data when the instrument is operating regardless of whether there is a sample being measured and hence data reduction consists of accessing the appropriate data file and averaging the signal for each crush or injection. A typical output from the data file of the concentration of water and the corresponding $\delta^{18}O$ and $\delta^{2}H$ signal is shown in Figure 2.3. For the purposes of this paper, data (H_2O ppm, $\delta^{18}O$ and $\delta^{2}H$ values) are averaged 2 minutes after the crushed or injected sample is introduced, as this is the amount of time for the sample to reach the water analyzer and stabilize. Integration continues up to 1 minute before the sample is flushed away. Integration of data over longer periods produced no significant change in the $\delta^{18}O$ and $\delta^{2}H$ values (the results are provided in Appendix B). This data reduction scheme has been compared with a water injection introduced through the Picarro vaporizer unit in Appendix B and demonstrates similar results for both the Picarro vaporizer unit and the Miami Device. Raw data are then corrected to VSMOW using the calibration line established between known and measured values of the injected waters. In the case of a crush, the data have been corrected for any size effects (see previous discussion).

2.4 Results

In this section, results for standard water injections and crushed samples for both the 100 and the 50 cm^3 volume are presented. In addition, data are presented of an inter laboratory comparison based on the same speleothem samples analyzed at the University of Miami utilizing CRDS (UM) and at Vrije Universiteit Amsterdam utilizing IRMS (VU).

2.4.1 Reproducibility

For calibration, four standard waters with a range of $\delta^{18}O$ and $\delta^{2}H$ values are each injected two or three times. The average standard deviation for all injections is 0.4‰ for $\delta^{18}O$ and 1.1‰ for $\delta^{2}H$ (see Appendix B). Injection sizes are approximately 0.5 μL, yielding an apparent concentration of ~ 6,000 and 9,000 ppm of water in the 100 and 50 cm^3 volumes. Similar results are obtained for the raw $\delta^{18}O$ and $\delta^{2}H$ values using the two volumes. As a result of the higher concentration of water using the 50 cm^3 volume, better precisions are achievable in the case of smaller samples (0.1-0.3 μL) for both $\delta^{18}O$ and $\delta^{2}H$ (Figure 2.2).

2.4.2 Crushes

In order to determine the precision of fluid inclusion isotopic analyses, repeated crushes have been conducted for both the 100 and 50 cm^3 volumes using the samples described in Table 2.1. Although all of the samples analyzed in this study are calcite speleothems, the method can also be applied to aragonite materials. For the 100 cm^3

Sample ID	Type of Speleothem	Cave	Location
DCF	Flowstone	Dan's Cave	Abaco, Bahamas
HBC2	Flowstone	Hatchet Bay	Eleuthera, Bahamas
SCF	Flowstone	Scladina	Belgium
DC-S	Stalagmite	Dan's Cave	Abaco, Bahamas
HS	Stalagmite	Huagapo	Peruvian Andes

Table 2.1: Description of speleothem samples analyzed for fluid inclusion isotopes. Samples chosen for this study are from a range of localities and are both stalagmites and flowstones.

volume, samples DCF and HBC2 were analyzed. The average $\delta^{18}O$ and $\delta^{2}H$ values for these samples are similar, and not unexpected considering the samples were collected from closely situated islands on the Bahamas platform (Table 2.2a). On average, for 0.5 g of calcite analyzed, the samples yielded about 0.4 µL of H_2O.

For the 50 cm^3 volume, DCF, Scladina, and Huagapo samples were analyzed. The average $\delta^{18}O$ and $\delta^{2}H$ values for the DCF sample are within error of the results from the 100 cm^3 volume for the same sample (Table 2.2b). The average $\delta^{18}O$ and $\delta^{2}H$ values for sample HS are -14.5 ‰ (±0.5 ‰) and -105.3 ‰ (±0.4 ‰) (*n*=4) respectively (Table 2.2b) with an average sample size of 0.3 g yielding approximately 1.1 µL of H_2O. The SCF fluid inclusion average value for $\delta^{18}O$ is -8.9 ‰ (±0.5 ‰) and -58.9 ‰ (±1.6‰) for $\delta^{2}H$ (*n*=7). The water content per crush is calculated from the amount of water released and the weight of the sample, demonstrating that the amount of water varied per sample (Table 2.2).

2.4.3 Comparison between laboratories

In order to compare the Amsterdam and Miami devices a series of samples have been crushed and analyzed in both laboratories (Table 2.3). The offset is found to be 0.7 and 2.5 ‰ respectively for $\delta^{18}O$ and $\delta^{2}H$ with the Miami data being more negative in both $\delta^{18}O$ and $\delta^{2}H$ values than the VU data.

Table 2.2(following page): a) Reproducibility tests of repeated analysis of fluid inclusion isotopes from 2 flowstones (DCF and HBC2) utilizing the 100 cm^3 volume. The $\delta^{18}O$ and $\delta^{2}H$ values are corrected to VSMOW and have been corrected for size as outlined in the text. The DCF sample analyzed on 2/13/2013 is an outlier due to low water content. The amount of water released from the sample was 0.1 µL. b) Reproducibility tests of repeated analysis of fluid inclusion water from 3 speleothems (DCF, HS and SCF) utilizing the 50 cm^3volume. The $\delta^{18}O$ and $\delta^{2}H$ values are corrected to VSMOW and have been corrected for size. Also shown are averages and standard deviations for each sample, sample size and water content.

Table 2.2 a:

Date	Sample ID	Sample size (g)	$\delta^{18}O$ (‰)	$\delta^{2}H$ (‰)	outlier $\delta^{18}O$ (‰)	outlier $\delta^{2}H$ (‰)	Water Content (µL/g $CaCO_3$)
1/21/2013	DCF	0.7	-3.6	-13.7			0.9
1/22/2013	DCF	0.6	-3.8	-11.8			1.0
1/30/2013	DCF	0.5	-3.8	-18.6			1.3
2/7/2013	DCF	0.4	-3.1	-13.6			0.6
2/13/2013	DCF	0.4			-3.5	-10.7	0.2
2/12/2013	DCF	0.5			-4.6	-27.3	0.3
	Average	*0.5*	*-3.6*	*-14.4*			*0.7*
	SD		*0.4*	*2.9*			
1/21/2013	HBC2	0.8	-4.8	-10.2			0.6
1/24/2013	HBC2	0.5	-4.2	-18.4			0.5
1/28/2013	HBC2	0.6	-3.2	-16.3			0.8
2/6/2013	HBC2	0.5	-4.4	-11.9			1.2
2/8/2013	HBC2	0.3	-4.0	-13.7			1.0
2/13/2013	HBC2	0.5	-5.3	-16.3			0.8
2/18/2013	HBC2	0.3	-4.2	-15.7			1.0
	Average	*0.5*	*-4.3*	*-14.7*			*0.8*
	SD		*0.7*	*2.9*			

Table 2.2 b:

Date	Sample ID	Sample size (g)	$\delta^{18}O$ (‰)	$\delta^{2}H$ (‰)	outlier $\delta^{18}O$ (‰)	outlier $\delta^{2}H$ (‰)	Water Content (µL/g $CaCO_3$)
2/19/2013	DCF	0.6	-3.5	-16.1			0.8
2/23/2013	DCF	0.4	-4.6	-19.8			0.3
2/27/2013	DCF	0.5	-3.3	-15.5			0.6
	Average	*0.5*	*-3.8*	*-17.1*			*0.6*
	SD		*0.7*	*2.4*			
2/23/2013	HS	0.4	-14.8	-105.2			3.0
2/25/2013	HS	0.3	-14.5	-104.9			3.2
2/28/2013	HS	0.3	-14.7	-105.9			3.9
5/8/2013	HS	0.2	-13.8	-105.3			3.5
	Average	*0.3*	*-14.5*	*-105.3*			*3.4*
	SD		*0.5*	*0.4*			
2/19/2013	SCF	0.5	-9.4	-56.4			2.0
2/20/2013	SCF	0.3	-8.3	-57.5			1.1
2/20/2013	SCF	0.3	-9.8	-61.0			1.2
2/26/2013	SCF	0.3	-8.5	-60.5			0.9
2/27/2013	SCF	0.5			-10.4	-70.6	0.9
2/28/2013	SCF	0.4	-9.0	-58.6			0.8
4/28/2013	SCF	0.3	-8.6	-59.2			1.0
5/8/2013	SCF	0.3	-8.9	-59.4			1.0
	Average	*0.4*	*-8.9*	*-58.9*			*1.1*
	SD		*0.5*	*1.6*			

	Measured at VU Amsterdam				Measured at UM					
SAMPLE ID	**Average O ‰**	**Average H ‰**	**n**	**Average water µL/g**	**Average O ‰**	**Average H ‰**	**n**	**Average water µL/g**	**Difference O UM-VU**	**Difference H UM-VU**
DC-S 10	-1.3	-2.1	2	0.7	-1.3	-6.9	1	2.1	0.0	-4.9
DC-S 12	-1.3	-6.3	1	0.2	-2.5	-12.0	1	1.3	-1.2	-5.7
DC-S 14	-1.5	-6.0	2	0.9	-1.3	-5.0	2	1.4	0.2	1.1
DC-S 18	-1.8	-4.2	2	0.7	-1.6	-7.2	1	2.0	0.2	-3.0
DC-S 24	-2.1	-7.4	2	1.4	-2.2	-8.4	2	1.8	0.0	-1.0
DC-S 27	-2.3	-6.4	3	2.1	-1.8	-8.0	1	3.0	0.6	-1.6
DC-S 28	-2.0	-8.1	2	2.7	-3.3	-12.1	1	1.0	-1.3	-3.9
DC-S 30	-1.7	-4.6	2	1.5	-1.8	-5.5	1	3.6	-0.1	-0.9
DC-S 33	-1.0	-0.6	2	0.8	-2.3	-8.2	1	2.6	-1.3	-7.6
DC-S 36	-2.2	-5.1	2	3.1	-1.5	-7.1	2	3.1	0.7	-2.0
DC-S 38	-1.5	-8.2	1	0.3	-2.5	-12.5	2	1.5	-1.0	-4.3
DC-S 39	-1.6	-5.4	3	1.2	-2.5	-9.0	1	1.4	-0.9	-3.5
DC-S 42	-1.7	-5.7	2	1.3	-2.0	-11.8	2	1.6	-0.3	-6.1
HS	-14.0	-105.0			-14.5	-105.3	4	3.4	-0.5	-0.3
SCF	-7.5	-55.0			-8.9	-58.9	7	1.1	-1.4	-3.9
	Average offset (UM- VU)				*-0.7*	*-2.5*				

Table 2.3: Comparison of fluid inclusion isotopic results between speleothems measured both at UM and VU. Results are for speleothems DC-S, HS and SCF. Average $\delta^{18}O$ and $\delta^{2}H$ values for both laboratories corrected to VSMOW. Also shown is the number of analyses conducted per sample and the average amount of water extracted.

2.5 Discussion

We have demonstrated the precision and accuracy of the Miami Device as well as its versatility in analyzing a range of sample types and sizes. Through repeated analysis of cave calcites, an average standard deviation of ±0.5 and ±2.0 ‰ for $\delta^{18}O$ and $\delta^{2}H$ in waters from fluid inclusions was determined.

2.5.1 Difference between Amsterdam and Miami Device

An inter laboratory offset of 1‰ for $\delta^{18}O$ and 3‰ for $\delta^{2}H$ was previously observed between the VU and Innsbruck University (IU), with the IU results being more depleted in $\delta^{18}O$ and $\delta^{2}H$ (Wainer et al., 2011). The average offset between the Amsterdam and Miami laboratories is found to be similar; with the data from the Miami Device also being more depleted in both $\delta^{18}O$ and $\delta^{2}H$ values.

2.5.2 Possible fractionation during injection and crushing

Although it is possible that some fractionation might have taken place during crushing (or injection) and subsequent expansion, it was observed that once a stable concentration of gas was attained within the analyzer, both the $\delta^{18}O$ and $\delta^{2}H$ values did not vary significantly (Figure 2.3) indicating that little fractionation occurred during this process. Furthermore, all samples analyzed with the Miami Device fall within 5‰ of the GMWL, the exception being sample HBC2 (Figure 2.4), suggesting that the $\delta^{18}O$ and $\delta^{2}H$ values have not been affected by fractionation and that the data therefore reflect a value representative of the original meteoric water composition.

As two of the samples (DCF and the HBC2) were collected from Pleistocene aged material in the Bahamas, it is possible to compare modern cave temperatures and $\delta^{18}O$water ($\delta^{18}Ow$) values of drip waters with values obtained from fluid inclusion

isotopic analysis. The oxygen isotope values of the calcite (+26.8‰ VSMOW for DCF; +25.8‰ VSMOW for HBC2) were determined and temperatures were calculated using

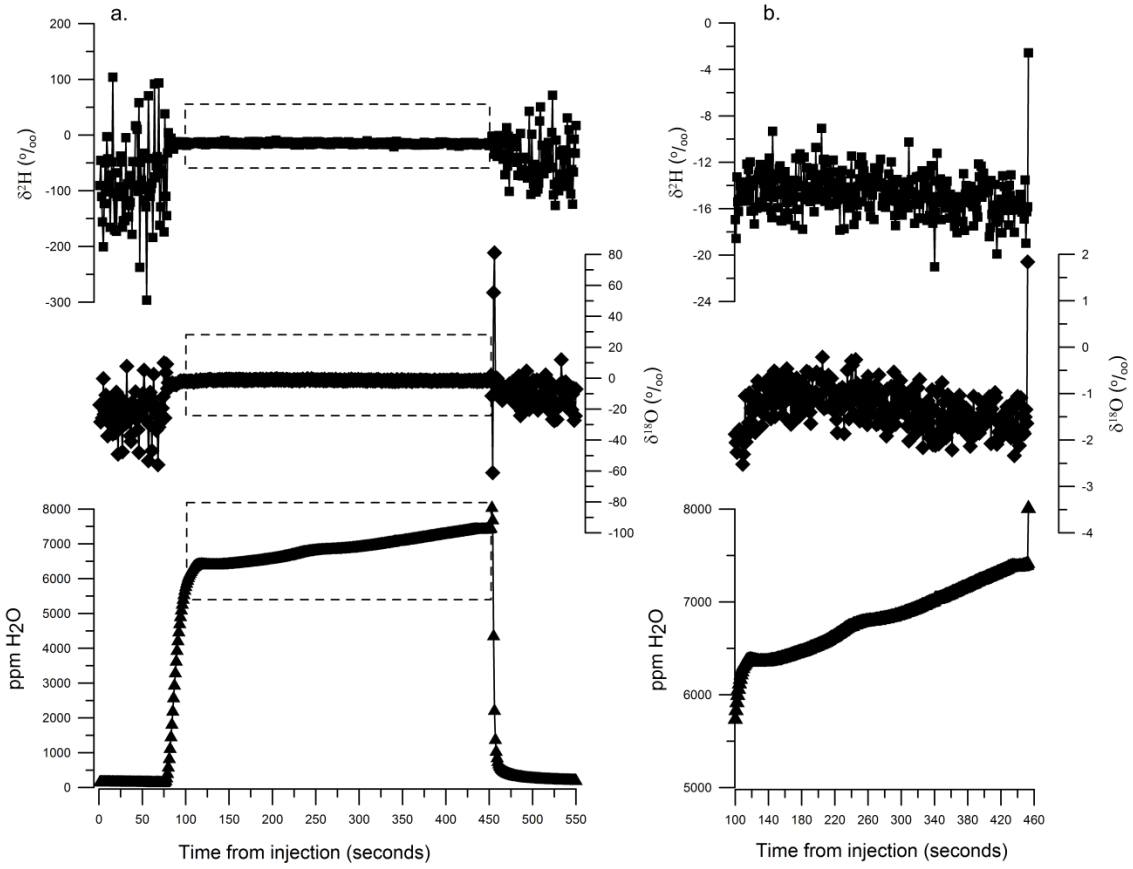

Figure 2.3: Water concentration, oxygen and hydrogen isotopes from a typical injection. a) The concentration of water (black triangles) with the corresponding $\delta^{18}O$ values (black diamonds, instrument scale) and $\delta^{2}H$ values (black squares, instrument scale) from a typical injection, demonstrating the time for the sample to reach the water isotope analyzer, stabilize and be pumped out using the method outlined in the text. Time represents seconds since injection. b) Close up of the water concentration, $\delta^{18}O$ and $\delta^{2}H$ data from the dashed square in a. The standard deviation of the concentration of H_2O during the analysis is ~ 150 ppm and close to that expected in this instrument.

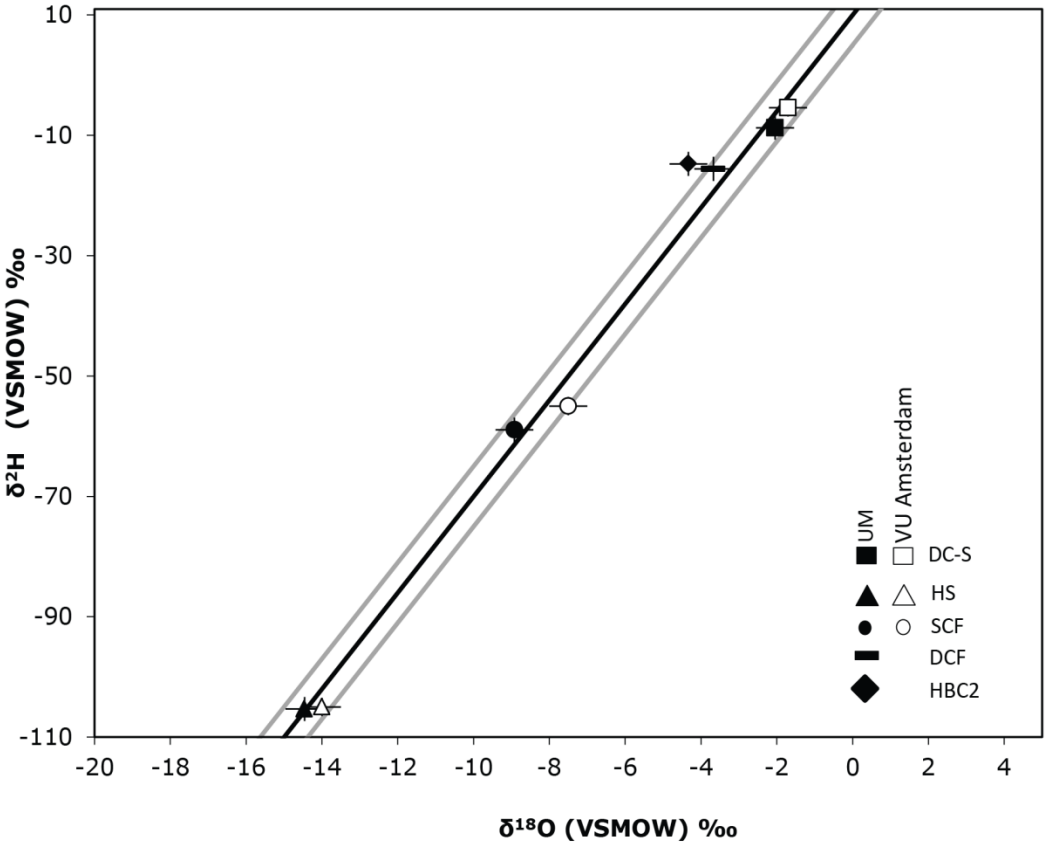

Figure 2.4: Average oxygen and hydrogen isotopes (VSMOW) plotted for all fluid inclusion isotope sample data. Black line represents the global meteoric water line and grey lines are ±5 ‰ $\delta^{18}O$. Open data symbols are sample data from VU, while black data symbols represent results from UM. Squares are DC-S data, triangles are HS data, circles are SCF results, black rectangle is DCF sample data and the black diamond is from HBC2.

the water-calcite oxygen isotope fractionation equation from Tremaine et al. (2011) Although it is not possible to know the precise $\delta^{18}Ow$ and temperature of formation as these samples are Pleistocene in age, the derived temperatures (+20.9ºC and +22.9ºC) and the measured $\delta^{18}Ow$ values of the fluid inclusions (-3.7 ‰ VSMOW for DCF and -4.3 ‰ VSMOW for HBC2), are close to that which we have observed in a modern cave in the in the Bahamas where stalagmites are currently forming (average annual

temperature = 23.2°C and drip water = -3.8 ‰ for δ^{18}Ow VSMOW). These data further support the accuracy of the analyses.

2.5.3 Possible interferences using CRDS

One of the potential drawbacks of utilizing CRDS is the possibility of interferences over the range of wavelengths used for measurement. In particular, interferences have been observed in the presence of ethanol and methanol (Brand et al., 2009) and dissolved organic carbon (DOC), such as organic contaminates from leaf (Schmidt et al., 2012; West et al., 2010) and soil extracts (Schmidt et al., 2012). Offsets as high as 15.4 ‰ for δ^{18}O and 46 ‰ for δ^{2}H have been observed when comparing CRDS to IRMS data, however, lower offsets have also been observed (Schmidt et al., 2012; West et al., 2010). The offset driven by these contaminants does not appear to be linear, and therefore is difficult to correct for (Schmidt et al., 2012; West et al., 2010). Although in an IRMS system such contaminants have the potential to be converted to either CO or H_2 gas, the concentrations are usually insignificant relative to the amount of water present and therefore their importance is minor and does not significantly impact the results (West et al., 2010). In order to alleviate the issues of interferences in CRDS systems, Picarro now offers a post-processing software, Chemcorrect™ (Picarro, Santa Clara, CA, USA) that flags samples for contamination. The software detects contaminations by monitoring the wavelength spectrum of the instrument for irregularities and comparing with known spectral features of water contaminates and the software also monitors the spectral baseline and the slope of the spectral baseline which are also indicators of potential contamination (West et al., 2011). Another potential solution from Munksgaard et al. (2011) is to diffuse the water through porous PTFE tubing which is shown to reduce the

interferences from DOC. For stalagmites, organic matter, which is typically comprised of humic and fulvic acid compounds, (Meyer et al., 2012) can be trapped in the speleothem calcite and can be useful for identifying environmental change through UV fluorescence (Perrette et al., 2005). Dissolved organic carbon is found in cave drip waters (Cruz et al., 2005), but it is not known if this extends to fluid inclusions and whether this is a potential source of contamination for fluid inclusion isotopic analysis. Future work combining UV fluorescence and fluid inclusion isotope analysis may shed light on these questions. Through careful observation of sample data, the use of correction software and the analysis of sample spectra, it is possible to identify samples which are affected by interferences.

2.6 Conclusion

Cavity ring-down spectroscopy is a lower cost and mechanically simpler alternative to the continuous flow IRMS method for the analysis of $\delta^{18}O$ and $\delta^{2}H$ values in fluid inclusions. For water extraction, we have developed a hybrid system utilizing aspects of the Amsterdam Device and the Picarro vaporizer unit. Through repeated crushes of cave calcites, the standard deviation of fluid inclusion isotope data from the Miami Device is shown to be comparable to errors reported by Dublyansky and Spotl (2009) and Vonhof et al. (2006) both which utilize IRMS based systems. Comparison of fluid inclusion isotope data between the Amsterdam Device and the Miami Device demonstrates that the Miami Device measurements accurately reflect the values of the water trapped in the mineral. Also the samples analyzed with the Miami Device fall near the GMWL, further supporting this conclusion. While we do observe offsets between the data from VU and UM, we attribute this offset to differences in the laboratory set up, considering that

similar inter-laboratory offsets have been observed between IRMS systems. As more fluid inclusion work is conducted, the ability to correct for inter laboratory biases must be addressed through the development of standards.

Chapter 3

Bahamian speleothem reveals temperature decrease associated with Heinrich stadials

Summary

Temperature reconstructions across Heinrich stadials 1-3 are presented from an absolute-dated speleothem from Abaco Island in the Bahamas to understand the nature of climate change across these intervals in the subtropical Atlantic. The stalagmite carbonate record, dated by the U-Th geochronometry technique, includes higher δ18O and δ13C values within Heinrich stadials 1, 2, and 3 followed by rapid declines at the end of the stadials. To aid in the interpretation of these results, the δ18O of fluid inclusions within the same intervals were also analyzed. These measurements, which allowed for the relative influence of temperature and δ18O of precipitation to be distinguished, suggest that changes in the δ18O values of the speleothem carbonate associated with Heinrich stadials 1 – 3 are principally driven by an average ~3 °C temperature decrease, rather than a change in the δ18O of the rainfall. These findings support previous work in other areas of the North Atlantic and are consistent with the climate response to a weakening of the Atlantic meridional overturning circulation.

3.1 Background

Ice core and deep sea sediment records of the last 65,000 years show 18 periods of abrupt climatic events known as the Dansgaard/Oeschger (D/O) cycles and 6 Heinrich stadials (Dansgaard et al., 1984). Dansgaard/Oeschger events are millennial scale alternations between warm (interstadial) and cold (stadial) periods (Bond et al., 1997). Heinrich stadials are characterized in the North Atlantic by cold periods, and are recognized in the sedimentary record as eroded terrigenous materials (Ice Rafted Debris,

IRD) deposited in the North Atlantic by ice bergs upon melting (Bond et al., 1997; Heinrich, 1988). Heinrich stadials are associated with a slowdown of the Atlantic meridional overturning circulation (AMOC) and an inter-hemispheric climate response (Wolff et al., 2010; McManus et al., 2004). Observations and models (Zhang and Delworth, 2005) support reduction in sea surface temperatures (SSTs) associated with Heinrich stadials, thought to be a result of the reduced northward heat transport, driven by the slowdown of the AMOC (Clement and Peterson, 2008) or the increase in sea/land ice (Chiang and Bitz, 2005). Reduced northern hemisphere SSTs lead to the meridional shift in the intertropical convergence zone (ITCZ) and drier conditions in the tropical northern hemisphere (Chiang and Bitz, 2005; Stager et al., 2011). During interstadial periods (*i.e.* D/O interstadial events), the inverse occurs with a poleward shift of the northern hemisphere summer ITCZ and the jet streams (Asmerom et al., 2010). However, the exact mechanisms driving these events are still not well understood (Clement and Peterson, 2008).

Various types of paleoclimate data support the global response to North Atlantic Heinrich stadials, as well as the abrupt nature of the events (Clement and Peterson, 2008). Paleoclimate records suggest that the global signature of Heinrich stadials includes: a drier Europe (Genty et al., 2003), weaker Asian monsoon (Wang et al., 2001), wetter southwestern North America (Asmerom et al., 2010; McGee et al., 2012), drier northern South America (Peterson et al., 2000), wetter southern South America (Kanner et al., 2012), an overall drier tropical Asia and Africa (Stager et al., 2011), and a gradually warming Antarctica (Wolff et al., 2010) (for a review of paleoclimate data across Heinrich stadials see Clement and Peterson, 2008). While a comprehensive picture of

climate across North Atlantic Heinrich stadials is emerging from records in both hemispheres, very few studies have been conducted in the subtropical western Atlantic (Grimm et al., 2006; Lachniet et al., 2013; Sachs and Lehman, 1999), which may be an important area for detecting the global propagation of these events and constraining climate models. In this study, geochemical data obtained from a speleothem spanning Heinrich stadials 1-3 is presented from a cave in Abaco Island, Bahamas. Each Heinrich stadial event exhibited unique characteristics, which is in agreement with other studies that have shown Heinrich stadial 1 is the strongest event (Stager et al., 2011), with almost complete shutdown in AMOC (McManus et al., 2004) and the provenance of Heinrich stadial 3 IRDs were different than the IRDs for Heinrich stadials 1 or 2 (Martins et al., 2013).

3.1.1 Speleothems as paleoclimate archives

Speleothems have proven to be valuable archives for paleoclimate reconstructions, particularly for the study of climate variability on millennial timescales (Asmerom et al., 2010; Wang et al., 2001). Stable isotope ratios of oxygen and carbon ($\delta^{18}O$ and $\delta^{13}C$) of the carbonate are the most common geochemical proxies analyzed within speleothems. There are several climatic factors that can lead to changes in the $\delta^{18}O$ values of the carbonate record (Lachniet 2004). In the case of tropical speleothems, the $\delta^{18}O$ of the carbonate is typically interpreted to be driven primarily by the $\delta^{18}O$ of the rainfall and/or the temperature of the cave (Kanner et al., 2012; van Breukelen et al., 2008) and some studies have shown that cave drip water has $\delta^{18}O$ values similar to local precipitation (Tremaine et al., 2011; van Breukelen et al., 2008). In the Bahamas and throughout the Caribbean and south Florida, there is an inverse relationship between the

amount of rainfall and the $\delta^{18}O$ of the rainwater (Baldini et al., 2007; van Breukelen et al., 2008), and therefore the amount of rainfall is considered to exert the main control on the $\delta^{18}O$ composition of the precipitation (the amount effect) (Dansgaard, 1964). However, distinguishing the competing influences of temperature and $\delta^{18}O$ of the rainwater is inherently complex when interpreting the carbonate $\delta^{18}O$ results. One approach to address the confounding influences of temperature and water $\delta^{18}O$ is through the $\delta^{18}O$ analysis of fluid inclusions. These inclusions are microscopic water filled cavities located within the speleothem calcite mineral structure which contain drip water trapped at the time of the stalagmite formation. As suggested above, the drip water is thought to directly represent precipitation, and therefore the isotopic analysis of the trapped water provides a direct measure of the temporal changes in the $\delta^{18}O$ of rainfall (hence rainfall amount). Determining the $\delta^{18}O$ value of both the trapped fluid and that of the accompanying mineral allows for the calculation of temperature at the time of speleothem formation (van Breukelen et al., 2008).

In contrast, the $\delta^{13}C$ of the carbonate is a function of the type and amount of vegetation above the cave, root respiration, organic material decomposition and the amount of water/rock interactions (Fairchild et al., 2006). Variation in the biogenic CO_2 component of the carbon is in turn influenced by precipitation amount and temperature (Genty et al., 2003). Generally the partial pressure of CO_2 (pCO_2) is expected to show an inverse correlation with $\delta^{13}C$ values in the soil horizon. Changes in the amount of rainfall or temperature could also alter the ratio of C_3 and C_4 plants, further causing isotopic changes, particularly over longer timescales (Fairchild et al., 2006). Cave ventilation may also exert control over the $\delta^{13}C$ of the CO_2 in the cave and therefore

ultimately the $\delta^{13}C$ in the cave fluids (Kowalczk and Froelich, 2010). Through the combination of both $\delta^{18}O$ and $\delta^{13}C$ of the carbonate as well as $\delta^{18}O$ of the fluid inclusions, variations in the temperature and amount of rainfall can be estimated over the sample time period.

1.2 Previous work on Bahamian speleothems

Several studies have been conducted on the formation, growth, age, and geochemistry of Bahamian speleothems, with most of the work carried out on samples from caves currently submerged in seawater (*e.g.,* Richards et al., 1994 and references therein). These speleothems formed during previous sea level low-stands and stopped forming when rising sea level flooded the caves, making the speleothems potential archives of paleo-sea level, however, it has also been shown in some instances that the speleothems ceased forming prior to seawater flooding, presumably as a result of drier conditions (Richards et al., 1994). Richards et al. (1994) also found no geochemical evidence of alteration in samples from submerged caves. Stalagmites from the Bahamas have been additionally utilized as recorders of past atmospheric $\Delta^{14}C$ concentration for radiocarbon calibrations (Hoffmann et al., 2010, Beck et al., 2001).

The aim of this work is to determine the paleoclimatic changes associated with Heinrich stadials over the last ~32,000 years by applying multiple geochemical tools. This study represents the first high resolution paleoclimate reconstruction utilizing a Bahamian speleothem and the first muti-collector ICP-MS dated speleothem from this region. Additionally, the combination of both stable isotope analyses of the carbonate and fluid inclusions is unique and the resolution of the fluid inclusion analyses for a stalagmite record from this time period is unprecedented. Finally, considering that

relatively few studies have been conducted in the subtropical western Atlantic (Escobar et al., 2012; Grimm et al., 2006; Hagen and Keigwin, 2002; Hodell et al., 2012; Keigwin and Jones, 1994; Sachs and Lehman, 1999), and even fewer studies are from terrestrial records, this study offers the opportunity to better understand abrupt climate change at this location during the Pleistocene.

3.2. Sample Locality and Methods

3.2.1 Regional setting

The modern climate of the Bahamas is primarily controlled by the easterly trade winds and winds from the west are limited to frontal passages (Baldini et al., 2007). The annual variation in air temperature ranges from 22 to 28 °C (Baldini et al., 2007). There are distinct wet and dry seasons with the wetter period between April to December driven by the Bermuda high.

The stalagmite (sample AB-DC-09) was collected from a currently submerged cave located in the middle of southern Abaco Island, Bahamas (N26°14, W77°10) in July of 2007 from a depth of 16.5 m below current sea level (Figure 3.1). The cave is accessed through a collapsed sinkhole and consists of three laterally extensive levels at ~22, 33.5 and 45 meters below sea level. The overlying bedrock of the cave is composed of Pleistocene limestone aeolianites and marine limestones (Walker et al., 2008). After collection, the speleothem was sectioned along the main growth axis (Figure 3.2 a) and sampled in the central region for U-Th geochronometry, stable C and O isotopes ($\delta^{13}C_c$ and $\delta^{18}O_c$), and $\delta^{18}O_w$ of fluid inclusions. Sample AB-DC-09 has a total length of 23 cm and is comprised of dense milky white calcite with no evidence of post-depositional diagenesis (Figure 3.2 a).

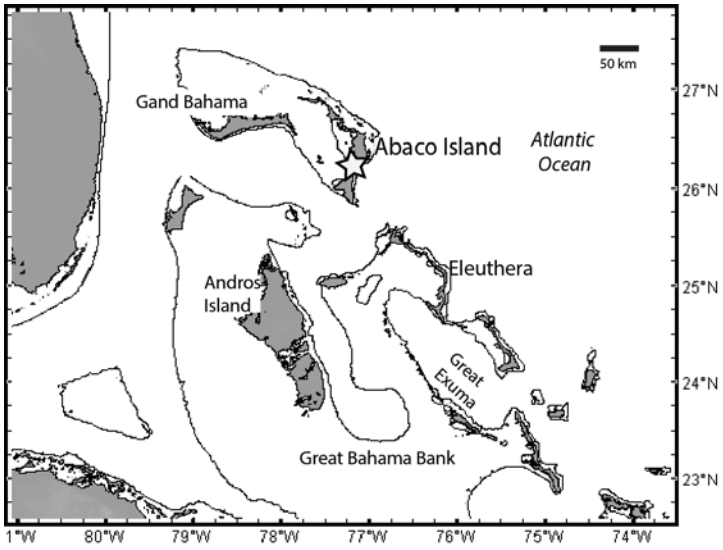

Figure 3.1: Sample AB-DC-09 was collected from Abaco Island in the Bahamas (N26°14, W77°10). Cave location is indicated by the star. Contours show 120 m bathymetry.

2.2 Geochemical methods

U-Th geochronometry: Twenty-three U-Th dates (Table 3.1) were measured at the Neptune Isotope Laboratory of the University of Miami - RSMAS utilizing a ThermoFisher-Neptune Plus multi-collector ICP-MS. Details of the U-Th geochronometry technique and propagation of random and systematic uncertainties are discussed elsewhere (Pourmand et al., 2014). Briefly, 100-200 mg of the sample was hand-drilled. Samples were then completely digested in 5 mL of 6 mol L-1 HNO_3 followed by the addition of 0.5 g of a previously calibrated ^{229}Th-^{233}U-^{236}U spike mixture (Pourmand et al., 2014). The concentrations of U and Th in the spike mixture were determined by isotope dilution mass spectrometry against a mixture of U and Th mono-elemental standard solutions and gravimetrically prepared U standard from ~1g of U

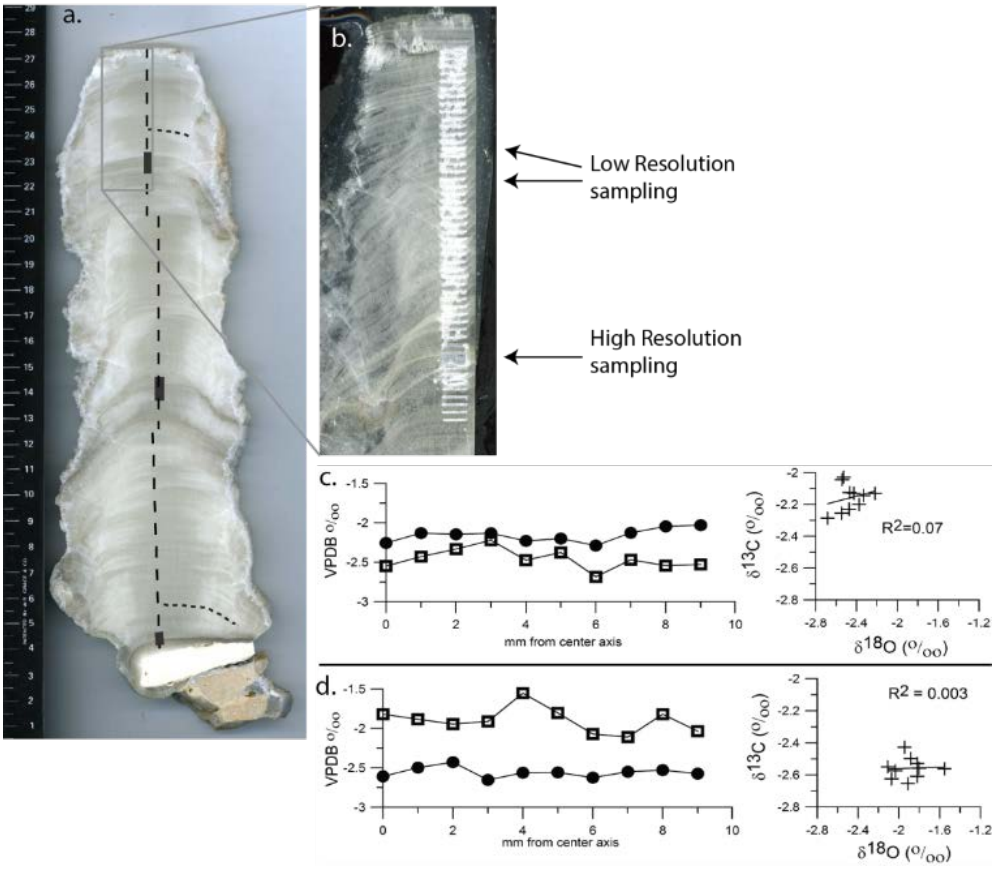

Figure 3.2: a) Photo of sample AB-DC-09 showing the sampling locations. Dashed line: low resolution analysis. Black bars: High resolution analysis. Horizontal dotted lines: location of Hendy tests. b) Photo of thin section after sampling for geochemical analysis of the upper most section of the speleothem. This demonstrates areas of both high and low resolution $\delta^{18}O_c$ & $\delta^{13}C_c$ analyses. Along the center axis, millimeter scale laminations of the speleothem calcite are found. Microscopic analysis displays no evidence of post depositional alteration or evidence of a hiatus in the center. However along the outer most portion of the stalagmite, blocky calcite is observed with minimal layering, suggesting this area may be affected by post-depositional diagenesis. c) Hendy test results from 3 cm from the top showing variation in carbon and oxygen isotopes (black circles and open squares respectively) from the center of the growth axis outward along a growth band, showing little variation in both carbon and oxygen isotopes. Also shown is low correlation between carbon and oxygen isotopes. d) Hendy test results from 23 cm from the top showing carbon and oxygen isotopes (black circles and open squares respectively) from the center of the growth axis outward, with little variation and low correlation across a growth band.

metal (full details on spike calibration are provided in Pourmand et al. (2014)). To separate U and Th from matrix elements (mainly Ca, Sr and Mg), the sample and spike mixture were loaded on to pre-packed 2-mL cartridges of U/TEVA resin (particle size 50–100 μm) from Eichrom Inc. After removal of the matrix elements, Th and U were quantitatively separated from each other in 10 mL of 3 and 0.1 mol L-1 HCl, respectively.

Higher abundance U (^{233}U, ^{235}U, ^{236}U and ^{238}U) and Th (^{229}Th, ^{232}Th) isotopes were measured in Faraday collectors while ^{234}U and ^{230}Th isotopes were measured in the secondary electron multiplier (SEM) after the ion beams passed through a Retardation Potential Quadrupole (RPQ) filter to reduce the abundance sensitivity effect. Each U and Th measurement was bracketed by two measurements of inlet system memory and measurements of CRM-112A and IRMM-035 standard solution spiked with IRMM-3636a ^{233}U-^{236}U spike, respectively. Data acquisition for U and Th isotopes and the half-masses were exported to Excel spreadsheet templates and processed using an open-source algorithm in Mathematica as presented in Pourmand et al. (2014) for calculating the U and Th concentrations, age and uncertainties (reported here as 95% confidence interval). A significant advantage of this technique is consideration for U and Th isotope covariance and propagation of uncertainties on decay constants and other sources of random and systematic uncertainties on corrected ages. The half-life values used are those presented in Edwards et al. (2003) and Fietzke et al. (2008).

The concentration of U and Th in procedural blanks, which were processed every five samples, were below 1 and 10 pg respectively and therefore no blank corrections were necessary. All ages are reported in years before present (yr BP).

Isotopic sampling on the carbonate: Sampling of the speleothem carbonate for $\delta^{13}C_c$ and $\delta^{18}O_c$ (calcite) was carried out using a New-Wave computerized micromill at both high and low resolution. Low resolution sampling consisted of one sample every 1000 μm throughout the length of the stalagmite (Figure 3.2 a & b). The low resolution analysis revealed three areas of rapid and significant isotopic shifts. These areas were subsequently analyzed at a higher resolution (20 μm sampling interval) (Figure 3.2 b). Isotopic measurements were made using a Kiel III interfaced with a Thermo-Finnigan Delta Plus Mass Spectrometer at the University of Miami. All data have been corrected for isobaric inferences at mass 45 and 46 and are reported relative to Vienna Pee Dee Belemnite (VPDB). The precision of the $\delta^{13}C_c$ and $\delta^{18}O_c$ values, determined by repeated measurement of a standard, is less than 0.1‰.

Fluid inclusions: Thirty-one oxygen and hydrogen isotopic analyses of the fluids trapped within inclusions ($\delta^{18}O_w$ and $\delta^{2}H_w$) were carried out at the University of Miami using a cavity ring-down spectroscopy instrument (L2130-i Picarro) as outlined in Arienzo et al. (2013). This system allowed for the determination of $\delta^{18}O$ of the water ($\delta^{18}O_w$) and $\delta^{2}H_w$ of the fluid inclusions from approximately 0.2 g samples, which on average yielded 0.4 μL of water from AB-DC-09 speleothem. Sampling for fluid inclusion analysis was conducted along the center of the growth axis, utilizing a band saw to extract 0.6 – 1.0 g cubes of calcite which were subsequently divided into ~0.2 g cubes for replicate analysis. The isotopic compositions of the fluid inclusions are reported relative to the Vienna Standard Mean Ocean Water (VSMOW). Each sample was analyzed 1-3 times with an average error of 0.5 ‰ for $\delta^{18}O_w$ and 2.0 ‰ for $\delta^{2}H_w$ values (Arienzo et al., 2013). As a result of the larger sample size, average sampling was

conducted at every 0.75 cm. The $\delta^{18}O_c$ of the calcite hosting the inclusion was measured on the crushed residue at the University of Miami using a Thermo-Finnigan Delta Plus mass spectrometer (see above).

3.3. Results

3.3.1 Age model

An important variable in U-Th geochronometry is the contribution of excess (unsupported) ^{230}Th to the U series equilibrium clock (Edwards et al., 2003). Isochron techniques and direct measurements from modern cave deposits provide estimates of the initial ^{230}Th. Previous studies of Bahamian speleothems forming over the last glacial maximum (LGM) utilizing isochrons suggested relatively high initial $^{230}Th/^{232}Th$ activity ratios, ranging from 7.8 ±4.0 (Hoffmann et al., 2010) to 18.7± 2.9 (Beck et al., 2001). These samples were collected from Grand Bahama Island, located to the north of Abaco Island and were forming over the LGM. To determine a representative ^{230}Th detrital activity ratio for this study, modern cave calcites from an actively forming cave in Eleuthera, Bahamas were analyzed. The results measured in the depositional slides yielded an average initial $^{230}Th/^{232}Th$ activity ratio of 2.2 ± 0.6 (for a full description of how the value was calculated, see supplementary material). These findings from speleothems suggest that for the Bahamas, there is a wide range of measured initial $^{230}Th/^{232}Th$ activity ratios from 2.2 to 18.7. The published data from samples with higher initial $^{230}Th/^{232}Th$ activity ratios were samples that were forming over the LGM, suggesting the cave had a higher Th input during the LGM than the modern samples from Eleuthera. Other studies have focused on characterizing the U and Th concentrations in carbonates and waters of the Bahamas, and these studies demonstrate wide variability in

concentrations and several potential sources of detrital Th, including aeolian inputs (*e.g.,* Robinson et al., 2004).

Considering that stalagmites from Abaco Island have yet to be studied, there are no available values to compare to for this island. Therefore, from the results outlined above (and the supplementary information), the activity ratio of 3.7 ± 0.6 for initial $^{230}Th/^{232}Th$ is considered a reasonable estimate. It must be noted that we make the assumption that the initial Th activity ratio was unchanging throughout the deposition of the stalagmite. Three U-Th ages resulted in age reversals and were not considered in the age model (Figure 3.3). Two of the ages located ~5 cm from the top were younger than the previous ages (Table 3.1), which may be driven by a reduction in the initial $^{230}Th/^{232}Th$ component during this time period (see supplementary Figure 3.1). Considering the disagreement between these two ages and the surrounding ages, we do not utilize these two ages as part of the age model. One U-Th age 11 cm from the top was older than the previous ages, possibly suggesting an increase in the initial $^{230}Th/^{232}Th$ component at this time. Considering the good agreement between surrounding ages, we discount this age as well and do not include it in the final age model.

An additional source of error may reside in the uncertainty of the initial $^{230}Th/^{232}Th$ activity ratio value. However, the age model does not significantly change with varying initial Th value for the younger interval of the sample (supplementary Figure 3.2). The initial $^{230}Th/^{232}Th$ activity ratio does impact the calculated age on the oldest U-Th ages, and these ages do consist of the largest errors. The final age model for the speleothem was therefore developed utilizing twenty U-Th ages through linear

Distance from Top µm	238U (ppb)	(95% CI) ±	(230Th/238U)	(95% CI) ±	(230Th/232Th)	(95% CI) ±	Uncorr. Age (y)	(95% CI) ±	(234U/238U) initial (corrected)	(95% CI) ±	Corr. Age (y)	(95% CI) ±
17000	201.838	0.124	0.1332	0.0007	57.6	0.94	15394	77	1.0131	0.00259	14468	166
35000	179.526	0.097	0.1360	0.0006	54.5	1.56	15882	71	1.0047	0.00267	14872	178
42500	209.472	0.103	0.1355	0.0009	66.8	2.30	15717	110	1.0112	0.00249	14902	174
60000	150.938	0.086	0.1552	0.0010	47.9	1.12	18572	123	0.9921	0.00278	17244	246
72500	188.150	0.113	0.1545	0.0014	102.5	1.90	18054	176	1.0145	0.00251	17453	198
89000	204.483	0.108	0.1607	0.0009	43.5	0.27	18956	109	1.0087	0.00265	17465	260
95000	203.633	0.110	0.1569	0.0007	81.8	2.81	18527	78	1.0053	0.00250	17753	146
103000	191.743	0.103	0.1615	0.0009	95.4	4.01	19043	111	1.0093	0.00248	18363	156
115000	245.881	0.129	0.1683	0.0008	144.4	8.89	19852	96	1.0129	0.00256	19385	126
124000	214.688	0.106	0.1732	0.0008	80.7	0.52	20586	96	1.0085	0.00274	19722	169
125000	212.781	0.109	0.1739	0.0009	86.9	3.56	20597	105	1.0117	0.00255	19795	168
133000	180.454	0.083	0.1781	0.0010	77.4	0.96	21486	120	0.9972	0.00245	20551	191
137000	183.408	0.109	0.1876	0.0022	128.6	1.69	22309	284	1.0159	0.00253	21727	299
145000	164.362	0.082	0.1923	0.0010	48.3	0.36	23646	124	0.9875	0.00258	22007	294
149000	179.101	0.104	0.2067	0.0009	47.0	0.85	25148	100	1.0051	0.00249	23366	299
156000	192.366	0.113	0.2210	0.0011	110.9	0.83	26649	126	1.0215	0.00258	25859	177
178000	202.090	0.127	0.2235	0.0011	139.6	0.93	27030	127	1.0201	0.00252	26394	162
199000	204.470	0.150	0.2427	0.0010	38.2	0.17	29794	122	1.0170	0.00271	27239	433
210000	229.838	0.113	0.2435	0.0010	44.5	0.86	30055	124	1.0125	0.00271	27849	378
222000	202.531	0.126	0.2879	0.0013	19.0	0.11	36204	172	1.0209	0.00261	30025	1036
Not used in age model:												
50000	128.045	0.084	0.1324	0.0009	53.9	0.92	15640	112	0.9918	0.00248	14633	194
55000	129.585	0.074	0.1281	0.0006	69.1	2.56	15145	62	0.9888	0.00251	14384	138
110000	211.462	0.127	0.1779	0.0009	79.5	0.55	20926	110	1.0206	0.00263	20038	177

Table 3.1: Stalagmite AB-DC-09 ^{230}Th dating results for samples dated in the Neptune Isotope Laboratory at the University of Miami (see Pourmand et al., 2014 for detailed methodology), ages have been corrected for a ^{230}Th/^{232}Th activity ratio of 3.7 ± 0.6 to account for detrital ^{230}Th. All uncertainties are calculated as 95% confidence interval (95% CI). Ratios in parentheses are activities.

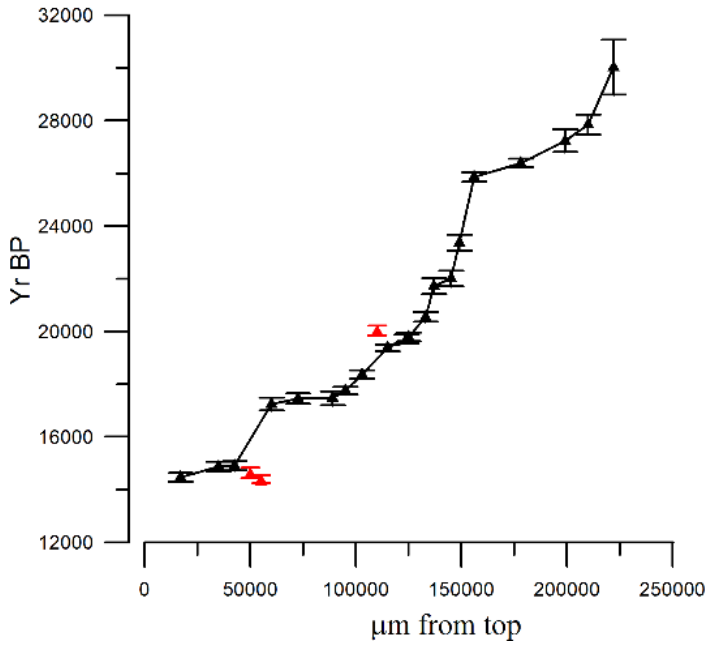

Figure 3.3: Age model (black) based on twenty U-Th ages, years before present (yr BP). Random and systematic sources of uncertainty, including the uncertainties on decay constants, are propagated and reported at 95% confidence interval (see Pourmand et al. (2014) for details). The age model was developed by linear interpolation between adjacent ages. Red triangles indicate U-Th results not included in the age model.

interpolation between nearest ages (Figure 3.3). When plotting the age model with other paleoproxies from the region, we find good agreement in the timing of isotopic shifts between records, (discussed in detail in section 4.4), which further validates the decision to utilize a value of 3.7± 0.6 for initial $^{230}Th/^{232}Th$ activity ratio.

The results for U-series geochronometry (Table 3.1) indicate that the stalagmite formed between 14.1 to 31.3 ka before present with a weighted average growth rate of 13 µm/year (Figure 3.3 & 3.4). There is no evidence for any growth hiatuses throughout the sample from either the age measurements or petrographic thin section analysis, however there is evidence for periods of decreased growth rate from the U-Th geochronometry. The lowest growth rate occurred from 22 to 26 ka BP (~ 14.5-15.5 cm from top) with an

average growth rate of 3 μm/year. There are two additional periods of decreased growth rate from 14.9 to 17.3 ka BP (~ 4.2 to 6 cm from the top) and 27.8 to 30 ka BP (~ 21 to 23 cm from the top). There is evidence of three small layers of darker laminations at ~5, 14.5 and 22 cm from the top (Figure 3.2 a & b) which correlate with the three short periods of reduced calcite precipitation. Based on the age model, however, there is no evidence for a hiatus at these three locations of darker lamina.

3.3.2 Tests for kinetic fractionation

Several studies have shown that the $\delta^{18}O$ and $\delta^{13}C$ can be affected by kinetically driven fractionations during the deposition of the carbonate which can overwhelm environmental and climatic signals (Hendy, 1971; Lachniet, 2009). An approach often used to examine the role of kinetic effects is known as the "Hendy test" (Hendy, 1971) in which the lateral variation in a chemical parameter within the speleothem is measured. Assuming that sampling can be carried out along a growth band, the following criteria must be met for the Hendy test: i) an absence of lateral increases in $\delta^{18}O_c$ and $\delta^{13}C_c$ values, and ii) a low correlation between $\delta^{18}O_c$ and $\delta^{13}C_c$ values. If these conditions are met, then it is assumed that minimal kinetic fraction has taken place. However, studies have demonstrated that this test may not be sufficient to rule out kinetic fraction (Mühlinghaus et al., 2009). Other authors have suggested a more robust method is to conduct replication tests, in which multiple stalagmites from the same cave are measured and if the $\delta^{13}C_c$ and $\delta^{18}O_c$ trends are replicated, this supports kinetic fractionation not having occurred (Dorale and Liu, 2009). We present two locations across which lateral variation of $\delta^{18}O_c$ and $\delta^{13}C_c$ values were measured. Sampling for kinetic fractionation was conducted at one millimeter increments from the center of the growth axis sampling

outward along a growth band. As shown in Figure 3.2 c and d, tests for kinetic fractionation demonstrate low correlation and no significant increase for both $\delta^{13}C_c$ and $\delta^{18}O_c$ across a lamina. This demonstrates that significant fractionation for $\delta^{13}C_c$ and $\delta^{18}O_c$ has not occurred for this speleothem. Additionally, in the currently active cave from Eleuthera Island, the measured $\delta^{18}O$ of the calcite, temperature of the cave, and drip water $\delta^{18}O$ support the calcite is precipitated in equilibrium (see supplementary material).

For fluid inclusions, isotopic fractionation after deposition can occur through fractionation between the water and the surrounding calcite, thereby altering the isotopic composition of the trapped water, however, such a fractionation in the humid subtropics should be minimal (van Breukelen et al., 2008). The fluid inclusions are representative of paleoprecipitation, therefore results should fall on the global meteoric water line (GMWL), which defines the linear $\delta^{18}O_w$ versus $\delta^{2}H_w$ relationship for all meteoric waters (Craig, 1961). Fluid inclusion results plot near the GMWL suggesting that the $\delta^{18}O_w$ and $\delta^{2}H_w$ values have not been affected by fractionation and the data therefore are representative of the original meteoric water composition (Figure 3.5).

3.3.3 Carbon and oxygen isotopes of carbonate

The speleothem AB-DC-09 was sampled at both high (one sample every ~2 years) and low resolution (one sample every ~50 years). To aid with the analysis of the data, the $\delta^{13}C$ and $\delta^{18}O$ carbonate isotope results are plotted with a 50 year rectangular interpolation (Figure 3.4 a & b). A comparison of the $\delta^{13}C$ and $\delta^{18}O$ of the speleothem calcite ($\delta^{18}O_c$ and $\delta^{13}C_c$) with the derived age model demonstrates significant variations in the isotopic value of the calcite (Figure 3.4 a & b). The variation in the $\delta^{13}C_c$ results are 6.2 ‰ for the sample, with the most positive $\delta^{13}C_c$ value of +3.2 ‰ V-PDB occurring at

30.9±1 ka BP. Above average $\delta^{13}C_c$ values are also found at 15±0.2 ka and 24.7±0.2 ka BP (Figure 3.4 a). Similar results are found in the $\delta^{18}O_c$ record with the most positive $\delta^{18}O_c$ value of -0.2 ‰ V-PDB at 15 ±0.2 ka and above average $\delta^{18}O_c$ values at 24.1±0.2 ka and 30.9±1 ka BP (Figure 3.4 b). Overall, a total of 3.5 ‰ variation is observed in the $\delta^{18}O_c$ results. A similar trend for each positive C and O isotope event is observed, with a gradual increase leading to a maximum, followed by a more rapid decline. For the 15 ka event, the gradual increase begins at 17.4 ka BP and reaches a maximum at ~15 ka BP, followed by a rapid decrease (~200 years) in $\delta^{18}O_c$ and $\delta^{13}C_c$. The trend is also observed across the 24.5 ka event with an increase beginning at 25.5 ka BP to a maximum, followed by a decrease. For the oldest event, maximum $\delta^{18}O_c$ and $\delta^{13}C_c$ values occurred at ~31 ka and declined over ~200 years after the maximum. In summary, the carbonate results support three unique shifts, of which the least significant in both $\delta^{13}C_c$ and $\delta^{18}O_c$ is the 24.5 ka BP event (Figure 3.4 a & b).

3.3.4 Fluid inclusions

A comparison of the $\delta^{18}O_w$ measured on the fluid inclusions with the derived age model from U-Th geochronometry demonstrates minimal variations in the isotopic value of the fluids (Figure 3.4 c). The $\delta^{2}H_w$ and $\delta^{18}O_w$ measured on the fluid inclusions support variations of 11.7 ‰ and 1.6 ‰ over the studied interval with average values of -8.6 ‰ and -2.5 ‰ V-SMOW in $\delta^{2}H_w$ and $\delta^{18}O_w$ (Table 3.2). The variability in $\delta^{18}O_w$ value is relatively small compared to the changes in the $\delta^{18}O_c$ value (~3.5 ‰, Figure 3.4 c). The data support a minimum $\delta^{18}O_w$ value at 25 ka BP and a maximum $\delta^{18}O_w$ value at 30.3 ka BP.

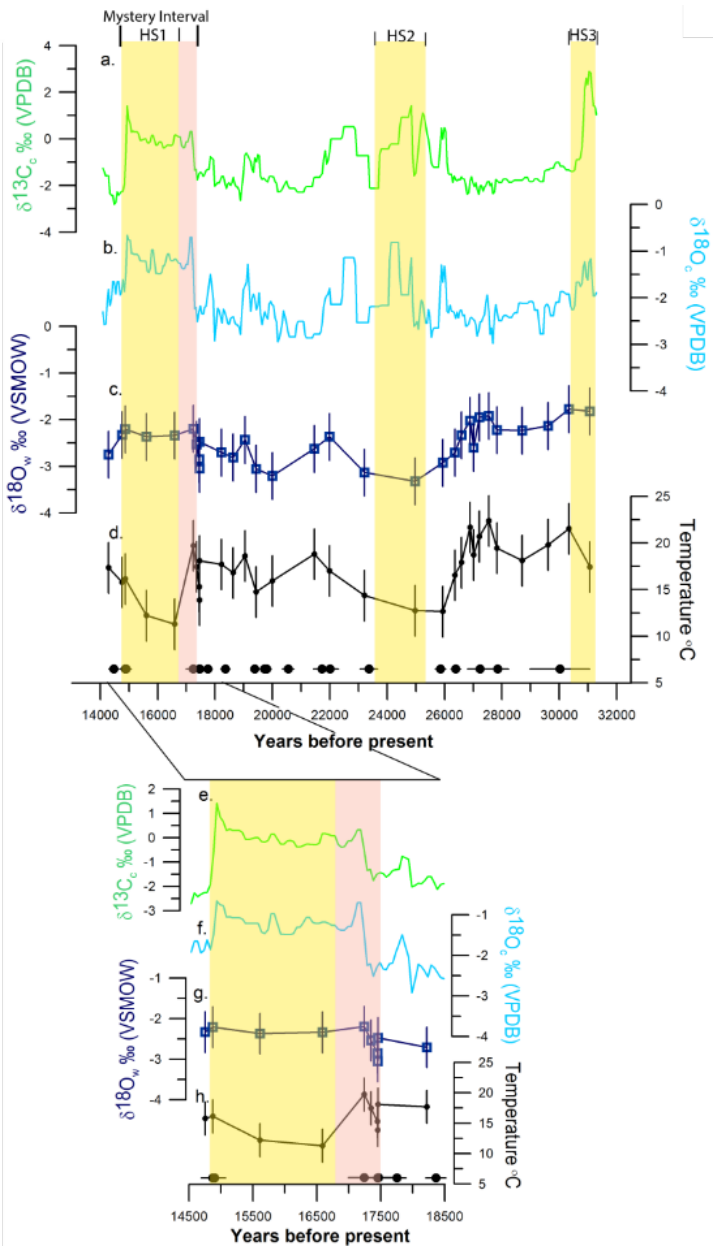

Figure 3.4: a and b) Carbon isotope values of the carbonate (green) time series from AB-DC-09 plotted with $\delta^{18}O_c$ (blue) from the same sample. Both are plotted with a 50 year interpolation. c) Dark blue squares are fluid inclusion $\delta^{18}O_w$ water results. d) Average temperature from fluid inclusion results time series is shown in the solid black line, calculated using the equation from Tremaine et al. (2011). e-g) Same as a-d from 18,500 to 14,500 years BP. Yellow bars are Heinrich stadials (HS) 1, 2 and 3, with the red bar indicating the beginning of the "Mystery Interval"(Denton et al., 2006).

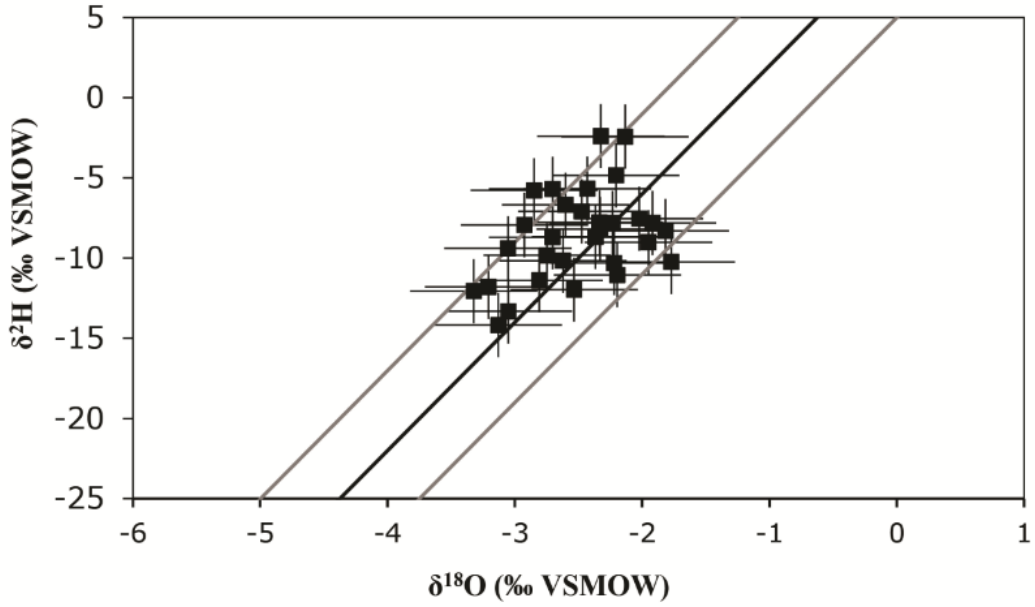

Figure 3.5: The $\delta^{18}O_w$ and δ^2H_w values from fluid inclusion water isotopes plotted with the GMWL in black and ±5 ‰ δ^2H of the GMWL in grey. Samples all fall near the GMWL suggesting that the water isotopes have not been significantly fractionated.

3.4. Discussion

3.4.1 Climate interpretation of the oxygen isotope record

The $\delta^{18}O_w$ values of the fluid inclusions shows an overall 1.6 ‰ decline from 30.3 to 25 ka. Decreases in $\delta^{18}O_w$ are normally attributed to the 'amount' effect (Dansgaard, 1964) and therefore this change suggests an increase in the amount of precipitation over this period, an interpretation supported by a progressively increasing growth rate. The $\delta^{18}O_c$ record shows maxima at ~15±0.2, 24.1±0.2, and 30.9±1 ka BP and the timing of these events is associated with Heinrich stadials 1, 2, and 3 (Figure 3.6). In contrast to a significant increase of $\delta^{18}O_c$ values within each of the three Heinrich stadials, the $\delta^{18}O_w$ data obtained from the fluid inclusions reveals only minimal changes. For example, the average change in the $\delta^{18}O_w$ value across Heinrich stadial 1, from 16.6

cm from top	Age YBP	Average $\delta^{18}O_w$ ‰ (VSMOW)	Average $\delta^{2}H_w$ ‰ (VSMOW)	n	$\delta^{18}O_c$ ‰ (VPDB)	Temperature [1] (°C)
		± 0.5 ‰	± 2.0 ‰			± 2.7 °C
0.9	14289	-2.7	-9.8	2	-2.3	17.3
3.0	14755	-2.3	-2.4	2	-1.6	15.8
3.6	14875	-2.2	-4.8	2	-1.6	16.1
4.8	15612	-2.4	-8.7	3	-1.0	12.2
5.5	16588	-2.3	-7.8	1	-0.7	11.3
6.0	17244	-2.2	-11.1	3	-2.2	19.7
6.6	17349	-2.5	-12.0	1	-2.1	17.5
7.2	17449	-2.8	-5.8	2	-2.0	15.3
8.0	17455	-3.1	-13.3	2	-2.0	13.9
8.5	17459	-2.5	-7.1	2	-2.2	18.1
10.1	18221	-2.7	-5.7	2	-2.4	17.7
10.6	18623	-2.8	-11.4	2	-2.3	16.8
11.1	19049	-2.4	-5.7	3	-2.3	18.6
11.6	19429	-3.1	-9.4	2	-2.1	14.8
12.7	19996	-3.2	-11.8	1	-2.5	15.9
13.6	21457	-2.6	-10.2	2	-2.5	18.8
14.5	21989	-2.4	-8.7	2	-1.9	17.0
14.9	23203	-3.1	-14.2	1	-2.1	14.4
15.4	24976	-3.3	-12.1	1	-2.0	12.8
16.0	25940	-2.9	-7.9	3	-1.6	12.6
17.7	26365	-2.7	-8.7	2	-2.1	16.6
18.3	26591	-2.3	-8.2	1	-2.0	17.9
19.1	26892	-2.0	-7.5	2	-2.4	21.7
19.4	27013	-2.6	-6.7	2	-2.5	18.7
19.9	27214	-1.9	-9.0	2	-2.2	20.7
20.5	27539	-1.9	-7.8	2	-2.5	22.4
21.0	27827	-2.2	-10.3	3	-2.2	19.5
21.5	28705	-2.2	-7.8	2	-2.0	18.1
22.0	29612	-2.1	-2.4	2	-2.2	19.8
22.4	30337	-1.8	-10.2	2	-2.1	21.5
22.8	31062	-1.8	-8.3	2	-1.4	17.4

[1] Temperature calculated from Tremaine et al., 2011

Table 3.2: Fluid inclusion oxygen and hydrogen isotope values with an average error of 0.5 and 2.0 ‰ respectively. Temperature was calculated from Tremaine et al. (2011), the average error of 2.7 °C was calculated by accounting for the errors on the fluid inclusion analyses.

to 15 ka BP, is 0.2 ‰ which is less than the analytical uncertainty. The average change across Heinrich stadial 2, from 26 to 24 ka BP, is 0.4 ‰ for $\delta^{18}O_w$ value (Figure 3.4 c). The increase in $\delta^{18}O_c$ values across the Heinrich stadials, which is much greater than that

found in the $\delta^{18}O_w$ results, most likely arises from lower temperatures, rather than a significant change in the $\delta^{18}O_w$ or precipitation amount. The $\delta^{18}O_w$ values, when combined with $\delta^{18}O_c$ values, allows for the calculation of the temperature at the time of mineral formation. While caves generally maintain a constant temperature throughout the year (representative of mean annual temperature), over longer time periods, speleothems can record decadal to centennial scale changes in temperature. Utilizing the equation presented in Tremaine et al. (2011), which defines the temperature dependent fractionation relationship for stalagmites, temperature variations on the order of 11 °C (Figure 3.4 d, Table 3.2) for the sample were calculated. The average temperature, 17.2 ±2.7 °C, is cooler than the average modern annual temperature for the Bahamas (average annual temperature = 22 to 28 °C (Baldini et al., 2007)) and typical temperatures within modern dry caves in the area (average annual cave temperature = 23.2°C (Arienzo et al., 2013)). Heinrich stadials 1, 2, and 3 are represented by cooler temperatures, with the average temperature across Heinrich stadials 1, 2 and 3 of 14.6 ±2.7 ºC, and Heinrich stadial 1 being the coolest event (Figure 3.4 d).

3.4.2 Climate interpretation of the carbon isotope record

Both the $\delta^{13}C_c$ and $\delta^{18}O_c$ results consists of increased values around 15±0.2, 24.1±0.2, and 30.9±1 ka BP suggesting that similar environmental factors influenced the $\delta^{13}C_c$ and $\delta^{18}O_c$ composition of the stalagmite during Heinrich stadials. As the $\delta^{18}O_c$ value across Heinrich stadial events is primarily driven by changes in the cave temperature, we suggest that the increases in the $\delta^{13}C_c$ values are indirectly driven by cooling during these Heinrich stadials. Potentially, the increased $\delta^{13}C_c$ values are a result of a decline in soil microbial activity which increases the $\delta^{13}C_{DIC}$ ratio of the drip water

during periods of cooler temperatures. Assuming changes in cave ventilation did not occur during sample deposition, the $\delta^{13}C_c$ ratio of the speleothem is most likely driven by changes in the soil zone or the vegetation above the cave. Support for this notion comes from similar results found in a cave in France, where lower $\delta^{13}C_c$ values during warm periods were driven by drip water having a greater biogenic CO_2 component (Genty et al., 2003). Nevertheless, it is not possible to rule out the potential influence of changes in the amount of precipitation on the $\delta^{13}C_c$ record, as is possibly supported by the decreases in growth rates during the periods of increased $\delta^{13}C_c$ values. An increase in the $\delta^{13}C_c$ ratio of the carbonate can be driven by aridity, which leads to a reduction in soil microbial activity, or a greater proportion of C_4 versus C_3 plants.

3.4.3 Climate variability in the context of the Atlantic basin

Proxy records from throughout the Atlantic not only support climatic shifts associated with Heinrich stadials, but are in good agreement with the timing of Heinrich stadials 1-3 in the sample studied here (Figure 3.6). These reconstructions support the global scale response to Heinrich stadials. The difference in climatic expression between northern hemisphere records (*e.g.,* Hulu Cave, Cariaco Basin, and the Bahamas) compared to southern hemisphere records (*e.g.,* Pacupahuain Cave) demonstrates the anti-phased response across Heinrich stadials (Broecker, 1998; Kanner et al., 2012; Peterson et al., 2000; Wang et al., 2001)(Figure 3.6). This anti-phased relationship between the hemispheres is in part due to a meridional shift in climate across Heinrich stadials and is well documented in the ice core records with the Greenland ice core records supporting cooling and the ice cores from Antarctica supporting warming during Heinrich stadials (Broecker, 1998; Wolff et al., 2010).

The Bahamian speleothem record, along with other proxies from the subtropical/tropical western Atlantic, support overall drying and/or cooling associated with Heinrich stadials (Escobar et al., 2012; Lachniet et al., 2013; Peterson et al., 2000)(Figure 3.6). This coherence in climate expression among the North Atlantic tropical records across Heinrich stadials can be explained by a meridional shift in climate. An alkenone-derived SST record from the Bermuda rise across Heinrich stadials 4 and 5 supports a ~3-5 °C decrease in SSTs (Sachs and Lehman, 1999) suggesting SSTs also may have declined during earlier Heinrich stadials. Further south, a lake record from Guatemala supports increased aridity and a 6-10 °C cooling associated with Heinrich stadial 1 (Escobar et al., 2012; Hodell et al., 2012). The temperatures observed during Heinrich stadial 1 are lower than modern mean annual temperature for Guatemala (mean annual temperature = 26 °C) (Hodell et al., 2012). The increased aridity and cooling in Guatemala is thought to be driven by a southerly shifted ITCZ and decreased tropical Atlantic SSTs (Escobar et al., 2012; Hodell et al., 2012). The amount of cooling observed in the Guatemala and the Bermuda records across Heinrich stadials is similar to the cooling observed in the Bahamas record. Modeling results also support decreased temperatures for the tropical northern hemisphere coincident with Heinrich stadials, however the modeled temperature changes are much less (Murphy et al., 2014; Zhang and Delworth, 2005).

As suggested above, while the geochemical data in the speleothem record from the Bahamas supports a decrease in temperature, it does not rule out the possibility of enhanced aridity across these events, which potentially may drive the variability in the

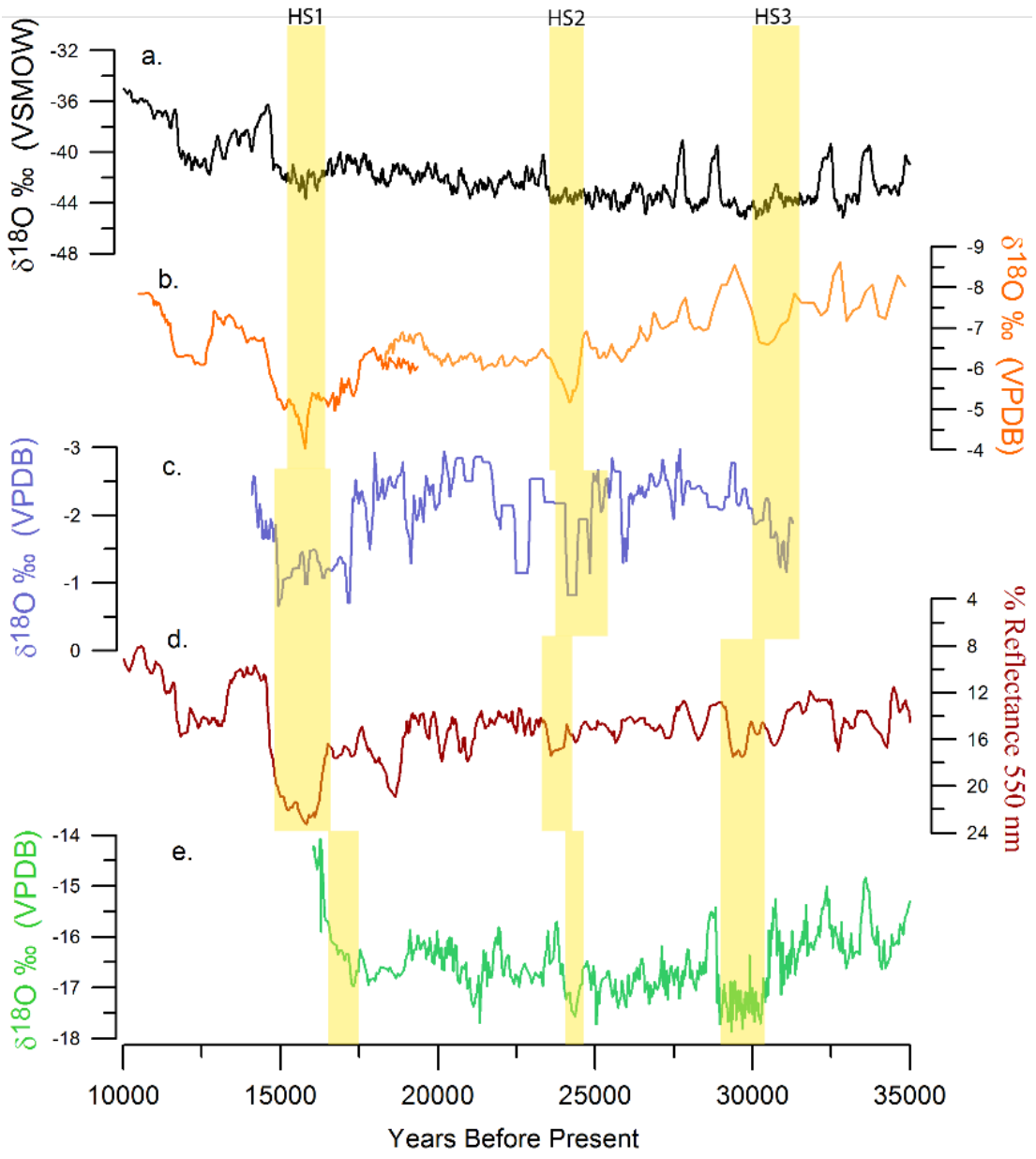

Figure 3.6: Compilation of paleoclimate studies from throughout the Atlantic. a) $\delta^{18}O$ time series from NGRIP ice core (black) data from Wolff et al. (2010) plotted with a 5 point running average. b) In orange, $\delta^{18}O$ time series from Hulu Cave, data from PD and MSD samples from Wang et al. (2001) note the axis is reversed. c) Oxygen isotope time series from this study (sample AB-DC-09) plotted with a 50 year interpolation. Note the axis is reversed. d) Cariaco Basin reflectance (red) at 550 nm, axis reversed from Peterson et al. (2000) with a 5 point smoothing. e) Green is $\delta^{18}O$ record from Pacupahuain cave, Peru from Kanner et al. (2012).

carbon isotopic record. A speleothem record from southwestern Mexico demonstrates a reduction in the North American Monsoon associated with Heinrich stadial 1 driven by the southerly shifted ITCZ and reduced AMOC (Lachniet et al., 2013). A southerly shift in the ITCZ would be accompanied by an expanded Bermuda high, which could have led to an increased aridity in the Bahamas across Heinrich stadials (Hodell et al., 2000).

In contrast to the data presented here, a record based on pollen from Lake Tulane, Florida in the southeastern U.S. suggests warmer and wetter Heinrich stadials (Grimm et al., 2006). These authors attributed the warming and increased rainfall to a slowdown of the AMOC leading to a reduction in the transport of heat from the Gulf of Mexico and thereby forcing the observed warmer and wetter climate in Florida (Grimm et al., 2006). Nevertheless the same climatic response may not be observed in the Bahamas as a result of the location of Abaco Island, on the eastern edge of the Bahamas platform, and therefore this study site may not have been influenced by changes in the Gulf of Mexico. Furthermore, the postulated warming of the Gulf of Mexico from the Florida record is not consistent with the simulated climate response to an AMOC shut down (Clement and Peterson, 2008 and references therein) rather, most climate models suggest a cooling of the entire North Atlantic, including the Gulf of Mexico.

In many paleoclimate proxy reconstructions, Heinrich stadial 1 is a larger magnitude event compared to stadials 2 and 3 (Stager et al., 2011) (Figure 3.6). In the record presented here, Heinrich stadial 1 is characterized by the greatest change in $\delta^{18}O_c$ and temperature (observed ~ 5 º C temperature decrease), while Heinrich stadial 2 exhibits minimal changes and Heinrich stadial 3 demonstrates a larger shift in $\delta^{13}C_c$ value. The reduced geochemical change across Heinrich stadial 2 may be due to a

minimal change in the AMOC during this event (Lynch-Stieglitz et al., 2014; McManus et al., 2004).

Based on paleoclimate reconstructions, Heinrich stadial 1 has been shown to be the strongest event and a period punctuated with climatic changes. Heinrich stadial 1 has also been considered a part of the so-called "Mystery Interval", from 17.5 to 14.5 ka BP (Denton et al., 2006) and corresponding to a period of prolonged hydrologic changes (Broecker et al., 2009; McGee et al., 2012). In this speleothem record from the Bahamas, there is evidence for climate variations associated with the "Mystery Interval" (Figure 3.4, e-h). Fluid inclusion results suggest a temperature increase and/or precipitation change from ~17.5 to ~16.9 ka BP followed by a progressively cooler period from ~16.9 to 15 ka BP (Table 3.2, Figure 3.4 g & h). The cooler period is identified as Heinrich stadial 1. Similarly, in Guatemala, a lake record indicates a cold and dry period beginning around 18 ka BP, interrupted by a wetter and warmer period around 17 ka BP, followed by a return to drier and cooler temperatures at approximately 16.1 ka BP (Escobar et al., 2012; Hodell et al., 2012). The authors suggest the two cold and dry periods observed in Guatemala are driven by two separate North Atlantic IRD events (Escobar et al., 2012). A multi-proxy study of a core from the Cariaco Basin of the "Mystery Interval" supports the drier climate associated with Heinrich stadial 1 is interrupted by a shift to wetter climate conditions (Escobar et al., 2012; Yurco, 2010). While the exact timing of these climatic shifts varies between the various records, these records do support that the "Mystery Interval" is a period of climate variability for the subtropical/tropical Atlantic.

Additional to the observed geochemical variability associated with the last three Heinrich stadials and the "Mystery Interval", there are observed increases in the $\delta^{18}O_c$ and $\delta^{13}C_c$ of the carbonate at 19±0.2 and 22.6±0.2 ka before present. The magnitude of the isotopic shifts at 19 and 22.6 ka BP are less than the isotopic shifts observed during Heinrich stadial events (at 19 ka BP, a 1.7‰ decrease in the $\delta^{13}C_c$ value and at 22.6 ka BP a 2 ‰ decrease for $\delta^{13}C_c$). This may suggest these isotopic variations are driven by climatic changes which are not as significant. Similarly, Bond et al. (1997) observed increased IRD deposits at similar time periods. Therefore these may also be periods of decreased temperatures and/or precipitation.

The resumption of AMOC at the end of Heinrich stadial 1 is believed to have caused an increase in SSTs in the North Atlantic (McManus et al., 2004), leading to the northward shift of the ITCZ and the observed shift to wetter and warmer conditions in the northern tropics and the start of the Bolling-Allerod period (Peterson et al., 2000). This is also supported by the increase in temperatures by ~ 4 ºC after Heinrich stadial 1 from the fluid inclusion results (Figure 3.4 d).

While other climate records for the same time period from nearby localities such as Cariaco Basin (Peterson et al., 2000) and stalagmites from the Peruvian Andes (Kanner et al., 2012) have recorded millennial scale variations (*e.g.,* Dansgaard/Oeschger (D/O) events) there is no evidence of D/O variability in the isotopic record of sample AB-DC-09. A similar observation was made from speleothems collected from Borneo in which the geochemistry of the speleothems recorded Heinrich stadials, but not the D/O events (Carolin et al., 2013). The lack of evidence for D/O events suggests that D/O events are different than Heinrich stadials either in the forcing mechanism, the global

propagation, the geographic expression, or how these events are recorded in the speleothems (Carolin et al., 2013).

3.5. Conclusion

The stalagmite record reported in this paper reveals three distinctive climatic changes during the last glacial period, each coincident with a Heinrich stadial. The $\delta^{18}O_c$ and $\delta^{13}C_c$ data support significant shifts within the Heinrich stadials, while minimal changes occur in the $\delta^{18}O$ of the water contained in fluid inclusions. The geochemical results demonstrate that Heinrich stadials 1- 3 are characterized by a temperature decrease and are in good agreement with regional paleoclimate data for Heinrich stadials. The observed temperature changes for the Bahamas speleothem across Heinrich stadials are consistent with paleoclimate records from the Western Atlantic. We propose the average temperature decline of ~3 ºC during Heinrich stadials, to an average temperature of 14.6 ±2.7 ºC, is due to the meridional shift in the climate that led to cooler subtropics. The results suggest variable geochemical responses to each of the events, with Heinrich stadial 1 being the most extreme event, with up to a 5 ºC temperature decline is observed. Finally, the results presented here support the teleconnection between the subtropical Atlantic and cooling in the North Atlantic and the sensitivity of the Bahamas temperature to changes in AMOC.

Chapter 4

Multi-proxy evidence of millennial scale climate variability from multiple Bahamian speleothems

Summary

This study represents an attempt to ascertain the climatic changes associated with Heinrich stadials 1-6 in the Bahamas, using multiple stalagmites from the same cave and comparing the geochemical results to results from a monitoring study from an active cave in the Bahamas.

The geochemistry of three stalagmites which formed between 14,000 to 65,000 yr BP have been compared to sample AB-DC-09, a stalagmite which showed significant $\delta^{18}O$ and $\delta^{13}C$ changes associated with Heinrich stadials 1, 2 and 3. In this study, the samples have been analyzed for $\delta^{18}O$ and $\delta^{13}C$, Sr/Ca and Mg/Ca ratios and in one sample, the $\delta^{18}O$ of the fluid inclusions. One of these samples extends the $\delta^{18}O$ and $\delta^{13}C$ record to Heinrich stadial 6 and two additional stalagmites, forming over Heinrich stadials 1 and 2, replicate the record from AB-DC-09. These analyses confirm the observation of an increase in $\delta^{18}O$ and $\delta^{13}C$ of the carbonate across Heinrich stadials 1-6. From the samples analyzed here, there is evidence for a decrease in $\delta^{18}O$ and $\delta^{13}C$ value of the calcite associated with D/O interstadials. Fluid inclusions are also measured across Heinrich stadials 4 and 5 and conclusions support decreasing temperatures across the two events, with temperature driving the increased $\delta^{18}O$ of the calcite. An average temperature decrease of ~3 °C is observed across Heinrich stadials, in agreement with previous records.

4.1 Background

4.1.1 Speleothem geochemistry

The geochemistry of speleothems (normally $\delta^{13}C$ and $\delta^{18}O$) has proven to be a valuable archive of modern, Holocene and millennial scale climate events (Fairchild et al., 2006; McDermott, 2004). Considering that the interpretation of $\delta^{18}O$ values of carbonates is inherently complex, studies have taken various approaches including the measurement of the $\delta^{18}O$ value of drip water from within the cave, the measurement of the $\delta^{18}O$ of the rainfall from a nearby monitoring station, modeling the $\delta^{18}O$ value of rainfall and/or measuring the fluid inclusion $\delta^{18}O$ values, representative of the local rainfall (Baker and Bradley, 2010; Carolin et al., 2013; Kanner et al., 2012; van Breukelen et al., 2008).

In the case of the $\delta^{13}C$ of the carbonate, biological soil activity, the type of vegetation (C_3 versus C_4) and amount, as well as the amount of water/rock interaction can impact the $\delta^{13}C$ of the dissolved inorganic carbon (DIC) (Fairchild et al., 2006; McDermott, 2004). These factors can be influenced by changes in temperature and amount of precipitation. The biogenic component of the CO_2 in the soil zone increases as a result of root respiration, organic material decomposition, and the amount of vegetation cover (Couchoud et al., 2009; Genty et al., 2003). Within the cave, studies have demonstrated that ventilation may influence the $\delta^{13}C$ of the CO_2 and hence $\delta^{13}C$ of the speleothem (Kowalczk and Froelich, 2010; Lambert and Aharon, 2011; Tremaine et al., 2011).

Elemental abundances have proven to be important for understanding the environment of formation of the carbonate minerals. In biogenic carbonates, particularly

corals, Sr/Ca ratios can be utilized as indicators of temperature change (Beck et al., 1992). In speleothems, minor elements have been utilized to reconstruct paleoclimate and are able to aid with the interpretation of $\delta^{13}C$ and $\delta^{18}O$ results (Cruz et al., 2007; Oster et al., 2010; Tremaine and Froelich, 2013). Factors that can influence the incorporation of minor elements into drip water include the type of overlying bedrock (Fairchild et al., 2000), the hydrologic conditions (Cruz et al., 2007), the routing path of the water (Fairchild and Treble, 2009), the amount of water/rock interaction (Fairchild et al., 2000), cave ventilation (Wong et al., 2011), and calcite precipitation rate (Lorens, 1981). During periods of enhanced aridity, prior calcite precipitation (PCP) can occur through evaporation or CO_2 degassing in the epikarst or within the cave ceiling. With increasing PCP, drip waters become enriched in Mg and Sr as these elements are excluded from the diagenetic solid phase. Evidence of PCP, and hence increased aridity, have been attributed to a positively correlated Mg to Sr variation in speleothems (Fairchild and Treble, 2009). In addition, during periods of low flow, increased residence time of waters in the epikarst leads to increased water/rock interaction and hence minor element concentrations will reflect the overlying bedrock (Fairchild and Treble, 2009).

Studies have demonstrated that changes in the $\delta^{13}C$ and $\delta^{18}O$ values in the speleothems may not be solely driven by climatic factors, but rather by kinetics. Kinetic isotope fraction results in disequilibrium and a test used to suggest that kinetic effects are not important is the 'Hendy' test (Hendy, 1971) which measures lateral $\delta^{13}C$ and $\delta^{18}O$ variation within a speleothem. Assuming that sampling can be carried out along a growth band, the following criteria must be met for the Hendy test: i) an absence of lateral increases in $\delta^{18}O_c$ and $\delta^{13}C_c$ values, and ii) a low correlation between $\delta^{18}O_c$ and $\delta^{13}C_c$

values. If these conditions are met, then it is assumed that minimal kinetic fraction has taken place. However studies have demonstrated that this test may not be sufficient to rule out kinetic fraction (Mühlinghaus et al., 2009). Other authors have suggested a more robust method is to conduct replication tests, in which multiple stalagmites from the same cave are measured and if the carbon and oxygen isotopic trends are replicated, this supports kinetic fractionation as not being significant (Dorale and Liu, 2009).

4.1.2 Millennial scale climate variability

The last 100,000 years of global climate have been punctuated by millennial scale, rapid climate change events such as Dansgaard/Oeschger (D/O) cycles and Heinrich events. Briefly, Heinrich events were first identified in the geologic record from the deposition of ice rafted debris (IRDs) in the North Atlantic (Bond et al., 1992; Bond et al., 1997; Heinrich, 1988). These cold (stadial) events are associated with the southerly extension of ice, due to the calving of the Laurentide ice margin. This calving leads to higher freshwater discharge (icebergs) to the North Atlantic and a reduced North Atlantic deep water formation and Atlantic meridional overturning circulation (AMOC) (Broecker et al., 1985; McManus et al., 2004). Additionally there is evidence of an inter-hemispheric climate response, with lower sea surface temperatures (SSTs) in the northern hemisphere, higher SSTs to the south, a southerly shift in the intertropical convergence zone (ITCZ) and enhanced aridity in the northern hemisphere tropics. These observations are supported both by models and proxy data (Chiang, 2009; Clement and Peterson, 2008; Voelker, 2002). D/O interstadials are recorded in the Greenland ice cores as periods of warming, followed by a gradual return to cooler temperatures (Capron et al., 2010; Dansgaard et al., 1984; Dansgaard et al., 1993). D/O cycles are global scale events

(Denniston et al., 2007; Fletcher et al., 2010; Jiménez-Moreno et al., 2010; Jouzel et al., 2007; Siddall et al., 2010), however the mechanisms driving D/O cycles and the global propagation are still not well understood (Clement and Peterson, 2008; Timmermann et al., 2003). Several theories have been suggested including AMOC changes (Broecker et al., 1985), sea ice changes (Li et al., 2010; Petersen et al., 2013), and tropical processes (Clement and Cane, 1999) to name a few. There is some evidence of IRD deposits associated with D/O stadials which suggests that D/O cycles are possibly driven by ice sheet mechanisms (Menviel et al., 2014). Modeling studies suggest D/O cycles are forced both by ice-sheet and AMOC variations (Menviel et al., 2014).

The goal of this study is to build upon a previous stalagmite record (AB-DC-09) (Chapter 3), by analyzing three additional stalagmites from the same cave to reconstruct millennial scale climate variations using multiple geochemical proxies. These four stalagmites from the Bahamas formed over the last 65,000 years. In Chapter 3 it was concluded that the main cause of increasing $\delta^{18}O$ of the speleothem carbonate was lower temperature, with lower temperature associated with Heinrich stadials 1 to 3. Also observed was higher $\delta^{13}C$ of the carbonate during Heinrich stadials, due to either a decrease in temperature or increase in aridity. Both a decrease in temperature and an increase in aridity can lead to a reduced biogenic CO_2 component of the DIC and heavier $\delta^{13}C$ values. Using these additional speleothems from the Bahamas, the climatic change across Heinrich stadials 1-6 was studied utilizing $\delta^{13}C$ and $\delta^{18}O$, minor elements and the $\delta^{18}O$ of fluid inclusions. The results from these stalagmites will be compared to results from a modern cave. The modern cave monitoring study consists of the measurement of drip waters and calcite samples $\delta^{13}C$ and $\delta^{18}O$ and minor elements, to aid with the

interpretation of the geochemical results from the ancient stalagmites. This study is of significance as it extends the original record to Heinrich stadial 6 and combines multiple geochemical proxies to determine the drivers of geochemical changes. Finally, combining both geochemical analyses of ancient stalagmites with a modern monitoring study is significant as it validates the interpretation of our results.

4.2 Sample Specimens for Study

The three main types of data presented in this report are: 1) a geochemical time series from four stalagmites over the last 65,000 years before present, 2) a spatial and temporal geochemical data from drip waters from a currently active cave, 3) geochemical dataset from calcites from the currently active cave.

4.2.1 Ancient stalagmites

For this study, four stalagmites (AB-DC-01, 03, 09 and 12) were selected from a currently submerged cave from Abaco Island, Bahamas (Figure 4.1). Samples were collected from a water depth of 33.5, 34.4, 16.5 and 11.9 meters, respectively, below sea level. Stalagmite sample AB-DC-09 has been previously analyzed for U-Th ages, $\delta^{13}C$ and $\delta^{18}O$ values of the carbonate, and $\delta^{18}O$ and $\delta^{2}H$ values of the fluid inclusions. All samples were analyzed for the presence of kinetic fractionation through the 'Hendy' test. Samples from the surrounding cave walls were not collected.

4.2.2 Modern

Samples were collected from Hatchet Bay Cave (HBC), a currently active cave in Eleuthera, the Bahamas (Figure 4.1). Monitoring was initiated in June of 2012. Overlying the cave is grasses and small *Metopium toxiferum* (poison wood) and trees of the Fabaceae family with well-developed soils (greater than 15 cm depth). Most of the

grasses are located near the entrance and at lower elevations around the cave, with the small trees located on the Aeolian ridge. HBC was accessed through a small ~1.7 m. by 0.9 m. opening located 10 to 15 m above sea level and exhibits an extremely linear pattern particularly west of the main entrance (Mylroie and Mylroie, 2009). The opening is immediately surrounded by thick grasses with larger trees (as described above) located 3 meters to the west, approximately following the cave direction and well developed soils (as described above). The first level exhibits evidence of phreatic dissolution (Mylroie and Mylroie, 2009). There is no evidence of cave breathing holes through the roof as suggested by the lack of changes in the overlying vegetation and soil. The cave is divided into three levels with the first level being the shallowest and the smallest level. The second level is a tubular passage accessed by a 1.6 m. ladder down from the first level and again contains evidence of phreatic dissolution (Mylroie and Mylroie, 2009). The second level is more extensive (300 m long) with active drip water and stalagmite formation (Mylroie and Mylroie, 2009). The 2nd level is thought to follow a thick, terra rossa paleosol, leading to the creation of the linear and tubular shape following the aeolian ridge (Mylroie and Mylroie, 2009). The third level is the deepest level and is accessed by another 1.8 m ladder from the second level. However continuing on the second floor lies a smaller passage which after several meters leads to a 7 m shaft to the surface, which may have been carved out for guano mining (Mylroie and Mylroie, 2009). The third level is partially filled with water, with active stalagmite formation occurring on raised rock ledges above the water, ~1.2 m above the water level. This water is tidally influenced and of marine salinity (Mylroie and Mylroie, 2009). There is no evidence of water flooding the rock ledges nor is there any evidence of calcite deposits forming from

the water. Most of the sampling conducted on the 2nd and 3rd levels. Located on the 3rd level ledges were experiments on the precipitation of calcite from drip water, henceforth known as calcite "farming" (Figure 4.2). The cave was visited every 3-5 months. This cave has more extensive speleothem formation than other caves in Eleuthera possibly driven by the 10-15 m of overlying calcite (Mylroie and Mylroie, 2009). Samples from the surrounding cave walls were not collected.

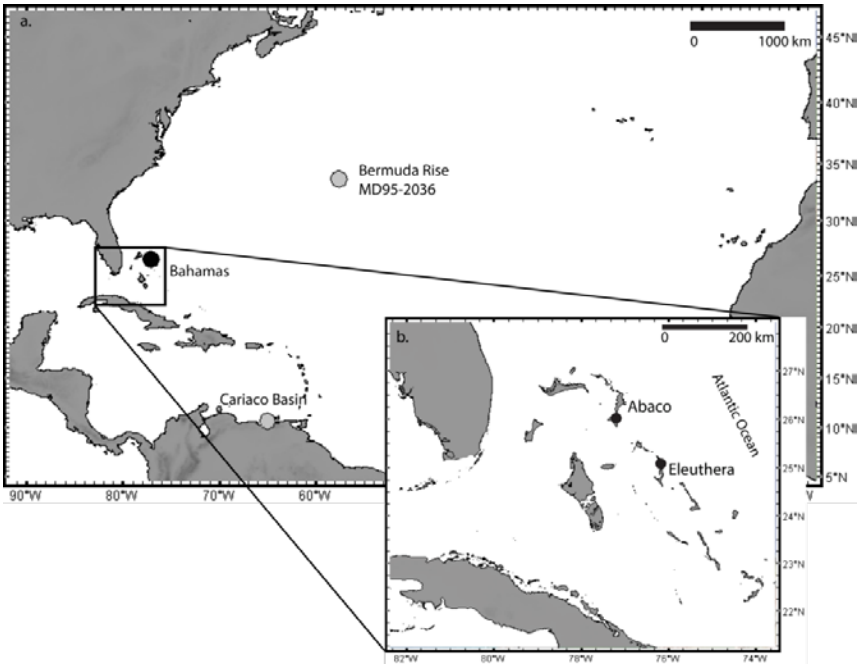

Figure 4.1: Map of the Western Atlantic (A) showing the locations of the Bahamas, Cariaco Basin (Deplazes et al., 2013) and Bermuda Rise (Core MD95-2038) (Sachs and Lehman, 1999). B) Close up of the Bahamas, including the location of Hatchet Bay Cave in Eleuthera, Bahamas where the modern sampling is being conducted. The submerged stalagmites were collected from Abaco Island, Bahamas from depths ranging from 11.9 to 34.4 m below sea level.

Figure 4.2 (following page): Schematic of the entire surveyed area including first, second and third levels. The eastern part of the cave was not surveyed due to difficulty accessing this part of the cave. The locations of water and air sampling are approximate. Also shown is the approximate location of water and air collection as well as calcite farming. Shown are photographs of the areas which were sampled including main site (MS), east site (ES) and the west site (WS).

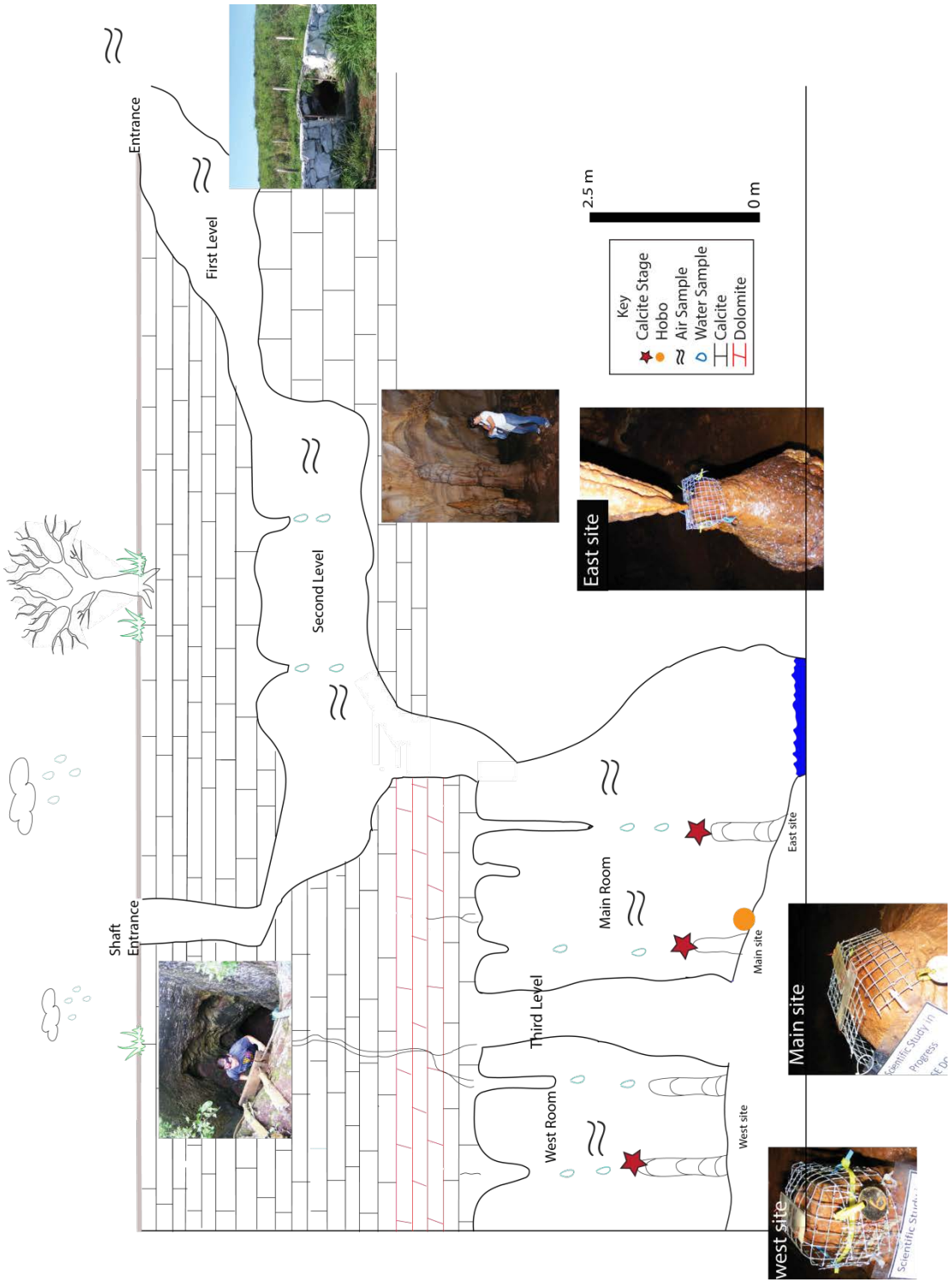
Entrance
First Level
Second Level
Shaft Entrance
Third Level
Main Room
West Room
East site
Main site
West site
2.5 m
0 m
Key
Calcite Stage
Hobo
Air Sample
Water Sample
Calcite
Dolomite
East site
Main site
west site

4.3 Methods

4.3.1 Stalagmite samples: Abaco Island cave

Uranium-Thorium:

For age dating of the speleothems, a total of 27 U-Th age dates were acquired at the Neptune Isotope Laboratory of the University of Miami - RSMAS utilizing a ThermoFisher-Neptune Plus multi-collection ICP-MS for stalagmites AB-DC-01, 03 and 12. Previously, 20 ages were acquired for sample AB-DC-09 and are reported elsewhere (Chapter 3). The U-Th geochronometry method and the propagation of random and systematic uncertainties is provided in Chapter 3 and in Pourmand et al. (2014b). For all samples, an initial $^{230}Th/^{232}Th$ activity ratio of 3.7± 0.6 was used to account for excess (unsupported) ^{230}Th (Chapter 3).

Calcite isotopes:

Sampling of the speleothem carbonate for $\delta^{13}C_c$ and $\delta^{18}O_c$ (calcite) was carried out using a New-Wave computerized micromill at both high and low resolution. Low resolution sampling consisted of one sample every 1000 μm throughout the length of the stalagmite (Figure 4.3 a-c). Two areas were analyzed at high resolution (20 μm sampling interval) for sample AB-DC-12 (Figure 4.3 a) and three areas from sample AB-DC-09 (Chapter 3). The areas were chosen because the low resolution analysis demonstrated areas of rapid and significant isotopic shifts in these intervals. C and O isotopic measurements were made using a Kiel III interfaced with a Thermo-Finnigan Delta Plus Mass Spectrometer at the University of Miami. All data have been corrected for the usual

isobaric inferences at mass 45 and 46 and are reported relative to Vienna Pee Dee Belemnite (VPDB) and the precision of the $\delta^{13}C_c$ and $\delta^{18}O_c$ values is less than 0.1‰.

Minor elements:

Splits of material sampled from AB-DC-01, 03 and 12 analyzed for $\delta^{13}C_c$ and $\delta^{18}O_c$ were additionally measured for minor elements utilizing the Varian inductively coupled plasma optical emission spectrometer (ICP-OES) at the University of Miami. For sample AB-DC-09, elemental sampling was conducted separately at a resolution of one sample every 500 μm. Samples were diluted in 4% trace grade HNO_3 to yield a concentration of approximately 4 ppm Ca and were analyzed with samples of similar concentration and matrix.

Fluid inclusions:

Sample AB-DC-12 was chosen for fluid inclusion analyses. Oxygen and hydrogen isotopic analysis of the fluid trapped within inclusions ($\delta^{18}O_w$ and $\delta^{2}H_w$) was carried out at the University of Miami using a cavity ring-down spectroscopy instrument (CRDS) L2130-i Picarro as outlined in Chapters 2 and 3. This system allowed for the determination of $\delta^{18}O$ of the water ($\delta^{18}O_w$) and $\delta^{2}H_w$ of the fluid inclusion from approximately 0.3 g of sample which on average yielded 0.4 μL of water from the AB-DC-12 speleothem. The isotopic compositions of the fluid inclusions are reported relative to Vienna Standard Mean Ocean Water (VSMOW). Each sample was analyzed 1-2 times with an average error of 0.5 ‰ for $\delta^{18}O_w$ and 2.0 ‰ for $\delta^{2}H_w$ values (Arienzo et al., 2013). Average sampling was conducted every 1.25 cm and the $\delta^{18}O_c$ of the calcite

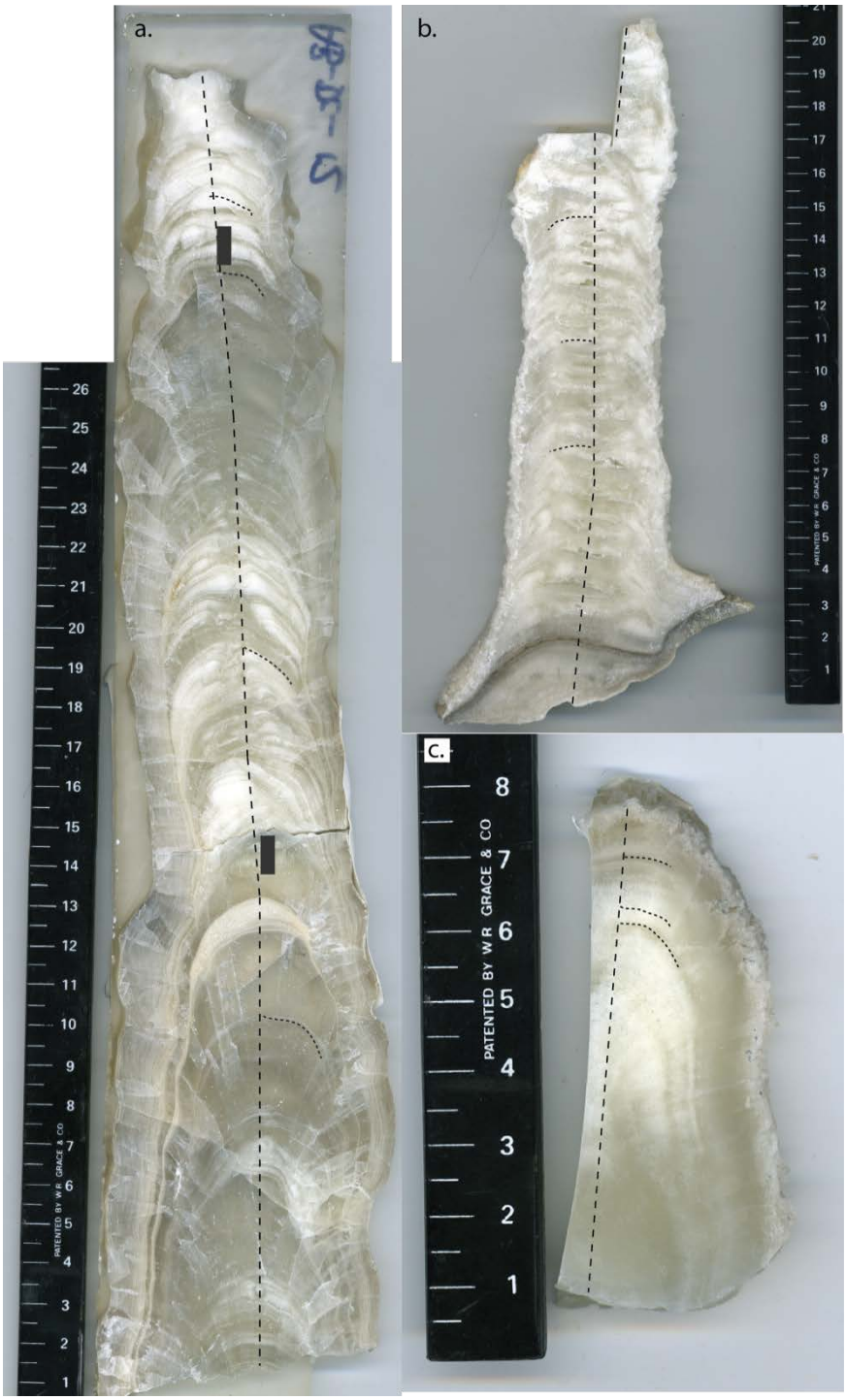

Figure 4.3: Photos of samples utilized in this study. A) Sample AB-DC-12, B) Sample AB-DC-03 and C) Sample AB-DC-01. All samples were analyzed at a low resolution (dotted vertical line) and Hendy tests were conducted (horizontal dotted line). Sample AB-DC-12 was analyzed at high resolution at two locations (black squares).

hosting the inclusion was measured on the carbonate using the Thermo-Finnigan Delta Plus mass spectrometer (see above).

4.3.2 Modern samples: Hatchet Bay Cave

Sampling within HBC began in June of 2012 and continued to November of 2013. Geochemical analyses of samples from HBC include the analyses of the CO_2 of air, drip waters and the precipitated calcite.

Air samples:

Air samples for carbon isotopes of the CO_2 ($\delta^{13}C_{CO2}$) were collected into 30 mL glass vials sealed with a septa, in a transect through the cave. Every visit to the cave an air sample was taken outside of the cave in an open field within 3 meters of the cave entrance prior to entering the cave. Carbon isotopes of the CO_2 were analyzed at the University of Miami on a gas bench coupled to a Thermo-Delta plus Advantage isotope ratio mass spectrometer (IRMS) and calibrated against internal standards. Data are reported relative to Vienna Pee Dee Belemnite (V-PDB). To determine CO_2 concentration, carbon peak intensity data were calibrated utilizing air samples with CO_2 concentrations of atmospheric condition using only one standard of atmospheric air.

Water samples:

Unfiltered water samples were collected throughout the second and third levels of the cave by holding clean plastic vials under dripping stalactites. Vials were filled completely (where possible) to avoid head space equilibration, then capped with a screw top cap the cap was then wrapped in either parafilm or electrical tape to prevent leaking during travel and stored until analysis. The waters were filtered (Whatman 0.2 μm pore filter) upon return to the laboratory (within 2-3 days) and transferred to a separate clean

plastic container, which was sealed with a screw cap. The filtered water was subsequently measured for minor elements and oxygen and hydrogen isotopes ($\delta^{18}O_w$ & $\delta^{2}H_w$). For minor element analyses, filtered samples were acidified and analyzed using the Varian ICP-OES. For $\delta^{18}O_w$ & $\delta^{2}H_w$ of the drip water, samples were measured using the Picarro Cavity Ring-Down Spectroscopy (CRDS). Four standard waters were analyzed with each set of samples and the standards used were previously calibrated to the VSMOW-GISP-SLAP scale. Data are reported relative to VSMOW with an average reproducibility of 0.05 ‰ for $\delta^{18}O_w$ and 0.1 ‰ for $\delta^{2}H_w$ from repeated analysis of a standard.

Chloride concentration was determined by titration with silver nitrate using dilute potassium chromate solution as the indicator. International Association for the Physical Science of the Oceans (IAPSO) seawater standard was utilized as a standard solution for Chloride and the average error was 5 ppm.

Calcite farming:

In June of 2012, collection of recently formed calcite began in Hatchet Bay Cave. Standard glass microscope slides (Figure 4.4) were placed on top of currently forming stalagmites and held in place by securing wire to the top of the stalagmite. The slides were fixed at a slight angle, similar to the methods of Tremaine et al. (2011) and Banner et al. (2007). Prior to installing the slides in the cave, the slides were pre-weighed in the laboratory. For the calcite farming, two farming set ups were installed in the main room (sites: middle (MS) and east (ES)), with a total of three slides deployed, and additionally a set up was installed in the west room (site: west (WS)) with one microscope slide

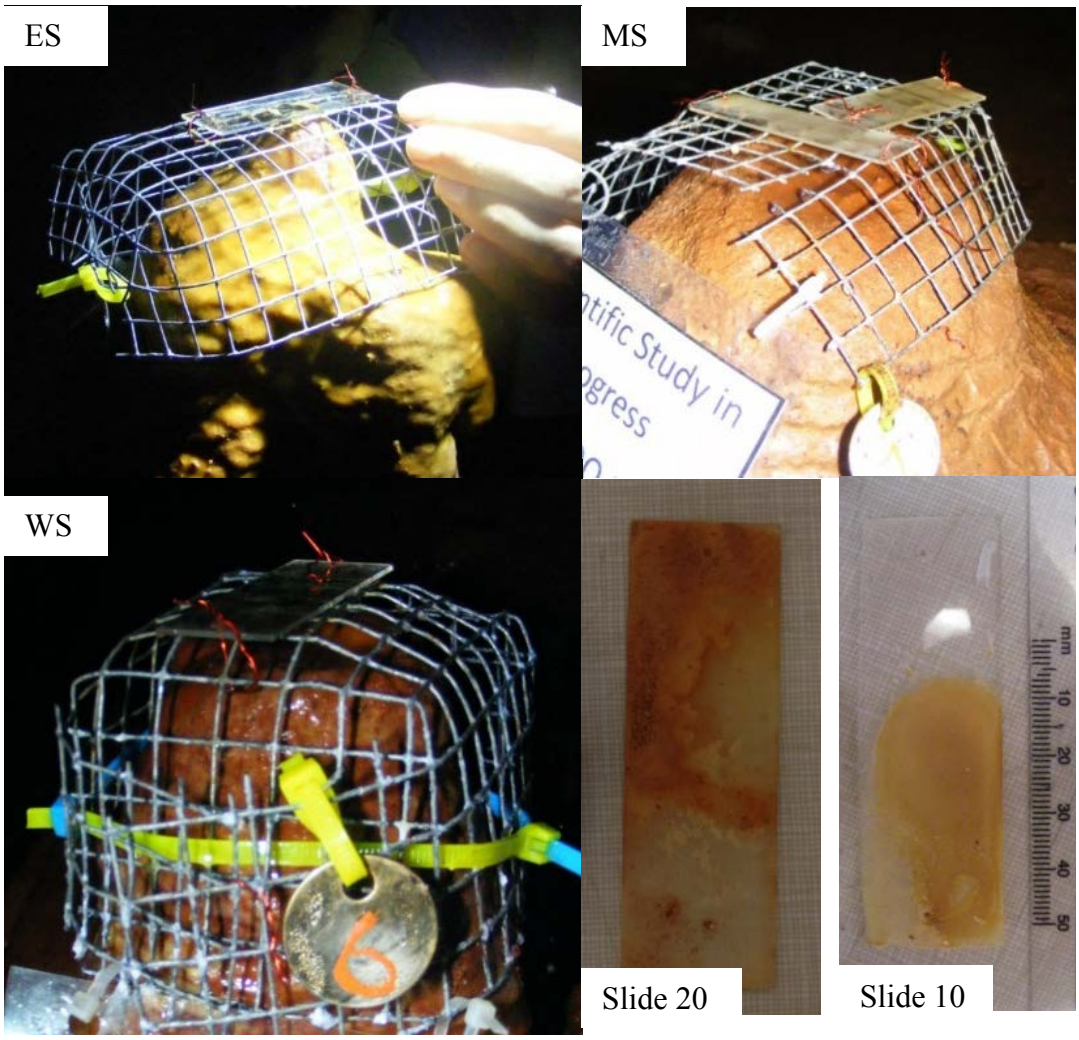

Figure 4.4: Photos of the calcite "farming" slide set up in the MS, ES and WS locations, with photos of two representative slides, slides #20 and 10.

(Figure 4.4). The microscope slides were left in the cave for 3-5 months between visits (Table 4.1). Drip rates were not measured in the cave.

The slides were recovered from the cave, brought back to the laboratory, dried at 40ºC and weighed (slides were not rinsed with DI water prior to drying, therefore may be contaminated with sea salt aerosols). For geochemical analyses, the calcite was removed

from the slides using a cleaned dental tool. For minor element analyses of the microscope slides, samples were dissolved in 4% HNO_3 and analyzed using the Varian ICP-OES as described above. Carbon and oxygen isotopic measurements were made using a Kiel III interfaced with a Thermo-Finnigan Delta Plus Mass Spectrometer (see above).

Slide#	Slide Weight (mg) no calcite	Location	Date removed	# days in cave	Calcite Precipitated (mg)	µmoles $CaCO_3/cm^2/day$
1	5833.1	Main Room	8/21/2012	79	140.3	1.8
3	5744.7	East Main Room	8/21/2012	79	228.7	2.9
4	5868.2	Main Room	8/21/2012	79	118.3	1.5
6	5803.7	West Room	8/21/2012	79	470.6	6.0
8	5853.3	Main Room	12/11/2012	110	80	0.7
9	5874.4	Main Room	5/1/2013	250	333.5	1.3
10	5853.5	East Main Room	12/11/2012	110	314.6	2.9
11	5857.3	West Room	12/11/2012	110	345.8	3.1
12	5808.5	Main Room	5/1/2013	140	40.2	0.3
13	5858.8	East Main Room	5/1/2013	140	245.3	1.8
14	5867.2	West Room	5/1/2013	140	790.7	5.6
15	5773.9	Main Room	8/6/2013	95	165.6	1.7
16	5817.4	Main Room	8/6/2013	95	Broken	Broken
17	5866.5	East Main Room	8/6/2013	95	214.5	2.3
18	5940.2	West Room	8/6/2013	95	491.2	5.2
19	5810.7	Main Room	11/21/2013	105	366.4	3.5
20	5777	Main Room	11/21/2013	105	262.5	2.5
21	5862.8	East Main Room	11/21/2013	105	160.3	1.5
22	5802.6	West Room	11/21/2013	105	609	5.8

Table 4.1: Summary table for each of the slides deployed in the cave. Growth rate is calculated from the weight of the slide before and after deployment in the cave. Slides 2 and 7 were destroyed in transport to the cave and therefore were not deployed. Slide 16 was broken after collection and therefore growth rate was not calculated.

Statistics:

Data were considered to be normally distributed and using a Pearson correlation coefficient, correlations were performed. Statistically significant relationships are reported at the 95% confidence limits.

4.4 Results

Results for the ancient stalagmite samples will be discussed first, followed by a discussion of the modern results. Comparisons between the two data sets will be made in order to aid with the interpretation of the results.

4.4.1 Abaco Island stalagmites

U-Th geochronometry:

Relevant data from the U-series analyses are shown in Figure 4.5 and Table 4.2 and b. Errors on ages were on average ±250 years. The age model for each speleothem was developed through linear interpolation between adjacent ages and each speleothem is plotted on its own independent time series (Figure 4.5). Results from U-series ages suggest the stalagmites were continuously forming from 14.1 to 63.5 ka before present (BP) with the only gap in the record between 31.3 and 35.9 ka BP, at which point of the sampled stalagmites, none were growing (Figure 4.5). Results demonstrate sample AB-DC-01 was forming from 22.9 to 29 ka BP and sample AB-DC-03 was forming from 14.4 to 15.6 ka BP. Sample AB-DC-09 overlaps with stalagmites AB-DC-01 and 03 and was forming from 14.1 to 31.3 ka BP. Finally sample AB-DC-12 was the oldest sample analyzed, forming from 35.9 to 63.5 ka BP (Figure 4.5).

Kinetic fractionation:

A test often used to suggest that kinetic effects are not important is the 'Hendy' test (Hendy, 1971) which measures lateral variation in a chemical parameter within the speleothem and has been widely used to examine kinetic effects. For speleothems AB-DC-01, -03 and -12, sampling was conducted at one millimeter increments using a hand drill to sample laterally outwards from the central growth axis and results are plotted in Figure 4.6 a-c. Results demonstrate only a minimal increase from the center of the stalagmite outwards for $\delta^{13}C_c$ and $\delta^{18}O_c$ values, suggesting minimal kinetic fractionation is driving $\delta^{13}C_c$ and $\delta^{18}O_c$ values for all three stalagmites.

Calcite isotopes:

When plotting the $\delta^{18}O$ record of the carbonate ($\delta^{18}O_c$) with the age model (Figure 4.7), the results support a decreasing trend (from -3 to -4.1 ‰) over the time period from 62 to 38 ka BP followed by an increase between 30 to 17 ka BP (to 0.7 ‰). Both AB-DC-03 and -09, which overlap, exhibit an approximate 3 ‰ $\delta^{18}O_c$ increase at ~15.5 and 14.9±0.2 ka BP, respectively. AB-DC-01 and -09 also overlap and both samples have maximum $\delta^{18}O_c$ values at ~25.5 and 24.8±0.2 ka BP, respectively, with a ~2 ‰ higher value in the $\delta^{18}O_c$ value (Figure 4.7). Similar results were observed for the $\delta^{13}C_c$ record with higher carbon isotope values for stalagmites AB-DC-01 and 03 occurring synchronously with the observed $\delta^{13}C_c$ changes in AB-DC-09 (Figure 4.7 b). Stalagmite AB-DC-09 also exhibits higher $\delta^{13}C_c$ and $\delta^{18}O_c$ values at 30.9±1 ka BP. Stalagmite sample AB-DC-12 has a maximum $\delta^{13}C_c$ and $\delta^{18}O_c$ value at 62.4±0.3 ka BP with distinct more positive $\delta^{13}C_c$ and $\delta^{18}O_c$ values at 38.8±0.2 and from 48 to 46.6±0.2 ka BP. In summary, both the $\delta^{13}C_c$ and $\delta^{18}O_c$ records for a composite of the four records yield

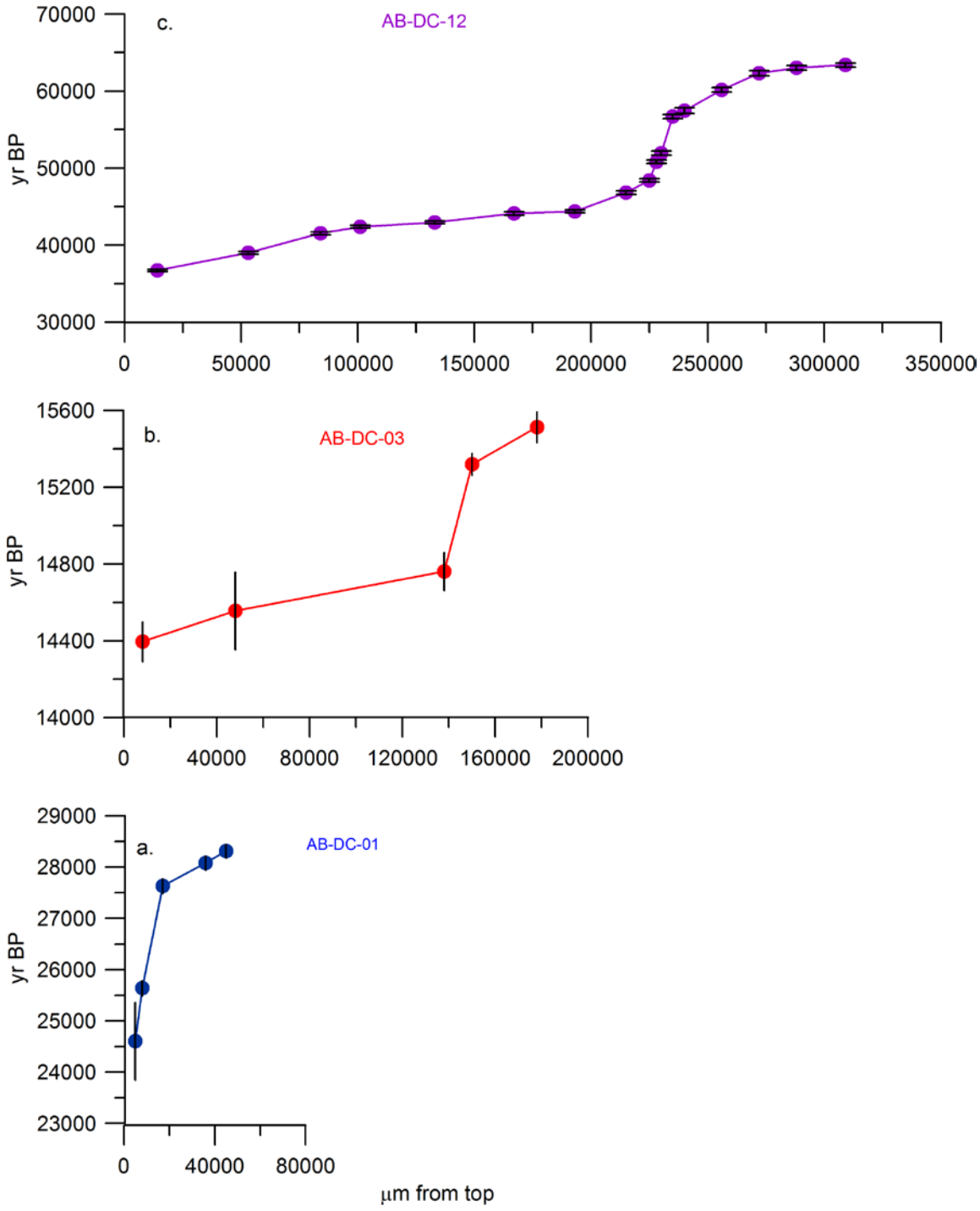

Figure 4.5: Age-depth plots for samples utilized in this study. a) Sample AB-DC-01 in blue, (b) sample AB-DC-03 in red, (c) sample AB-DC-12 in purple.

Sample Id	Distance from Top	^{238}U	(95% CI)	$[^{230}Th/^{238}U]$	(95% CI)	$[^{230}Th/^{232}Th]$	(95% CI)	Uncorr. Age	(95% CI)	$[^{234}U/^{238}U]$ initial	(95% CI)	Corr. Age	(95% CI)
	µm	(ppb)	±	(activity)	±	(activity)	±	(y)	±	(corrected activity)	±	(y)	±
DC-01	5000	112.994	0.087	0.2069	0.0037	32.7	2.74	27397	555	0.93	0.00259	24604	755
	8000	182.614	0.104	0.2128	0.0011	223.7	6.84	26024	138	1.004	0.00254	25640	148
	17000	316.354	0.174	0.23	0.0012	555.3	54.07	27798	144	1.025	0.00265	27634	145
	36000	335.15	0.17	0.2339	0.0011	401.4	3.86	28311	130	1.025	0.00261	28081	136
	45000	347.287	0.212	0.2363	0.0011	792.7	16.24	28431	127	1.032	0.00268	28315	129
DC-03	8000	566.682	0.265	0.1305	0.0006	97.7	0.9	14925	60	1.022	0.00244	14396	103
	48000	355.148	0.204	0.1377	0.0006	45.9	0.38	15745	65	1.026	0.00254	14556	202
	138000	349.702	0.161	0.1319	0.0006	104.9	1.69	15266	57	1.012	0.00245	14762	98
	150000	358.728	0.19	0.1347	0.0005	337.9	3.54	15478	51	1.02	0.00248	15320	56
	178000	389.329	0.183	0.1373	0.0006	187	3.98	15804	65	1.019	0.00244	15513	80

Table 4.2a: ^{230}Th dating results for samples AB-DC-01 and AB-DC-03. (See Pourmand et al., 2014 for detailed methodology). All uncertainties are calculated as 95% confidence interval (95% CI).

Distance from Top	^{238}U	(95% CI)	$[^{230}Th/^{238}U]$	(95% CI)	$[^{230}Th/^{232}Th]$	(95% CI)	Uncorr. Age	(95% CI)	$[^{234}U/^{238}U]$ initial	(95% CI)	Corr. Age	(95% CI)
µm	(ppb)	±	(activity)	±	(activity)	±	(y)	±	(corrected activity)	±	(y)	±
14000	775.204	0.422	0.2914	0.0011	268.1	1.92	37148	144	1.011	0.00264	36712	159
53000	260.535	0.163	0.3022	0.0014	490.8	2.88	39247	190	1.001	0.0027	38999	191
84000	361.556	0.174	0.3204	0.0012	249.3	3.48	42059	164	1.003	0.00263	41539	180
101000	395.053	0.351	0.3261	0.0014	1266.5	9.18	42500	192	1.012	0.0029	42397	191
133000	624.8	0.29	0.3309	0.0013	2330.9	58.92	43035	164	1.017	0.00267	42979	164
167000	301.034	0.192	0.336	0.0015	792	8.53	44287	219	1.008	0.00281	44117	219
193000	612.42	0.275	0.3395	0.0013	2654.1	72.22	44444	174	1.017	0.00263	44394	174
215000	330.759	0.2	0.3532	0.0014	646.8	36.18	47031	206	1.01	0.00282	46812	209
225000	537.129	0.295	0.3648	0.0014	480.3	5.73	48713	205	1.015	0.00279	48410	211
228000	319.361	0.159	0.3762	0.0015	921.8	18.78	50999	213	1.009	0.00276	50836	215
230000	300.241	0.191	0.384	0.0017	420.8	16.65	52327	269	1.009	0.00287	51960	274
235000	224.135	0.122	0.4072	0.0017	1118.4	101.68	56846	276	1.004	0.00298	56699	277
240000	375.277	0.219	0.4202	0.0022	514.2	3.2	57771	368	1.025	0.00285	57449	371
256000	209.07	0.104	0.4249	0.0017	393.2	10.86	60592	295	0.997	0.00292	60153	302
272000	262.334	0.164	0.4445	0.002	1247.8	61.52	62474	334	1.022	0.00293	62333	335
288000	338.949	0.155	0.4485	0.0018	1286.4	23.23	63164	299	1.023	0.00288	63026	300
309000	535.342	0.255	0.4554	0.0018	1108.7	17.08	63540	277	1.036	0.00276	63379	276

Table 4.2b: ^{230}Th dating results for samples AB-DC-12. (See Pourmand et al., 2014 for detailed methodology). All uncertainties are calculated as 95% confidence interval (95% CI).

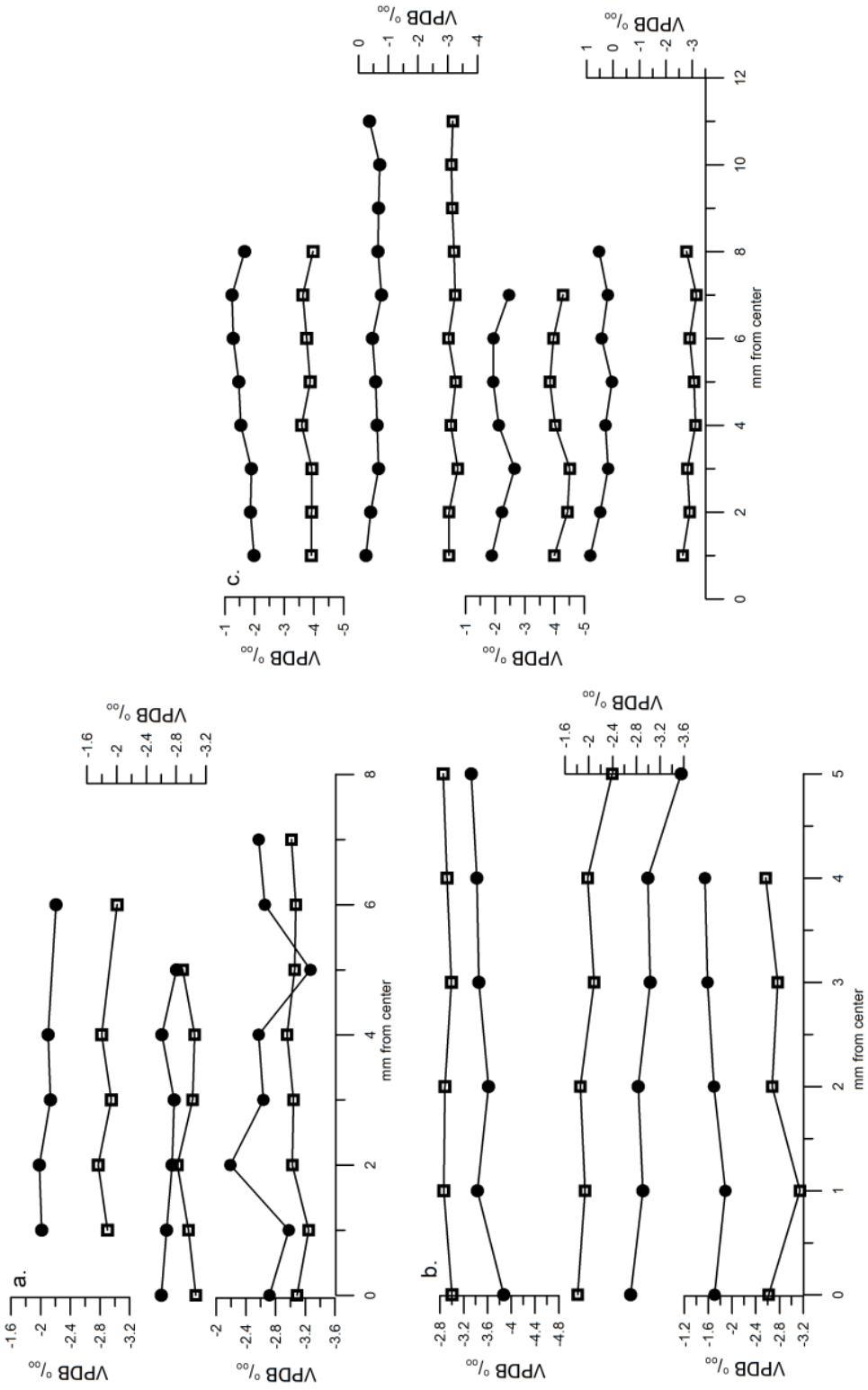

Figure 4.6: Hendy tests for the three stalagmites presented in this study. Results include: a) three Hendy tests for samples AB-DC-01, b) three Hendy tests sample AB-DC-03 and c) four Hendy tests for sample AB-DC-12. The $\delta^{13}C$ values are represented by open squares, $\delta^{18}O$ values by closed circles. Results are shown as mm from center axis. For the location of each of the Hendy tests, see Figure 4.2.

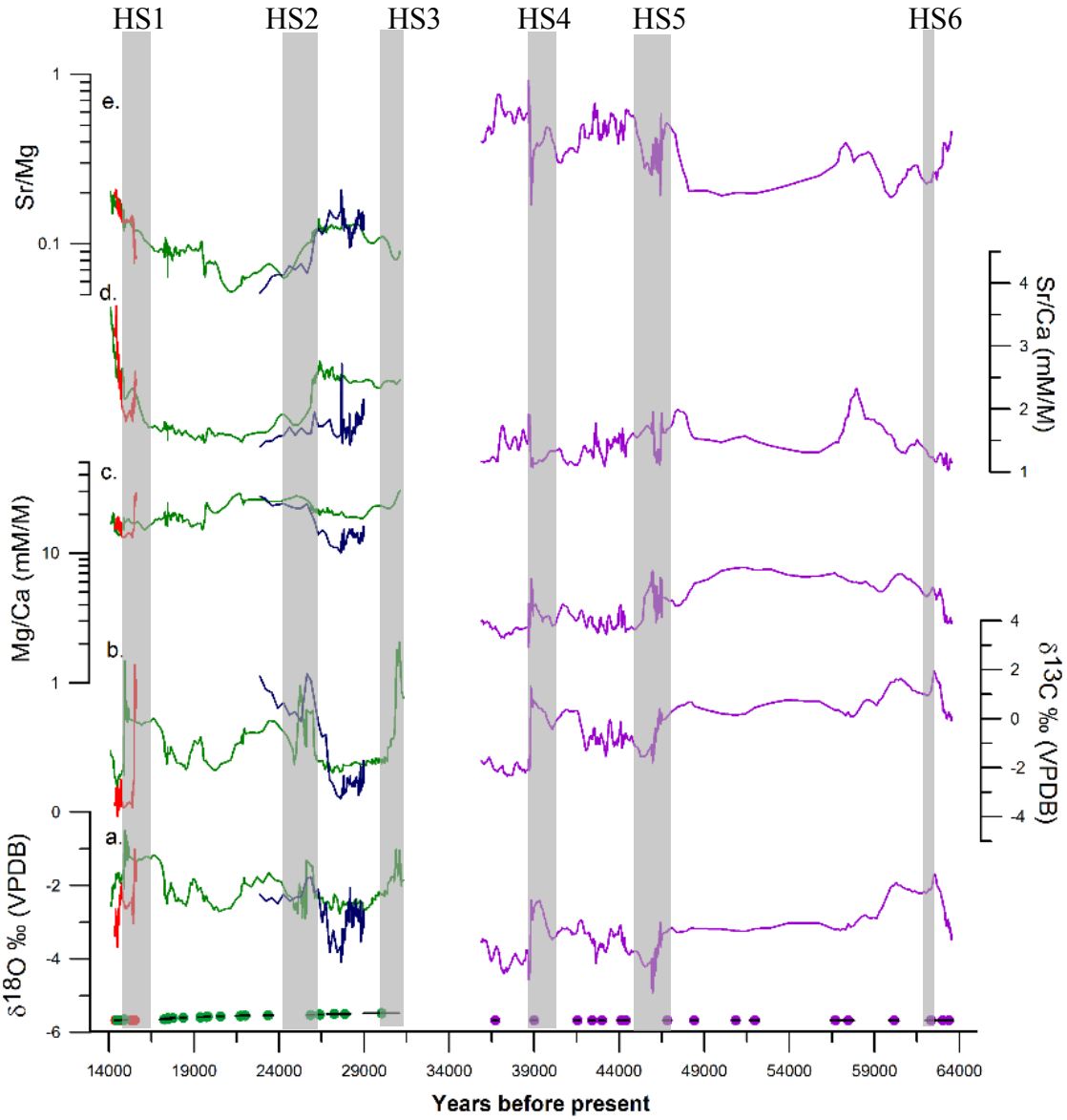

Figure 4.7: Geochemical results for stalagmite AB-DC-01 (blue), AB-DC-03 (5-point running average, red), AB-DC-09 (5 point running average, green) and AB-DC-12 (5 point running average, purple). The $\delta^{18}O$ record (a) and $\delta^{13}C$ record (b) of the carbonate demonstrate increasing values associated with Heinrich stadials 1-6. The Mg/Ca ratio (c) increases for AB-DC-01 (blue) and AB-DC-03 (red) across Heinrich stadials while the Sr/Ca ratio (d) remains relatively constant for all samples. The grey bars represent Heinrich stadials 1-6.

positive isotopic shifts at approximately 14.9 to 15.3 ±0.2, 24.8 to 25.5±0.2, 31.1 to 30.9 ±1, 38.8 to 40.2±0.2, 46.8 to 47.4 to ±0.2 and 62.2 to 62.8±0.3 ka BP (Figure 4.7 a & b).

Minor elements:

Similar to $\delta^{13}C_c$ and $\delta^{18}O_c$ results the minor elements are plotted with the age model in Figure 4.7 c and d. The Mg/Ca values varied between 10 to 34 mM/M with the exception of sample AB-DC-12 which had a range from 1.8 to 12 mM/M (Figure 4.7 c). For Sr/Ca the range of values for all samples was between 0.87 to 4.3 mM/M (Figure 4.7 d). There is no evidence from any of the stalagmites for a significant correlation between Sr/Ca and Mg/Ca. For samples AB-DC-01 and AB-DC-03 there is a positive correlation between Mg/Ca and $\delta^{13}C_c$ ($r^2 = 0.8$, $p<0.01$), but no other significant correlations were found (Figure 4.8). For sample AB-DC-09, a maximum Mg/Ca ratio was found at 31 ka BP and for sample AB-DC-12 a maximum Mg/Ca ratio was found at 46.0 ka BP (Figure 4.7 c). For Sr/Mg ratios, there are relatively minimal changes in the Sr/Mg ratios for samples AB-DC-01, 03 and 09 (Figure 4.7 e). For Sr/Mg ratio, the variability is 0.15 for samples AB-DC-01, -03, -09 observed, with AB-DC-12 exhibiting much greater variability of 0.88 for Sr/Mg.

Fluid inclusions:

In the case of sample AB-DC-12, the $\delta^{18}O_w$ of the fluid inclusions was measured to help with the interpretation of the variability in the $\delta^{18}O_c$ values. Periods of higher $\delta^{18}O_c$ values were targeted (Figure 4. 9 a). A comparison of the $\delta^{18}O_w$ measured on the fluid inclusions with the derived age model from U-Th geochronometry demonstrates minimal variations in the isotopic value of the fluids (Figure 4. 9 b). The $\delta^{2}H_w$ and $\delta^{18}O_w$ measured on the fluid inclusions show variations of 10.3 ‰ and 1.7 ‰ over the studied

interval with average values of -10.6 ‰ and -2.3 ‰ V-SMOW for δ^2H_w and $\delta^{18}O_w$ (Table 4.3, Figure 4.9 b). The variability in $\delta^{18}O_w$ value (~1.7 ‰) is relatively small compared to the changes in the $\delta^{18}O_c$ (~3.5 ‰, Figure 4.9 a). The data support a minimum $\delta^{18}O_w$ value at 35.9 ka BP and a maximum $\delta^{18}O_w$ value at 39.4 ka BP. The large break in sampling after 46.5 ka BP is due to there being no water present in the stalagmite until the sample at 57.5 ka BP.

Comparison of the fluid inclusion results to the global meteoric water line (GMWL) may shed light on the factors influencing the fluid inclusion data. The GMWL defines the linear $\delta^{18}O_w$ versus δ^2H_w relationship for precipitation (Craig, 1961) (Figure 4.10). The data from the fluid inclusions plot near the GMWL which suggests that samples have not been significantly fractionated (Figure 4.10). If samples had been significantly fractionated, then the results would not fall near the GMWL, and rather would fall below the GMWL. One potential source of contamination is from the stalagmites having been submerged since the deglaciation. One potential mechanism to determine if seawater has contaminated the fluid inclusions would be to measure the salt content of the inclusions. Unfortunately, this was unable to be measured in this stalagmite. However given the dense crystalline nature of the stalagmite and the lack of any evidence of seawater infiltration, it is not thought that seawater has contaminated this speleothem. Additionally, Richards et al. (1994) demonstrated minimal impact of submersion on geochemistry.

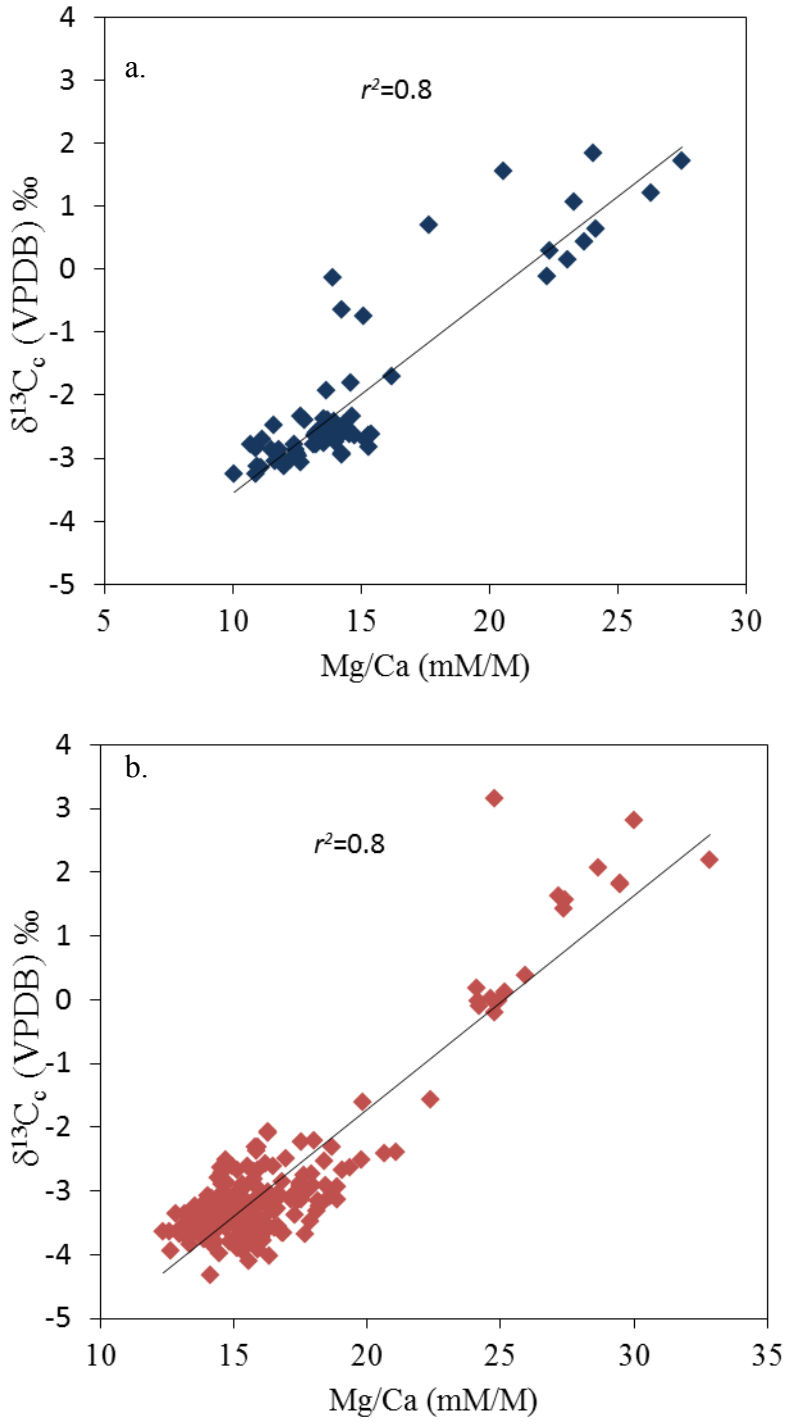

Figure 4.8: Cross plots of Mg/Ca versus $\delta^{13}C_c$ values for sample AB-DC-01 (blue) in (A) and (B) are results from AB-DC-03 (red). Results demonstrate a strong positive correlation for both samples. Similar results for both samples are found for Mg/Ca versus $\delta^{18}O_c$ results.

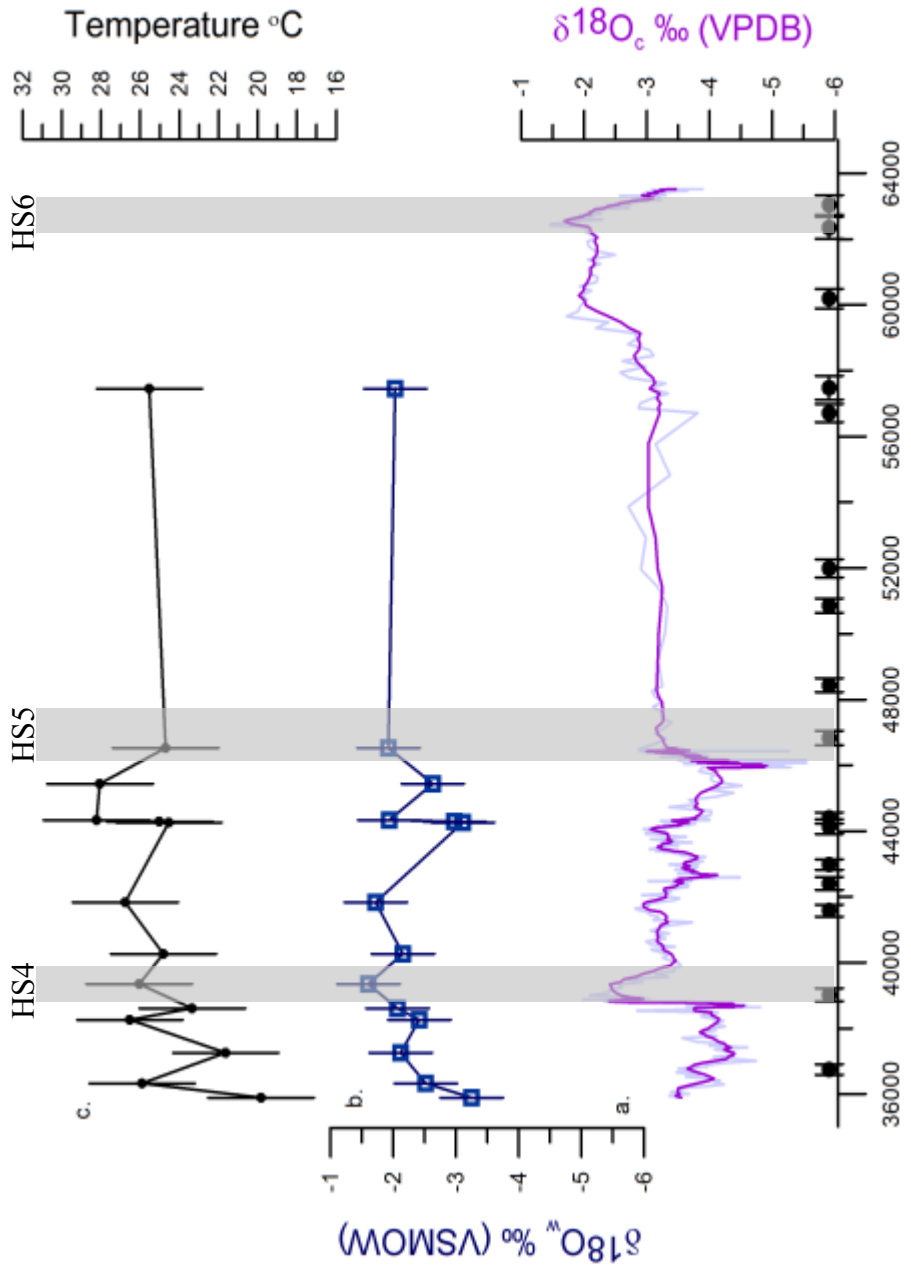

Figure 4.9: Fluid inclusion results for stalagmite AB-DC-12. The $\delta^{18}O_c$ record (a) is shown in light blue, with a 5 point running average in purple, demonstrating increasing $\delta^{18}O_c$ for Heinrich stadials 4 and 5. B) The fluid inclusion isotope record $\delta^{18}O_w$ demonstrates minimal change in the $\delta^{18}O_w$ across the time interval. C) Temperatures varied, with decreasing temperatures associated with increased $\delta^{18}O_c$ values. Temperature was calculated using the equation from Tremaine et al. (2011). Grey bars indicate the timing of Heinrich stadials 4, 5 and 6.

cm from top	Age	Average $\delta^{18}O_w$ ‰ (VSMOW)	Average $\delta^{2}H_w$ ‰ (VSMOW)	n	$\delta^{18}O_c$ ‰ (VPDB)	Temperature (°C)
	YBP	± 0.5 ‰	± 2.0 ‰			± 2.7 °C
0	35892	-3.2	-9.2	2	-3.3	19.8
0.8	36332	-2.5	-13.1	2	-3.7	25.9
2.3	37257	-2.1	-8.4	1	-2.5	21.6
4.0	38254	-2.4	-12.5	2	-3.7	26.5
4.6	38605	-2.1	-6.7	2	-2.8	23.4
5.7	39354	-1.6	-9.5	1	-2.8	26.1
6.8	40256	-2.2	-8.6	1	-3.2	24.8
9.0	41834	-1.7	-13.3	1	-3.1	26.8
18.0	44252	-3.1	-16.5	1	-4.1	24.6
18.4	44290	-3.0	-10.0	1	-4.0	25.0
18.8	44332	-1.9	-11.3	1	-3.6	28.2
20.3	45433	-2.6	-14.8	1	-4.2	28.1
21.3	46532	-1.9	-6.2	2	-2.9	24.7
24.0	57451	-2.0	-8.0	1	-3.2	25.5

Table 4.3: Fourteen fluid inclusion results for sample AB-DC-12. Temperature is calculated using the equation from Tremaine et al. (2011).

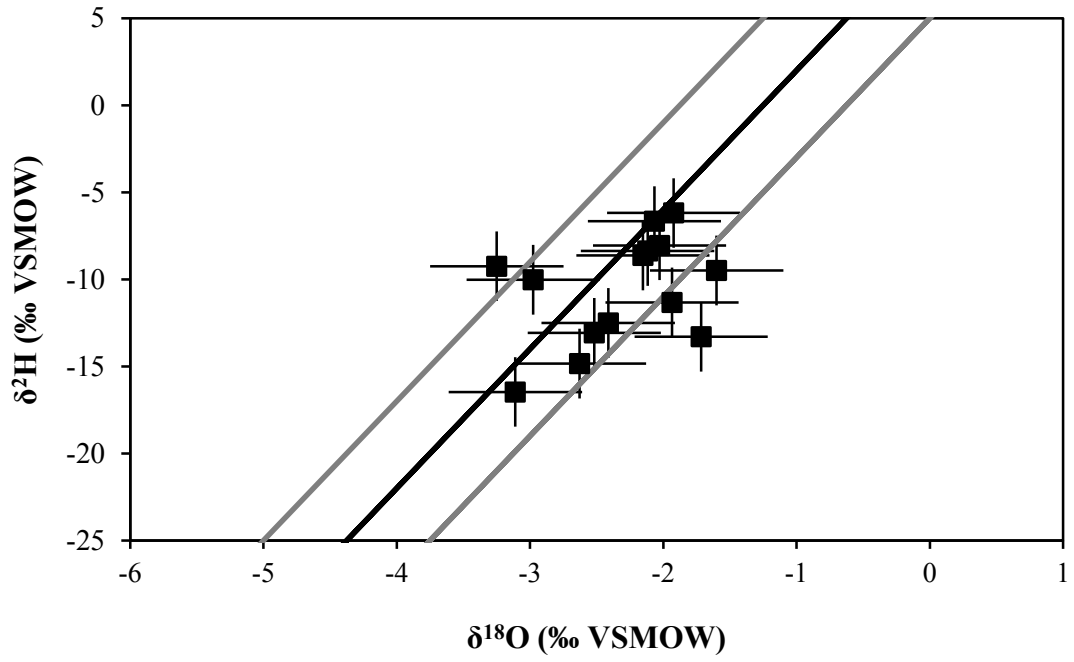

Figure 4.10: Fourteen fluid inclusion results from sample AB-DC-12. The results are plotted with the GMWL (black) with ± 5 ‰ δ^2H shown in grey.

4.4.2 Modern samples

Air CO_2:

Measurements of $\delta^{13}C_{CO2}$ from the cave air was conducted along a transect throughout the cave. The results demonstrate a co-variation between $\delta^{13}C_{CO2}$ and $[CO_2]$ with decreasing $\delta^{13}C_{CO2}$ occurring with increasing $1/[CO_2]$ (Figure 4.11) (Keeling, 1958). This is thought to be driven by the mixing of two end members, an atmospheric end member and a soil gas end member which is estimated in Figure 4.11 (Tremaine et al., 2011). Most of the sample results plot near the atmospheric end member. The high atmospheric end member is most likely driven by the two entrances on either side of the cave.

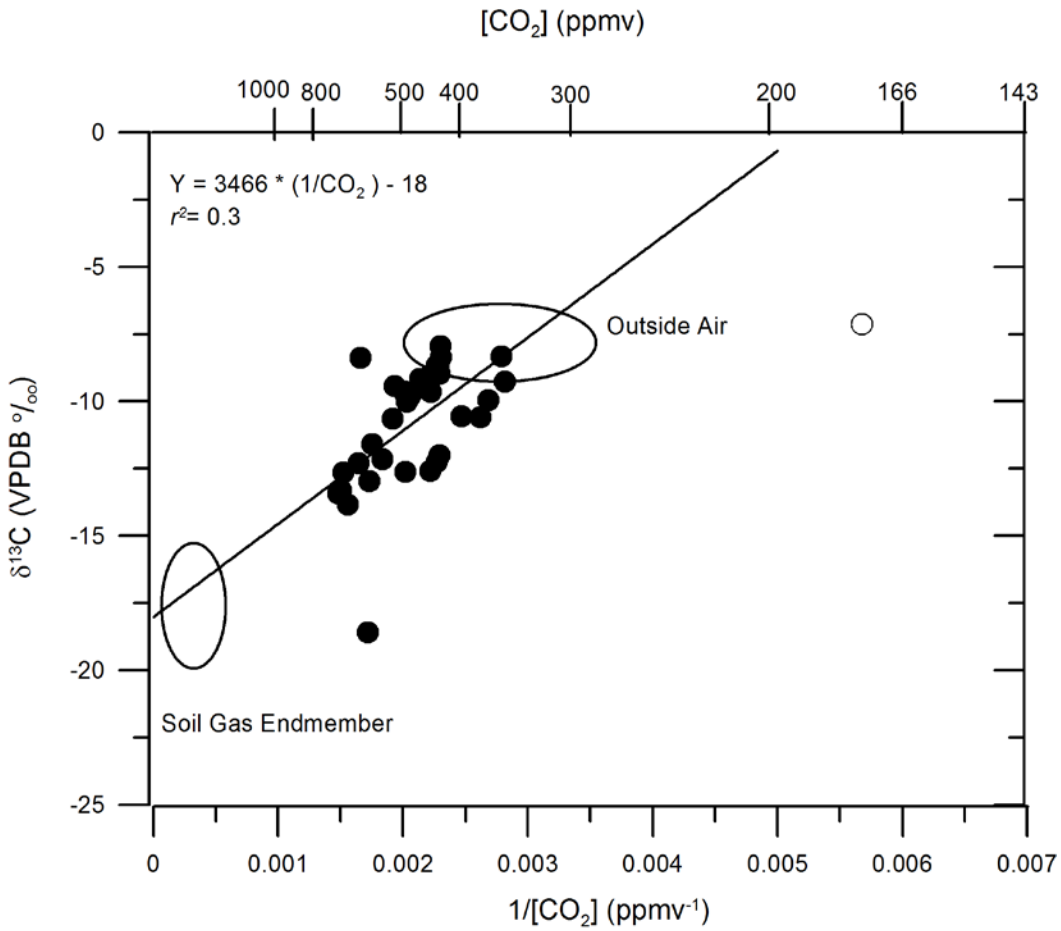

Figure 4.11: Keeling plot of HBC air samples (Keeling, 1958). Samples were collected in a transect through the cave. The atmospheric end member represents the low concentration, heavier $\delta^{13}C_{CO2}$ samples, while the soil gas end member is characterized as a high CO_2 concentration, light $\delta^{13}C_{CO2}$ end member, which was not measured. The air within the cave lies closest to the outside air end member suggesting the cave is well ventilated. Outlier at 0.006, -6 (open circle) was not included in the calculation of the line of best fit.

Water: Isotopes

For HBC the $\delta^{18}O$ of drip waters ($\delta^{18}O_w$) are found to be variable within the cave, but nevertheless plot along the GMWL (Figure 4.12). The 2nd level $\delta^{18}O_w$ annual average was -3.9 ‰ ±1 and more positive than the 3rd level values. The average $\delta^{18}O_w$ of the drip waters for the 3rd level main room and the west room were -4.2±0.5 ‰ and -4.8±0.4 ‰, respectively (Table 4.4). When comparing the average $\delta^{18}O_w$ value for each

location by sample month, the August 2012 results from the second level are the most positive (Figure 4.13). These findings are compared to modeled rainfall $\delta^{18}O_w$ values from Baldini et al. (2007) for San Salvador, Bahamas in Figure 4.13a. The results demonstrate seasonality in the second floor drip water results as well as a possible 2 month residence time when compared to the San Salvador data (Figure 4.13 a). Also observed on the 2nd level was an inverse correlation between rainfall amount and drip water $\delta^{18}O_w$ value (Figure 4.13 a & b). While there is observed variability on the 2nd level, the drip water $\delta^{18}O_w$ values of the third level are annually very stable and do not exhibit seasonality (Figure 4.13 a).

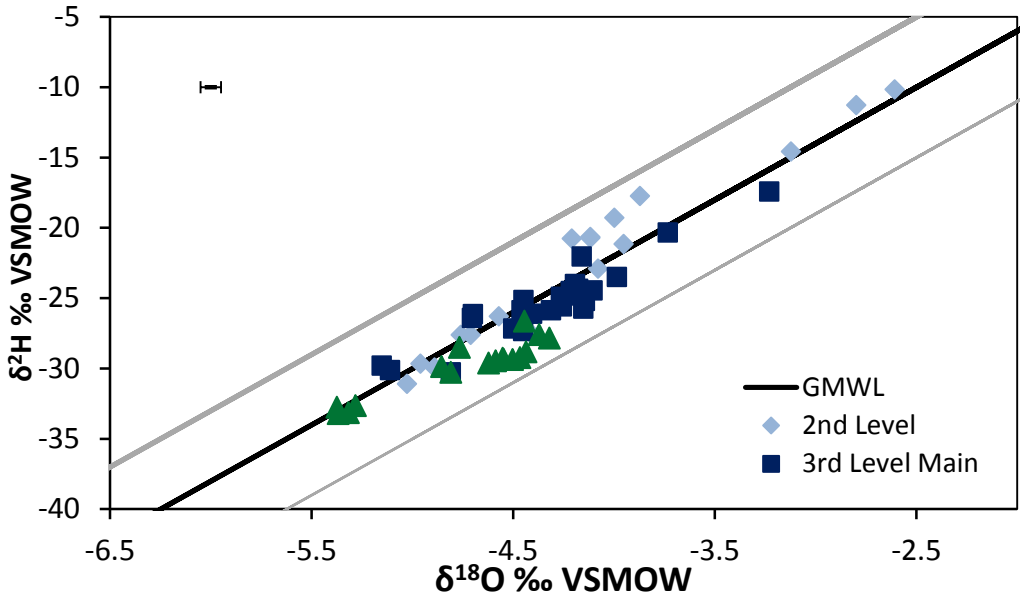

Figure 4.12: $\delta^{18}O_w$ and $\delta^{2}H_w$ for drip water samples from the 2nd level (light blue), 3rd level main (dark blue) and 3rd level west (green triangles). Results are plotted on the GMWL (black) with ± 5 ‰ $\delta^{2}H$ shown in grey. Average errors are shown in the upper left corner in black.

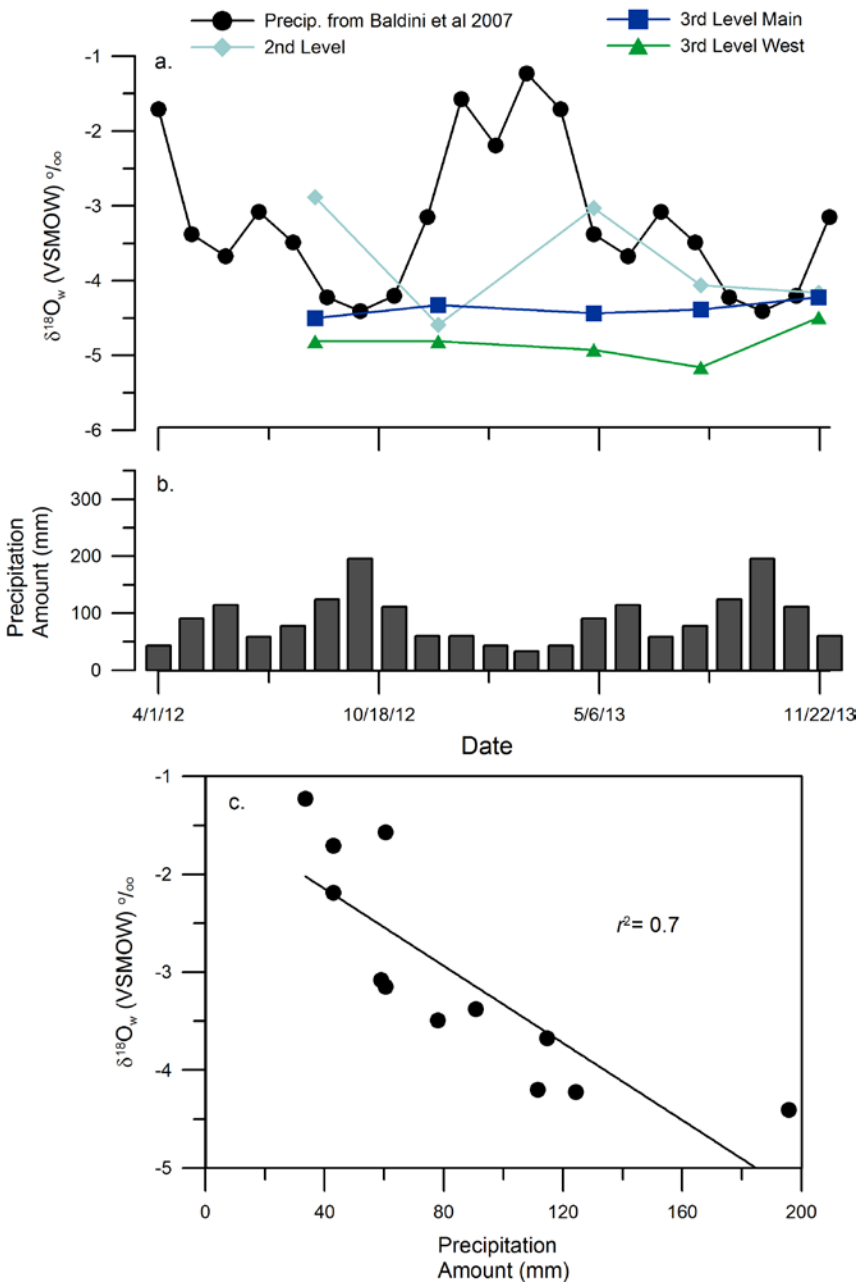

Figure 4.13: Relationship between rainfall and drip waters. A) Monthly rainfall $\delta^{18}O_w$ value from San Salvador, Bahamas shown in black. Precipitation oxygen isotope data are from Baldini et al. (2007). Light blue is 2nd level $\delta^{18}O_w$ drip water results. Dark blue squares are 3rd level main room and green triangles are 3rd level west room. Note the preliminary 2nd level seasonal changes in $\delta^{18}O_w$ drip water particularly when compared to the San Salvador results. B) Amount of precipitation by month for the Bahamas. Precipitation amount data are from San Salvador, Bahamas from Baldini et al. (2007). C) $\delta^{18}O_w$ of precipitation versus precipitation amount demonstrating the relationship between the two.

	δ18Ow ‰ VSMOW	σ	δ2Hw ‰ VSMOW	σ	Sr/Ca	σ	Mg/Ca	σ	Cl- ppm
2nd Level	-3.9	1.0	-21.3	7.1	2.2	0.4	509	132.0	539
3rd Level Main	-4.2	0.5	-24.9	2.9	2.4	0.6	956	280.4	2025
3rd Level West	-4.8	0.4	-29.6	2.0	2.2	0.2	1005	76.9	2811

Table 4.4: Annual average water results from the 2nd, 3rd level main and 3rd level west locations. Results include both isotopic and minor element results.

Water: Minor elements

Results from the elemental analyses of the water also demonstrate variability within the cave. The Mg/Ca ratio is the lowest in the 2nd level drip waters (m= 509 ±132 mM/M), the Mg/Ca ratio of the drip water from the 3rd level west room was higher and remained more stable throughout the year (m= 1005±77 mM/M) than the 3rd level main room Mg/Ca ratio (Table 4.4). For Sr/Ca, average Sr/Ca values for the third level were similar at both locations with a larger spread in the main room (Figure 4.14, Table 4.4). When plotting the Mg/Ca versus the Sr/Ca, the samples from the main and west rooms exhibit higher Mg/Ca corresponding to higher Sr/Ca ratios (Figure 4.14). Possibly indicating the influence of prior calcite precipitation (PCP) impacting both locations on the third level.

As demonstrated by Tremaine and Froelich (2013) drip water Mg/Ca and Sr/Ca which co-vary reveal dissolution of the overlying bedrock (dolomite or limestone) and evolve away from this original value with PCP. Therefore, one can back calculate the contribution from bedrock dolomite and limestone from drip water geochemistry. Figure 4.15 demonstrates both locations have high dolomite/high Mg calcite bedrock signature.

Additional information with respect to the influences of PCP on the drip waters can be made by the Mg/Sr ratio. When comparing the Sr/Mg ratio to the $\delta^{18}O_w$ results, there is no significant correlation (Figure 4.16) and very little variation in the Sr/Mg ratio particularly for the West room.

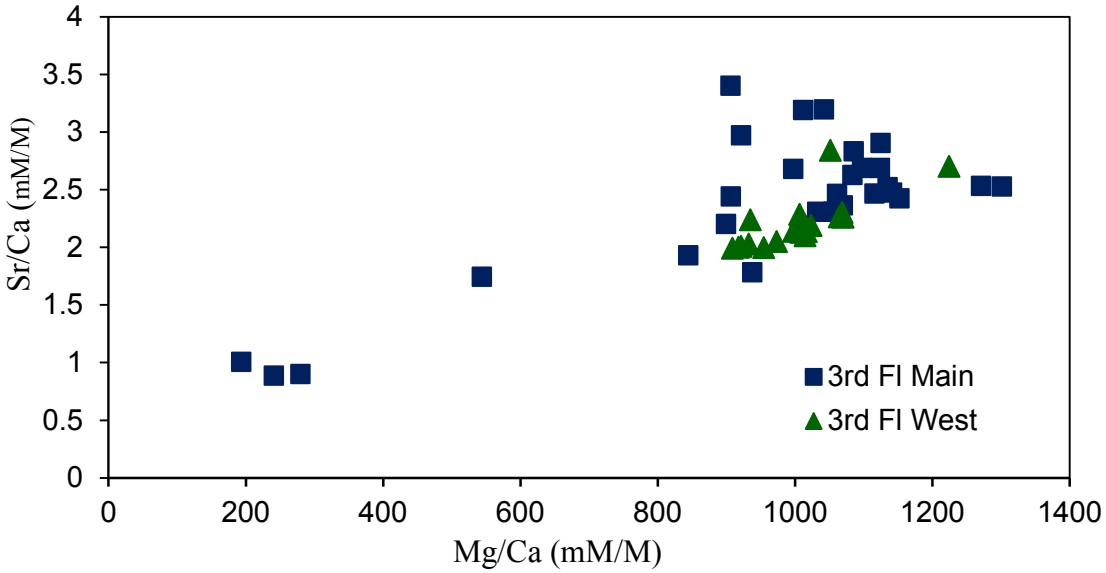

Figure 4.14 Mg/Ca versus Sr/Ca results for drip water samples from the 3rd floor main (dark blue) and 3rd floor west (green triangles).

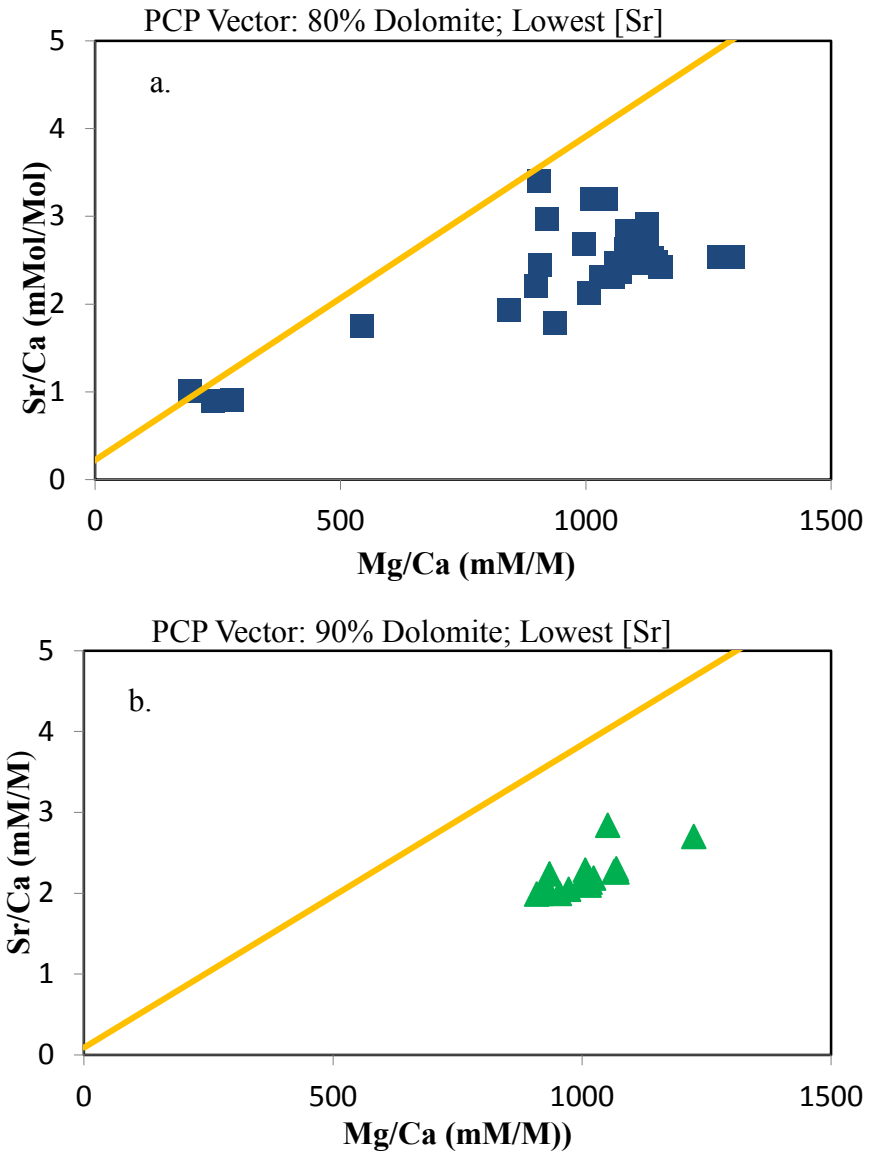

Figure 4.15: Drip water Sr/Ca and Mg/Ca data plotted with PCP vector in orange. The PCP vector is modeled after (Tremaine and Froelich, 2013) using dissolved limestone bedrock mixtures. For this study, the bedrock limestone was assumed to have a Mg/Ca of 9 mM/M, dolomite 1000 mM/M. The Sr/Ca value was assumed to be 1.99 mM/M, and it was assumed that the contribution from sea salts was negligible. Data in (a) are from the Main room drip waters, and data in (b) are from the West room drip waters. Results demonstrate a greater dolomite contribution to the West room (90%) versus the Main room (80%), however overall the samples demonstrate a high dolomite or Mg calcite bedrock. Future work will measure the Sr/Ca and Mg/Ca of bedrock around the cave. The greatest Mg/Ca and Sr/Ca values for both the Main and West rooms were found in November 2013, which was the beginning of the dry season. Further work is needed to verify the seasonality of the trace elements.

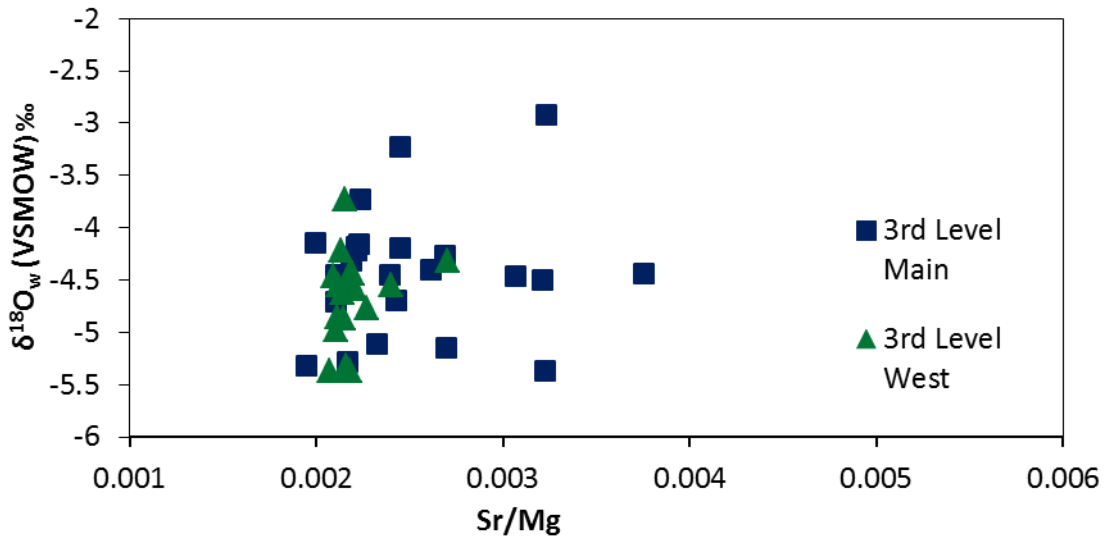

Figure 4.16: Drip water Sr/Mg versus $\delta^{18}O_w$ for drip water. Sr/Mg relationship is relatively unchanging particularly for the West room.

Calcite: Elements and isotopes

For the precipitated calcite from the modern, the concentration of minor elements varied amongst different sites. The average Sr/Ca ratio from WS location was 0.3 and for Mg/Ca was 23.2 ±1.5 mM/M (Table 4.5). The values from ES and MS locations were similar, with the MS containing higher Mg/Ca ratios (Tale 4.5). The results from the WS and ES sites fell on a positive co-varying trend for Sr/Ca versus Mg/Ca (r^2=0.8, n=10, p<0.01) while results from the MS location exhibited a much greater minor element variability (Figure 4.17).

A complete interpretation of the $\delta^{13}C_c$ and $\delta^{18}O_c$ from the slides are provided in Chapter 5 and for this study the $\delta^{13}C_c$ and $\delta^{18}O_c$ will be considered in terms of the relationship with minor element results only. The Mg/Ca versus $\delta^{18}O_c$ results

	$\delta^{18}O_c$ ‰ VPDB	σ	$\delta^{13}C_c$ ‰ VPDB	σ	Sr/Ca mM/M	σ	Mg/Ca mM/M	σ
ES	-4.6	0.6	-9.4	7.1	0.4	0.03	28.6	1.5
MS	-3.9	0.6	-8.8	2.9	0.5	0.07	37.5	3.9
WS	-5.1	0.3	-10.9	2.0	0.3	0.01	23.2	1.5

Table 4.5: Annual average calcite results from the ES, MS and WS locations. Results include both isotopic and minor element results.

demonstrate a strong positive correlation for the MS location (r^2=0.7, n=8, p<0.01) with no correlation for the ES and WS locations (Figure 4.18). Similar results are found for Mg/Ca versus $\delta^{13}C_c$ values, with a strong positive correlation (r^2=0.9, n=8, p<0.01) for the MS location and no correlation for the ES and WS locations (Figure 4.19).Similar to the results from the waters, the Sr/Mg versus $\delta^{18}Oc$ and Sr/Mg versus $\delta^{13}Cc$ demonstrate no significant correlation and a small amount of variability for the WS location (Figure 4.20 & 21).

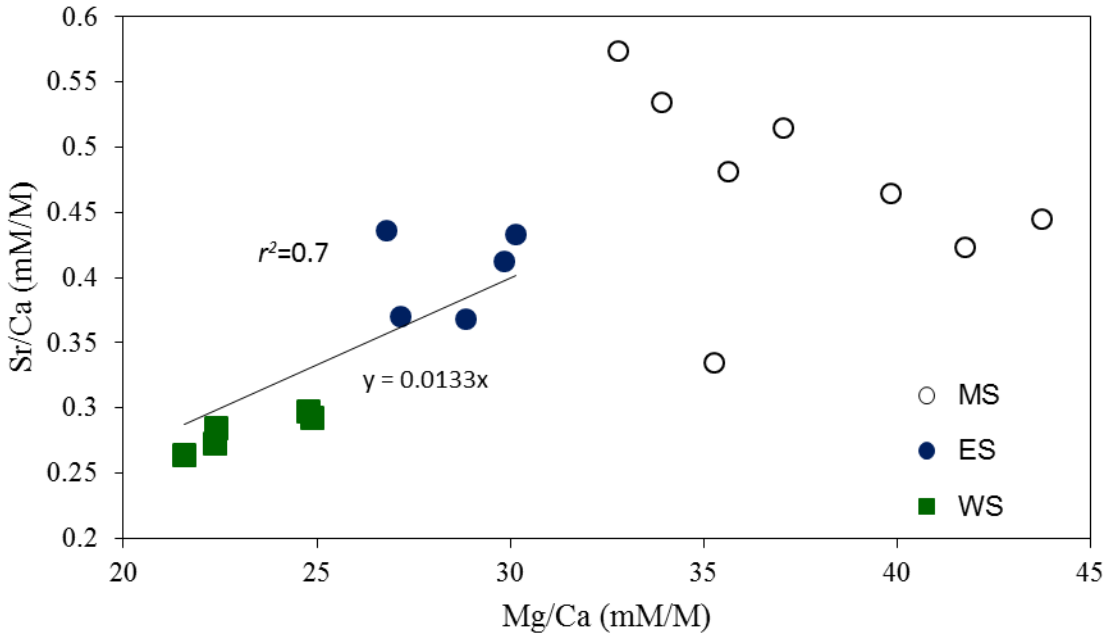

Figure 4.17: Mg/Ca and Sr/Ca for the farmed cave calcites. Sample results demonstrate a strong positive co-variation for the ES and WS calcites. There is no statistically significant correlation for the calcites from the MS location.

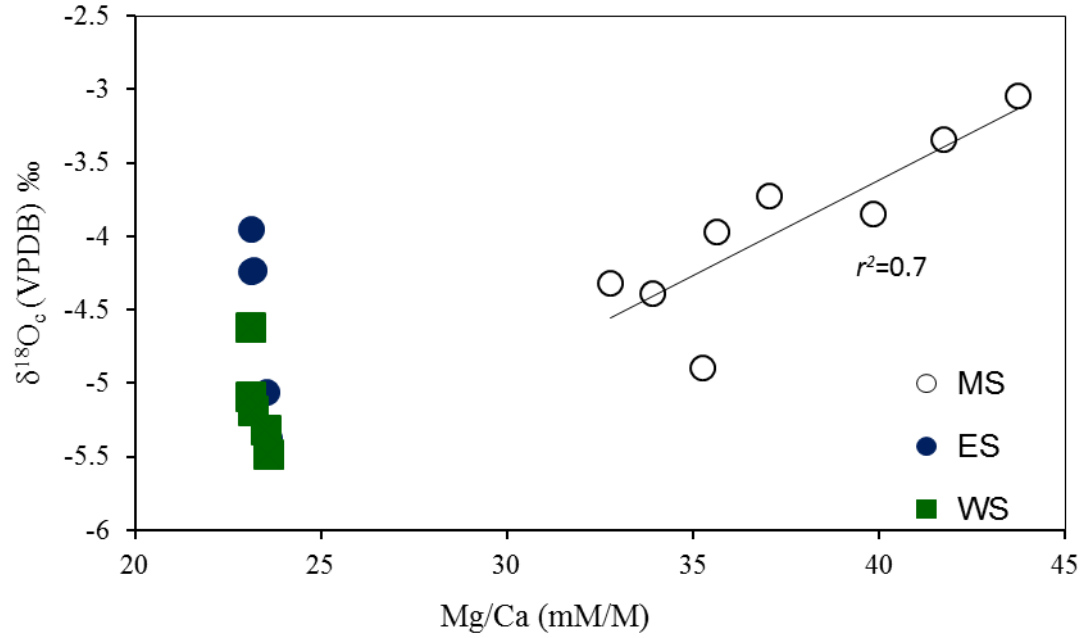

Figure 4.18: Mg/Ca versus $\delta^{18}O_c$ for the cave calcites. Results demonstrate a positive co-variation for the MS location. There is no statistically significant correlation for the calcites from the WS or ES location.

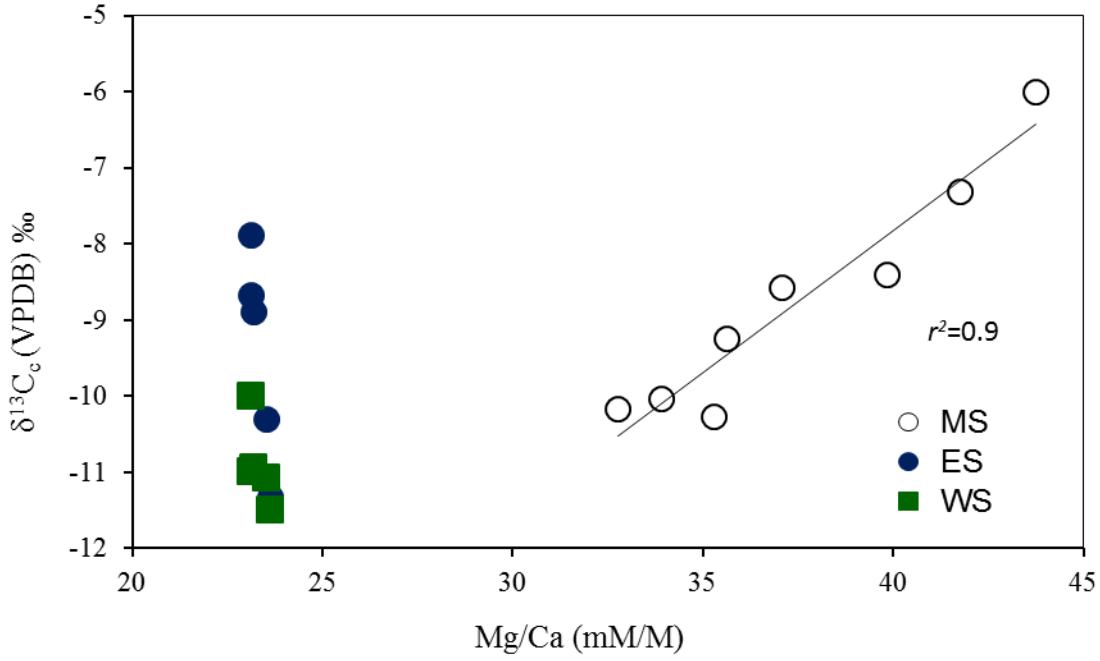

Figure 4.19: Mg/Ca versus $\delta^{13}C_c$ for the cave calcites. Sample results demonstrate a high positive co-variation for the MS location. There is no statistically significant correlation for the calcites from the WS or ES location.

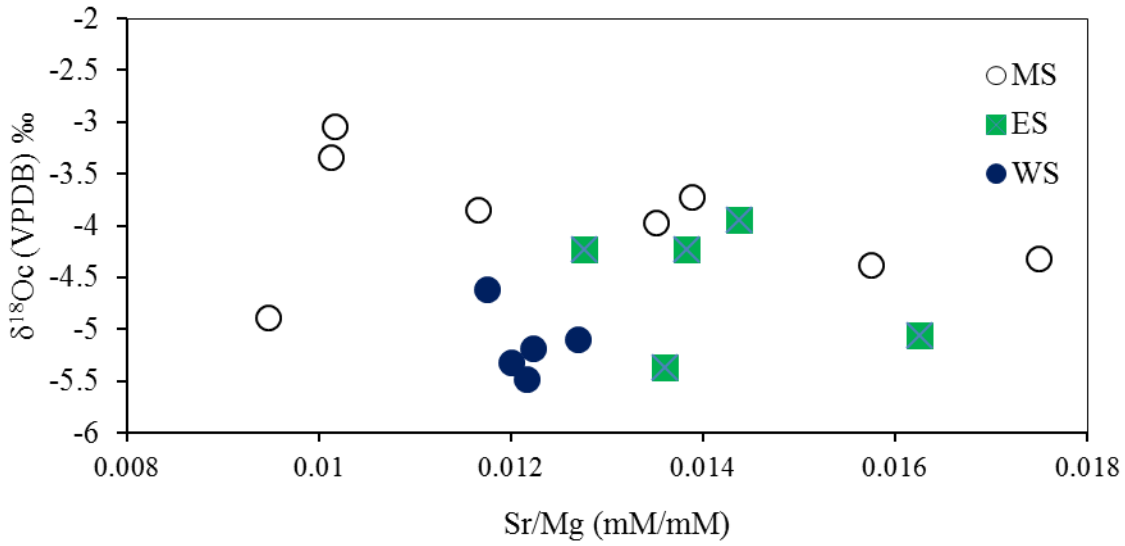

Figure 4.20: Sr/Mg versus $\delta^{18}O_c$ demonstrating no significant correlation for MS location and the least amount of spread for the WS location.

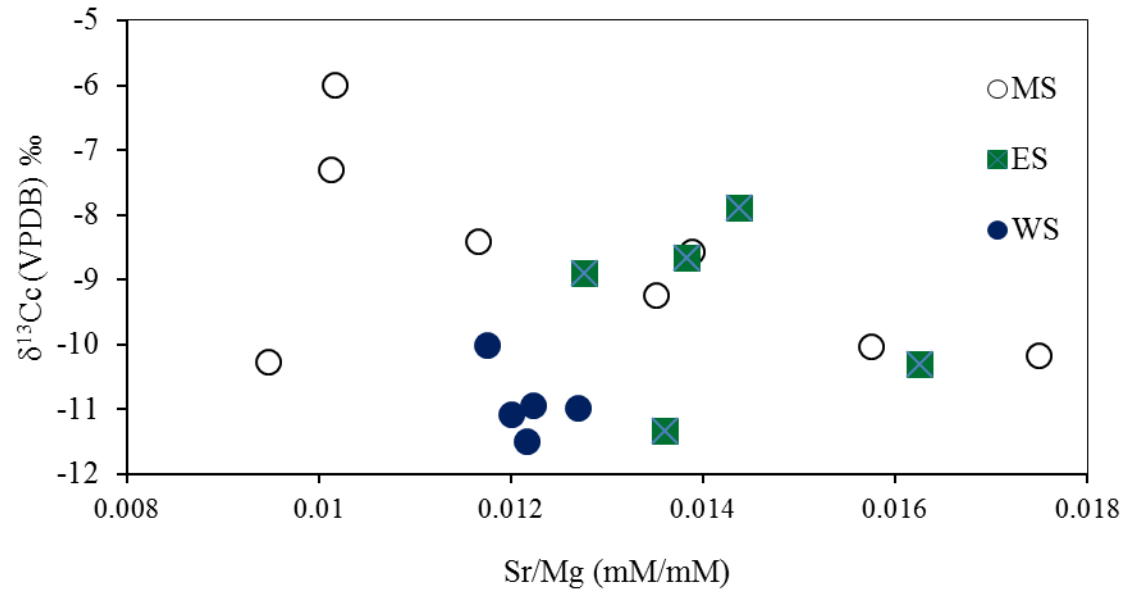

Figure 4.21: Sr/Mg versus $\delta^{13}C_c$ demonstrating no significant correlation for MS location and the least amount of spread for the WS location.

4.5 Discussion

4.5.1 Oxygen and carbon isotopes: records of temperature?

Ancient:

The higher $\delta^{13}C_c$ and $\delta^{18}O_c$ values at ~15.2±0.2, 25±0.2, 30.9±1, 38.8±0.2, 47±0.2 and 62.4±0.3 ka BP are associated with Heinrich stadials 1-6 as supported by the good agreement between the timing of Heinrich stadials in the Bahamas record and other paleoproxies (Figure 4.22) (Deplazes et al., 2013; Peterson et al., 2000; Wang et al., 2001). In addition, there is evidence for more negative $\delta^{13}C_c$ and $\delta^{18}O_c$ values associated with D/O interstadials 3, 4, 8, 9, 11 and 12 and the timing of these negative changes are shown to correlate with other records (Figure 4.22). The isotopic shifts associated with D/O interstadials are not as significant as the shifts associated with Heinrich stadials and are on the order of ~0.5 ‰ (3, 4, 8, 9, 11) to ~1‰ (12) for $\delta^{18}O_c$ and $\delta^{13}C_c$ (Figure 4.22). The interpretation that the changes in the $\delta^{13}C_c$ and $\delta^{18}O_c$ values are due to by climatic events is geochemically supported by the fact that multiple speleothems from the same cave record similar changes over time intervals which overlap. This validates that the geochemistry records climatic changes and is not influenced by kinetic isotope effects. As previously suggested, the interpretation of $\delta^{13}C_c$ and $\delta^{18}O_c$ of the carbonate is inherently complex and therefore the carbon and oxygen results will be summarized below with the interpretation of the minor elements and fluid inclusion isotope results.

Fluid inclusion isotopes:

The $\delta^{18}O_c$ record for stalagmite AB-DC-12 exhibits maximum values at ~38.8 and 46.6 ka BP associated with Heinrich stadials 4 and 5 (Figure 4.9). The higher $\delta^{18}O_c$ values are either due to higher $\delta^{18}O_w$ values or a lower temperature. Changes in the

$\delta^{18}O_w$ in the tropics is primarily thought to be due to the amount effect (Dansgaard, 1964) and this has been shown to be the primary driver of precipitation $\delta^{18}O_w$ in South Florida (Price et al., 2008). In contrast to the significant increase of $\delta^{18}O_c$ values within the Heinrich stadials, the $\delta^{18}O_w$ data obtained from the fluid inclusions reveal only minimal changes. The average change in the $\delta^{18}O_w$ across Heinrich stadial 4 (from 39.4 to 38.6 ka BP) is 0.5 ‰, close to the analytical uncertainty of the method. The average change across Heinrich stadial 5 (46.5 to 45.4 ka BP) is greater than for Heinrich stadial 4 with a 0.7 ‰ change for the $\delta^{18}O_w$ value (Table 4.4). The $\delta^{18}O_w$ values when combined with $\delta^{18}O_c$ values, allow for the calculation of the temperature at the time of mineral formation. Utilizing the equation presented in Tremaine et al. (2011), which defines the temperature dependent fractionation relationship for speleothems, a temperature variation of approximately 8 °C (Figure 4.9, Table 4.3) was calculated for the entire sampling interval. The average temperature of 25 ±2.7 °C, is similar to the average modern annual temperature for the Bahamas (average annual temperature = 22 to 28 °C) (Baldini et al., 2007), but warmer than average temperatures within modern dry caves in the area (average annual cave temperature = 23.3 °C) (Chapter 5). The average temperature change across Heinrich stadial 4 from 40 ka BP to 38 ka BP was about 2 ºC while Heinrich stadial 5 exhibits lower temperatures by about 4 ºC when compared with temperature results before and after the events. The average calculated temperature during Heinrich stadials was 24 ºC and Heinrich stadial 4 being cooler than Heinrich stadial 5. Following Heinrich stadial 4, there appears to be a progressive decrease in temperatures which could be a result of a progressive cooling leading into the glacial period.

Overall the temperatures calculated from sample AB-DC-12 are higher than previously reported for sample AB-DC-09, by approximately 8 °C (Chapter 3). As sample AB-DC-12 was collected from a shallower depth (11.9 m versus 16.5 m) than stalagmite AB-DC-09, it is possible that the cave environment between the two samples was different. Since sample AB-DC-12 was a shallower sample, it is possible that the sample was impacted by increased ventilation, which has been shown to influence speleothem geochemistry via evaporation (Kowalczk and Froelich, 2010; Tremaine et al., 2011). Additionally there may be variations in the residence time of the water in the epikarst between the two stalagmites, which may cause one stalagmite to be offset from the other. As shown in HBC, there is a 0.5 up to 1.0 ‰ difference in the $\delta^{18}O_w$ of the drip water within the cave. If we assume the drip water $\delta^{18}O_w$ values for AB-DC-12 are systematically higher relative to the drip water of AB-DC-09, and apply a correction of 1 ‰ to the $\delta^{18}O_w$ value, the average temperature difference between the two stalagmites decreases to ~2.4 °C, which is within the uncertainty of the measurements. Finally, sample AB-DC-09 formed during the LGM which may have been cooler, and in the youngest portion of sample AB-DC-12, temperatures begin to decline.

Even with the temperature differences between the two stalagmites, there are many similarities in the two fluid inclusion records. Overall the average temperature change across Heinrich stadials 4 and 5 for sample AB-DC-12 is similar (~3 °C) to the average temperature changes observed in sample AB-DC-09 for Heinrich stadials 1 -3 (~3 °C). The fluid inclusion results from samples AB-DC-09 and AB-DC-12 do not suggest a significant change in the $\delta^{18}O_w$ across Heinrich stadials, but rather both records agree that Heinrich stadials are characterized by lower temperature and higher $\delta^{18}O_c$

values. These results support the main driver of the higher $\delta^{18}O_c$ values at 15.2±0.2, 25±0.2, 30.9±1, 38.8±0.2, 47±0.2 and 62.4±0.3 ka BP associated with Heinrich stadials 1-6 are due to temperature decreases.

Oxygen isotopes of modern drip water:

There are variations observed within the oxygen isotopes of HBC drip water including: 1) second level potentially exhibits greater variation, 2) the 2nd level potentially consists of overall higher $\delta^{18}O_w$ values and 3) the west room may exhibit a lower average $\delta^{18}O_w$ value compared to the main room. In contrast to the ancient, there is no evidence from the modern for a temperature control on the $\delta^{18}O_c$ values. Rather, the δ18Ow of the modern drip water for the 2nd level negatively correlates with rainfall amount, as would be expected for the 'amount effect' driving isotope variability (Dansgaard, 1964). Also there appears to be seasonality to the $\delta^{18}O_w$ of the modern drip water however, more data is needed to verify this. Variations in the $\delta^{18}O_w$ of the modern drip water samples from throughout the cave were approximately <1‰, lower than the range observed in modern rainfall of South Florida and San Salvador, Bahamas (Baldini et al., 2007; Price et al., 2008) as would be expected due to longer residence times in the epikarst. The third level $\delta^{18}O_w$ is characterized by less annual variability than the second level, which suggests that the waters feeding the third level undergo an even longer residence time allowing for the homogenization and integration of the $\delta^{18}O_w$ seasonal signal. When compared with the $\delta^{18}O_w$ of precipitation model results (Baldini et al., 2007), the $\delta^{18}O_w$ value of the drip waters feeding the third level are primarily derived from wet season precipitation, which is the most negative $\delta^{18}O_w$ value (Tremaine and Froelich, 2013)(Figure 4.13). Other studies of cave drip waters demonstrate more

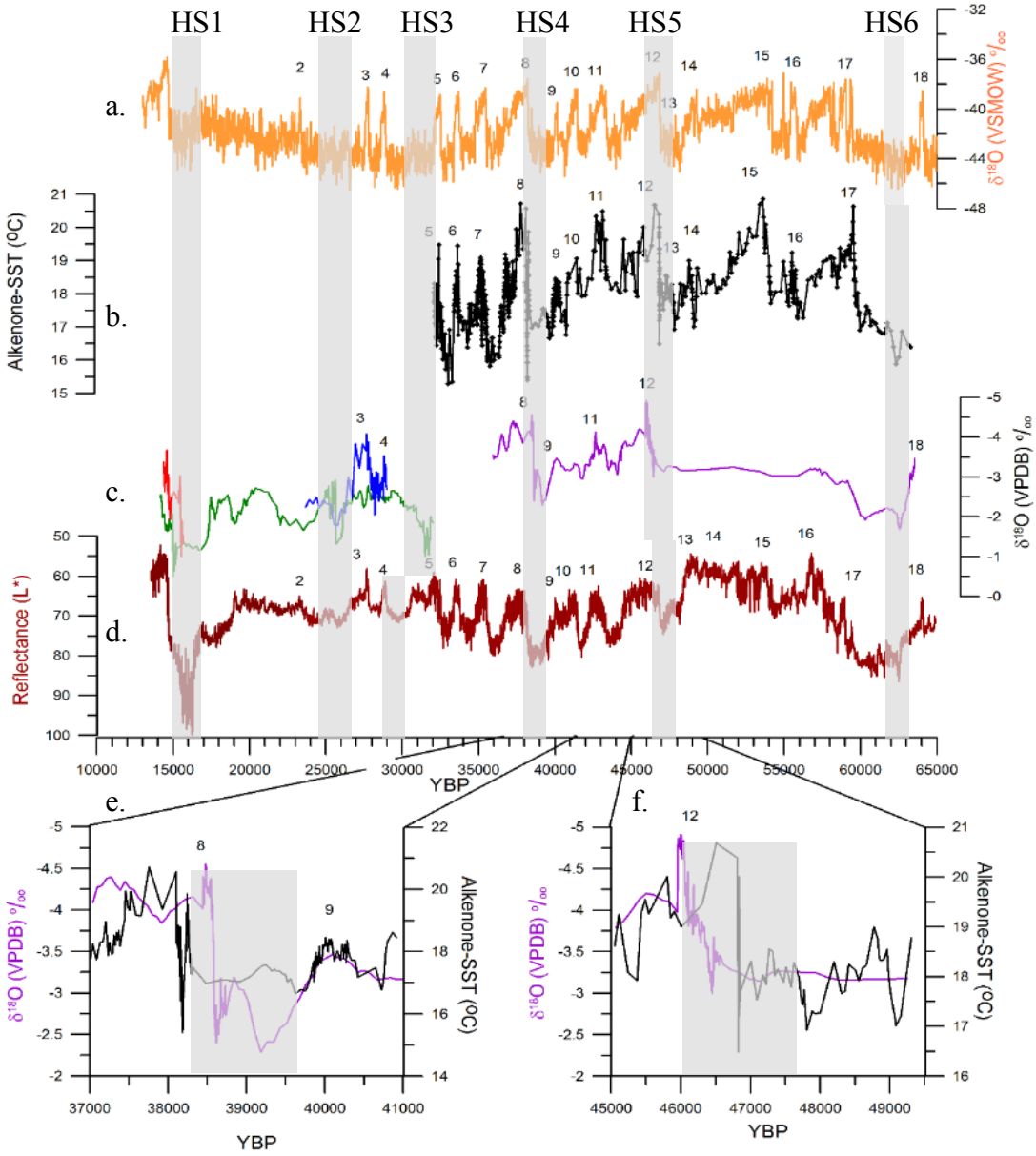

Figure 4.22: NGRIP ice core $\delta^{18}O$ values (a) with higher $\delta^{18}O$ value associated with interstadials followed by a gradual decline. Data from (Wolff et al., 2010) in orange. Alkenone derived SST record from the Bermuda Rise (b). Data from Sachs and Lehman (1999), plotted in black. Oxygen isotopes from four Bahamas stalagmites (c) plotted with the axis reversed (same as Figure 4.7 a). Sample AB-DC-01 in blue, AB-DC-09 in green, AB-DC-03 in red and AB-DC-12 in purple. Cariaco Basin reflectance data (d) in red demonstrates higher reflectance with stadials from Deplazes et al. (2013), plotted with a 50 point running average. Close up of Heinrich stadial 4 (e) and Heinrich stadial 5 (f) with the alkenone-SST record from Sachs and Lehman (1999) in black and $\delta^{18}O$ from sample AB-DC-12 in purple. Each record is plotted on its own timescale. The grey bars represent the timing of Heinrich stadials (HS) and the numbers represent interstadials.

negative $\delta^{18}O_w$ values of the water deeper in the cave, also due to the deeper parts of the cave being fed when rainfall is high and $\delta^{18}O_w$ value is low (Baldini et al., 2007; Dansgaard, 1964; Genty et al., 2014).

An additional factor that may lead to the higher $\delta^{18}O_w$ values in the main room versus the west room is higher evaporation in the epikarst, soil zone or within the cave during calcite precipitation, which may result in heavier $\delta^{18}O_w$ values. The increasing Cl^- concentration (as well as the other ions) within the cave with depth suggests that evapotranspiration is occurring. The third level west room exhibits the highest Cl- concentrations (discussed further in section 4.5.2) suggesting these waters maybe impacted by evapotranspiration (Tremaine and Froelich, 2013). Direct evaporation with in the cave can occur via ventilation and as shown in Figure 4.11, the CO_2 concentration of the cave air represents a mixture between the outside atmospheric air and a soil gas end member. Most of the air samples plot near the atmospheric end member suggesting that the cave is well ventilated and heavily impacted by atmospheric air, via ventilation. Increased ventilation and hence lower [CO_2] can lead to enhanced evaporation (Tremaine et al., 2011). If evaporation is a significant contributor to the $\delta^{18}O_w$ value, the $\delta^{18}O_w$ and $\delta^{2}H_w$ data of the drip water would not fall on the GMWL at this location, rather the drip waters would fall below the GMWL (Gat, 1996). Therefore, it does not appear that evaporation is significantly impacting the $\delta^{18}O_w$ value.

The drip water results from the modern also may explain the difference in the $\delta^{18}O_w$ values between sample AB-DC-09 and DC-12 from the fluid inclusion analyses. Sample AB-DC-09 was collected from a deeper section of the cave, therefore may lead to an overall more annually homogenized and hence lower $\delta^{18}O_w$ value.

4.5.2 Minor elements: records of precipitation amount?

In interpreting the trace element concentration of the cave, it is important to understand the various factors that can influence the drip water chemistry including: (1) bedrock dissolution, and bedrock type, (2) mixing of waters from different bedrocks and (3) Prior Calcite Precipitation.

Ancient speleothems: Magnesium

Changes in Mg concentration in stalagmites have been suggested to arise from variations in Mg concentration of the bedrock, water/rock interactions, the amount of PCP and temperature (Fairchild and Treble, 2009). Two stalagmites (AB-DC-01 and 03) collected from the deepest depths (33.5 and 34.4 m below sea level) contain a high correlation between the concentration of Mg and $\delta^{13}C_c$ values. Typically, co-variation in Sr/Ca and Mg/Ca ratios are associated with PCP and therefore PCP is not thought to be driving the high correlation between Mg and $\delta^{13}C_c$ values. Rather, the higher Mg concentration may be a result of two factors: i) increased dolomite in the bedrock, and ii) slower flow rates in the epikarst. Studies show that on Abaco Island, there is dolomite present ~24.3 m below the surface (Kaldi and Gidman, 1982) and the two samples (AB-DC-01 and -03) with a high correlation between Mg and $\delta^{13}C_c$ values are located within the dolomitized interval. Other studies which have been conducted on speleothems forming within dolomitic bedrock observed elevated Mg/Ca ratios and periods of lowered flow rates further elevated Mg/Ca ratios (Fairchild et al., 2000), as the dolomite provides a source for Mg. The associated higher $\delta^{13}C_c$ values is also impacted by lower flow rates, leading to lower biogenic CO_2 component of the DIC (Cruz et al., 2006). The periods of higher Mg/Ca and $\delta^{13}C_c$ values for stalagmites AB-DC-01 and 03 are

associated with Heinrich stadials 1 and 2 suggesting that Heinrich stadials in the Bahamas are characterized by increased aridity (Figure 4.7). Possibly the higher Mg/Ca ratio observed at 31 ka BP for stalagmite AB-DC-09 is due to increased aridity and a greater bedrock component.

The overall lower Mg/Ca ratio in speleothem AB-DC-12 may be due to the fact that this stalagmite was the shallowest sample, and therefore contained lower concentrations of Mg relative to Ca. Previous studies have also demonstrated lower minor element concentrations shallower in the cave (Verheyden, 2004). Similarly, in the modern, the shallowest drip water samples (second floor) also exhibited the lowest Mg/Ca ratios.

Ancient speleothems: Strontium

The concentration of Sr remains relatively invariant in most of the stalagmites across Heinrich and D/O events. There are, however, periods of higher Sr/Ca ratios, which are not associated with changes in Mg/Ca ratio. Both stalagmites AB-DC-09 and AB-DC-03 exhibit higher Sr/Ca ratio starting at approximately 14.6 ka BP. This period is characterized by higher amounts of rainfall (based on fluid inclusion $\delta^{18}O_w$ results and $\delta^{18}O_c$ results), which may lead to the higher Sr/Ca values and the low Mg/Ca values. This possibly suggests that during wetter periods, the flow paths for the drip water change, leading to a greater Sr bedrock signature driving the variations in minor elements (Tooth and Fairchild, 2003). Studies also demonstrate that the incorporation of Sr in stalagmites can be influenced by growth rates (Huang and Fairchild, 2001; Lorens, 1981). Both of these factors may influence the higher Sr/Ca ratio of AB-DC-09 and -03 at 14.6 ka BP.

Comparing the Sr/Mg ratio can be useful for identifying the factors influencing elemental concentrations in speleothems. Constant Sr/Mg ratio would be expected if PCP was driving the elemental concentration. Non-constant Sr/Mg was shown by (Tremaine and Froelich, 2013) to be driven by changes in bedrock mixing, cave morphology, temperature changes, growth rate, mineralogy, and incongruent dissolution of bedrock. It appears that stalagmite AB-DC-12 contains largest changes in the Sr/Mg ratio than the other stalagmites (Figure 4.7) possibly driven by the overall lower Mg/Ca ratio in this sample compared to the other samples. However, all of the stalagmites exhibit variability in Sr/Mg ratios, supporting that PCP is not the primary driver of the elemental variations in these stalagmites.

Modern minor elements: Water and calcite

Elemental variability of drip waters within the same cave has been observed in several studies (Fairchild et al., 2000; Genty et al., 2014; Partin et al., 2013; Tremaine and Froelich, 2013; Verheyden et al., 2000). Such variability within cave water has been suggested to be due to the variations in the routing path and the residence time of the water (Tooth and Fairchild, 2003). From a cave in Borneo PCP influences minor elements at one location, while minor elements at other sites are influenced by residence time at other sites (Partin et al., 2013). In HBC, a similar variability is found suggesting that two different processes are occurring within the same cave.

Prior calcite precipitation is the primary driver of minor element variability in calcites from many caves (Fairchild and Treble, 2009; Partin et al., 2013; Tremaine and Froelich, 2013). The observed positive co-varying trend between Sr/Ca and Mg/Ca in the drip waters and calcites of HBC supports that PCP is the primary driver of the elemental

variability of the calcite precipitated at the WS and ES sites. The lower Sr/Ca and Mg/Ca ratios observed in the WS compared with the ES site calcite may be indicative of less PCP occurring, as with increasing PCP, Sr and Mg concentrations will be higher (Tremaine and Froelich, 2013). As shown by Tremaine and Froelich (2013) with increased evapotranspiration (lower net rainfall, drier epikarst) there is an increase in PCP. The extent of PCP in the karst is controlled by fluctuations in net rainfall amount (Precipitation minus Evapotranspiration) which can affect the amount of PCP (Tremaine and Froelich, 2013). With decreasing net rainfall, there will be a decrease in hydrologic head and therefore a reduction in drip rate. Considering the Bahamas rainfall seasonality, this would create a generally lower net rainfall during the dry season. Evapotranspiration is shown in a cave in Florida to lead to increased concentration of Cl- (Tremaine and Froelich, 2013) while transpiration is not shown to impact the $\delta^{18}O_w$ or $\delta^{2}H_w$ of soil water. Therefore the increased Cl- deeper in the cave may be due to evapotranspiration processes influencing the water in this region in the overlying karst, and hence the increased ionic concentrations. Considering the close proximity of the cave to the ocean, there is the possibility of increased Cl- in the drip waters due to sea spray. The West room is an interesting location as this location not only has slightly higher Cl- concentration and the lowest δ^{18}Ow values, suggesting the drip waters here are driven by either increased evapotranspiration or a pool of saline water above it, both which could account for the increased ionic concentration and the lowest δ^{18}Ow values. The Wet room is thought to have the highest water throughput and the stalagmites were precipitating from active stalactites. The Sr/Ca and Mg/Ca ratios suggest that the West

room exhibits the least amount of evaporation and hence the lowest Sr/Ca and Mg/Ca ratios.

Opposite to the ES and WS sites, at the MS site, calcite does not exhibit co-varying Mg/Ca and Sr/Ca ratios. At the MS location, Mg and Sr concentrations are characterized by much greater variability of both, due to an increased bedrock signature feeding this location. This interpretation is supported by the strong relationship between Mg/Ca and $\delta^{18}O_c$ and $\delta^{13}C_c$ values (Fairchild et al., 2000; Tremaine and Froelich, 2013). Fairchild et al. (2000) demonstrated that higher Mg/Ca ratio occurred during periods of increased water-rock interactions and during periods of increased aridity. In fact, at the MS location, the periods of higher Mg/Ca, $\delta^{18}O$ and $\delta^{13}C$ values are during the dry season (January to May) when residence time is thought to be greatest due to a decrease in the amount of precipitation (Figure 4.23).

These interpretations are supported by the Sr/Mg ratio of the calcite results, which demonstrate the least amount of spread in the Sr/Mg for the WS location (variability = 0.0035 Sr/Mg) and the greatest spread in the MS results (variability = 0.008 Sr/Mg) (Figure 4.20 & 21). These results support PCP driven variability for the WS location, and hence limited Sr/Mg spread (Tremaine and Froelich, 2013). While the MS location exhibits increased Sr/Mg variability due to increased water-rock interaction at this location. This observed variability in the modern is much less than the Sr/Mg variability observed in the ancient stalagmites.

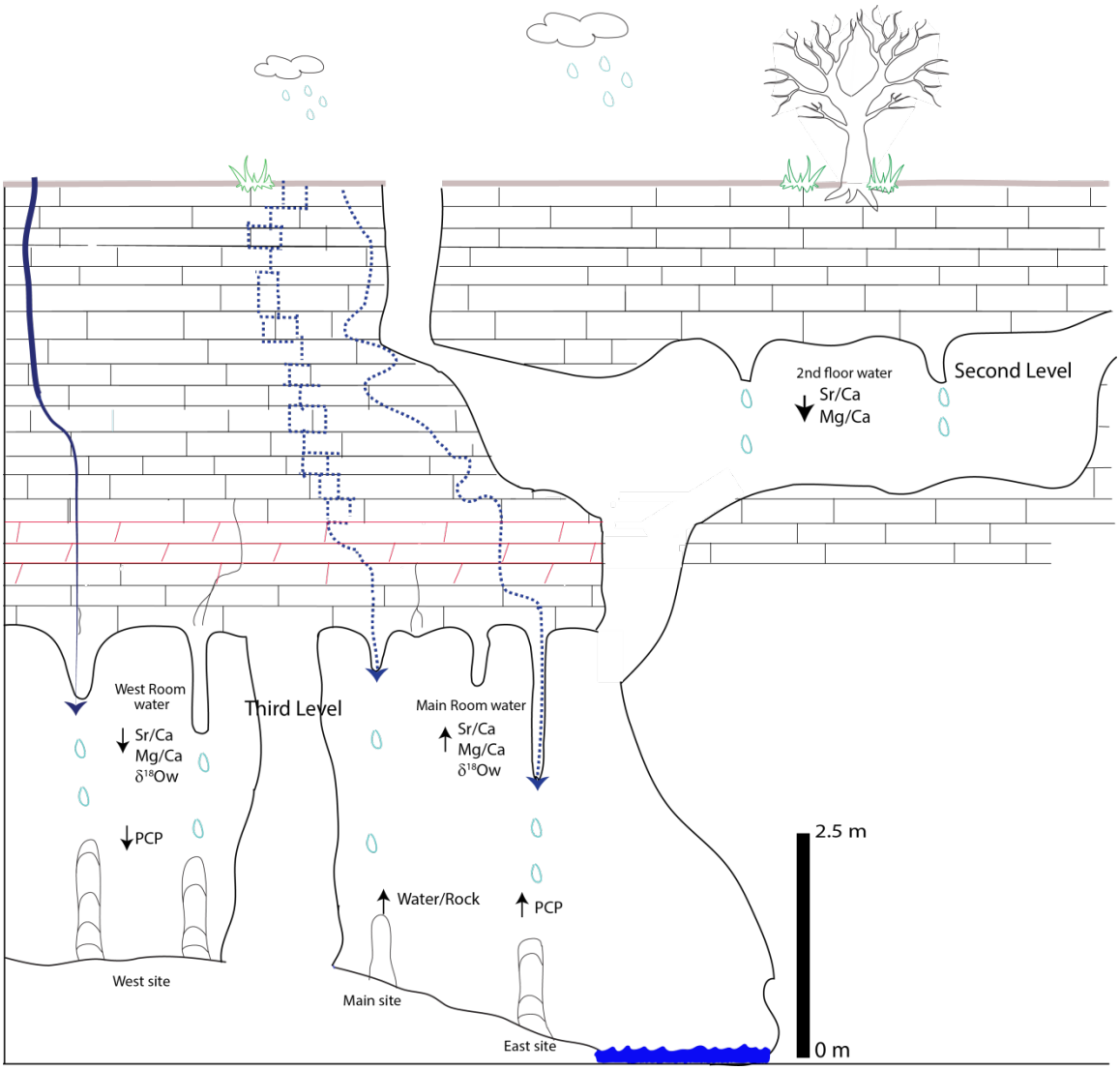

Figure 4.23: Summary of findings from the monitoring study of HBC. Results suggest the 3rd level west room is characterized by PCP, the MS location is characterized by greater water/rock interactions and the ES contains evidence of increased PCP. In contrast the second level exhibits lower Mg/Ca and higher $\delta^{18}O_w$ values. The increased PCP at the East Site may be due to increased ventilation, evaporation in the soil zone, or increased residence time in the epikarst.

As demonstrated by Tremaine and Froelich (2013) drip water Mg/Ca and Sr/Ca which co-vary are impacted by dissolution of the overlying bedrock (dolomite or limestone) and evolve away from this original value with increasing PCP. Therefore, one can back calculate the contribution from bedrock dolomite and limestone from drip water geochemistry which has been impacted by prior calcite precipitation. The results demonstrate a significant contribution of dolomite to both the West and Main locations. However this was conducted with assumptions of the bedrock minor element concentrations and future studies will analyze the bedrock trace elements.

To summarize, evaporative processes are thought to impact the ionic concentrations of the third floor drip waters. PCP has been demonstrated to occur in two of the three site and is found to be the most severe in the East Main site. The difference in PCP in the East versus West sites is thought to be a result of a greater residence time of the waters in the East site or due to ventilation differences. In contrast to the East and West site, the Main site is dominated by bedrock mixing. When comparing with the results from the ancient stalagmites, there is no evidence of PCP driving the elemental variability of the past, as is supported by the lack of Mg/Ca versus Sr/Ca correlation and the variable Sr/Mg ratio.

4.6 Interpretation of Paleoclimate Results: Comparison with Atlantic Proxies

Below follows a brief interpretation of the regional paleoclimate across millennial scale climate events, to place the Bahamas records in a regional context. The geochemistry of stalagmites AB-DC-01, -03, -09 and 12 are compared to published paleoclimate records from the Atlantic.

4.6.1 Heinrich stadials

The geochemical records from stalagmites presented in this paper, and from other proxies from the subtropical/tropical western Atlantic indicate cooling associated with Heinrich stadials as a result of lowered SSTs in the North Atlantic (Hagen and Keigwin, 2002; Hodell et al., 2012; Keigwin and Jones, 1994). This cooling is observed in an alkenone-derived SST record from the Bermuda rise (MD95-2038), located north of the Bahamas (Sachs and Lehman, 1999) (Figure 4.1). The alkenone derived SST record supports a 4-5 ºC decline in SSTs during Heinrich stadials 4 and 5 (Sachs and Lehman, 1999). When comparing the Bermuda Rise record to the Bahamian speleothem record, the two records agree with the timing of Heinrich stadial 4 and 5 within the error of the age models. The shift to cooler temperatures across Heinrich stadials in the Bermuda Rise record is greater for Heinrich stadial 4 than for Heinrich stadial 5 (Figure 4.22) and in the Bahamas record, Heinrich stadial 5 is characterized by a smaller isotopic change in $\delta^{13}C_c$ and $\delta^{18}O_c$ values (Figure 4.22 e & f). However, the fluid inclusion results support a greater decline in temperatures associated with Heinrich stadial 5 than Heinrich stadial 4 (Figure 4.9). One important consideration is that the Bahamas is dominated by seasonal rainfall (Figure 4.13), there may be enhanced precipitation of calcite during the rainy season, which may bias results to a rainy season signal. This however should not impact the temperature record as temperature of the cave is thought to reflect mean annual temperature. Sea surface temperatures in the northern hemisphere are thought to decline during these events as a result of the shutdown of the AMOC, possibly driving the lower temperature observed in the Bahamas (Deplazes et al., 2013; McManus et al., 2004).

For the $\delta^{13}C_c$ results, the interpretation is more complex. As previously suggested, the biogenic CO_2 component of the soil will decrease during periods of lowered biological activity. Lowered soil biological activity can occur during periods of lowered temperatures or increased aridity (Genty et al., 2003). The minor element results from the modern and ancient suggest that during Heinrich stadials not only may temperatures have declined; precipitation amount may have also declined, leading to a greater bedrock signature (Couchoud et al., 2009; Genty et al., 2006).

Further south of the Bahamas, there is evidence for climate variations associated with Heinrich stadials. Records from Cariaco Basin support an increased aridity (Figure 4.1 & 4.22 d) (Deplazes et al., 2013; Peterson et al., 2000) and records from Guatemala support lowered temperatures and increased aridity (Escobar et al., 2012; Hodell et al., 2012). The increased aridity associated with Heinrich stadials is thought to be impacted by a southerly shifted ITCZ and reduced SSTs (Deplazes et al., 2013; Hodell et al., 2012). Therefore for the Bahamas, the increased aridity may be caused by an expansion of the Bermuda high associated with a southerly shifted ITCZ (Hodell et al., 2000).

4.6.2 Interstadials

Both the NGRIP and Bermuda Rise records contain evidence for D/O events and are expressed in the Bermuda Rise record as periods of warmer SSTs (reaching 19 to 21 ºC) (Sachs and Lehman 1999) (Figure 4.22 a & b). The NGRIP and Bermuda Rise records demonstrate a characteristic saw-tooth pattern, with rapidly increasing temperatures followed by a steady decline (Figure 4.22 a & b). In the case of samples AB-DC-01 and 12, D/O interstadials are expressed as more negative $\delta^{13}C_c$ and $\delta^{18}O_c$ values (Figure 4.22 c) and the isotopic shifts across interstadials are not as significant as

those associated with Heinrich stadials. The lower $\delta^{13}C_c$ and $\delta^{18}O_c$ values supports warmer and/or wetter conditions for the Bahamas during interstadials. Further south, proxy data from the Cariaco Basin sediments support a wetter climate across D/O interstadials, due to the northerly shift in the ITCZ associated with higher SSTs (Figure 4.22 d) (Deplazes et al., 2013; Peterson et al., 2000). Similar to the Cariaco Basin record, the Bahamas record does not contain the saw-tooth pattern for D/O cycles as observed in the Greenland ice core record (Deplazes et al., 2013). Modeling studies suggest the large temperature change observed in Greenland during D/O stadial to interstadial transitions is a local effect and thought to be impacted by feedbacks related to sea-ice extent (Deplazes et al., 2013; Li et al., 2010; Menviel et al., 2014). This may explain the reduced response of the tropics relative to the North Atlantic during D/O interstadials. In addition, there are some D/O interstadials which do not appear in the geochemistry of sample AB-DC-12 while other speleothem samples from the Bahamas (AB-DC-03 and -09) do not contain evidence for isotopic shifts associated with D/O interstadials (Figure 4.22). This may be driven by variable strength of D/O interstadials or a minimal climate response in the Bahamas to D/O warming. Cave records from Borneo also do not contain geochemical evidence for D/O interstadials, but contain evidence for Heinrich stadials (Carolin et al., 2013), which possibly suggests that the mechanisms driving D/O interstadials are different than the mechanisms driving the global propagation of Heinrich stadials.

4.7 Conclusions

Through the application of $\delta^{13}C$ and $\delta^{18}O$ and minor element analyses on multiple speleothems from stalagmites forming over the last 65,000 years, millennial scale climate

variations have been resolved. From analysis of the $\delta^{13}C$ and $\delta^{18}O$ values of the carbonate, there is evidence of higher isotopic ratios associated with Heinrich stadials 1-6. This is thought to be due to lower temperature across these events as supported by fluid inclusion work from two Bahamas stalagmites. The minor elements support higher water/rock interactions during Heinrich stadials based on co-varying Mg/Ca and $\delta^{13}C_c$ values from two stalagmites. Covariation is driven by reduced flow rates in the epikarst and higher aridity associated with Heinrich stadials. Similarly, in the modern, the MS location results demonstrate a strong correlation between Mg/Ca and $\delta^{18}O_c$ and Mg/Ca and $\delta^{13}C_c$ supporting the interpretation of increased water/rock interactions driving the geochemistry at this location. This additionally provides confidence in our interpretation of the ancient speleothem record. Also observed in the modern is the influence of PCP on the minor elements of the precipitated calcites, with no evidence of PCP on minor element variability in the past. Finally, analysis of fluid inclusions from a stalagmite over Heinrich stadials 4 and 5 supports the previous observations that temperatures lowered during Heinrich stadials.

In conclusion, the robust relationship between Bermuda SSTs and the Bahamas speleothem records supports the influence of decreased northern hemisphere temperatures on the climate of the Bahamas. During D/O interstadials, lowered $\delta^{13}C$ and $\delta^{18}O$ values are thought to be a result of warmer and/or wetter climate; however the isotopic shifts are not as significant as the isotopic excursions associated with Heinrich stadials, possibly indicating D/O events are not significant climate events in the Bahamas or the events are not well recorded in speleothem geochemistry.

Chapter 5

Determining the causes of oxygen, carbon and clumped isotope fractionation in modern and ancient Bahamian speleothems

Summary

This study attempts to improve the understanding of oxygen, carbon and clumped isotopes using modern cave calcites and ancient stalagmites from the Bahamas. Recent studies of caves from around the world indicate that the temperature dependent oxygen isotopic fractionation of carbonate in cave calcites may be greater than previous laboratory studies indicated. Additionally, recent work applying the clumped isotope method to cave calcites produces temperatures which are too warm.

This study sheds light on the environmental causes of the $\delta^{18}O$ and Δ_{47} offsets using results from a monitoring study. This monitoring study includes the analyses of temperature, relative humidity, drip waters, cave air and the chemical composition of modern calcite ($\delta^{18}O$, $\delta^{13}C$, Δ_{47}, and minor elements). The results from the modern demonstrate the least ventilated portion of the cave is characterized by the highest growth rate, the lowest $\delta^{13}C$ of the CO_2 of the air and produces calcites which are closest to equilibrium for both $\delta^{18}O$ and Δ_{47} value when compared to the rest of the cave. This suggests that growth rate and ventilation may be primary causes of the decreased fractionation. Results from all locations in the cave demonstrate an increasing Δ_{47} offset correlated with an increased oxygen isotope offset, similar to the observations from other cave studies. This suggests that the processes driving kinetic fractionation in clumped isotopes are also driving fractionation in the oxygen isotopes.

The results from the modern are compared with $\delta^{18}O_w$ of fluid inclusions and Δ_{47} values from an ancient stalagmite collected from a currently submerged cave in Abaco

Island, Bahamas. This allows for a direct comparison of the temperature records from both methods. The Δ_{47} results demonstrate that periods with the greatest Δ_{47} offset (when compared to fluid inclusion temperatures) are associated with lower fluid inclusion temperatures, suggesting a climatic control on the kinetics. Using the methods outlined in Wainer et al. (2011), the clumped isotope results have been corrected to equilibrium. To correct to equilibrium, the relationship observed in the modern for the fractionation between water and calcite oxygen isotopes (expressed as 1000ln(α)) offset from expected versus Δ_{47} offset from expected was utilized. With α representing the fractionation factor between two substances (in this case water and calcite oxygen isotopes) and 1000ln(α) representing the per mil fractionation (Sharp, 2007). The Δ_{47} results after correction are closer to the fluid inclusion results, however offset between the two records are greatest during Heinrich stadial events 1 and 2. This suggests that the offset between oxygen isotopes and clumped isotopes may change with time and between various cave systems.

5.1 Background

Traditionally carbon and oxygen isotope analyses of speleothems have been used to unravel paleoclimate history (Fairchild et al., 2006; Lachniet, 2009) from decadal scale climatic changes (Mattey et al., 2008), to centennial scale (Lachniet, 2004) and to interglacial/glacial time scales (Carolin et al., 2013; Fleitmann et al., 2003). However, interpretation of the $\delta^{18}O$ of the carbonate is complex as the $\delta^{18}O$ of the carbonate is dependent both on the variations in temperature and the $\delta^{18}O$ of the water. The oxygen isotope paleotemperature proxy relies on the determination of the temperature of formation from the $\delta^{18}O$ of the calcite and the $\delta^{18}O$ of the formation water and numerous studies have been conducted to determine this fractionation (Craig, 1965; Epstein et al.,

1953; Kim and O'Neil, 1997; O'Neil et al., 1969). The resulting temperature dependent fractionation equations were determined from laboratory experiments in which inorganic calcite was precipitated under controlled laboratory conditions with an average fractionation of ~ -0.2 ‰/°C. For example the O'Neil et al. (1969) experiment was conducted in the laboratory at a range of temperatures (0-500 °C) and the temperature dependent fractionation equation as modified by Friedman and O'Neil (1977) is:

$$1000\ln(\alpha) = 2.78*10^6/T^2 - 2.89 \quad (1)$$

Contrary to this earlier study, the Kim and O'Neil (1997) equation was developed using the precipitation of synthetic carbonates at temperatures from 10-40°C. The Kim and O'Neil 1997 equation utilized in this study is the modified equation by Kim et al. 2007:

$$1000\ln(\alpha)_{calcite\text{-}H2O} = 18.03*10^3/T - 32.17 \quad (2)$$

A recent cave monitoring experiment demonstrated a slightly lower fractionation factor for speleothems at -0.177 ‰/°C and this relationship was found to be applicable to cave environments around the globe (Tremaine et al., 2011):

$$1000\ln(\alpha) = 16.1(10^3/T) - 24.6 \quad (3)$$

The difference between the laboratory and cave findings may be driven by kinetic isotope effects during the precipitation of cave calcites.

Without prior knowledge of the $\delta^{18}O$ of the water at the time of formation, temperature cannot be accurately calculated, therefore requiring an additional method to estimate one of the two unknowns. For ancient speleothems, this typically includes fluid inclusion isotopic analysis. Fluid inclusion isotope analysis is the isotopic analysis of water filled cavities in the speleothem calcite which is assumed to preserve drip water at the time of formation. Isotopic analysis provides information on the formation water

($\delta^{18}O_w$) and temperature can be calculated utilizing one of the temperature dependent oxygen isotope fractionation equations (Chapter 2, 3 and 4) (Arienzo et al., 2013; van Breukelen et al., 2008; Vonhof et al., 2006; Wainer et al., 2011). When fluid inclusion analyses is not possible, temperature can only be determined through the measurement of modern cave drip waters or by making assumptions of past $\delta^{18}O_w$ values.

Several studies have shown that kinetic isotopic fractionation can occur during the deposition of the carbonate in speleothems and can overwhelm any environmental signals present in the carbon and oxygen isotopes (Hendy, 1971; Lachniet, 2009; Mickler et al., 2006). Studies have analyzed variability in carbon and oxygen isotopes of cave calcites (Lambert and Aharon, 2011; Mickler et al., 2004; Riechelmann et al., 2011; Tremaine et al., 2011) and found that isotope enrichment of both carbon and oxygen isotopes is in part driven by the mechanisms of CO_2 degassing and $CaCO_3$ precipitation (Guo, 2008; Mickler et al., 2004). The production of $CaCO_3$ in caves is through the degassing of CO_2:

$$Ca^{2+}+2HCO_3^- \rightarrow CaCO_3+H_2O+CO_{2\,(g)} \quad (4)$$

and during fast degassing, one mole of carbonate is precipitated for every mole of CO_2 degassed (Guo, 2008). Degassing of CO_2 proceeds through two mechanisms (Guo, 2008; Mickler et al., 2004):

<u>CO_2 Dehydration:</u>

$$HCO_3^-(aq) + H^+ \leftrightarrow CO_2 + H_2O \quad (5)$$

<u>CO_2 Dehydroxylation:</u>

$$HCO_3^-(aq) \leftrightarrow CO_2 + OH^- \quad (6)$$

<u>Rate limiting step:</u>

$$2HCO_3^- \leftrightarrow H_2O+CO_2+CO_3^{2-} \quad (7)$$

At the pH of cave drip waters, the dominant mechanism is dehydration (equation 5) (Guo, 2008; Mickler et al., 2004). Dehydration has been documented to be accompanied by significant kinetic isotope effects both of the degassed CO_2 and the precipitated carbonate mineral (Mickler et al., 2006). This fractionation has been attributed to the HCO_3^-(aq) not undergoing re-equilibration with the water. This results in the isotopic composition of the HCO_3^-(aq) to follow Rayleigh distillation (Guo, 2008). However, studies suggest that the kinetic isotope fractionation driven by degassing can be minimal with varying environmental parameters such as saturation state and degassing rate (Tremaine et al., 2011). It is important to note that water is the main oxygen species during the precipitation of $CaCO_3$. For carbon, during the process of degassing the DIC of the water can undergo requilibration with the CO_2 air.

Clumped isotope analysis (reported as Δ_{47}) provides an additional method of constraining the mechanisms driving $\delta^{18}O$ of the carbonate. The Δ_{47} clumping method relies on the determination of the proportion of ^{13}C and ^{18}O bonds within a carbonate mineral as increased 'clumping' will be favored at lower temperatures (Ghosh et al., 2006). The Δ_{47} value has been shown to be dependent only upon the temperature of formation, and therefore prior knowledge of the $\delta^{18}O$ of the water is not necessary. By combining conventional $\delta^{18}O$ measurement of the carbonate with the Δ_{47} value, it is possible to determine the $\delta^{18}O$ of the fluid. Ghosh et al. (2006) present the original calibration of the Δ_{47} to temperature relationship utilizing inorganically precipitated calcite at known temperatures following the methods of Kim and O'Neil (1997). Since the publication of the original relationship between temperatures and Δ_{47} (Ghosh et al., 2006) other laboratories have established their own empirical and theoretical calibrations. These

include a theoretical equation developed by Guo et al. (2009), an equation proposed by Dennis and Schrag (2010) determined through inorganic calcite precipitation by passive degassing, and an equation of Zaarur et al. (2013) which utilized an active degassing method similar to Ghosh et al. (2006). All of these calibrations were conducted at Earth surface temperatures, while Passey and Henkes (2012) developed a high temperature calibration equation. The Δ_{47} to temperature equations which have been published can be divided into two main groups based on the slope between Δ_{47} and temperature: (1) a greater slope as observed in Ghosh et al. (2006), Ghosh et al. (2007), Tripati et al. (2010) and Zaarur et al. (2013) and (2) a lower slope as seen in Guo et al. (2009), Dennis and Schrag (2010), Eagle et al. (2010), Passey and Henkes (2012), Henkes et al. (2013), Hill et al. (2014), Tang et al. (2014) and Fernandez et al. (2014). Each equation produces variable temperature results, an issue which still remains to be addressed, and possible explanations for these discrepancies are well outlined in Fernandez et al. (2014) and Tang et al. (2014) (Figure 5.1).

Temperature determination from clumped isotopes has been 'successfully' applied to a range of biogenic and inorganic calcites including deep-sea corals, mollusks, brachiopods, foraminifera, dolomites and paleosols (Came et al., 2007; Dennis and Schrag, 2010; Ferry et al., 2011; Ghosh et al., 2006; Henkes et al., 2013; Hough et al., 2014; Passey et al., 2010; Thiagarajan et al., 2011; Tripati et al., 2010; Zaarur et al., 2011) (For a review on the application of clumped isotopes see Eiler, (2011)) and the Δ_{47}

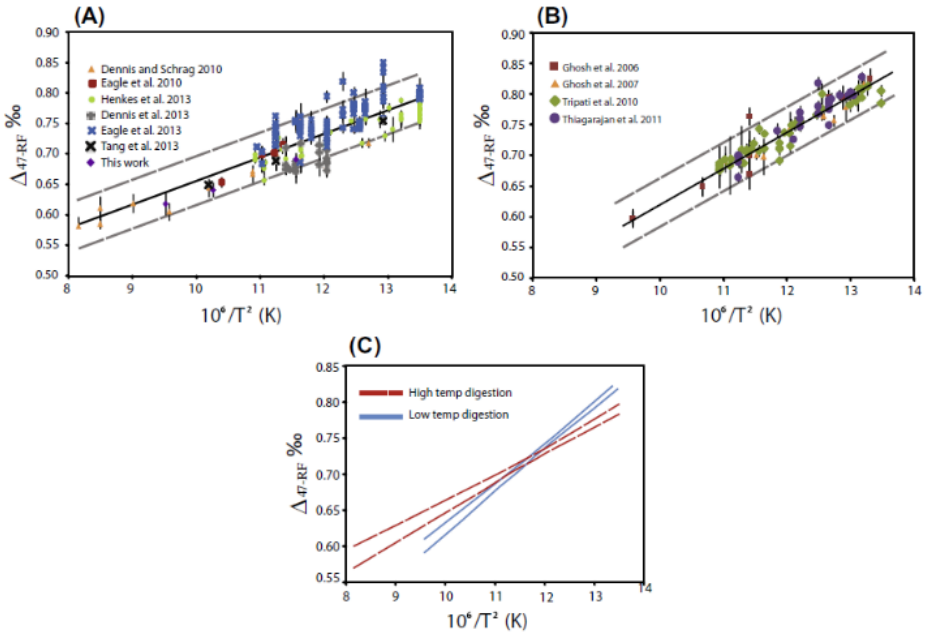

Figure 5.1: a) Studies which have analyzed the Δ_{47} to temperature relationship at high digestion temperatures. B) studies which were conducted at lower temperatures. C) 95% confidence intervals for the regression coefficients of the samples digested at high temperatures (red dotted) and low temperatures (blue). Figure from Fernandez et al. (2014).

of most carbonates appear to agree well with the temperature relationship found in Ghosh et al. (2006). The clumped isotope methodology has additionally been applied to speleothems and cryogenic cave carbonates (Affek et al., 2008; Daëron et al., 2011; Kluge and Affek, 2012; Kluge et al., 2012; Kluge et al., 2014; Wainer et al., 2011), but these studies have revealed a deviation from the Δ_{47} to temperature relationship, even in speleothems which are thought to be precipitated in equilibrium (*i.e.,* the samples pass the 'Hendy' test). This suggests that Δ_{47} is more sensitive to fractionation than $\delta^{18}O$ of the calcite (Kluge and Affek, 2012). There is one important distinction between carbonate precipitated in speleothems and carbonate precipitation in other systems; carbonate precipitation in speleothems is a three phase (air, water, calcite) system.

The first speleothem Δ_{47} isotope measurements were conducted on a stalagmite from Soreq Cave and reconstructed temperatures were found to be greater than modern expected temperatures by ~8 °C (Δ_{47} was lower) (Affek et al., 2008). Similar results have been found in other caves (Daëron et al., 2011; Kluge and Affek, 2012; Wainer et al., 2011) and in laboratory precipitation experiments which mimicked the cave environment (Daëron et al., 2011). Studies have also found a strong correlation between $\delta^{18}O$ and Δ_{47} offsets, with Δ_{47} exhibiting more negative values than predicted and $\delta^{18}O$ values more positive than predicted (Affek, 2013; Daëron et al., 2011; Kluge and Affek, 2012). A study focusing on stalagmites from Bunker Cave, Germany found reduced kinetic isotope fractionation occurred across periods with a reduced super saturation of drip water (Kluge and Affek, 2012). The preciptiation of calcite occurs through the degassing of CO_2 from very high pCO_2 drip water to a low CO_2 cave and it is thought that during the degassing process, fractionation can occur.

This study represents an additional attempt to determine the causes of kinetic fraction from speleothems through a cave monitoring experiment from the subtropical Bahamas. In addition, by also sampling an ancient speleothem sample from the Bahamas for clumped isotopes and fluid inclusion isotopes, a direct comparison between the two temperature methods demonstrates that the causes of kinetic fractionation in speleothems may vary between cave systems and with space and time.

5.2 Samples

5.2.1 Modern samples: Hatchet Bay Cave

Samples were collected from Hatchet Bay Cave (HBC), a currently active cave in Eleuthera, the Bahamas (Figure 5.1). Monitoring was initiated in June of 2012.

Overlying the cave is grasses and small *Metopium toxiferum* (poison wood) and trees of the Fabaceae family with well-developed soils (greater than 15 cm depth). Most of the grasses are located near the entrance and at lower elevations around the cave, with the small trees located on the Aeolian ridge. HBC was accessed through a small ~1.7 m. by 0.9 m. opening located 10 to 15 m above sea level and exhibits an extremely linear pattern particularly west of the main entrance (Mylroie and Mylroie, 2009). The opening is immediately surrounded by thick grasses with larger trees (as described above) located 3 meters to the west, approximately following the cave direction and well developed soils (as described above). The first level exhibits evidence of phreatic dissolution (Mylroie and Mylroie, 2009). There is no evidence of cave breathing holes through the roof as suggested by the lack of changes in the overlying vegetation and soil. The cave is divided into three levels with the first level being the shallowest and the smallest level. The second level is a tubular passage accessed by a 1.6 m. ladder down from the first level and again contains evidence of phreatic dissolution (Mylroie and Mylroie, 2009). The second level is more extensive (300 m long) with active drip water and stalagmite formation (Mylroie and Mylroie, 2009). The 2nd level is thought to follow a thick, terra rossa paleosol, leading to the creation of the linear and tubular shape following the aeolian ridge (Mylroie and Mylroie, 2009). The third level is the deepest level and is accessed by another 1.8 m ladder from the second level. However continuing on the second floor lies a smaller passage which after several meters leads to a 7 m shaft to the surface, which may have been carved out for guano mining (Mylroie and Mylroie, 2009). The third level is partially filled with water, with active stalagmite formation occurring on raised rock ledges above the water, ~1.2 m above the water level. This water is tidally

influenced and of marine salinity (Mylroie and Mylroie, 2009). There is no evidence of water flooding the rock ledges nor is there any evidence of calcite deposits forming from the water. Most of the sampling was conducted on the 2nd and 3rd levels. Located on the 3rd level ledges were experiments on the precipitation of calcite from drip water, henceforth known as calcite "farming" (Figure 5.2). The cave was visited every 3-5 months. This cave has more extensive speleothem formation than other caves in Eleuthera possibly driven by the 10-15 m of overlying calcite (Mylroie and Mylroie, 2009). Samples from the surrounding cave walls were not collected.

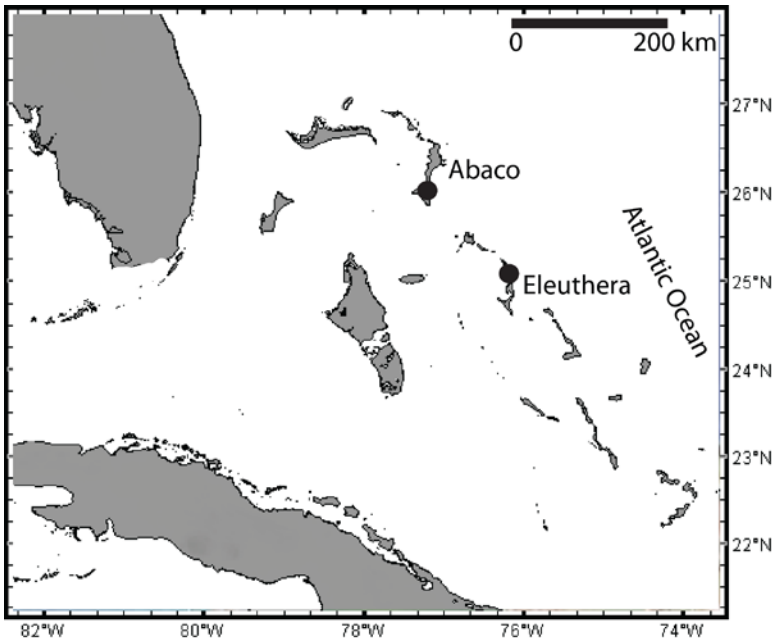

Figure 5.2: Map of the Bahamas showing the location of Abaco Island and Eleuthera Island, both islands located on the eastern edge of the Bahamas platform.

Figure 5.3: (following page): Schematic of the entire surveyed area including first, second and third levels. The eastern part of the cave was not surveyed due to difficulty accessing this part of the cave. The locations of water and air sampling are approximate. Also shown is the approximate location of water and air collection as well as calcite farming. Shown are photographs of the areas which were sampled including main site (MS), east site (ES) and the west site (WS).

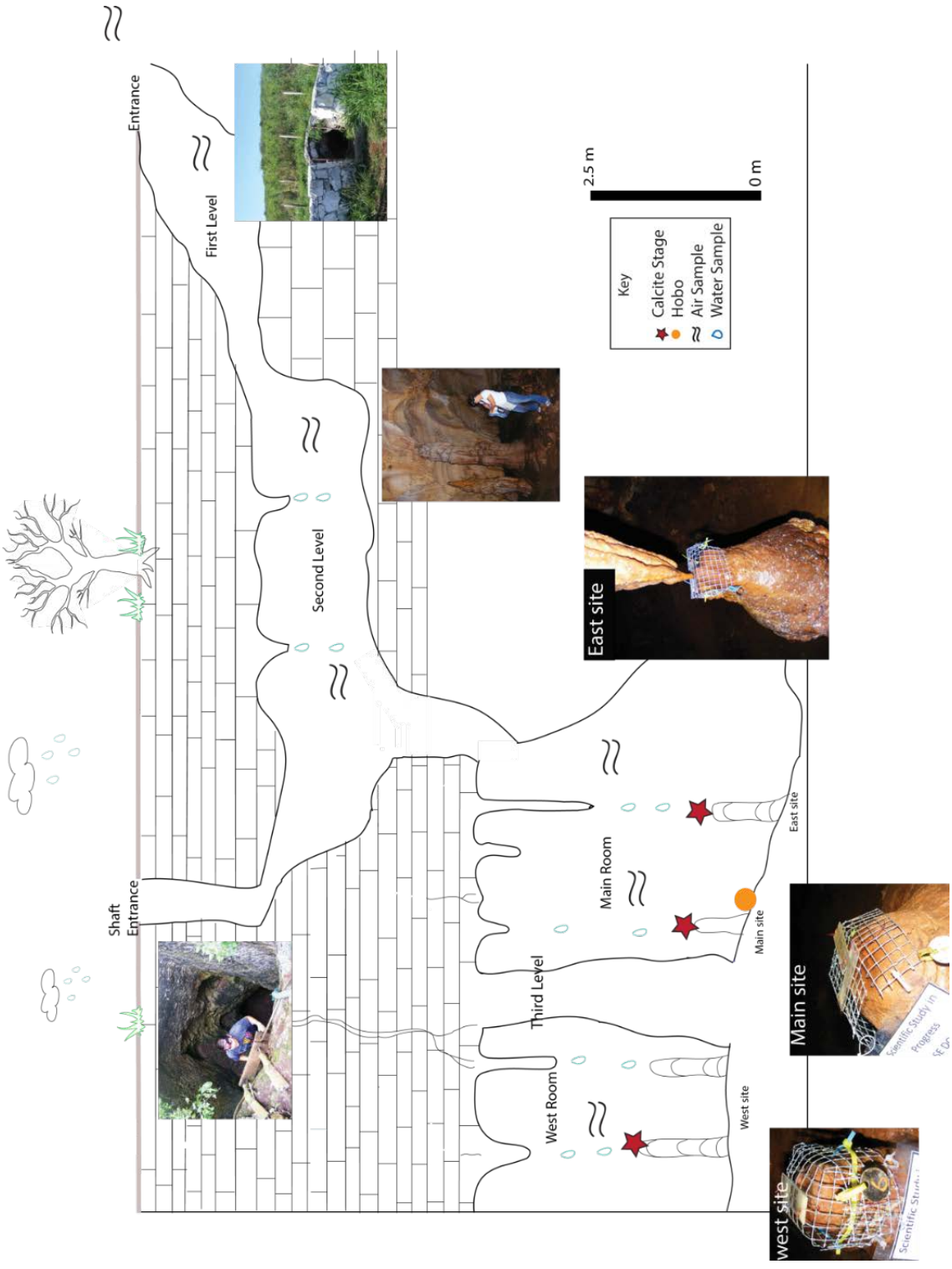
Entrance
First Level
Second Level
Shaft Entrance
Main Room
Third Level
West Room
East site
Main site
West site
2.5 m
0 m
Key
Calcite Stage
Hobo
Air Sample
Water Sample
East site
Main site
west site

5.2.2 Ancient stalagmite

The stalagmite (sample AB-DC-09) was collected from a currently submerged cave on Abaco Island, Bahamas, in July of 2007 from a depth of 16.5 m. The stalagmite was not currently forming, but rather formed when sea-level was low and the cave was exposed to air (Figure 5.2).

5.3 Methods

5.3.1 Hatchet Bay Cave

Analyses were conducted on the air ($\delta^{13}C$ of CO_2, CO_2 concentration), drip water ($\delta^{18}O_w$, $\delta^{2}H_w$, $\delta^{13}C$ of DIC and minor elements) and the farmed calcite ($\delta^{13}C_c$, $\delta^{18}O_c$, Δ_{47}, and trace elements) deposited on microscope slides which were deployed in the cave. A description of the monitoring methods is included in the following.

HBC Environmental:

Hatchet Bay Cave was continuously monitored for temperature and relative humidity from June 2012 to November of 2013. Temperature and relative humidity were measured every two hours utilizing a HOBO U23 Pro v2 Temperature/Relative Humidity Data Logger from Onset. The manufacturer specifications are for temperature: ±0.21°C from 0° to 50°C and for relative humidity: ±2.5% from 10% to 90% relative humidity, to a maximum of ±3.5%, therefore for humidity levels above 90%, errors increase. The temperature and relative humidity sensor was located in the main room (Figure 5.3). Air samples for carbon isotopes of the CO_2 ($\delta^{13}C_{AIR}$) and CO_2 concentration were collected into 30 mL glass vials sealed with a septa, in a transect through the cave. Every visit to the cave an air sample was taken outside of the cave in an open field prior to entering the cave. Air samples for carbon isotopes of the CO_2 ($\delta^{13}C_{CO2}$) were collected into 30 mL

glass vials sealed with a septa, in a transect through the cave. Every visit to the cave an air sample was taken outside of the cave in an open field within 3 meters of the cave entrance prior to entering the cave. Carbon isotopes of the CO_2 were analyzed at the University of Miami on a gas bench coupled to a Thermo-Delta plus Advantage isotope ratio mass spectrometer (IRMS) and calibrated against internal standards. Data are reported relative to Vienna Pee Dee Belemnite (V-PDB). To determine CO_2 concentration, carbon peak intensity data were calibrated utilizing air samples with CO_2 concentrations of atmospheric condition using only one standard of atmospheric air of CO_2 concentration. Unfortunately, CO_2 concentration was only measured for a subset of the sample analyzed for $\delta^{13}C_{CO2}$ value.

Unfiltered water samples were collected throughout the second and third levels of the cave by holding clean acid washed vials under dripping stalactites. Vials were filled completely (where possible) to avoid head space equilibration, then capped and stored until analysis. Samples were filtered using a Whatman 0.2 μm pore filter upon return to the laboratory and stored in clean vials (within 2-3 days). Water samples were measured for oxygen and hydrogen isotopes ($\delta^{18}O_w$ and $\delta^{2}H_w$), carbon isotopes of the dissolved inorganic carbon (DIC) ($\delta^{13}C_{DIC}$), pH, Chloride concentration and total alkalinity.

For oxygen and hydrogen isotopes of the water samples, samples were measured using a L2130-i Picarro cavity ring down spectroscopy (CRDS) instrument. In house standards are analyzed with the samples which have been previously calibrated to the VSMOW-GISP-SLAP scale. One milliliter of each sample or standard is measured into a glass vial and sealed with a rubber septum. Each sample or standard is injected into the Picarro A0211 vaporizer unit at 0.2 ml per injection six times into the vaporizer. The

vaporizer is held at 110ºC for the duration of the sample run. The injection port of the A0211 is fitted with a fine stainless steel mesh for trapping salt crystals to minimize interferences and clogging downstream. The mesh basket is periodically removed, rinsed, dried and reinserted into the injection port. The vaporized water gas is transferred to the Picarro CRDS analyzer in a stream of N_2 gas. The measurement cycle of each sample lasts about 8 minutes and data are reported relative to VSMOW.

For $\delta^{13}C_{DIC}$ measurements, samples were injected in a previously evacuated 30 mL glass vial sealed with septa which contained 0.5 mL of 103% phosphoric acid (H_3PO_4) previously flushed with Helium. Samples were then mixed utilizing a vortex mixer producing CO_2 from the reaction between DIC and the phosphoric acid. The CO_2 was sampled using a gas bench and measured on a Thermo-Delta V Advantage IRMS. The $\delta^{13}C$ was calibrated to three reference pulses of CO_2, two at the start of the sample and two at the end. In house reagent grade $NaHCO_3$ standards were also utilized for standardization and consist of a similar molarity to the samples and were analyzed in the same manner as the samples. The $\delta^{13}C$ of the in house standards have been previously standardized using a dual inlet mass spectrometer (Finnigan MAT 251), calibrated relative to Vienna Pee Dee Belemnite (V-PDB). The reproducibility determined from multiple replicates of standards is < 0.1‰ and data are reported relative to Vienna Pee Dee Belemnite (V-PDB).

Alkalinity was measured utilizing a double endpoint auto titrator using 0.01 N HCl. Average error determined from the repeated measurement of a standard was 0.02 mM. Chloride concentration was determined by titration with silver nitrate using dilute potassium chromate solution as the indicator. International Association for the Physical

Science of the Oceans (IAPSO) seawater standard was utilized as a standard solution for Chloride and the average error was 5 ppm. Carbonate saturation state was calculated using Geochemist Workbench utilizing the React program in SpecE8. Saturation state results were then averaged from when the slide was deployed and when it was collected to characterize the saturation state during the time the slide was in the cave.

Precipitate:

Standard glass microscope slides were placed on top of currently forming stalagmites. Microscope slides were held in place by wire and were tied down at an angle similar to the methods of Tremaine et al. (2011) and Banner et al. (2007). Prior to installing the slides in the cave, the slides were weighed in the laboratory. Two calcite precipitation sites were set up, one in the main room of the third level (these two will be referred to in the text as east main site (ES) (1 slide) and main site (MS) locations (2 slides)) and one in the west room (1 slide) (referred to in the text as west main site (WS)) (Figure 5.3). The microscope slides were left in the cave for 3-5 months at which point they were replaced with new slides.

Slides were brought back to the laboratory, dried, weighed, and the calcite mineralogy for select samples was verified using X-ray diffraction (XRD) on a Panalytical X'pert Pro. Slides were not rinsed prior to analysis, therefore may be contaminated with sea salts. To test for the occurrence of kinetic isotope fractionation, one slide (Slide #6) was chosen for spatial C and O isotopic analysis of the calcite ($\delta^{13}C_c$ and $\delta^{18}O_c$). Samples were taken at 5 mm increments across the entire slide. For the remaining slides, the calcite of the slides was divided into "center" and "outside" (Figure 5.4). The calcite was removed from the slide utilizing a dental tool to scrape the calcite

off of the slide, homogenized, and analyzed for clumped isotopes (Δ_{47}) as well as C and O isotopes (Figure 5.4). The C and O isotopic measurements were made using a Kiel III interfaced with a Thermo-Finnigan Delta Plus IRMS at the University of Miami. All data have been corrected for isobaric inferences at mass 45 and 46 and are reported relative to Vienna Pee Dee Belemnite (V-PDB). The precision of the $\delta^{13}C_c$ and $\delta^{18}O_c$ values is better than ±0.1‰. The method for the clumped isotope analysis is discussed in section 5.3.2.

Statistics:

Data were considered to be normally distributed and using a Pearson correlation coefficient, correlations were performed. Statistically significant relationships are reported at the 95% confidence limits.

5.3.2 Clumped isotopes

The calcite from sample AB-DC-09 and from the HBC slides were both analyzed for clumped isotopes (Δ_{47} value). The methods for clumped isotope analyses at the University of Miami are outlined in Murray et al. (Submitted) and Swart et al. (In Prep).

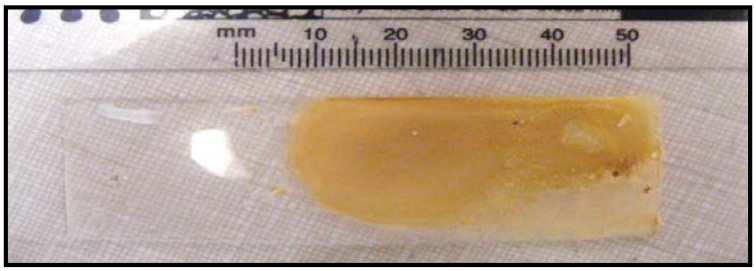

Figure 5.4: Example of the slides from HBC monitoring. Slide #10 after collection and drying in 40 ºC oven. Sampling of the slide was conducted at the center of the slide and along the outside of the slide for $\delta^{18}O_c$, $\delta^{13}C_c$ and Δ_{47} value. The calcite was removed using a dental tool, homogenized with a mortar and pestle and stored in Eppendorf vials until analysis.

Briefly, 8 mg of sample were weighed into copper boats and reacted at 90 °C for 30 minutes in 103% H_3PO_4 using the common acid bath method (Swart et al., 1991). After reaction, CO_2 was purified utilizing two H_2O removal traps held at -80 to -90 °C and a PoraPak Q trap held at -25 to -30 °C to remove contaminants. The CO_2 gas was cryogenically frozen into a sealed vessel and transferred to the IRMS for analysis. The entire process from reaction to the IRMS takes approximately 90 minutes. In between samples, the entire line is evacuated through two turbo molecular pumps and the line is heated up to 200 °C for 30 minutes. A complete description of the extraction line can be found in Appendix D.

Sample CO_2 gas was measured on the Thermo MAT 253 IRMS. The $\delta^{13}C$ and $\delta^{18}O$ of the CO_2 reference gas was calibrated using NBS-19 and results reported relative to Vienna Pee Dee Belemnite (VPDB). Samples were analyzed for 10-20 acquisitions and run at 12 V on mass 44 with peak centering and pressure balancing before each acquisition. The sample δ45, δ46, δ47 and δ48 values were measured to obtain a standard error of ~±0.008‰ for the Δ_{47} value.

Calculation of Δ_{47} was conducted utilizing the methods outlined in Affek and Eiler (2006) and Huntington et al. (2009). All data are reported in the reference framework outlined in Dennis et al. (2011) utilizing both heated and water equilibrated gases (1000, 50 and 25 °C). All data have been corrected for an acid fractionation factor of -0.00141 ‰/°C for reaction at 90°C as reported in Henkes et al. (2013).

A typical set of sample analyses includes an internal carbonate Carrara marble standard, followed by 2-4 samples. Monthly, heated and water equilibrated gases were analyzed and the data corrected to account for long term drift in the machine. Samples

have been analyzed in this method since May of 2012 to March of 2014 and the long term reproducibility of the internal Carrara standard over this time period was ±0.032 ‰ 1 S.D. (or ±0.0032 ‰ 1 S.E) for Δ_{47} value with an average Δ_{47} value of 0.379 ‰ (reference frame). Appendix D contains the long term reproducibility of the internal Carrara marble standard. Results from heated and water equilibrated gases can be provided upon request.

All results have been corrected to the absolute reference frame as outlined by Dennis et al. (2011). The absolute reference frame was first proposed by Dennis et al. (2011) as a means to standardize between laboratories to minimize the potential for measurement artifacts. Samples are placed in the reference frame by analyzing a suite of heated (1000 °C) and low temperature, water equilibrated (25, 50°C) gases. Heated gases were prepared by sealing a set of pre-cleaned CO_2 gases with a range of δ47 values in to quartz tubes and heated for at least 2 hours in a furnace. Heated gases were then quenched and analyzed on the MAT-253 using the same method as used for samples. For water equilibrated gases, CO_2 with a range of δ47 values were sealed in to Pyrex tubes which contained 150 μL of in house standard water (-1.07 ‰ $\delta^{18}O$ VSMOW, and -5.32 ‰ $\delta^{2}H$ VSMOW), sealed and placed in a water bath for 3 days at either 25 °C or 50 °C. After equilibration, CO_2 was cleaned using the same method used for samples, and subsequently analyzed on the MAT-253, again utilizing the same method used for samples. Greater detail of this method can be found in the Appendix D. The results from the heated and water equilibrated gases are then utilized to place the measured samples into the reference frame.

As noted earlier, there are several published temperature to Δ_{47} calibration

equations. For this project, the results will be expressed using the equation from Ghosh et al., 2006 in the reference frame as reported by Dennis et al., 2011:

$$\Delta_{47} = 0.0636*10^6/T^2 - 0.0047 \quad (8)$$

This equation was chosen as it has been utilized in most speleothem studies to date. Considering this is a relatively new field of geochemistry all raw data and heated gas results can be provided. For the HBC slides and samples from the AB-DC-09 stalagmite, samples were each run 2 to 5 times and the data collected include δ47, Δ_{47}, $\delta^{13}C_c$ and $\delta^{18}O_c$ values. Results for $\delta^{13}C_c$ and $\delta^{18}O_c$ are reported relative to V-PDB while Δ_{47} values are reported in the reference frame of Dennis et al. (2011).

5.3.3 AB-DC-09

Fluid Inclusion Isotopes:

Oxygen and hydrogen isotopes ($\delta^{18}O_w$ and $\delta^{2}H_w$) were measured on 31 fluid inclusion samples from AB-DC-09 (Chapter 3). Fluid inclusion data are reported relative to Vienna Standard Mean Ocean Water (VSMOW) with an average error of 0.5 ‰ for $\delta^{18}O_w$ and 2.0 ‰ for $\delta^{2}H_w$ values (Arienzo et al., 2013). The $\delta^{18}O_c$ of the calcite hosting the inclusion was measured at the University of Miami using a Thermo-Finnigan Delta Plus IRMS as described above. Stalagmite AB-DC-09 was also radiometrically dated using U-Th dating methodologies for a total of 20 U-Th dates, as described in Chapter 3.

Clumped Isotopes:

For stalagmite AB-DC-09, the same 31 water samples which were analyzed for fluid inclusions were also measured for clumped isotopes utilizing the methods described in section 5.3.2. An additional 7 samples were measured for Δ_{47} value only.

5.4 Results

5.4.1 Environmental variation in Hatchet Bay Cave

Below follows a summary of the findings of the monitoring project at HBC. All of the individual sample results, are provided in Appendix D.

Temperature, humidity and air:

Throughout the duration of the experiment (June 2012 to November 2013), the relative humidity remained at >90 % ±2.5. Temperature varied from 22.8 °C to 23.8 °C at as reported by the temperature logger, with an average value of 23.3 °C. The maximum temperature occurred at the end of October to beginning of November of 2013 (Figure 5.5). Minimum temperature was found in mid-April of 2013.

The $\delta^{13}C$ of cave air CO_2 ($\delta^{13}C_{CO2}$) demonstrates a progressive depletion in $\delta^{13}C_{CO2}$ value from the outside of the cave to the third level west room (Figure 5.6). On average, the 3rd level west room is 1.5 ‰ more negative than the 3rd level main room. $\delta^{13}C$ of the soil or soil CO_2 concentration was not measured. The results demonstrate a co-variation between $\delta^{13}C_{CO2}$ and $1/[CO_2]$ with decreasing $\delta^{13}C_{CO2}$ occurring with increasing $[CO_2]$ (Figure 5.7)(Keeling, 1958). This is thought to be driven by the mixing of two end members, an atmospheric end member and a soil gas end member which is estimated in Figure 5.6 (Tremaine et al., 2011). Most of the sample results plot near the atmospheric end member and the line of best fit has a y-intercept at -18 ±2‰ which is thought to be the soil gas value. The deeper in the cave, the lower contribution from atmospheric air (Figure 5.8).

Water:

Isotopic analyses of the drip waters include the analyses of $\delta^{13}C_{DIC,}$ $\delta^{18}O_w$ and $\delta^{2}H_w$ values. Overall the $\delta^{13}C_{DIC}$ results decrease with increasing depth within the cave (Figure 5.9) similar to the trend observed in the $\delta^{13}C_{CO2}$ results (Figure 5.6). The $\delta^{18}O_w$ of the drip waters were also more negative in the 3rd level west room when compared with the 2nd level or the 3rd level main room (Table 5.1). The average $\delta^{18}O_w$ of the drip waters for the 3rd level main room was -4.2±0.5 ‰ while the west room was -4.8±0.4 ‰. Total alkalinity and pH were relatively invariant (Alkalinity = 3.5 to 4.0 mM and pH 7.8 to 8.0) within the cave, with a slight increase from the 2nd to 3rd level. Chloride concentration was greater in the 3rd level drip waters than the 2nd level (538 ppm) and within the third level, the west room waters contained the highest Cl- concentrations (2811 ppm in West Room, with 2025 ppm in Main room) (Table 5.1). Evapotranspiration is shown in a cave in Florida to lead to increased concentration of Cl- (Tremaine and Froelich, 2013) while transpiration is not shown to impact the $\delta^{18}O_w$ or $\delta^{2}H_w$ of soil water. Therefore the increased Cl- deeper in the cave may be due to evapotranspiration processes influencing the water in this region in the overlying karst, and hence the increased ionic concentrations. Considering the close proximity of the cave to the ocean, there is the possibility of increased Cl- in the drip waters due to sea spray. Results demonstrate that for May, August and November, saturation state was higher in the 3rd level than the 2nd level (Figure 5.10), and saturation state does not significantly change within the third level (Saturation state 1.1 to 1.0 for Main and West rooms respectively) (Table 5.1, Figure 5.10). Chloride is known to be a conservative element. However increasing Cl- concentration deeper in the cave is thought to be in part driven by

increased evapotranspiration affecting these waters leading to increased ionic concentration (Table 5.1) (Tremaine and Froelich, 2013).

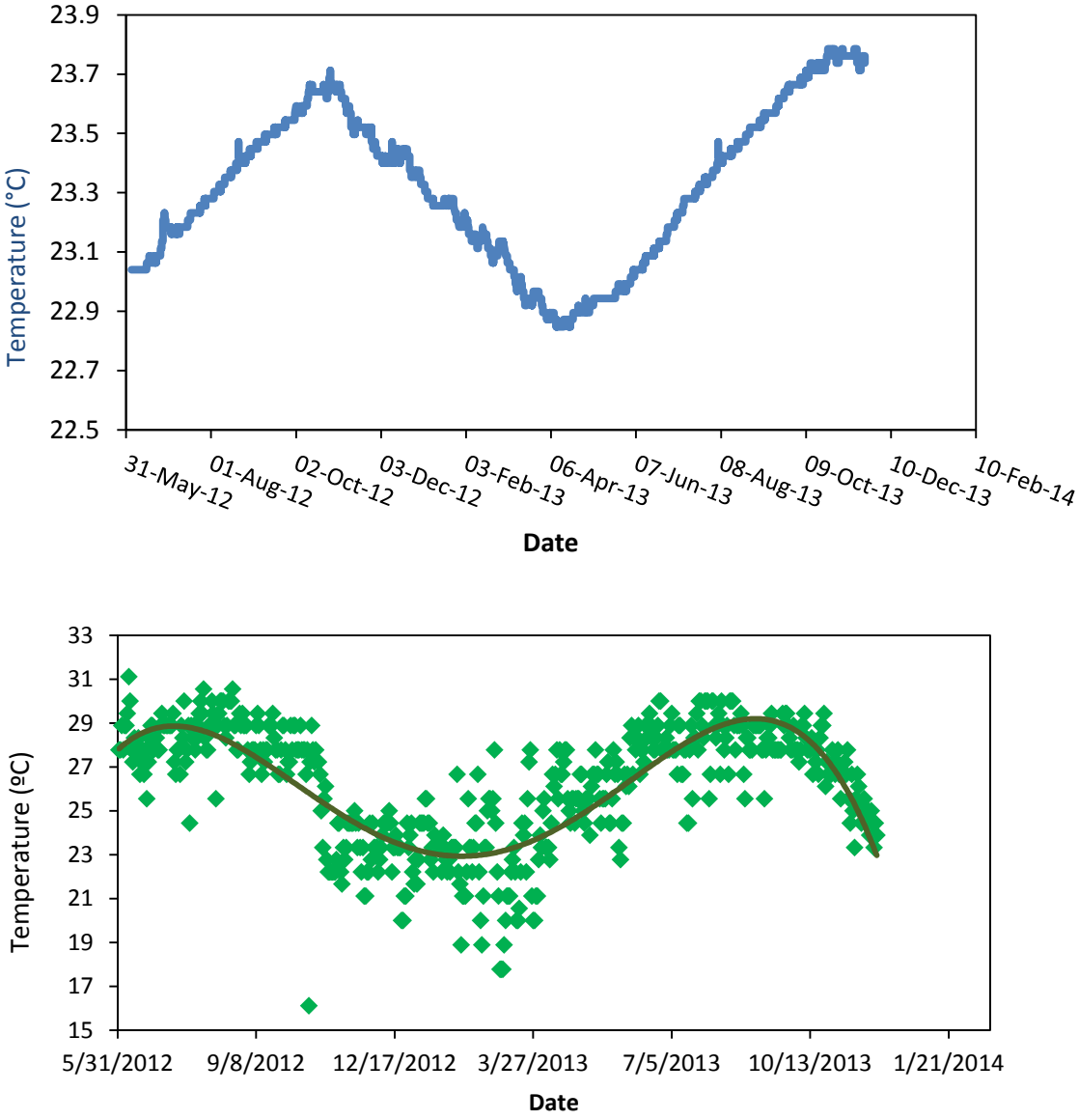

Figure 5.5: Top) Temperature (blue) measured every 2 hours in the cave from June 2012 to November 2013. Note relative humidity over this time periods was >90%. Bottom) Daily mean temperature from Govenor's Harbor airport, 23 km south of HBC for the same time period.

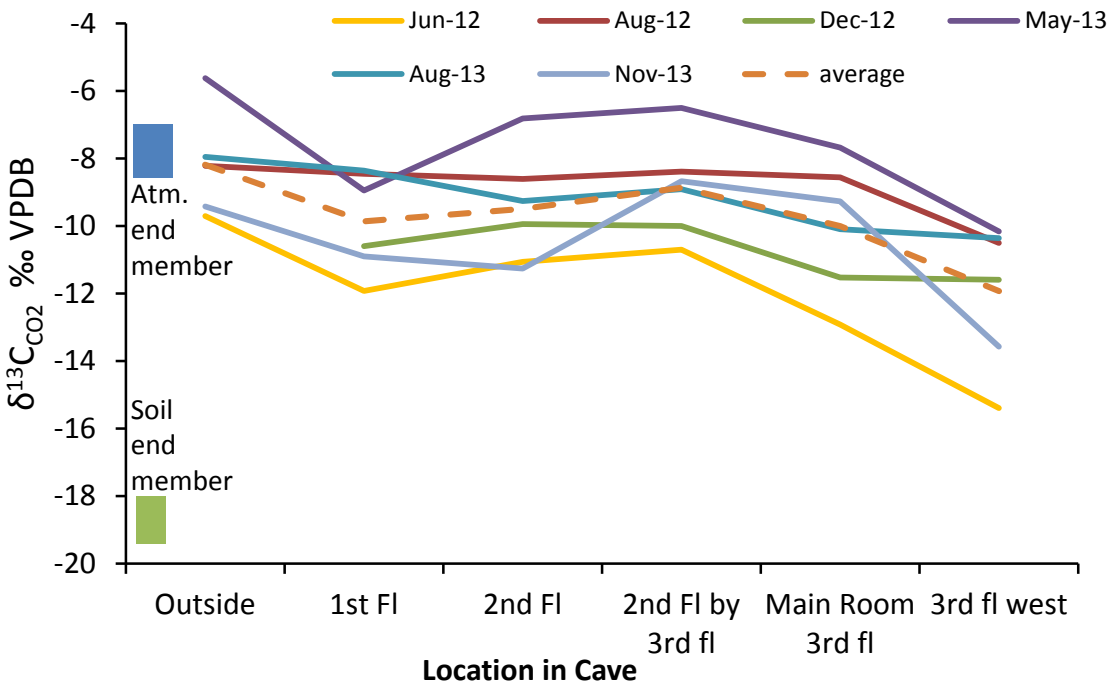

Figure 5.6: Carbon isotopes of cave air CO_2. $\delta^{13}C_{CO2}$ from the outside of the cave to the 3rd level west room from June 2012 to November 2013. "Outside" air sample was taken outside of the cave in an open field located 20 m from the entrance of the cave. The sample was taken prior to entering the cave. Also shown are the approximate values for atmospheric air and the soil gas end members from Figure 5.7.

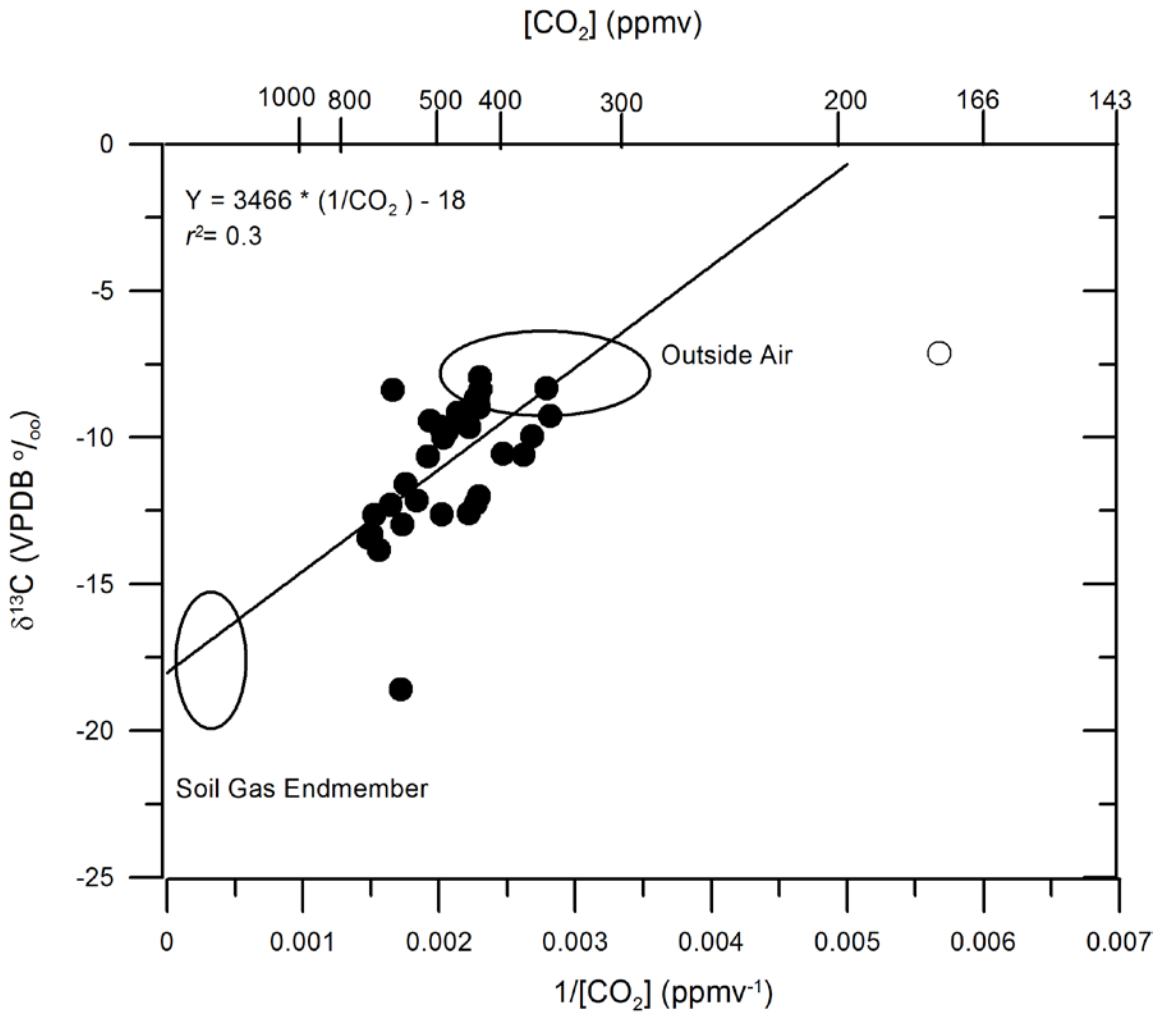

Figure 5.7: Keeling plot of HBC air samples. Samples were collected in a transect through the cave. The atmospheric end member represents the low concentration, heavier $\delta^{13}C_{CO2}$ samples, while the soil gas end member is characterized as a high CO_2 concentration, light $\delta^{13}C_{CO2}$ end member. The air within the cave lies closest to the outside air end member suggesting the cave is well ventilated. Outlier at 0.006, -6 was not included in the calculation of the line of best fit.

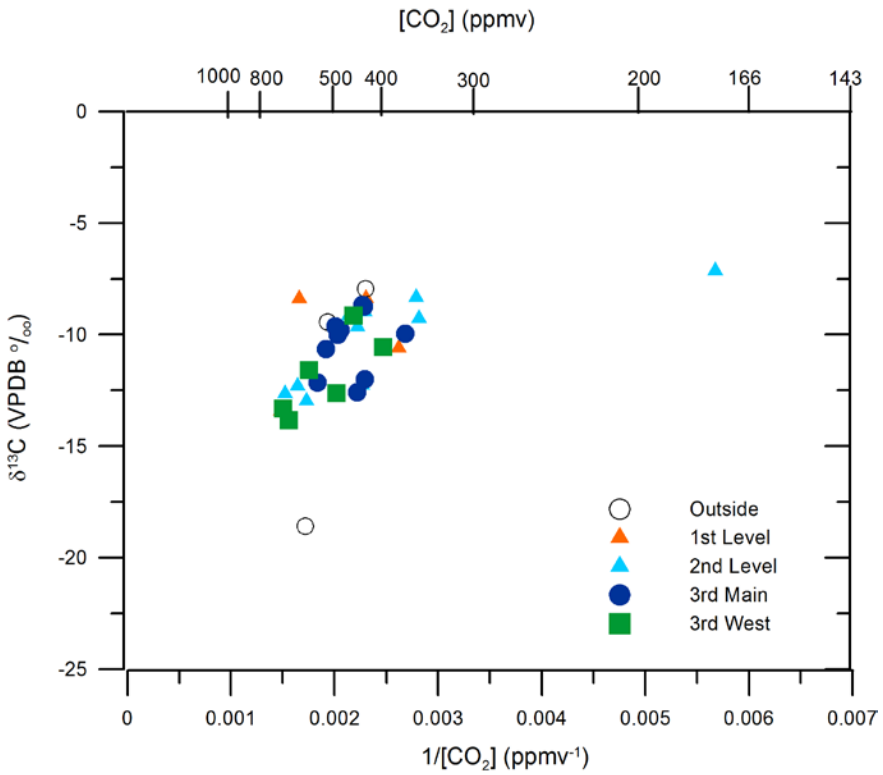

Figure 5.8: Same as Figure 5.7, however results are grouped by sampling location. This demonstrates that overall, the 3rd Level West are closest to the soil gas end member, while the 1st floor samples plot closer to the atmospheric end member.

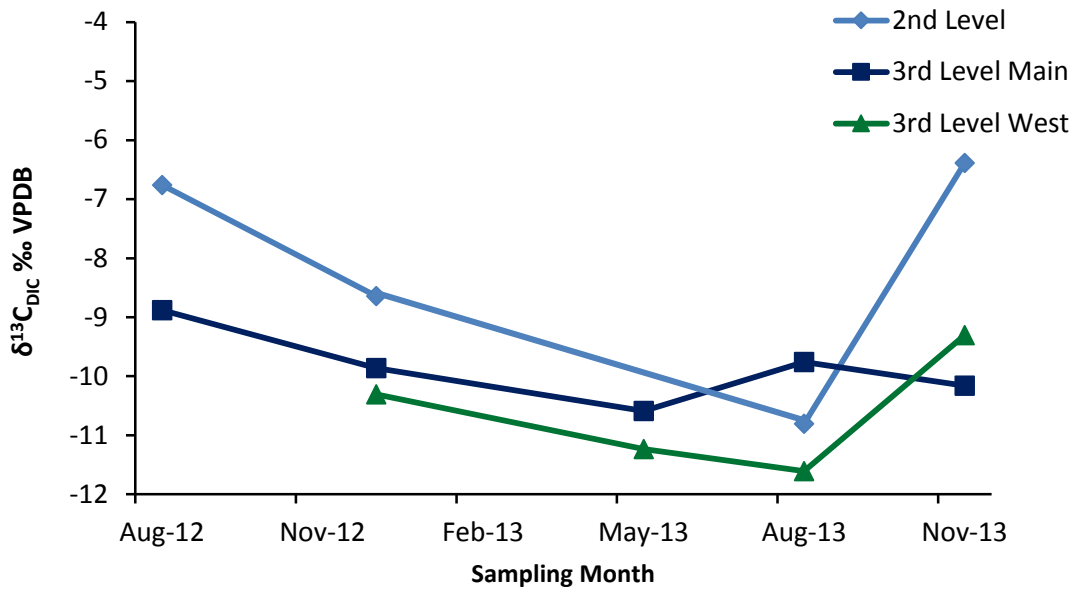

Figure 5.9: $\delta^{13}C_{DIC}$ of the drip waters for the 2nd level (light blue), 3rd level main (dark blue) and 3rd level west (dark green) from August 2012 to November 2013.

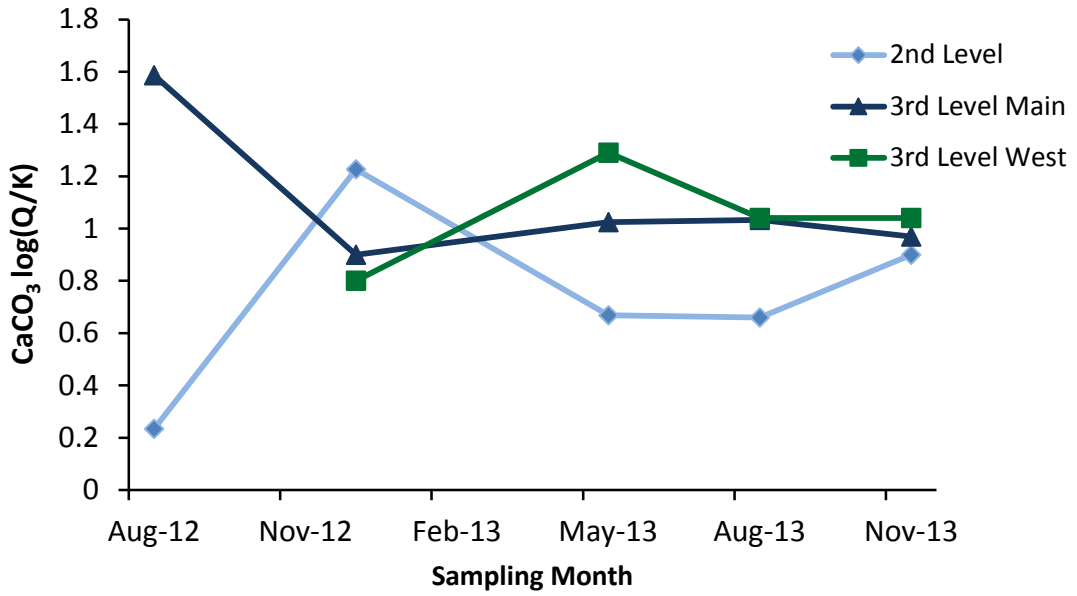

Figure 5.10: Results from 2nd level (light blue), 3rd level main (dark blue) and 3rd level west (dark green) from August 2012 to November 2013 for calcite saturation state. Saturation state was not calculated for June because there was not enough drip water collected to accurately measure alkalinity.

	$\delta^{13}C_{CO2}$ ‰ VPDB	σ	$\delta^{18}O_W$ ‰ VSMOW	σ	$\delta^{2}H_w$ ‰ VSMOW	σ	$\delta^{13}C_{DIC}$ ‰ VPDB	σ	Alkalinity mM	Cl- ppm	pH	Saturation log Q/K
			±		±				± 0.02	± 5		
2nd Level	-9.5	1.7	-3.9	1.0	-21.3	7.1	-8.1	3.6	3.5	538.8	7.8	0.8
3rd main	-10.0	1.9	-4.2	0.5	-24.9	2.9	-9.5	3.0	4.0	2025.4	8.0	1.1
3rd west	-11.9	2.1	-4.8	0.4	-29.6	2.0	-10.2	1.6	3.8	2811.2	8.0	1.0

Table 5.1: Summary of the average dripwater results from the Hatchet Bay Cave monitoring. Results have been averaged over the sampling period for each location.

Slide#	Slide Weight (mg) no calcite	Location	Date removed	# days in cave	Calcite Precipitated (mg)	µmoles $CaCO_3/cm^2/day$
1	5833.1	Main Room	8/21/2012	79	140.3	1.8
3	5744.7	East Main Room	8/21/2012	79	228.7	2.9
4	5868.2	Main Room	8/21/2012	79	118.3	1.5
6	5803.7	West Room	8/21/2012	79	470.6	6.0
8	5853.3	Main Room	12/11/2012	110	80	0.7
9	5874.4	Main Room	5/1/2013	250	333.5	1.3
10	5853.5	East Main Room	12/11/2012	110	314.6	2.9
11	5857.3	West Room	12/11/2012	110	345.8	3.1
12	5808.5	Main Room	5/1/2013	140	40.2	0.3
13	5858.8	East Main Room	5/1/2013	140	245.3	1.8
14	5867.2	West Room	5/1/2013	140	790.7	5.6
15	5773.9	Main Room	8/6/2013	95	165.6	1.7
16	5817.4	Main Room	8/6/2013	95	Broken	Broken
17	5866.5	East Main Room	8/6/2013	95	214.5	2.3
18	5940.2	West Room	8/6/2013	95	491.2	5.2
19	5810.7	Main Room	11/21/2013	105	366.4	3.5
20	5777	Main Room	11/21/2013	105	262.5	2.5
21	5862.8	East Main Room	11/21/2013	105	160.3	1.5
22	5802.6	West Room	11/21/2013	105	609	5.8

Table 5.2: Summary table for growth rate for each of the slides deployed in the cave. Slides 2 and 7 were destroyed in transport and therefore were not deployed. Slide 16 was broken after collection and therefore growth rate was not able to be calculated.

5.4.2 HBC slides

Summary of when each slide was recovered and the length of time in the cave are found in Table 5.2.

XRD:

X-ray diffraction was conducted for select slides. Results demonstrate the slides are comprised of low magnesium calcite (LMC). With no other significant minerals found. Results are provided in Appendix D.

Growth rate:

Growth rates vary within the cave both spatially and temporally. The main room on average has a lower growth rate than the west room and for all locations growth rates are found to be lowest from December to May (Figure 5.11).

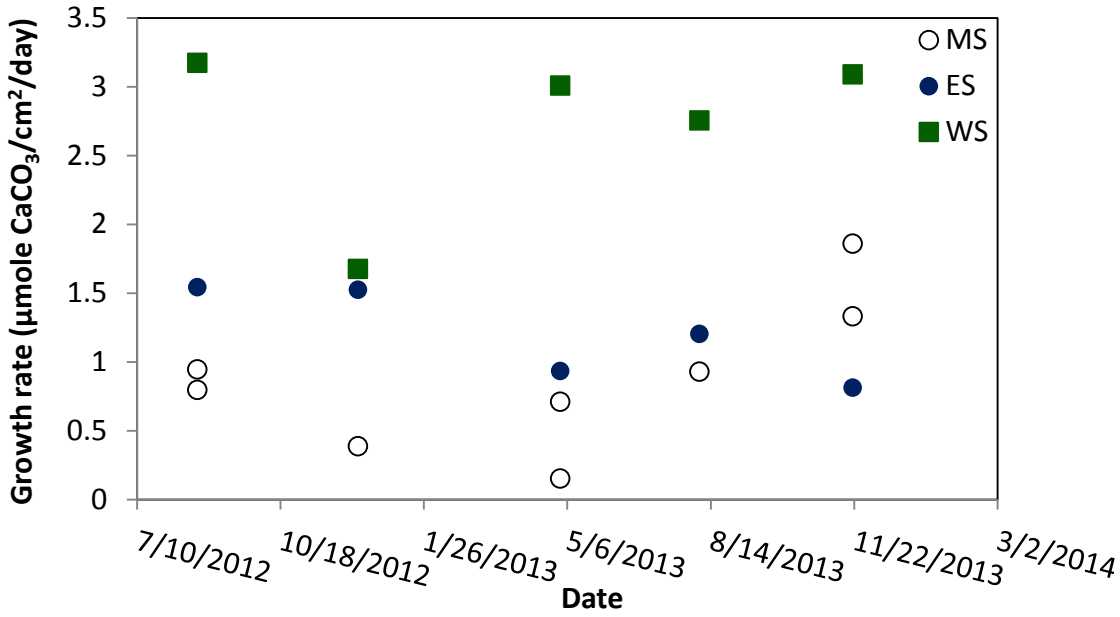

Figure 5.11: Growth rate of the slides from Table 5.2 plotted by date collected. White circles are samples from the MS location, blue from ES and green from WS location. Growth rate is shown to be lowest from December to May.

5.4.3 Kinetic isotope fractionation

Carbon, Oxygen and Δ_{47} variability within a slide:

Upon recovery of the nineteen slides, the slides were tested for evidence of kinetic fractionation using the Hendy test. A test often used to suggest that kinetic effects are not important is the 'Hendy' test (Hendy, 1971) which measures lateral variation in a chemical parameter within the speleothem and has been widely used to examine kinetic effects. The following criteria must be met for the Hendy test: i) an absence of lateral

increases in $\delta^{18}O_c$ and $\delta^{13}C_c$ values, and ii) a low correlation between $\delta^{18}O_c$ and $\delta^{13}C_c$ values along a growth band. If these conditions are met, then it is assumed that minimal kinetic fraction has taken place. The slides were analyzed for $\delta^{18}O_c$, $\delta^{13}C_c$ and Δ_{47} values at the center and at the outside of the slide (Figure 5.4). Two slides did not have sufficient material to analyze both the center and the outside for (Slides # 3 and 15) therefore, these samples were not analyzed further. Slide 1 was not analyzed as it was utilized for the initial Th measurements (see Chapter 3).

For this study, the Hendy test was conducted on each of the slides for which there was enough material present. This test was conducted by scraping off calcite utilizing a clean dental tool to remove calcite from the center and the outside of the slide. These sub-samples were then analyzed for $\delta^{18}O_c$, $\delta^{13}C_c$ and Δ_{47} values utilizing the methods provided above. The results for the $\delta^{18}O_c$ and $\delta^{13}C_c$ from the center compared with the outside for the16 slides are shown in Figures 5.12 a & b. Of the 16 slides analyzed for $\delta^{18}O_c$ and $\delta^{13}C_c$, three slides consisted of increased C and O isotopes on the outside of the slide relative to the center and therefore were not considered further (Slides # 8, 9 and 14). These results demonstrate minimal enrichment from the center to the outside for C and O isotopes. Maximum enrichment of $\delta^{18}O_c$ of 0.36 ‰ was found for Slide 10 and for carbon isotopes there is a maximum enrichment of 0.8 ‰ also for Slide 10 (Figures 5.12 a & b, Table 5.3). One additional sample was not considered further (Slide #12) as this slide exhibited higher than average Δ_{47} variability for three replicates. However the results from all 16 slides analyzed for $\delta^{18}O_c$, $\delta^{13}C_c$ and Δ_{47} value are provided in Figure 5.12 and Table 5.3, however slides 8, 9, 12 and 14 will not be included in figures beyond this point, as these samples are thought to be kinetically fractionated. For the remaining

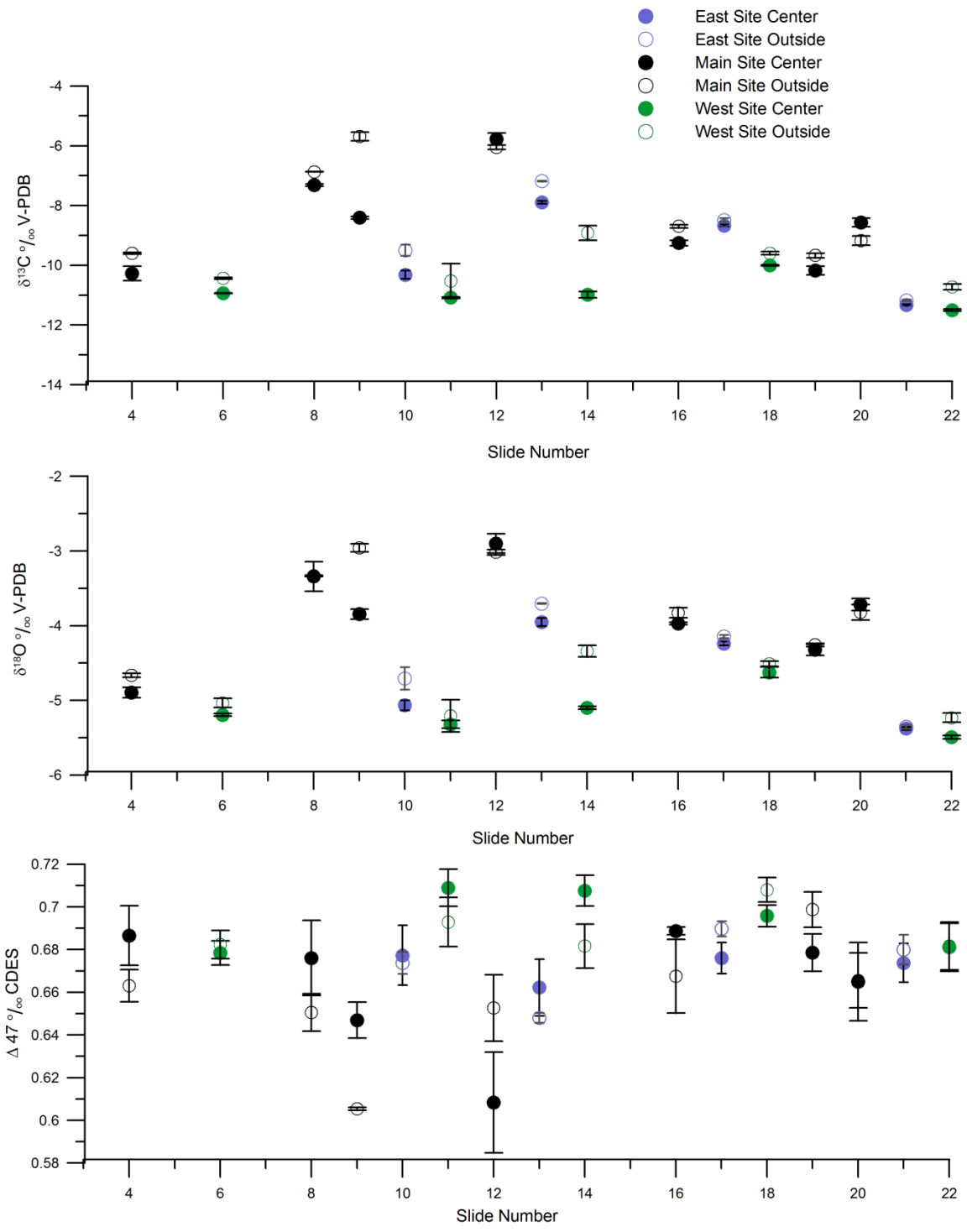

Figure 5.12: Geochemical results from slides. a) Oxygen isotope values for the center of the slide (black triangle) and the outside of the slide (white triangle) plotted by slide number. B) $\delta^{13}C_c$ values for the center of the slide (black triangle) and the outside of the slide (white triangle) plotted by slide number. C) Δ_{47} values for the center of the slide (black triangle) and the outside of the slide (white triangle) plotted by slide number.

12 slides, 4 were collected from the MS location, 4 from the ES, and 4 from the WS location.

For the 12 slides which exhibited minimal kinetic fractionation, the average Δ_{47} value for the 12 slides (24 samples) was 0.681 ‰ which is 31.8 °C from Ghosh et al. (2006) with an average Δ_{47} error of 0.009 ‰ (1 S.E.) which is approximately 2.0 °C (Table 5.3). Of the 12 slides, the center was found to give a higher Δ_{47} value (lower temperature) for 7 of the slides when compared to the outside (Figure 5.12 c, Table 5.3). Given the variability found in the samples from the outside of the slide, the data from this point forward will only contain the results from the center of the slides as the center is thought to exhibit minimal fractionation (Hendy, 1971).

Comparison of oxygen and clumped isotopes with monitoring:

Utilizing the monitoring results, the oxygen isotopic fractionation factor (α) can be calculated from the $\delta^{18}O$ of the drip water and the $\delta^{18}O$ of the farmed precipitated calcite. With α representing the fractionation factor between two substances (in this case water and calcite oxygen isotopes) and 1000ln(α) representing the per mil fractionation (Sharp, 2007). The measured 1000ln(α) was calculated from the annual average $\delta^{18}O_w$ for each room (-4.24 ‰ for the main room, -4.76 ‰ for the west room) and the measured $\delta^{18}O$ of the calcite. The expected 1000ln(α) was calculated using the temperature at the time of formation applied to the equation from Kim and O'Neil (1997). Results demonstrate an observed offset from the expected 1000ln(α) with the sample results consisting of a higher 1000ln(α) value than expected from Kim and O'Neil (1997) (Table 5.4, Figure 5.13a). Further analysis of the mechanisms driving the observed offsets for 1000ln(α) are described in section 5.5.3. As previously suggested, there are several

equations for the temperature dependent fractionation for $\delta^{18}O$ of calcite. Here, the 1000ln(α) offset value has been calculated using the Kim and O'Neil (1997) equation as other speleothem studies have reported 1000ln(α) offset values using this equation. This allows for the offsets to be compared between studies.

The Δ_{47} values from the farmed calcite average of 0.6810 ‰ (Table 5.4, Figure 5.13 b) which is an average temperature of 31.4 ºC utilizing the Ghosh et al. (2006) equation. This is an average ~8 ºC warmer than expected, with the measured average temperature of the cave being 23.3 °C. However, there is variability in the Δ_{47} value between the various rooms within the cave (Figure 5.14). The WS location (n=4) average Δ_{47} value (0.691 ‰) is higher than the ES location Δ_{47} value (0.679 ‰ n=4), and the MS location contains the lowest average Δ_{47} value (0.669 ‰ n=4) (Figure 5.14). The greatest offset from the expected (black cross, Figure 5.14) was observed in May of 2013 for Slide 13 collected from ES location and the lowest offset was observed on December of 2012 for Slide11 from the WS location (Figure 5.14). Expected Δ_{47} value was calculated using the Ghosh et al., (2006) equation and the temperature for that time period from the HOBO logger.

The Δ_{47} value can be expressed as an offset from the expected Δ_{47} value. Expected Δ_{47} value was calculated using the Ghosh et al., (2006) equation and the temperature for that time period from the HOBO logger. In Figure 5.15 this offset is plotted versus saturation state for the period the sample was in the cave. The results suggest increased saturation state may be associated with a decreased Δ_{47} offset (r^2= 0.7, p<0.05) (Figure 5.15). As described earlier, saturation state was averaged between slide deployment and

Slide #	Loc	n	δ13Cc ‰ VPDB	1 S.D.	δ18Oc ‰ VPDB	1 S. D.	δ47 ‰	SE	Δ47 ‰ RF	SE
4	Main	3	-10.3	0.24	-4.9	0.07	1.56	0.29	0.687	0.014
6	West	3	-10.9	0.01	-5.2	0.02	0.57	0.02	0.678	0.006
8	Main	2	-7.3	0.04	-3.3	0.20	6.18	0.19	0.676	0.018
9	Main	3	-8.4	0.04	-3.8	0.07	4.53	0.13	0.647	0.008
10	East Main	4	-10.3	0.14	-5.1	0.07	1.33	0.18	0.677	0.014
11	West	3	-11.1	0.03	-5.3	0.05	0.31	0.05	0.709	0.009
12	Main	3	-5.8	0.20	-2.9	0.13	8.15	0.30	0.608	0.024
13	East Main	3	-7.9	0.05	-4.0	0.06	4.95	0.09	0.662	0.013
14	West	4	-11.0	0.11	-5.1	0.02	0.64	0.11	0.708	0.007
16	Main	2	-9.3	0.09	-4.0	0.02	3.57	0.11	0.689	0.002
17	East Main	3	-8.7	0.04	-4.2	0.02	3.86	0.05	0.676	0.007
18	West	3	-10.0	0.02	-4.6	0.07	2.12	0.08	0.696	0.005
19	Main	3	-10.2	0.15	-4.3	0.07	2.26	0.23	0.679	0.009
20	Main	4	-8.6	0.14	-3.7	0.08	4.52	0.23	0.665	0.018
21	East Main	3	-11.3	0.03	-5.4	0.02	-0.03	0.03	0.674	0.009
22	West	4	-11.5	0.04	-5.5	0.02	-0.32	0.06	0.681	0.011

Table 5.3a: Results from the center of the slide for each of the 16 slides for the center of the slides including the slide number, location in the cave, the number of replicates, $\delta^{13}C_c$, $\delta^{18}O_c$, δ47, and Δ_{47} results.

Slide #	Loc	Replicates	δ13Cc ‰ VPDB	1 S.D.	δ18Oc ‰ VPDB	1 S. D.	δ47 ‰	SE	Δ47 ‰ RF	SE
4	Main	3	-9.6	0.03	-4.7	0.03	2.47	0.05	0.663	0.008
6	West	5	-10.4	0.03	-5.0	0.06	1.25	0.09	0.682	0.007
8	Main	1	-6.9	0.01	-3.3	0.01	6.61	0.09	0.651	0.009
9	Main	3	-5.7	0.15	-3.0	0.05	8.19	0.21	0.605	0.001
10	East Main	4	-9.5	0.19	-4.7	0.15	2.53	0.34	0.674	0.005
11	West	3	-10.5	0.57	-5.2	0.22	0.99	0.80	0.693	0.012
12	Main	3	-6.1	0.08	-3.0	0.04	8.15	0.30	0.653	0.016
13	East Main	2	-7.2	0.02	-3.7	0.00	5.92	0.02	0.648	0.002
14	West	4	-8.9	0.24	-4.3	0.08	3.52	0.33	0.682	0.010
16	Main	2	-8.7	0.06	-3.8	0.07	4.27	0.14	0.668	0.017
17	East Main	3	-8.5	0.06	-4.1	0.02	4.16	0.07	0.690	0.004
18	West	3	-9.6	0.05	-4.5	0.04	2.67	0.11	0.708	0.006
19	Main	3	-9.7	0.08	-4.3	0.02	2.85	0.07	0.699	0.008
20	Main	4	-9.2	0.15	-3.8	0.10	3.78	0.26	0.666	0.013
21	East Main	3	-11.2	0.03	-5.4	0.03	0.15	0.01	0.680	0.007
22	West	4	-10.7	0.10	-5.2	0.06	0.75	0.14	0.682	0.011

Table 5.3b: Results for each of the 16 slides for the sample from the outside of the slide including the slide number, location in the cave, the number of replicates, $\delta^{13}C_c$, $\delta^{18}O_c$, δ47, and Δ_{47} results.

Slide #	Cave Temp °C	Cave * Δ47 ‰ RF	δ18Oc ‰ VPDB	1 S. D.	Δ47 ‰ RF	SE	Ghosh Temp. °C Δ47 ‰ RF	SE	Cap offset **	Offset δ18O***
4	23.2	0.719	-4.9	0.07	0.687	0.014	30.3	3.1	-0.03	1.10
16	23.1	0.720	-4.0	0.02	0.689	0.002	29.7	0.4	-0.03	2.01
19	23.6	0.717	-4.3	0.07	0.679	0.009	32.0	2.0	-0.04	1.76
20	23.6	0.717	-3.7	0.08	0.665	0.018	35.3	4.4	-0.05	2.37
17	23.1	0.720	-4.2	0.02	0.676	0.007	32.5	1.6	-0.04	1.74
21	23.6	0.717	-5.4	0.02	0.674	0.009	33.1	2.1	-0.04	0.71
13	23.1	0.720	-4.0	0.06	0.662	0.013	35.8	3.1	-0.06	2.03
10	23.5	0.718	-5.1	0.07	0.677	0.014	32.4	3.1	-0.04	1.00
6	23.2	0.719	-5.2	0.02	0.678	0.006	32.0	1.3	-0.04	1.33
11	23.5	0.718	-5.3	0.05	0.709	0.009	25.4	1.8	-0.01	1.27
18	23.1	0.720	-4.6	0.07	0.696	0.005	28.2	1.1	-0.02	1.88
22	23.6	0.717	-5.5	0.02	0.681	0.011	31.5	2.5	-0.04	1.11

* Calculated using the Ghosh et al Δ47 to temperature relationship.
** Cap offset is the measured Δ47 value minus the Δ47 value of the cave air temperature.
*** Calculated using fractionation factor from Kim and O'Neil 1997 as shown in equation 2 with:
δ18OW = -4.24 ‰ VSMOW Main Room, -4.76 ‰ VSMOW West Room

Table 5.4: Data from the center of the slides. Data includes the slide number, the temperature of the cave from the loggers, the $\delta^{18}O$ and Δ_{47} of the calcite, the calculated temperature from Ghosh et al. 2006. The cap offset and $\delta^{18}O$ offset are both calculated from the measured-expected values.

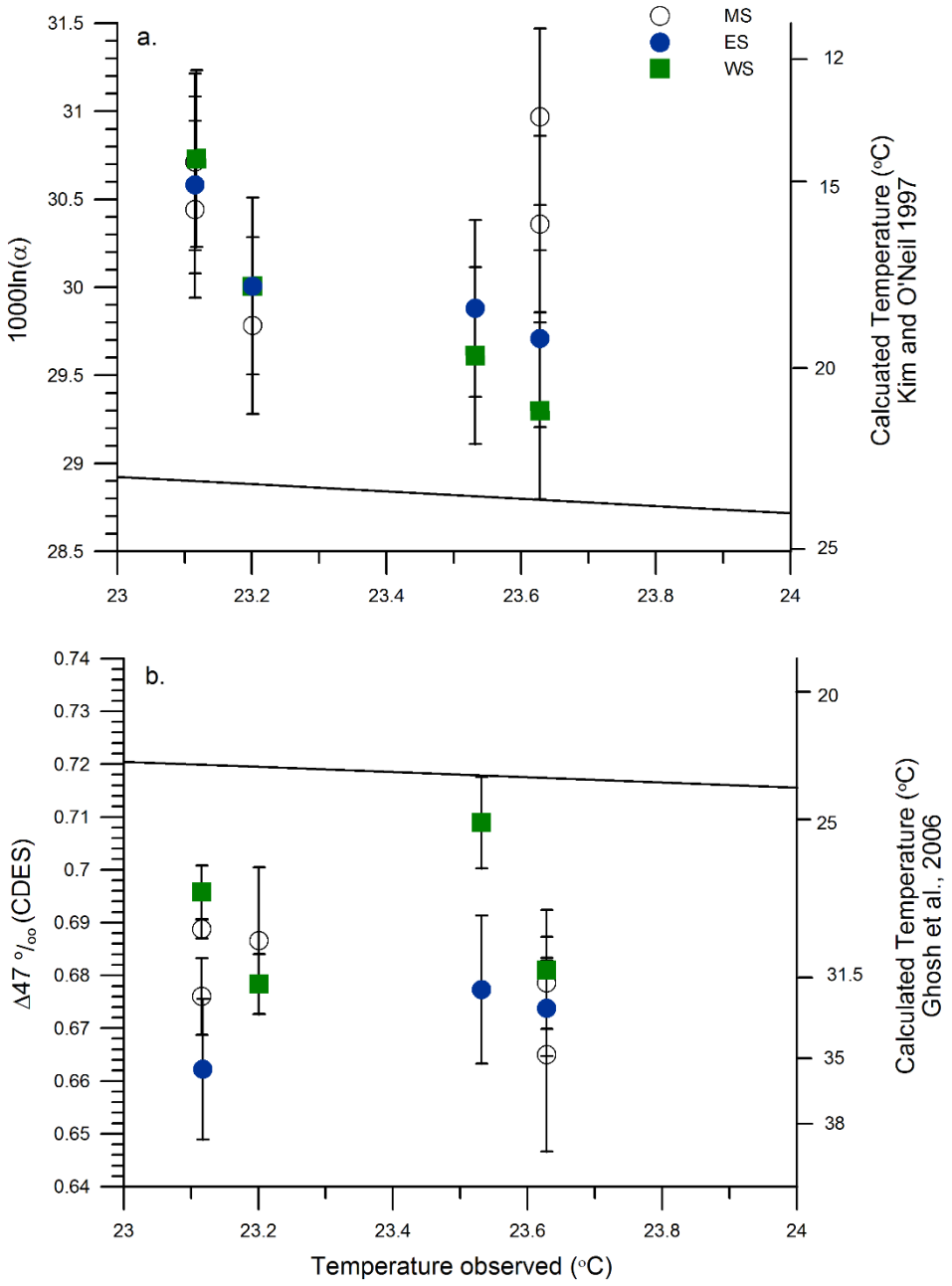

Figure 5.13: a) Temperature observed versus 1000ln(α) for Hatchet Bay Cave samples. Calculated temperature was calculated using equation 2. 1000ln(α) was calculated for the main room (MS and ES) samples using $\delta^{18}O_W$ = -4.24 ‰ VSMOW and for the WS location $\delta^{18}O_W$ = -4.76 ‰ VSMOW. The black line is the expected equilibrium values from Kim and O'Neil 1997 demonstrating the speleothem results plot above the equilibrium line. b) Temperature observed versus Δ_{47} value for Hatchet Bay Cave samples. Samples plot below the Ghosh et al. 2006 equilibrium line (black line) demonstrating lower Δ_{47} value (warmer temperature) for the samples from the expected Δ_{47} value.

its recovery; therefore there are fewer data points as calculating the saturation state was not possible in June (as described above).

Of further significance may be the relationship between growth rate and Δ_{47} offset (Figure 5.16). In the west room, where growth rates are higher than the rest of the cave, there is a significant relationship between growth rate and Δ_{47} offset, with lower growth rate correlating with a lower Δ_{47} offset (r^2=0.9, p<0.05) (Figure 5.17). Conversely, in the main room there is no relationship between growth rate and Δ_{47} offset for either the MS or ES location (Figure 5.16 & 17).

A weak relationship was found between $\delta^{18}O_c$ value and Δ_{47} offset as well as $\delta^{13}C_c$ value and Δ_{47} offset (r^2=0.2, p<0.1) (Figure 5.18 and 19).

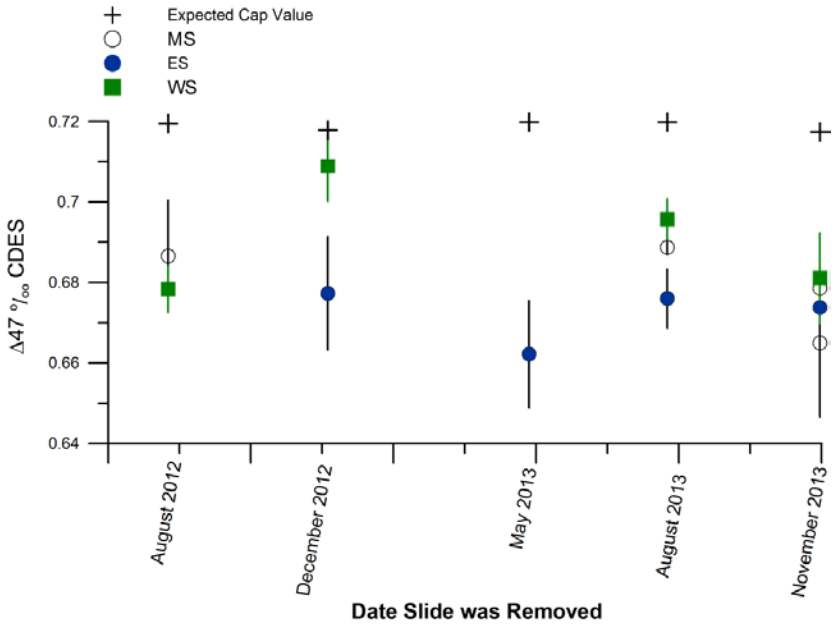

Figure 5.14: Plot for Δ_{47} by location plotted versus the date removed from the cave. Note all samples fall below the expected Δ_{47} value. Results demonstrate increased Δ_{47} values for the WS location compared to the MS and ES locations. Expected cap value (black cross) is the Δ47 value expected for each month.

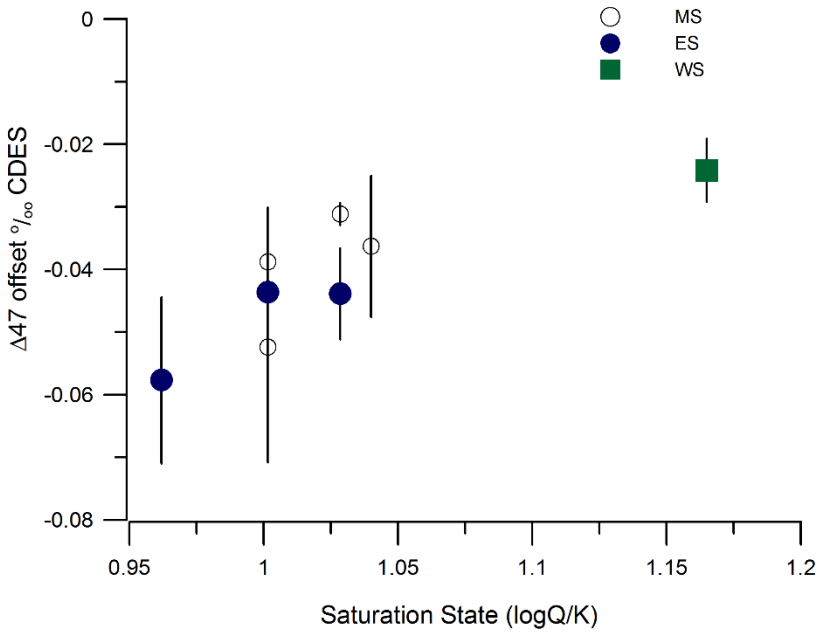

Figure 5.15: Results from Hatchet Bay Cave for saturation state (log(Q/K)) versus Δ_{47} offset. Log(Q/K) defines the saturation index and when the saturation index is above 1, saturation has been reached. Samples demonstrate a trend of decreasing Δ_{47} offset with increasing saturation state. Saturation state was not calculated for June because there was not enough drip water collected to accurately measure alkalinity. The point at 1.17 has minimal influence on the r^2 value, with the value with the point is r^2=0.7 and without the point is r^2=0.6.

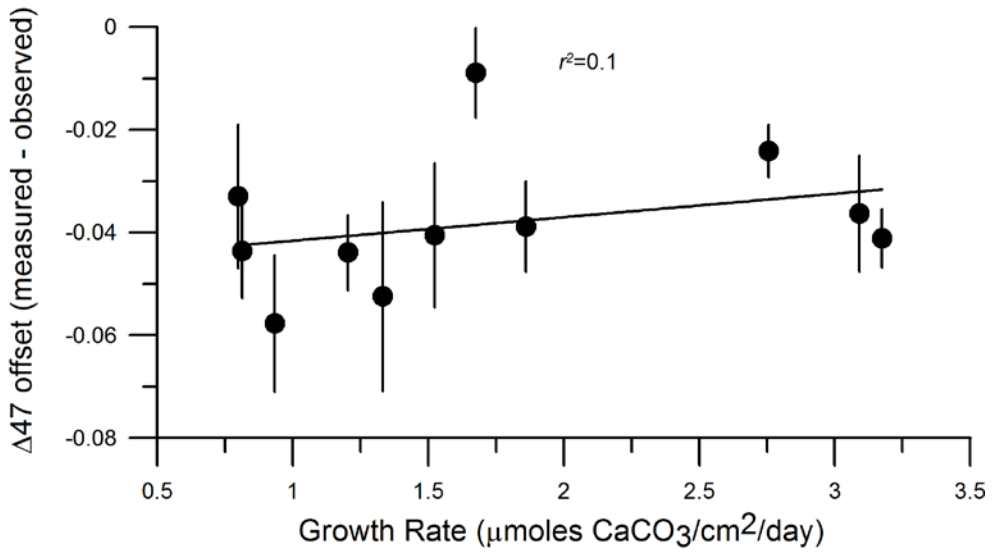

Figure 5.16: Results from Hatchet Bay Cave for growth rate versus Δ_{47} offset for all locations, demonstrating no statistically significant relationship. If the data point at 1.6 and -0.009 is removed, the relationship is slightly improved with a r^2 value of 0.2.

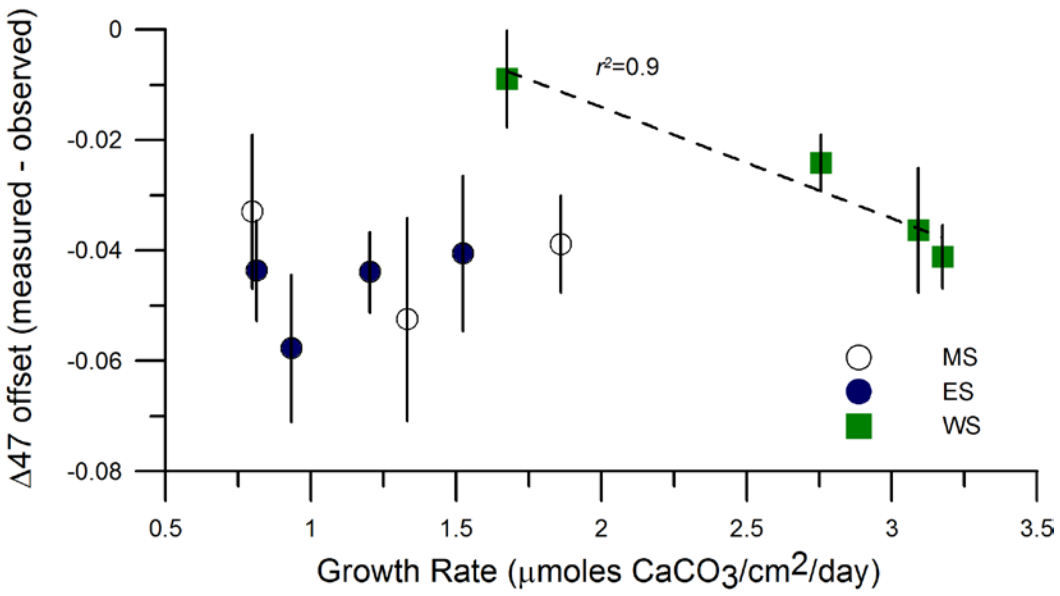

Figure 5.17: Results from Hatchet Bay Cave for growth rate versus Δ_{47} offset grouped by location in the cave. Samples demonstrate an increased Δ_{47} offset with increasing growth rate for the WS location. No statistically significant relationship was found for the MS or ES locations. For the West Room, there is a significant negative correlation between growth rate and Δ_{47} offset, with decreasing Δ_{47} offset occurring with a decrease in growth rate. The relationship for the WS location is robust even if the data point at 1.6 and -0.009 is removed.

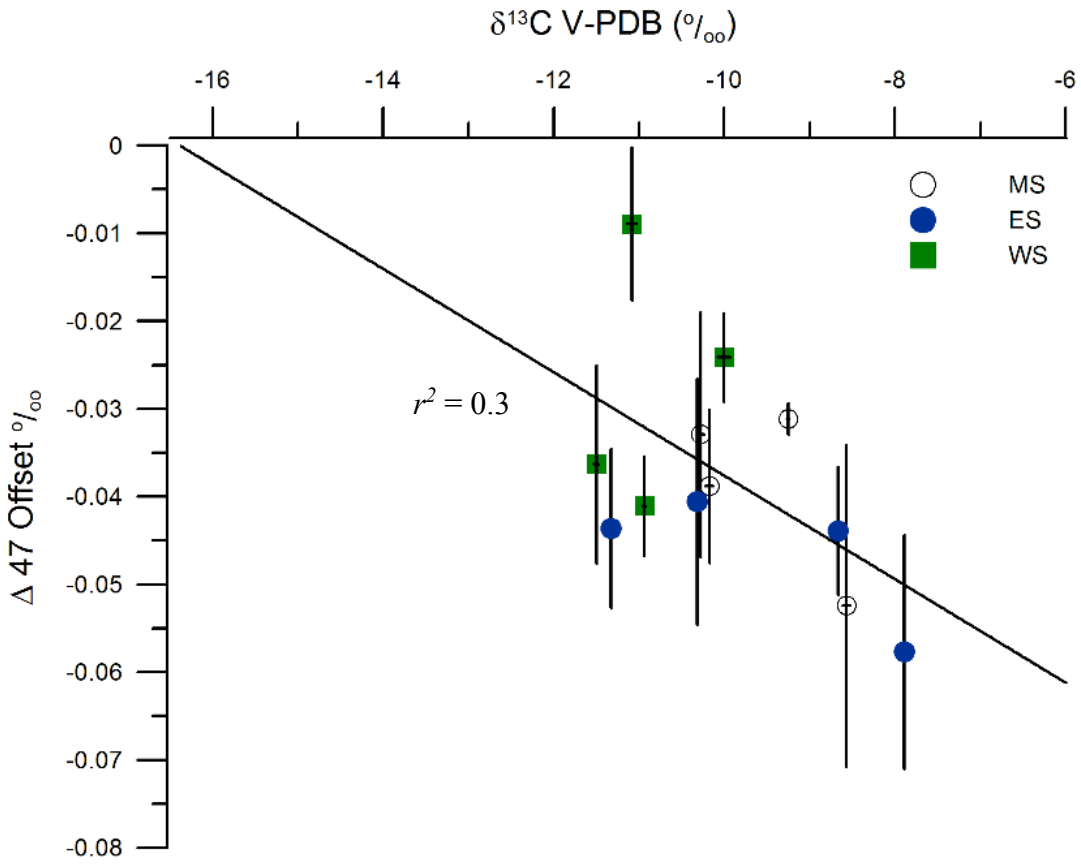

Figure 5.18: Results from Hatchet Bay Cave for carbon isotope value of the calcite versus Δ_{47} offset. Samples demonstrate a larger Δ_{47} offset with higher carbon isotope value of the calcite. The y intercept of the regression line is at -16.5 ‰ for $\delta^{13}C$, which is a similar value to the soil gas end member found in Figure 5.6. This suggests that the carbon isotopes of the water (hence calcite) are heavier than the original value, this is most likely driven by degassing processes which lead to heavier isotopic values.

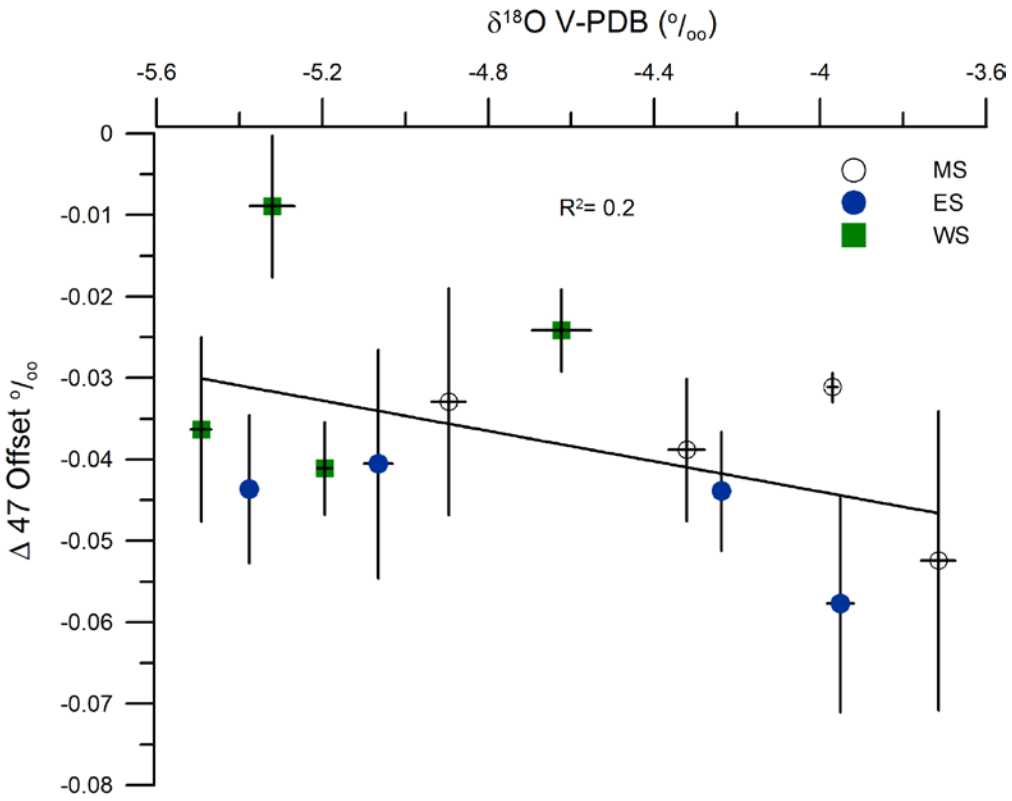

Figure 5.19: Results from Hatchet Bay Cave for calcite oxygen isotope versus Δ_{47} offset. Samples demonstrate a larger Δ_{47} offset with higher oxygen isotope value of the calcite.

5.4.4 Stalagmite AB-DC-09

The age model for this sample is discussed in chapter 3, and results demonstrate the sample formed between 14.1 to 31.3 ka before present. For sample AB-DC-09, 38 samples were analyzed for clumped isotopes and the average Δ_{47} value for the 38 samples was 0.663 ‰ (in the reference frame as defined in Dennis et al. (2011)) and an average standard error of 0.009 ‰ (Table 5.5). This equated to an average temperature of 36.2ºC ±2ºC (1 S.E.) (Table 5.5, Figure 5.20).

The determination of the $\delta^{18}O_c$ and $\delta^{18}O_w$ values from the fluid inclusion results allows for the calculation of temperature at the time of formation utilizing the equation from Tremaine et al. (2011). The equation from Tremaine et al. (2011) was utilized

because this equation was determined from cave studies from around the world. Thirty one of the 38 samples analyzed for clumped isotopes were previously analyzed for fluid inclusion isotopes (see Chapter 3). This allowed for a direct comparison between the fluid inclusion and clumped isotope results as shown in Figure 5.20 and Table 5.5. Similar to the modern, the clumped isotope values from AB-DC-09 demonstrate warmer temperatures than expected from the fluid inclusion results. The average temperature from the fluid inclusion isotope results was 17.2 ±2.7 °C which is 18 °C cooler than the average temperature derived from the clumped isotopes (Figure 5.20).

The temperatures calculated using the clumped isotope method demonstrate higher variability than the results from fluid inclusions (Figure 5.20). A minimum clumped temperature was at 26.2 ka BP and a maximum temperature at 14.9 ka BP. The largest offsets are observed at 15.6 ka and 17.5 ka, corresponding with periods of lowered temperatures from fluid inclusions (Figure 5.20, Table 5.5).

Table 5.5 (following page): Results from sample AB-DC-09 for clumped isotopes and fluid inclusion analyses. Age was determined from U-Th methods as described in Chapter 3. $\delta^{13}C$, $\delta^{18}O$ and Δ_{47} values were determined from clumped isotope analyses. Δ_{47} values are reported in the reference frame of Dennis et al. (2011) using the methods outlined above. Temperature from fluid inclusions were determined using the equation from Tremaine et al. (2011) as described in chapter 3. Temperature offset represents the temperature difference between clumped isotopes and fluid inclusion temperatures.

Age	Age error	Clumped Isotope Results n	δ13C VPDB ‰	SD	δ18O VPDB ‰	SD	Δ47 ‰ RF	SE	Temp. °C* Ghosh RF	SE	Temp. °C Fluid Inclusion **	Temp offset °C ***
14087	0.17	2	-1.3	0.77	-2.6	0.29	0.654	0.015	37.6	3.7		
14289	0.17	3	-2.4	0.02	-2.2	0.04	0.679	0.012	32.0	2.7	17.3	14.7
14513	1.7	3	-2.0	0.06	-1.7	0.15	0.622	0.005	45.4	1.2		
14755	0.17	3	-2.0	0.03	-1.8	0.02	0.655	0.010	37.4	2.4	15.8	21.6
14875	0.18	3	-1.4	0.06	-1.6	0.06	0.651	0.002	38.3	0.5	16.1	22.2
14887	0.18	3	-1.7	0.38	-1.8	0.50	0.641	0.007	40.8	1.6		
14943	0.18	3	0.1	0.26	-1.0	0.20	0.654	0.015	37.7	3.6		
15612	0.19	3	0.1	0.05	-1.3	0.04	0.645	0.004	39.7	1.0	12.2	27.5
16588	0.2	5	-0.1	1.31	-1.6	0.76	0.665	0.012	35.1	2.7	11.3	23.8
17244	0.25	3	-1.3	0.11	-2.3	0.07	0.670	0.009	33.9	2.1	19.7	14.2
17349	0.22	3	-1.7	0.03	-2.4	0.06	0.648	0.014	39.0	3.4	17.5	21.6
17449	0.2	4	-1.3	0.03	-2.3	0.04	0.670	0.008	34.0	1.8	15.3	18.7
17455	0.22	3	-1.1	0.06	-2.2	0.08	0.643	0.010	40.2	2.4	13.9	26.3
17459	0.25	3	-1.5	0.02	-2.4	0.03	0.670	0.013	33.9	2.9	18.1	15.8
17763	0.15	5	-1.2	0.26	-2.3	0.20	0.659	0.014	36.7	3.2		
18221	0.15	3	-1.4	0.03	-2.4	0.05	0.668	0.003	34.3	0.6	17.7	16.6
18623	0.14	5	-2.0	0.02	-2.6	0.02	0.671	0.006	33.7	1.3	16.8	16.9
19049	0.13	3	-1.7	0.01	-2.5	0.02	0.672	0.005	33.4	1.1	18.6	14.8
19429	0.13	3	-1.2	0.02	-2.4	0.03	0.666	0.008	34.8	1.9	14.8	20.0
19654	0.15	3	-1.7	0.10	-2.6	0.04	0.651	0.005	38.3	1.3		

		Clumped Isotope Results										
Age	Age error	n	δ13C VPDB ‰	SD	δ18O VPDB ‰	SD	Δ47 ‰ RF	SE	Temp. °C* Ghosh RF	SE	Temp. °C Fluid Inclusion **	Temp offset °C ***
19996	0.17	4	-1.9	0.39	-2.6	0.12	0.670	0.006	33.8	1.4	15.9	17.9
21457	0.3	4	-2.5	0.04	-2.8	0.08	0.665	0.015	35.1	3.3	18.8	16.3
21960	0.3	3	-0.7	0.17	-2.2	0.08	0.656	0.009	37.1	2.0	17.0	20.1
23140	0.3	3	-2.3	0.05	-2.8	0.25	0.669	0.003	34.0	0.6	14.4	19.7
24976	0.22	3	-1.4	0.12	-2.5	0.04	0.666	0.010	34.8	2.2	12.8	22.0
25940	0.18	3	-0.7	0.07	-2.3	0.02	0.672	0.006	33.4	1.3	12.6	20.7
26086	0.16	3	-1.4	0.06	-2.6	0.06	0.637	0.011	41.7	2.7		
26207	0.16	3	-1.0	0.03	-2.3	0.05	0.691	0.011	29.3	2.3	16.6	12.8
26591	0.17	3	-1.2	0.01	-2.4	0.05	0.659	0.012	36.5	2.7	17.9	18.6
26892	0.18	2	-1.7	0.03	-2.2	0.02	0.668	0.002	34.3	0.4	21.7	12.6
27013	0.3	4	-1.7	0.03	-2.6	0.04	0.675	0.011	32.7	2.5	18.7	14.0
27214	0.4	3	-1.9	0.08	-2.7	0.05	0.635	0.010	42.1	2.3	20.7	21.4
27539	0.4	4	-1.8	0.09	-2.7	0.15	0.672	0.014	36.4	1.9	22.4	14.0
27827	0.38	4	-1.8	0.10	-2.6	0.10	0.658	0.006	36.7	1.4	19.5	17.3
28705	0.6	4	-2.0	0.05	-2.3	0.06	0.667	0.010	36.5	1.0	18.1	18.4
29612	0.8	3	-1.3	0.02	-2.4	0.07	0.677	0.009	32.2	1.9	19.8	12.4
30337	0.1	3	-0.7	1.49	-1.9	0.79	0.638	0.010	41.5	2.4	21.5	20.0
31062	0.1	3	0.7	0.03	-1.7	0.07	0.681	0.009	31.4	1.9	17.4	14.0

*Temperature calculated from the Ghosh et al., 2006 equation (equation 8 in the text)

**Temperature from Fluid Inclusion calculated using the equation from Tremaine et al., 2011 (equation 3 in the text)

*** Temperature offset is calculated as temperature from clumped isotopes minus temperature from Fluid inclusions

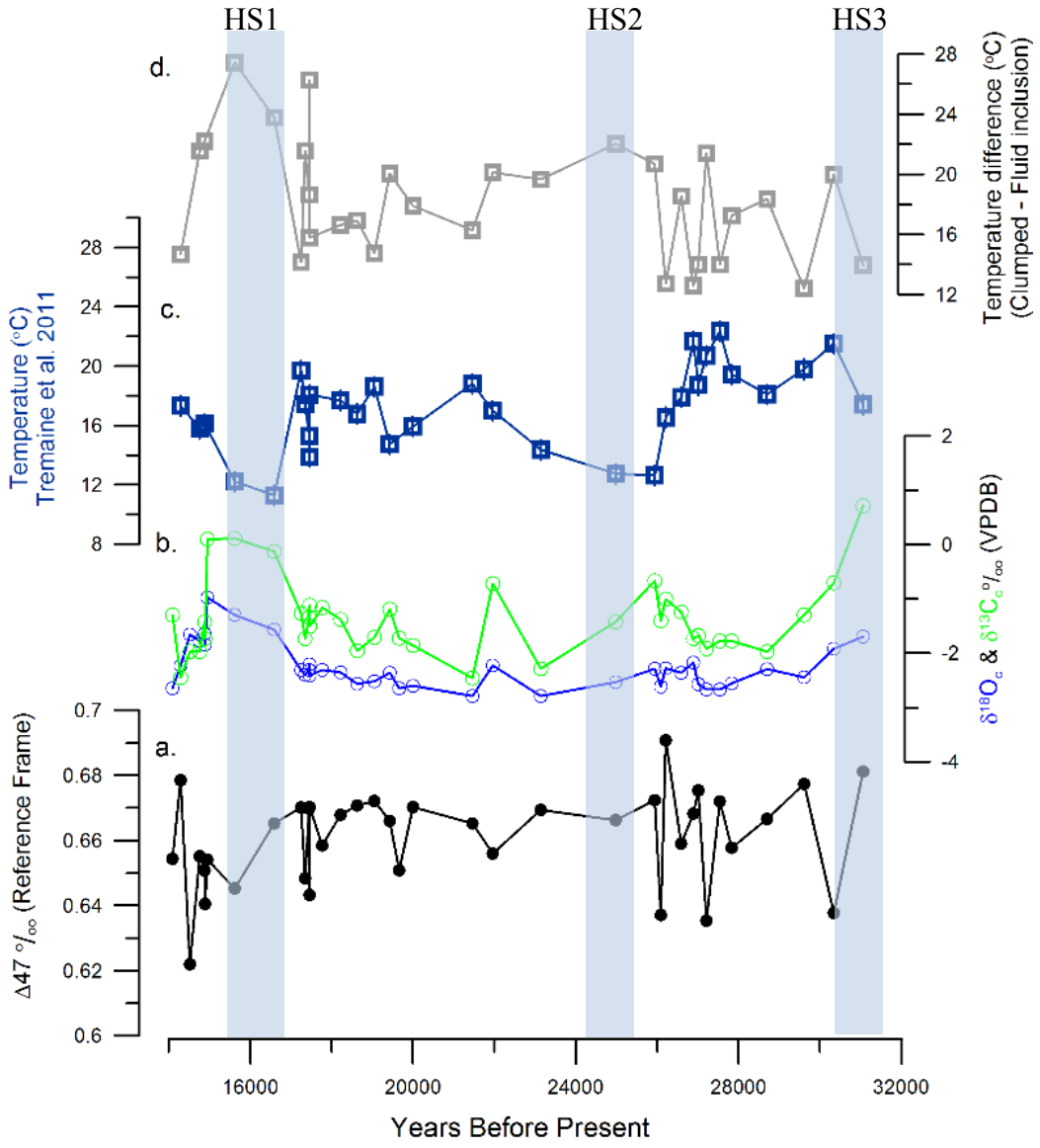

Figure 5.20: Results from clumped isotope analysis of sample AB-DC-09 plotted with the age scale. A) Clumped isotope values for all samples analyzed. B) Carbon and oxygen isotopes of the carbonate determined during the clumped isotope analysis. C) Fluid inclusion temperature results from Chapter 3. D) Temperature offset reported as the difference in temperature from clumped and from fluid inclusions. Blue bars represent Heinrich stadials which are global climatic events and are shown to be periods of temperature decrease in the Bahamas.

5.5 Discussion

5.5.1 Modern: Environment of the cave

Published records suggest modern annual variation in air temperature ranges from 22 to 28 °C in the Bahamas, with the coldest month being January and the warmest in July and August (Baldini et al., 2007). Relative humidity averages ~77%, with little annual variation (Yanes and Romanek, 2013). There are distinct wet and dry seasons with the wetter period between May to November driven by the Bermuda high and an observed break in the wet season in July due to the westward expansion of the Bermuda high (Magana et al., 1999). Growth rates are found to be lowest corresponding to the dry season, suggesting that there is not a significant lag for the rainfall to reach the cave (Figure 5.11). The pH, $\delta^{13}C_{DIC}$ and $\delta^{13}C_{CO2}$ results are similar to observations from cave monitoring studies (Lambert and Aharon, 2011; Mattey et al., 2008; Tremaine et al., 2011) and the total alkalinity results are similar to the calculated results from Tremaine et al. (2011).

Fluctuations in net rainfall amount (Precipitation minus Evapotranspiration: P-ET) can affect drip water. With decreasing net rainfall, there will be a decrease in hydrologic head and therefore a reduction in drip rate and with the Bahamas rainfall seasonality, this would create a generally negative net rainfall during the dry season. Evapotranspiration is shown in a cave in Florida to lead to increased concentration of Cl- with no effect on the $\delta^{18}O_w$ or $\delta^{2}H_w$ of the drip water (Tremaine and Froelich, 2013). Therefore the increased Cl- deeper in the cave may be due to evapotranspiration processes influencing the water in this region, leading to increased Cl- water.

5.5.2 Modern: Carbon isotopes

The DIC of the drip water reflects bedrock carbon, soil gas CO_2 and a component of atmospheric CO_2 (Fohlmeister et al., 2011; Lambert and Aharon, 2011; Tremaine et al., 2011). Carbon isotopic ratio from the soil zone is dependent on the type of overlying vegetation (C3 vs C4), the amount of vegetation, the soil microbial activity and the ventilation processes occurring (Genty et al., 2003; Lambert and Aharon, 2011). In HBC, it appears that the soil zone end member is approximately -18 ‰ VPDB (Figure 5.7). Within the epikarst, the DIC can be impacted by prior calcite precipitation (PCP) in which calcite precipitates prior to the drip water reaching the cave. This occurs through degassing of CO_2 being present in the epikarst, particularly during dry events when the groundwater table is depressed. Prior calcite precipitation leads to the CO_2 exchange with the epikarst air, and an opportunity for the carbon isotopes of the DIC to be altered (Tremaine and Froelich, 2013). Once the drip waters reach the cave environment, the difference of the pCO_2 of the water and the cave air leads to the exchange and degassing of CO_2 and precipitation of $CaCO_3$ (equation 4). This can again lead to prior calcite precipitation. The rate of CO_2 degassing varies with drip water flow rates and the pCO_2 of the cave environment and drip water. Variation of the pCO_2 of the cave is typically thought to be related to ventilation changes, with increased ventilation decreasing the pCO_2 of the cave and hence increasing the rate of degassing and calcite precipitation (Kowalczk and Froelich, 2010; Lambert and Aharon, 2011).

Several cave studies have demonstrated that $\delta^{13}C_c$ values in cave calcites are enriched relative to the expected equilibrium values based on $\delta^{13}C_{DIC}$ measurements (Mickler et al., 2004; Riechelmann et al., 2013; Tremaine et al., 2011). Carbon isotopic

fractionation from HCO_3^-(aq) to carbonate has been suggested to be minimal, with some studies suggesting fractionation of up to 1 ‰ (Romanek et al., 1992; Rubinson and Clayton, 1969; Tremaine et al., 2011). The observed δ13Cc enrichment in caves relative to the $\delta^{13}C_{DIC}$ value has been attributed to ventilation driven CO_2 degassing causing an enhanced enrichment of the $\delta^{13}C_{DIC}$ or as CO_2 exchange between gas phase and aqueous phase is more rapid than net degassing. Periods of increased ventilation is associated increased net degassing of CO_2 and calcite precipitation via dehydration (equation 5). Increased rate of degassing leads the remaining HCO_3^-(aq) to become progressively enriched in ^{13}C resulting in an increased calcite $\delta^{13}C_c$ value (Lambert and Aharon, 2011; Mickler et al., 2004; Tremaine et al., 2011). During degassing processes the carbon isotope of the drip water will become progressively will be heavier also due to the DIC-CO_2 exchange with ventilated cave air (Tremaine et al., 2011). In HBC, the cave air is heavily influenced by atmospheric air, and therefore a much greater $\delta^{13}C$ value and hence driving the increased $\delta^{13}C_c$ value of the precipitated calcite.

In HBC, there is evidence of some enrichment of $\delta^{13}C_c$ value from the center to the outside of the slide. This may in part be driven by degassing processes which leads to increased $\delta^{13}C_c$ from the center and due to exchange with the heavier cave air.

As suggested above, ventilation changes and degassing processes can greatly impact the degassing rate of CO_2 and hence kinetic isotope fractionation. In this study, results from the $\delta^{13}C_C$ of the slides are shown to be more positive than the original soil zone carbon isotopic value (Figure 5.18) suggesting that isotopic exchange has occurred since the soil zone, most likely due to degassing and exchange with the air. The $\delta^{13}C_{CO2}$ value is lowest in the west room suggesting that this is the least ventilated room (Mattey

et al., 2008; Spotl et al., 2005; Tremaine et al., 2011), which is supported by the [CO_2] data, however other measurements (*e.g.* radon) are needed to verify that this room is in fact the least ventilated. This interpretation is also supported by the lower $\delta^{13}C_c$ and $\delta^{13}C_{DIC}$ of the west room (Figure 5.9) (Lambert and Aharon, 2011; Spotl et al., 2005). When comparing the $\delta^{13}C_{DIC}$ to the $\delta^{13}C_c$ results, there appears to be minimal offset between the carbonate and DIC for the main room, while the west room $\delta^{13}C_c$ values are lower than the average $\delta^{13}C_{DIC}$ values (Figure 5.9, Table 5.6a). However the $\delta^{13}C_{DIC}$ values are highly variable for all locations (Table 5.9a).

Studies have also shown that ventilation may vary seasonally as processes in the soil zone change (Lambert and Aharon, 2011; Tremaine et al., 2011) In order to better understand seasonalilty of ventilation, a longer sampling period is necessary in HBC. However, the limited sampling suggests that the summer may be characterized by increased $\delta^{13}C_{CO2}$ value for both locations on the third level, while winter is characterized by decreased $\delta^{13}C_{CO2}$ values, suggesting decreased ventilation in the winter (Table 5.7). This is similar to the ventilation regime observed in a cave in Gibraltar, where cave pCO_2 increases in the winter and decreases in the summer (ventilation decreases in the winter and increases in the summer) (Mattey et al., 2008). As previously demonstrated, ventilation can impact degassing with periods of increased ventilation associated with increased degassing rates and ventilation will bring heavy $^{13}CO_2$ from outside air into the cave. HBC is a well-ventilated cave therefore the impacts of ventilation are thought to be driving the $\delta^{13}C_c$ results.

A.

Location	$\delta^{13}C_C$ (VPDB ‰)	S.D.	$\delta^{13}C_{DIC}$ (VPDB ‰)	S.D.	$\delta^{13}C$ difference calcite - DIC
MS	-9.57	0.8	-9.47	3.0	-0.09
ES	-9.54	1.5	-9.47	3.0	-0.07
WS	-10.88	0.6	-10.16	1.6	-0.72

B.

Location	Corrected Kim and O'Neil 1997 offset (VPDB ‰)	S.D.	O'Neil et al. 1969 offset (VPDB ‰)	S.D.	Tremaine et al. 2011 offset (VPDB ‰)	S.D.
MS	1.81	0.53	1.72	0.54	0.76	0.53
ES	1.38	0.61	1.29	0.61	0.32	0.62
WS	1.15	0.64	1.31	0.33	0.34	0.34

Table 5.6: $\delta^{18}O_c$ (A) and $\delta^{13}C_c$ (B) differences for the Hatchet Bay Cave samples. A) Measured $\delta^{13}C_c$ values compared to measured $\delta^{13}C_{DIC}$ results from the drip waters. The results demonstrate limited fractionation between the DIC and the calcite $\delta^{13}C_c$ values, which may be due to the large errors of the $\delta^{13}C_{DIC}$ results. B) Measured $\delta^{18}O_w$ of drip waters and cave temperature were used to calculate the predicted $\delta^{18}O_c$ values based on the Kim and O'Neil (1997) (equation 2), O'Neil et al. (1969) (equation 1), and Tremaine et al. (2011) (equation 3) equations. Predicted $\delta^{18}O_c$ values were then compared to the measured $\delta^{18}O_c$ values (measured – observed). Results demonstrate increased difference in the MS location compared to ES and WS.

	$\delta^{13}C_{CO2}$ (‰ V-PDB)	
	Summer	Winter
Main	-9.81	-10.40
West	-11.60	-12.58

Table 5.7: Average summer and winter results for $\delta^{13}C_{CO2}$ for both the main room and the west room. All sampling results are reported in the appendix. Results support lower $\delta^{13}C_{CO2}$ values for the winter for both locations. Unfortunately due to the number of samples which were unable to be analyzed for $[CO_2]$, $[CO_2]$ is not included in this analysis.

5.5.3 Modern: Oxygen isotopes of calcite

When analyzing the variability within the slide for $\delta^{18}O_c$ values, there does appear to be some instances of increased $\delta^{18}O_c$ value along the outside of the slide when compared to the center (Figure 5.12). This may be driven by evaporative processes driving the increasing $\delta^{18}O_c$ value with distance from the center, due to splashing of the drip water and hence evaporation or due to the amount of time the drip water spends on the slide.

Utilizing the measured $\delta^{18}O_w$ and the temperature at the time of formation, predicted $\delta^{18}O_c$ can be calculated based on published calibrations. Such calibrations of the temperature dependent fractionation of oxygen isotopes include the calibrations of O'Neil et al. (1969) as modified by Friedman and O'Neil (1977) (equation 1) Kim and O'Neil (1997) (equation 2), and Tremaine et al. (2011) (equation 3) as previously outlined. At HBC, the offsets between the measured $\delta^{18}O_c$ and predicted $\delta^{18}O_c$ from Kim and O'Neil (1997) and O'Neil et al. (1969) (Table 5.6 b) are greater than the offsets

observed during the monitoring study of Tremaine et al. (2011). Results demonstrate the greatest offset is observed in the MS location, while ES and WS calcites agree best with the temperature dependent fractionation equation from Tremaine et al. (2011) (Figure 5.21,Table 5.6 b). This suggests either there is enhanced fractionation occurring at MS through evaporation or the limited sampling has not captured the full $\delta^{18}O_w$ of the drip waters for this site and therefore has offset the calculations of the expected $\delta^{18}O_c$ values.

From the drip water $\delta^{18}O_w$ results, the residence time of the water is thought to be long enough that the $\delta^{18}O_w$ of the drip water should not be affected by rapid short lived events, such as hurricanes, which are known to have isotopically light $\delta^{18}O_w$ values (Price et al., 2008).

The observed $\delta^{18}O_c$ results for HBC are compared to published cave monitoring results in Figure 5.21. These results demonstrate the large variability for the oxygen isotope fractionation in the cave, with a majority of the samples falling near the equation from Tremaine et al. (2011). These results further support that the temperature dependent fractionation is offset for speleothems from previously published laboratory studies and agree well with the findings by Tremaine et al. (2011).

Factors that can influence the fractionation of oxygen isotopes during precipitation include the rate of net precipitation as demonstrated in the $\delta^{13}C_c$ system and/or evaporative processes. Evaporative processes can lead to the oxygen isotopes of the water and hence calcite to become progressively heavier (Tremaine et al., 2011). This can occur as a result of evaporative processes in the soil zone or in the cave.

Precipitation rate can influence the kinetic fractionation if the rate of precipitation is faster than the rate of HCO_3^-(aq) re-equilibration. Studies have also demonstrated the

importance of saturation state driving kinetic fraction (Tremaine et al., 2011). Over saturation drives rapid calcite precipitation and increased kinetic fractionation. However, as saturation state does not appear to be significantly changing in the cave, it is not thought to be a significant driver of the $\delta^{18}O_c$ disequilibrium and in fact the results

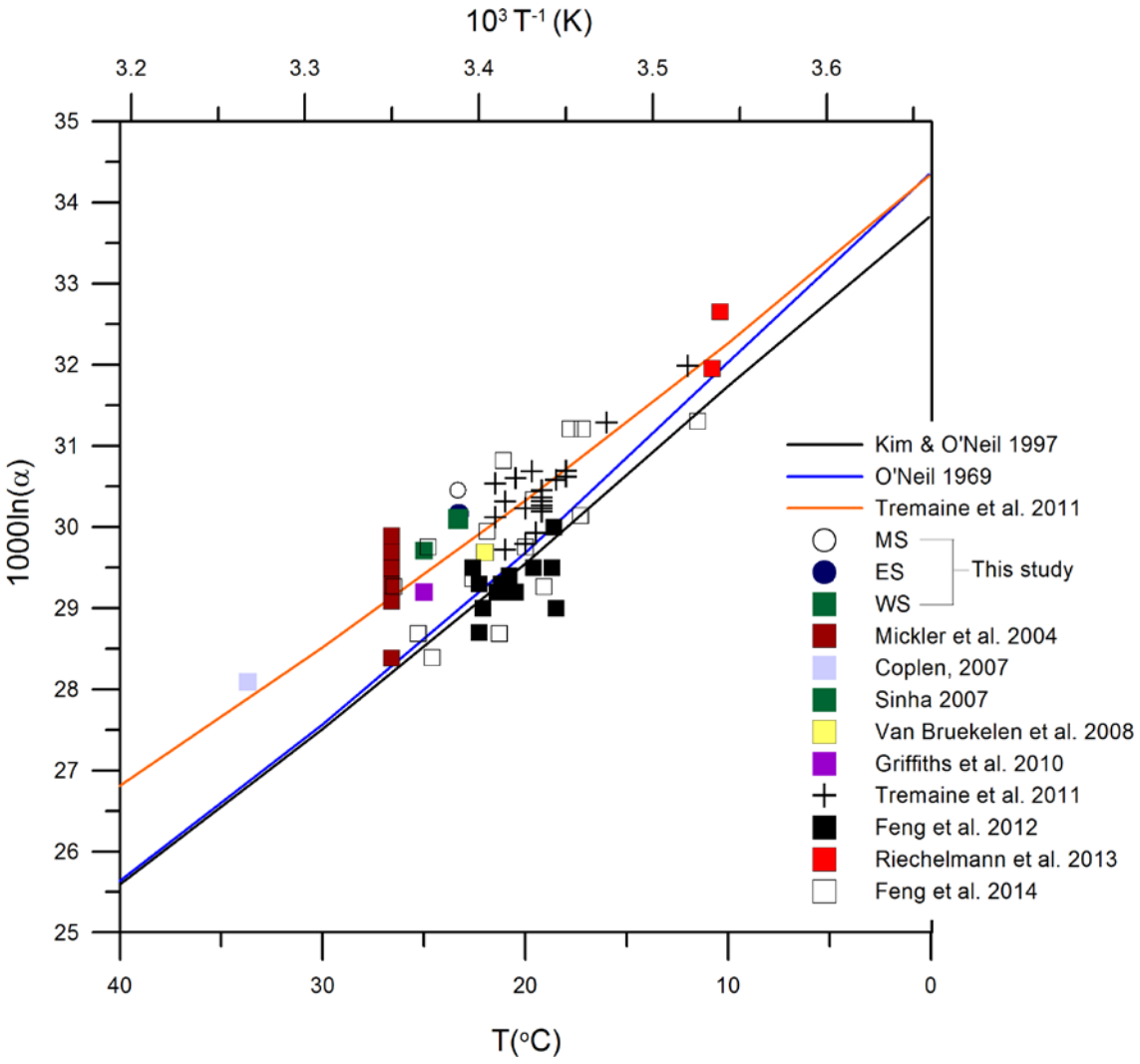

Figure 5.21: 1000ln (α) versus temperature (and $10^3/T$ plotted on the top axis) for calcite from theoretical studies (Kim and O'Neil, 1997; O'Neil et al., 1969) as well as cave studies. Circles are the results from Hatchet Bay Cave, while squares represent samples from various cave studies as demonstrated in Tremaine et al. (2011). Results demonstrate the large spread in results from caves, however most caves fall closer to the Tremaine et al. (2011) relationship. For details on the samples plotted see Appendix D.

do not support a statistically significant relationship between $\delta^{18}O_c$ and saturation state. Rather, the primary driver of fractionation for $\delta^{18}O_c$ and $\delta^{13}C_c$ isotopes is thought to be the CO_2 exchange between drip water and cave air during degassing fractionation. Additionally it has been proposed that during the process of dehydration, when CO_2 degassing occurs rapidly, can lead to $\delta^{18}O_c$ and $\delta^{13}C_c$ isotope fractionation.

5.5.4 Modern: What drives clumped isotope offset?

Previous studies demonstrate that the temperatures calculated using the clumped isotope value in speleothems are consistently warmer than expected (Δ_{47} values are lower than expected) (Affek et al., 2008; Daëron et al., 2011; Kluge and Affek, 2012). This would suggest that certain mechanisms unique to speleothems may be causing Δ_{47} to be out of equilibrium. As demonstrated above, samples may pass the Hendy test, but may still exhibit Δ_{47} value variability within a slide. This suggests that clumped isotopes may be more sensitive to kinetic effects, as also found in Kluge and Affek (2012).

The offset observed in the modern is similar to the observations by Affek et al. (2008) with an average offset of 8 ºC, Kluge and Affek (2012) observed a mean offset of 10 ºC and Daëron et al. (2011) observed offsets ranging from 3.5-22 ºC. The results of HBC clumped isotopes will be utilized to better understand clumped isotope offsets and variability.

<u>Temporal and spatial variability:</u>

Studies have shown that saturation state can impact the Δ_{47} offset with supersaturation driving an increased Δ_{47} offset, as increased saturation is driven by higher degassing rates, hence the degree of kinetic fractionation (Kluge and Affek, 2012). However, in HBC the reverse is observed with increasing saturation being correlated with

decreasing Δ_{47} offset (Figure 5.15). Given the limited number of datasets for which saturation state is available, further studies are necessary to validate these results.

Growth rate variability is found within HBC, with increased growth rate in the WS, compared to the MS and ES locations. The strong relationship between growth rate and Δ_{47} offset observed in the WS location may be due to degassing rates. The sample with the lowest offset was found in December 2012, when ventilation was the lowest and hence the degassing rate was the lowest. Conversely, no relationship is observed between growth rate and Δ_{47} offset at either the ES or MS locations. Kluge and Affek (2012) also observed no significant relationship between growth rate and Δ_{47} offset.

The relationship between increasing $\delta^{18}O_c$ disequilibrium and Δ_{47} offset (Figure 5.22) may be driven by the degassing rate and exchange rates of CO_2 and/or evaporative processes (Affek et al., 2008; Daëron et al., 2011). During fast degassing, the product CO_2 may have a greater Δ_{47} value than the HCO_3^-(aq) and if the residual HCO_3^- does not re-equilibrate with the remaining water, fractionation of the isotopic composition follows a Rayleigh type distillation (Guo, 2008). However, with slow degassing, re-equilibration can occur, and the Δ_{47} value will remain in equilibrium (Affek et al., 2008; Kluge and Affek, 2012). Guo (2008) theoretically calculated the impacts of dehydration and dehydroxylation on the $\delta^{13}C$, $\delta^{18}O$, and Δ_{47} values and found that for every 1 ‰ increase in $\delta^{18}O$, the $\delta^{13}C$ value increases by 1.1-3.2 ‰ and the Δ_{47} value decreases by 0.017 to 0.026 ‰. The variability of fractionation is dependent upon the pathway of the CO_2 degassing and how much carbonate forms (Guo, 2008). Evaporative processes can also drive $\delta^{18}O$ offset in HBC, while CO_2 degassing and exchange processes can lead to offset

in Δ_{47} value, resulting in a linear relationship between the two, however it is unclear if should influences were considered in Guo (2008).

The trend shown in Figure 5.22 demonstrates the relationship between increasing $\delta^{18}O$ offset and Δ_{47} offset for HBC, for the study by Kluge and Affek (2012) and for theoretical modeling (Guo, 2008) utilizing Kim and O'Neil (1997) as equilibrium to calculate the $\delta^{18}O$ offset. The theoretical model plotted assumes the primary pathway for degassing is dehydration, with a 1:1 precipitation rate and assuming for a 1 ‰ increase in $\delta^{18}O_c$, a -0.0175 ‰ decrease in Δ_{47} and a +2.34 ‰ increase in $\delta^{13}C_c$ value (Figure 5.22). The slope for HBC (-0.023 ‰) is shallower than the slope from Kluge and Affek (2012) (-0.047 ‰) and from Daëron et al. (2011) (not shown) suggesting that disequilibrium may vary by cave and with time. However the results from HBC fall closer to the fractionation predicted from Guo (2008) for degassing processes driving the offset for $\delta^{18}O_c$ and Δ_{47} (Figure 5.22).

The trend shown in Figure 5.23 demonstrates the relationship between increasing $\delta^{18}O$ offset and Δ_{47} offset for this study, utilizing Tremaine et al. (2011) as equilibrium. Since the data from Kluge and Affek (2012) were calculated using Kim and O'Neil (1997), the data cannot be plotted on Figure 5.23. The slope for the HBC data is steeper (-0.042 ‰) when calculated using the Tremaine et al. (2011) equation.

The above mentioned explanation for the drivers of the observed Δ_{47} offset relies heavily on the influences of degassing processes (and subsequent dehydration) in driving the observed offsets. However, the exchange between the heavier cave air (Figure 5.7) and the drip water may also lead the observed Δ_{47} offset. When comparing the $\delta^{13}C_c$ results to the Δ_{47} value, the $\delta^{13}C_c$ value is offset from the soil gas end member (Figure

5.18). This is thought to be due the exchange between the heavier cave air (Figure 5.7) and the drip water. This exchange leads to the increasing $\delta^{13}C_c$ value and Δ_{47} value observed in Figure 5.18 and would be expected to occur in a well-ventilated cave such as HBC. This also accounts for the strong relationship between $\delta^{13}C_c$ value and the Δ_{47} value, while conversely there is a weak relationship between $\delta^{18}O_c$ and Δ_{47} value. When comparing the $\delta^{13}C_c$ to the $\delta^{13}C_{DIC}$ values, (Figure 5.24) the $\delta^{13}C_{DIC}$ values are more negative suggesting the drip water has not yet equilibrated with the cave air, but rather during the precipitation of $CaCO_3$ there has been exchange, hence increased $\delta^{13}C_c$ values. When compared to the expected results from Guo (2008), the HBC results plot below the Guo (2008) line (Figure 5.24). However the errors on the $\delta^{13}C_{DIC}$ are large. With increased sampling for $\delta^{13}C_{DIC}$ and a better characterization, in the future a greater understanding of the factors driving $\delta^{13}C_c$ and Δ_{47} offset can be developed.

Summary of HBC observations:

Overall, geochemical results suggest variation in kinetic fractionation for different parts of the cave. Fractionation is enhanced in the main room compared with the west room for both $\delta^{18}O_c$ and Δ_{47} values (Figure 5.13 & 5.19). The two clear differences between the main room and west room are growth rate and ventilation (Figure 5.8 & 5.11). The west room overall has a higher growth rate and an observed decreased Δ_{47} offset during periods of slower growth. In addition, the period of decreased growth rate (winter) is also the period of decreased ventilation and therefore a decreased degassing rate. This suggests that a combination of these factors may drive the Δ_{47} towards equilibrium.

The main room is considered to be more ventilated and based on the $\delta^{13}C_c$ and $\delta^{18}O_c$ data, more fractionated. The greater fractionation in this part of the cave may be a result of increased ventilation or an increase in evaporation.

5.5.5 Clumped isotopes versus fluid inclusions: Stalagmite AB-DC-09

The average offset between the clumped isotope temperature and the temperature determined from fluid inclusions in sample AB-DC-09 is 18 ºC. This value is much larger than the temperature offset observed in the modern between clumped isotope and measured temperature (8.6 ºC). This suggests that either the temperatures (based on the $\delta^{18}O_w$ of the fluid inclusions and the $\delta^{18}O_c$ of the calcite) are lower than expected, possibly driven by fractionation, or that the clumped isotopes are more fractionated thereby leading to an increased offset. Based on the fluid inclusion data, there does not

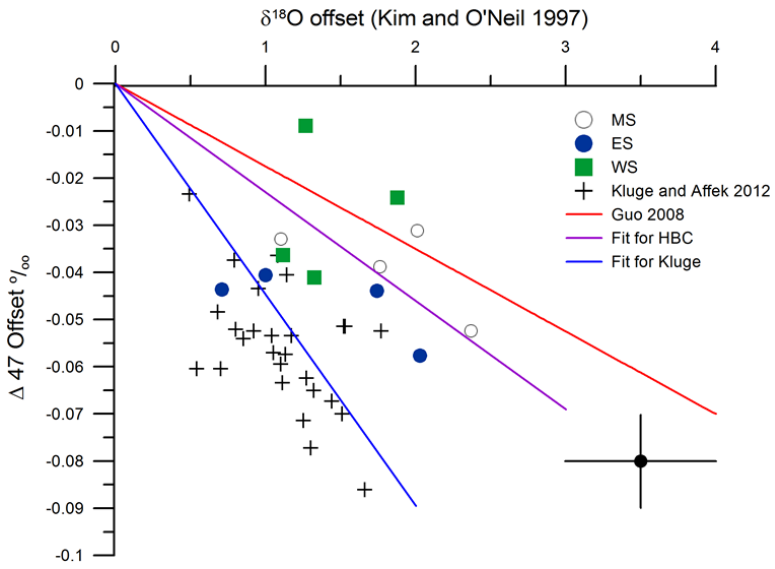

Figure 5.22: Results from Hatchet Bay Cave (circles) demonstrating the systematic offset from the expected value for both Δ_{47} and $\delta^{18}O_c$ values. Also plotted are results from Kluge and Affek (2012), demonstrating a positive $\delta^{18}O_c$ offset and a negative Δ_{47} offset. The purple line represents the average slope of -0.023 ‰ observed for HBC, the blue line is the -0.047 ‰ slope for Kluge and Affek results and red is the theoretical slope from Guo, 2008 as described in the text. The correlation between both Δ_{47} and $\delta^{18}O_c$ supports similar factors drive both. Average error from the HBC results is represented by the black circle.

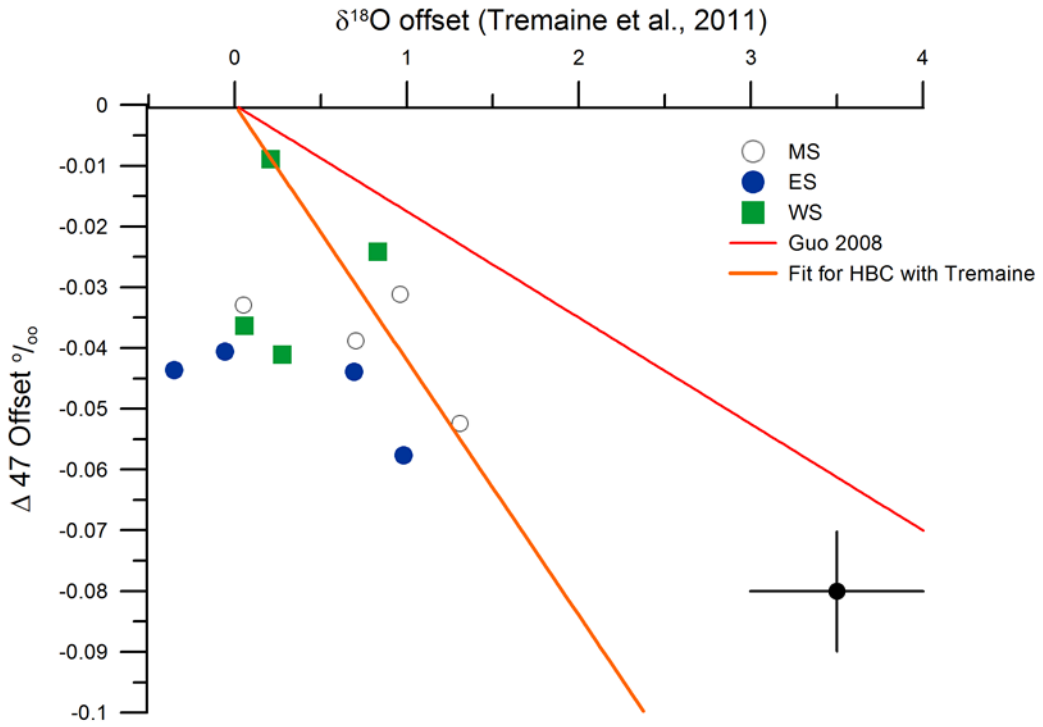

Figure 5.23: Results from Hatchet Bay Cave demonstrating the systematic offset from the expected value for both Δ_{47} and $\delta^{18}O_c$ values. Δ_{47} offset was determined as the offset from the temperature measured in the cave and the $\delta^{18}O_c$ offset was determined as the offset from the expected from Tremaine et al. (2011). The orange line represents the average slope of -0.042 ‰ observed for HBC and red is the theoretical slope from Guo, 2008 as described in the text. The correlation between both Δ_{47} and $\delta^{18}O_c$ supports similar factors drive both. Average error from the HBC results is represented by the black circle.

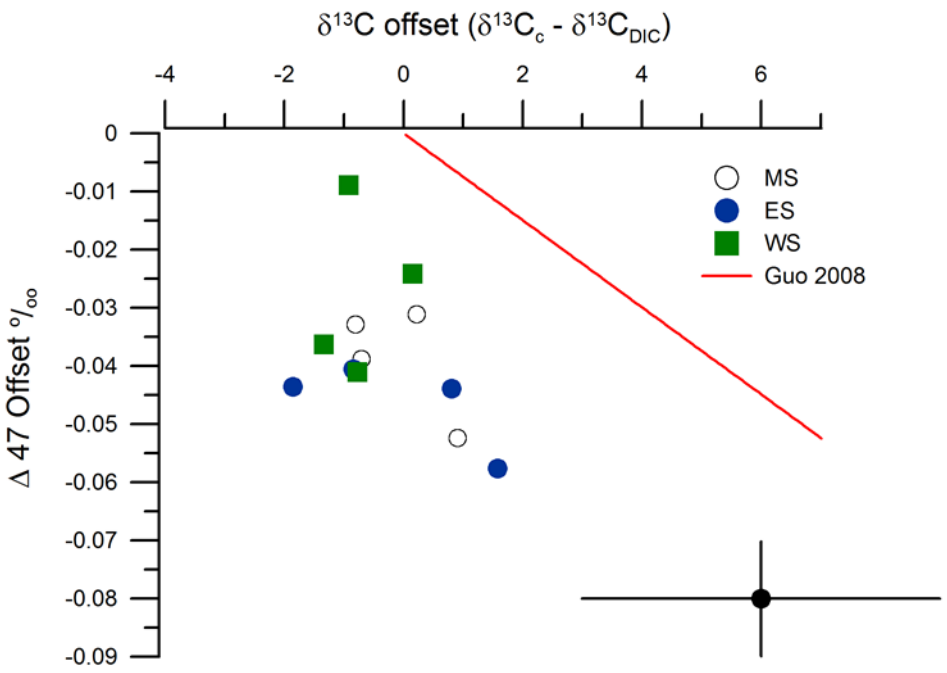

Figure 5.24: Results from Hatchet Bay Cave (circles) demonstrating the systematic offset from the expected value for both Δ_{47} and $\delta^{13}C_c$ values. The red line represents the theoretical slope from Guo, 2008 as described in the text, with an intercept at the origin as this plot represents offsets. The results from HBC plot below the expected from Guo, 2008 and have large errors suggesting additional work is necessary. Average error from the HBC results is represented by the black circle.

appear to be any indication of significant fractionation taking place (see Chapter 3), and therefore we propose that differences arise as a result of increased Δ_{47} kinetic fractionation. The periods with the greatest offset between the clumped isotope and fluid inclusion records are found at 15.6 and 17.5 ka BP (Figure 5.20). This is a period characterized by decreasing temperatures in the fluid inclusion results, reflecting the impact of a global scale climate event, known as a Heinrich stadial. In the Bahamas, Heinrich stadials have been shown to be periods of lower temperature and lower precipitation (Chapters 3 and 4). Therefore, it is possible that during these events there was an associated change in the rate of degassing leading to the observed enhanced Δ_{47}

offset. This change in the degassing rate can be driven by changes in the amount of water in the overlying limestone. With less water in the epikarst (due to aridity) there is the potential for increased cave ventilation through the passages which are normally filled with water. Increased ventilation could lead to a decrease in the pCO_2 and hence increased rate of degassing and Δ_{47} fractionation.

5.5.6 Correction of clumped data

A method for correcting Δ_{47} values has been proposed by Wainer et al. (2011) utilizing the fluid inclusion results and monitoring data. As demonstrated from the modern data from HBC, the 1000ln(α) and Δ_{47} offset correlates with a slope of -0.042 ‰ (Figure 5.23) when utilizing Tremaine et al. (2011) as equilibrium. As proposed by Wainer et al. (2011), the slope of this disequilibrium line can be utilized to project the Δ_{47} results back to equilibrium allowing for the calculation of a "corrected" temperature. This assumes the sample was offset from the original temperature along a kinetic isotope fractionation vector with a known slope. Four clumped isotope samples were chosen to demonstrate this method and are presented in Figure 5.25. Utilizing the fluid inclusion results to correct the clumped isotope results is circular reasoning; however, as is described below, a worthwhile exercise as this may shed light on kinetic fractionation over time.

The four samples chosen to demonstrate this correction method are from a range of 1000ln(α) values and are plotted as 1000ln(α) versus Δ_{47} value in Figure 5.25. The 1000ln(α) value was calculated from the $\delta^{18}O_c$ of the carbonate and the $\delta^{18}O_w$ of the fluid inclusion water and the Δ_{47} value is the measured value. From this original point, the 1000ln(α) and Δ_{47} values are transformed along the slope of the 1000ln(α) versus Δ_{47}

offset previously determined (i.e. -0.042 ‰ from HBC). The values are corrected to the point of equilibrium, using Tremaine et al. (2011) for equilibrium. At the point of equilibrium, the Δ_{47} and 1000ln(α) values have been corrected such that temperature calculated using Ghosh et al. (2006) and the temperature calculated by Tremaine et al. (2011) are equal. Figure 5.25 transforms the Δ_{47} and 1000ln(α) along the slope determined from the modern Hatch Bay Cave from Figure 5.23. Since we have defined equilibrium as the Tremaine et al. (2011) equation, we cannot utilize the slopes calculated in Figure 5.22 (calculated using Kim and O'Neil (1997)).

This same transformation was applied to all samples which were analyzed for clumped isotopes and fluid inclusions and the results are presented in Figures 5.26. Utilizing the slope observed in the modern produces samples which are on average 6 ºC ±3 warmer than indicated by the fluid inclusion data (Figure 5.26).

The offset between the corrected clumped isotope and fluid inclusion data is the greatest from 15 to 16.8 ka BP. This indicates a steeper Δ_{47} offset to 1000ln(α) characterizes these two time periods. Overall the trend for the corrected samples is similar to the trend from the original fluid inclusion results, with both the corrected Δ_{47} and the fluid inclusion temperature records demonstrating decreased temperatures associated with Heinrich stadials. These results indicate that fractionation of both the Δ_{47} and $\delta^{18}O_c$ occurs and also that fractionation varies between with time, with the Heinrich stadials 1 and 2 exhibiting the greatest offset after correction, suggesting a steeper $\delta^{18}O_c$ offset versus Δ_{47} offset at these time periods.

In the modern cave, the results from the Bahamas support the conclusion that factors such as growth rate and ventilation drives kinetic isotope fractionation.

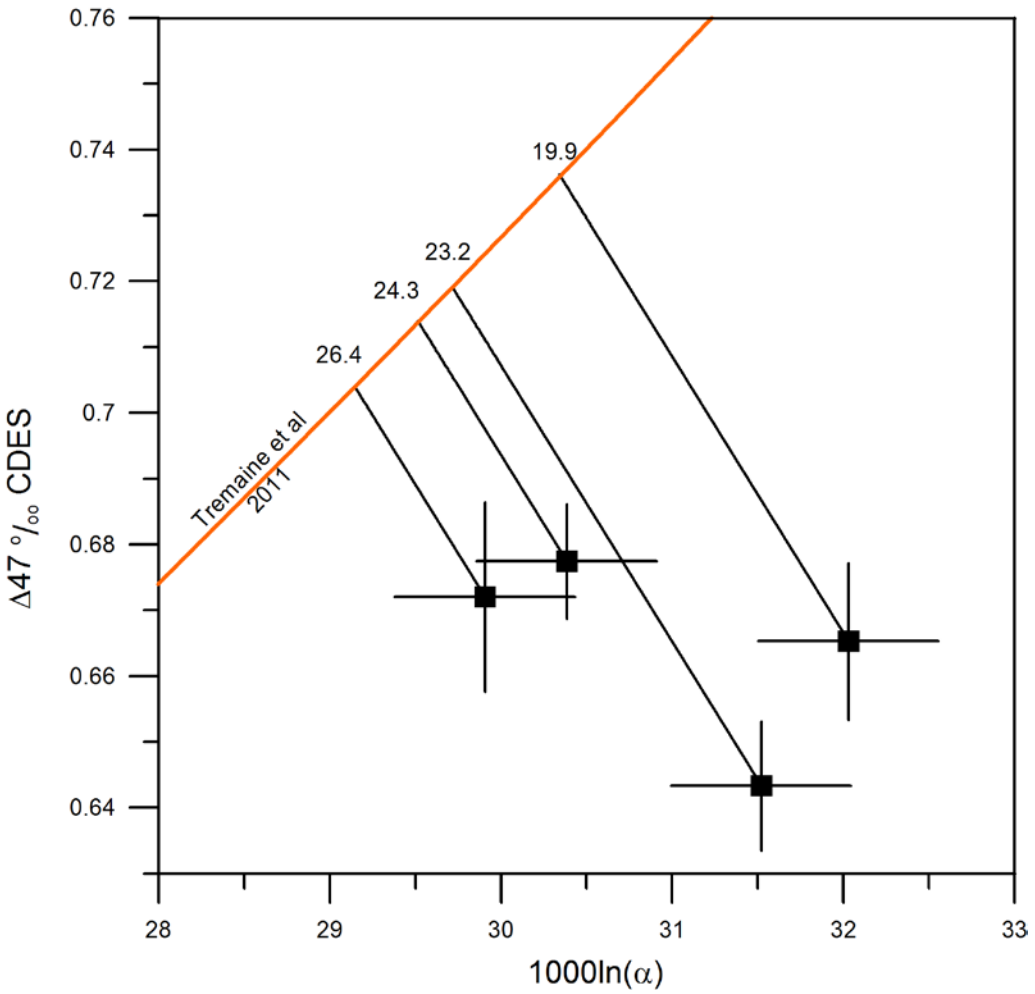

Figure 5.25: Samples from AB-DC-09 plot below the equilibrium line defined by Tremaine et al., 2011 and Ghosh et al., 2006 as outlined above. Using the modern slope for disequilibrium from Figure 5.23, samples can be corrected back to equilibrium using the observed slope. A) Four samples projected back to the equilibrium line of Tremaine et al. (2011) using the observed slope of HBC from Figure 5.23, with a slope of -0.042. The new equilibrium temperatures are shown for each sample. The original fluid inclusion data was calculated using the Tremaine equation (see chapter 3).

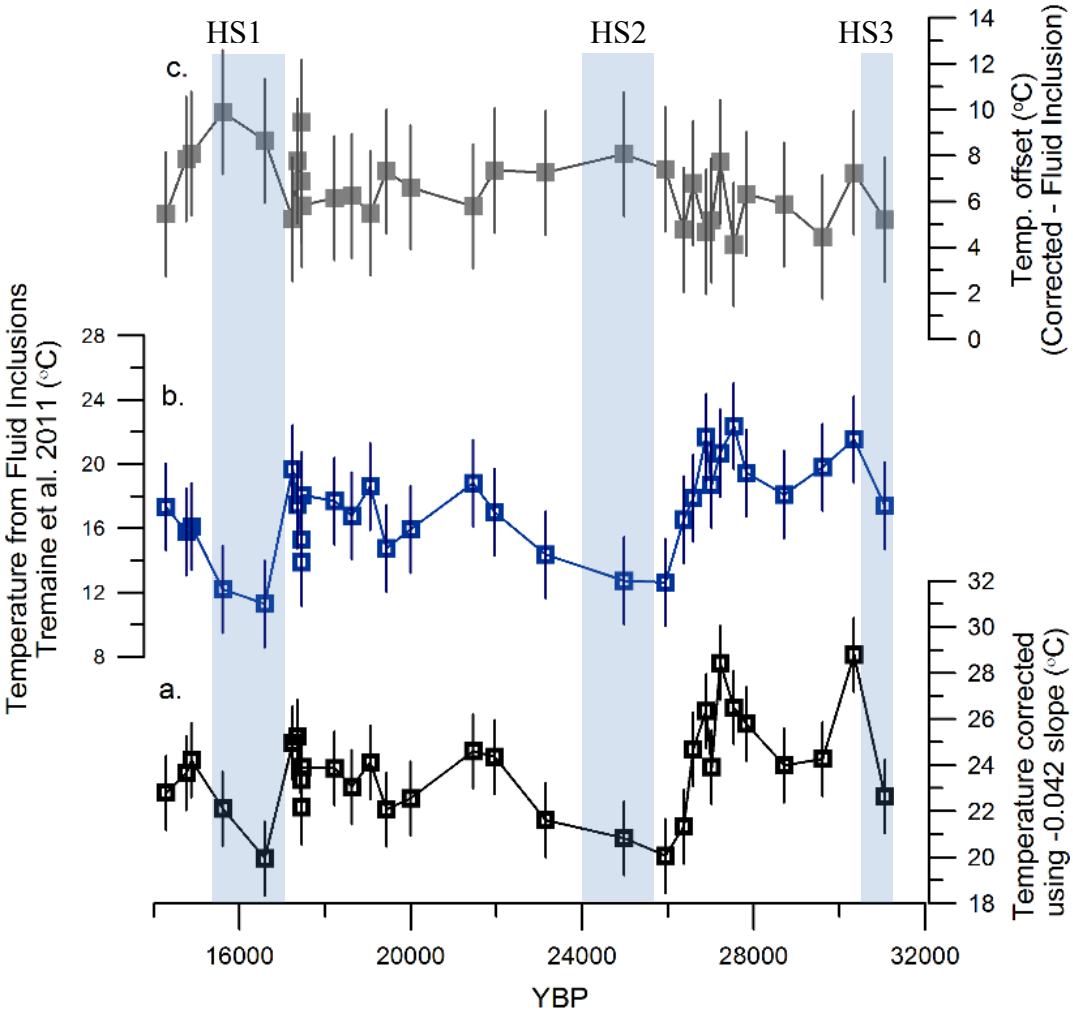

Figure 5.26: Results from samples AB-DC-09 after correction. (a) Temperature from Δ_{47} after correction using the slope from HBC modern data of -0.042 from Figure 5.23. The results are compared with the fluid inclusion temperature results in (b). Also shown is the difference between the corrected clumped isotope record and the fluid inclusion temperature reconstructions (c) demonstrating the greatest offset is found at 16.6 ka. Blue bars represent Heinrich stadials (HS) which are global climatic events and are shown to be periods of temperature decrease in the Bahamas.

Therefore, in the ancient, periods of enhanced offset (*e.g.* Heinrich stadials) may be due to environmental processes increasing the rate of degassing such as changes in ventilation. Enhanced ventilation may occur during Heinrich stadials, as these periods are shown to be periods of decreased rainfall and hence a more ventilated cave.

5.6 Conclusion

This study represent an attempt to better understand carbon, oxygen and clumped isotope fractionation in a cave using modern and ancient cave carbonates. The results from the modern demonstrate enhanced fractionation for carbon and oxygen isotopes of the calcite for the Main site compared to the East and West locations. The west room is thought to be less fractionated with respect to carbon and oxygen isotopes as a result of the reduced ventilation. For the clumped isotope results, the temperatures calculated from the clumped isotope data are 6 °C warmer than the monitored temperature in the cave. The growth rate and ventilation appear to be driving the clumped isotope offset for the west room as both processes influence the degassing process. Overall, for the three locations, fractionation driven by either DIC-CO_2 of the cave air equilibration or hydration processes appears to be primarily driving both $\delta^{18}O_c$ and Δ_{47} offset.

For speleothem sample AB-DC-09, the temperatures calculated from the clumped isotope method are offset from those estimated using the $\delta^{18}O_w$ from the fluid inclusions and the carbonate of the same samples. The difference in temperature between these two methods is greater than that observed in the modern farmed calcite. When the Δ_{47} value is compared to the fluid inclusion results, periods with the lowest temperatures from fluid inclusions are the periods with the greatest offset, suggesting a climatic control on the kinetic isotope fractionation. One possibility is that the periods with the lowest temperatures are also the periods with decreased precipitation, hence increased ventilation, which would lead to greater degassing and evaporation, which would further fractionate the clump isotopes, driving the greater offset at this time period. Using the methods outlined in Wainer et al. (2011) the clumped isotope results have been corrected

to equilibrium using the relationship observed in the modern for 1000ln(α) offset versus Δ_{47} offset. The corrected clumped isotope results suggest a greater Δ_{47} offset for every 1 ‰ $\delta^{18}O$ offset for sample AB-DC-09 particularly from 16.8 to 15 ka BP.

Chapter 6

Speleothems from Bahamas Blue Holes: Geochemical archives of past dust events

Summary

Modern studies of atmospheric dust demonstrate that there is seasonal deposition today in the Caribbean derived from Africa. There is however a paucity of data on the deposition of dust during past time periods in the Bahamas. This study represents an attempt to understand modern and ancient deposition of dust in the Bahamas utilizing speleothems. The isolated Bahamas platform represents an ideal location to study the deposition of dust as its pristine limestone bedrock restricts the detrital source of trace and minor elements to atmospheric deposition. In this study, iron will be utilized as a proxy for atmospheric dust. Results from the study of a modern cave demonstrate good agreement between the trace element concentrations of the water and that in the associated precipitated calcite. Iron concentrations are found to be heterogeneous in drip waters and calcite both temporally and spatially. The temporal variation is thought to be due to annual variations in dust delivery and amount of precipitation. The spatial variability within the cave is thought to be due to variations in drip water flow rates and flow paths within the soil zone and limestone bedrock.

In order to supplement the work in the modern, two stalagmites collected from the Bahamas which formed from 64,000 to 14,000 years before present were analyzed for their Fe/Ca ratios. The Fe/Ca ratios of the ancient stalagmites are shown to increase concurrently with changes in the oxygen and carbon isotopes that are associated with Heinrich stadials. Other paleoclimate records from the Northern Hemisphere support the notion that Heinrich stadials are dusty events, the increased Fe/Ca ratios in speleothems

associated with the Heinrich stadial terminations can potentially be explained by an increase in precipitation at the end of each Heinrich stadial, bringing into the cave Fe rich waters derived from prior deposited dust. The periods of the Fe increases in the Bahamas are in good agreement with other Heinrich stadial dust records from Africa and Greenland. This study supports the scenario that Heinrich stadials are dusty events in the Northern Hemisphere and that dust is transported and deposited in the Bahamas.

6.1. Background

Atmospheric dust has been shown to impact sea surface temperatures (SSTs) (Evan et al., 2011; Evan et al., 2009), precipitation (Yoshioka et al., 2007) and primary productivity (Martinez-Garcia et al., 2011) both in the modern and in the past, making dust an important component of the climate system (Mahowald et al., 2010; Mahowald et al., 2006). Studies suggest decrease SSTs and precipitation with increasing atmospheric dust (Evan et al., 2011; Evan et al., 2009; Yoshioka et al., 2007) and the global scale impact of dust on the climate system supports the importance of studying dust fluxes of the past.

Evidence recorded in ice and sediment cores suggests increased concentrations of dust in the atmosphere during glacial periods. Overall, studies support that atmospheric mineral dust was approximately 2-4 times higher worldwide during glacial periods than interglacial periods (McGee et al., 2010), and up to 7 times higher over Africa (Just et al., 2012). An even greater amount of dust in the atmosphere occurs synchronously with millennial scale climate events, particularly during Heinrich stadials. Cores from the western coast of Africa indicate increased dust originating from Africa during Heinrich stadials (Jullien et al., 2007; Mulitza et al., 2008; Tjallingii et al., 2008) with estimates of

dust fluxes ranging from a 2.5 (McGee et al., 2013) to an 80 fold increase (Just et al., 2012). Other evidence of increased aridity in the Northern Hemisphere during these events is from sediment cores from the Arabian Sea (Pourmand et al., 2004) and records from Eastern Europe (Sima et al., 2013). The increased Northern Hemisphere aridity during stadials is thought to be driven by a reduction in Atlantic meridional overturning circulation (AMOC), a decrease in Northern Hemisphere SSTs and a southerly shift in the ITCZ (Bond et al., 1992; Clement and Peterson, 2008; Peterson et al., 2000).

6.2. Study Site

The Bahamas platform is an isolated carbonate platform approximately 80 km east of South Florida (Figure 6.1) that includes low lying islands comprised of relatively pure carbonate with no terrigenous input from rivers (Swart et al., 2014). The isolated nature of the platform and the pure nature of the carbonate should be reflected in the geochemistry of stalagmite calcite and the concentrations of minor and trace elements should therefore remain low. Any departure from these low concentrations should reflect an increase in dust delivery to the Bahamas. To understand modern dust fluxes to the Bahamas, drip waters and calcites have been collected from a currently active cave from Hatchet Bay Cave, Eleuthera Island, Bahamas. For the study of the past deposition of dust to the Bahamas, stalagmite samples forming over the last six Heinrich stadials have been collected from Abaco Island, Bahamas from a currently submerged cave. Both Eleuthera and Abaco Islands are on the eastern edge of the Bahamas platform (Figure 6.1).

6.2.1 Dust delivery to the Bahamas: Past and present

Modern studies have shown that the Bahamas and much of the Caribbean are receiving dust from the Sahel (Kumar et al., 2014; Muhs et al., 2007; Pourmand et al., 2014a; Prospero and Lamb, 2003; Reid, 2003) (Figure 6.1). Monitoring of dust delivery in Barbados and Miami demonstrates that the summer months have the highest concentrations of dust (Prospero and Lamb, 2003; Trapp et al., 2010). The Saharan Air Layer (SAL) is the major transport process across the Atlantic, and dust is transported within the SAL by the African Easterly Jet (AEJ) (Just et al., 2012). The SAL and dust transport are intricately linked to the migration of the ITCZ and when the ITCZ migrates north in the summer, the convergence of hot dry Saharan air with southern air leads to the vertical advection of dust to the SAL. The SAL transports dust across the Atlantic Ocean between 15 ºN and 22 ºN and dust within the SAL is transported west from the African coast across the Atlantic to Barbados and the Caribbean within a week (Muhs, 2012).

Over longer timescales, the amount of dust reaching the Bahamas has been significant. Provenance studies of the insoluble soil components from the Bahamas indicate that between 60-80% of the soils are derived from African dust and 20-40% is derived from Mississippi Valley Loess (Muhs et al., 2007).

Figure 6.1 (Following Page): a) Time-averaged map of subtropical/tropical Atlantic Aerosol Optical Depth (AOD) which is related to dust, from the MISR satellite retrieved from the Giovanni online data repository. Optical depth at λ=555nm from July 1, 2012 to July 30, 2012. B) Sampling location of Eleuthera Island where the currently active cave, Hatchet Bay Cave is located. Also shown is Abaco Island, where the currently submerged cave is located.

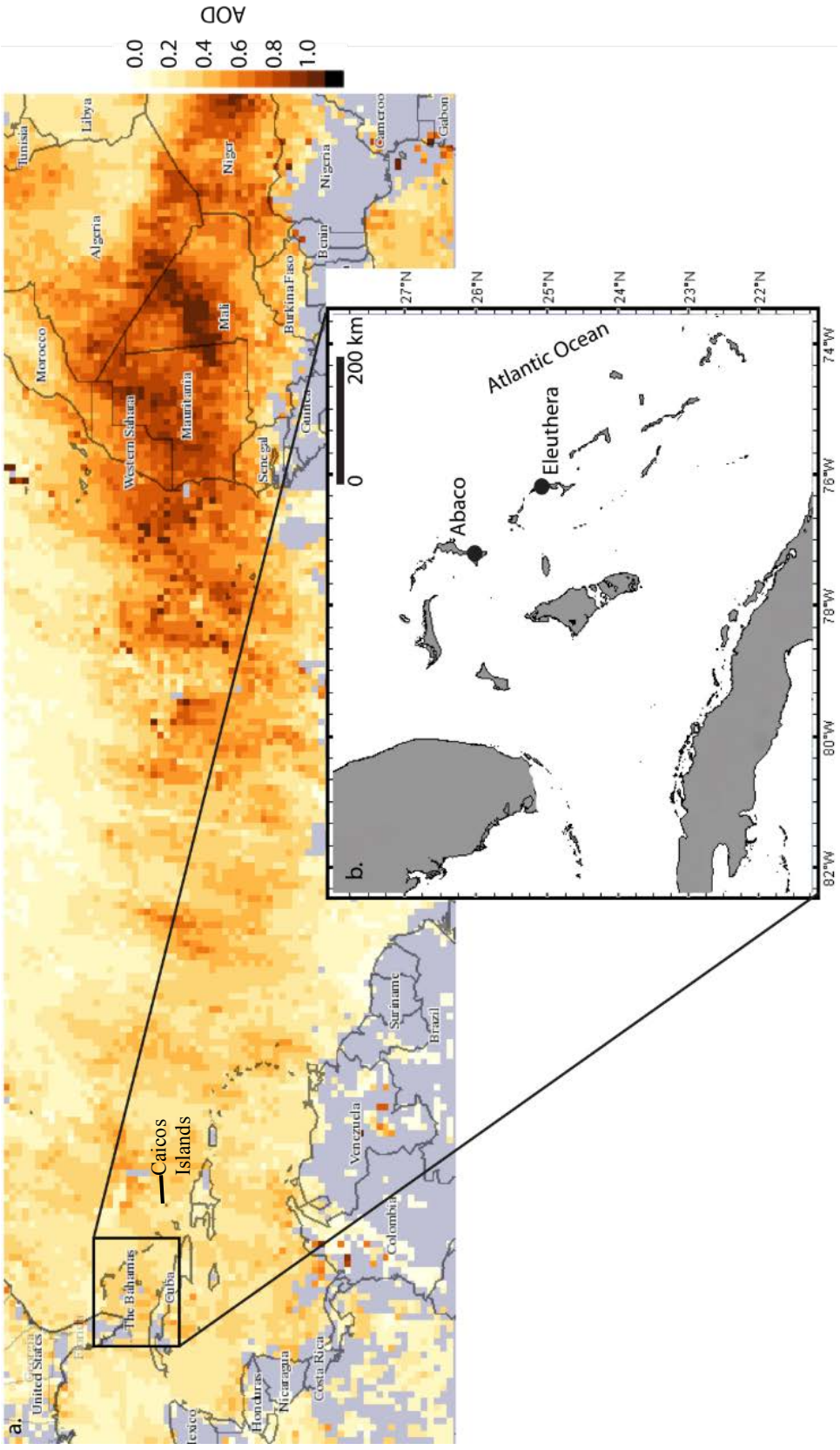
AOD
0.0
0.2
0.4
0.6
0.8
1.0
a.
b.
Caicos Islands
The Bahamas
Cuba
United States
Mexico
Honduras
Nicaragua
Costa Rica
Colombia
Venezuela
Suriname
Brazil
Morocco
Western Sahara
Algeria
Tunisia
Libya
Mauritania
Mali
Niger
Senegal
Guinea
Burkina Faso
Benin
Nigeria
Cameroon
Gabon
Atlantic Ocean
Eleuthera
Abaco
200 km
0
27°N
26°N
25°N
24°N
23°N
22°N
82°W
80°W
78°W
76°W
74°W

6.3. Speleothems as Archives of Dust

Several studies have analyzed speleothems for records of atmospheric dust deposition (Dredge et al., 2013; Frumkin and Stein, 2004; Zhou et al., 2009). The deposition of dust on the soil layer above the cave and the subsequent leaching of elements from the dust to the drip water allows for a record of past dust deposition within the calcite of speleothems (Frumkin and Stein, 2004; Richter et al., 2004). During this process Fe^{2+} is mobilized and transported into the drip water (Kieber et al., 2001). Zhou et al. (2008) demonstrated that elements such as Al, Fe and Mn are also mobilized in colloidal/particulate phases in the groundwater. These elements will either be incorporated into the calcite lattice or incorporated as deposits. An additional study from a cave in Ireland found that the increase in colloid bound elements was driven by increased rainfall and a breakdown of soil material in the soil zone (Baldini et al., 2012). Dry deposition of aerosols to stalagmites has been identified in a modern cave where there is air movement within the cave which carries and deposits aerosols (Christoforou et al., 1994).

For this study, trace elements will be utilized as provenance indicators of dust deposition to the Bahamas, as African dust has been shown to be primarily comprised of Al, Fe and Mn (Trapp et al., 2010) while Mississippi Valley Loess deposits are primarily comprised of Al, Fe, and Si (Pye and Johnson, 1988).

6.4. Methods

6.4.1 Modern samples

Samples were collected from Hatchet Bay Cave (HBC), a currently active cave in Eleuthera, the Bahamas (Figure 6.2). Monitoring was initiated in June of 2012.

Overlying the cave is grasses and small *Metopium toxiferum* (poison wood) and trees of the Fabaceae family with well-developed soils (greater than 15 cm depth). Most of the grasses are located near the entrance and at lower elevations around the cave, with the small trees located on the Aeolian ridge. HBC was accessed through a small ~1.7 m. by 0.9 m. opening located 10 to 15 m above sea level and exhibits an extremely linear pattern particularly west of the main entrance (Mylroie and Mylroie, 2009). The opening is immediately surrounded by thick grasses with larger trees (as described above) located 3 meters to the west, approximately following the cave direction and well developed soils (as described above). The first level exhibits evidence of phreatic dissolution (Mylroie and Mylroie, 2009). There is no evidence of cave breathing holes through the roof as suggested by the lack of changes in the overlying vegetation and soil. The cave is divided into three levels with the first level being the shallowest and the smallest level. The second level is a tubular passage accessed by a 1.6 m. ladder down from the first level and again contains evidence of phreatic dissolution (Mylroie and Mylroie, 2009). The second level is more extensive (300 m long) with active drip water and stalagmite formation (Mylroie and Mylroie, 2009). The 2nd level is thought to follow a thick, terra rossa paleosol, leading to the creation of the linear and tubular shape following the aeolian ridge (Mylroie and Mylroie, 2009). The third level is the deepest level and is accessed by another 1.8 m ladder from the second level. However continuing on the second floor is a smaller passage which after several meters leads to a 7 m shaft to the surface, which may have been carved out for guano mining (Mylroie and Mylroie, 2009). The third level is partially filled with water, with active stalagmite formation occurring on raised rock ledges above the water, ~1.2 m above the water level. This water is tidally

influenced and of marine salinity (Mylroie and Mylroie, 2009). There is no evidence of water flooding the rock ledges nor is there any evidence of calcite deposits forming from the water. Most of the sampling was conducted on the 2nd and 3rd levels. Located on the 3rd level ledges were experiments on the precipitation of calcite from drip water, henceforth known as calcite "farming" (Figure 6.2). The cave was visited every 3-5 months. This cave has more extensive speleothem formation than other caves in Eleuthera possibly driven by the 10-15 m of overlying calcite (Mylroie and Mylroie, 2009). Samples from the surrounding cave walls were not collected.

Analyses were conducted on the air ([CO], $\delta^{13}C$ of CO_2), drip water ($\delta^{18}O_w$, $\delta^{2}H_w$, $\delta^{13}C$ of DIC and minor elements) and the farmed calcite ($\delta^{13}C_c$, $\delta^{18}O_c$, Δ_{47}, and trace elements) deposited on microscope slides which were deployed in the cave. For this study, results will focus on the drip water $\delta^{18}O_w$, $\delta^{2}H_w$, and minor elements and for the farmed calcite trace and minor elements. A description of the monitoring methods is included in the following.

Waters:

Unfiltered water samples were collected throughout the second and third levels of the cave by holding clean (10% HCl clean) vials under dripping stalactites. Vials were filled completely (where possible) to avoid head space equilibration, then capped and stored until analysis. The waters were filtered (Whatman 0.2 μm pore filter) upon return to the laboratory (within 2-3 days) into unused 10% HCl clean vials. For $\delta^{18}O_w$ & $\delta^{2}H_w$ of the drip water, samples were measured using the Picarro cavity ring-down spectroscopy instrument (CRDS). Four standard waters were analyzed with each set of samples and the standards used were previously calibrated to the VSMOW-GISP-SLAP scale. Data

are reported relative to VSMOW with an average reproducibility of 0.05 ‰ for $\delta^{18}O_w$ and 0.1 ‰ for $\delta^{2}H_w$ from repeated analysis of a standard. One milliliter of each sample or standard is measured into a glass vial and sealed with a rubber septum. Each sample or standard is injected into the Picarro A0211 vaporizer unit at 0.2 ml per injection six times into the vaporizer. The vaporizer is held at 110ºC for the duration of the sample run. The injection port of the A0211 is fitted with a fine stainless steel mesh ideal for trapping salt crystals to minimize interferences and clogging downstream. The mesh basket is periodically removed, rinsed, dried and reinserted into the injection port. The vaporized water gas is transferred to the Picarro CRDS analyzer in a stream of N2 gas. The measurement cycle of each sample lasts about 8 minutes and data are reported relative to VSMOW.

For trace and minor elements, samples were acidified using OmniTrace® HNO_3 and then analyzed using a Varian Vista Pro inductively coupled optical emissions spectrometer (ICP-OES) at the University of Miami within 2-3 days of returning. For long term storage, the waters were acidified. Results from procedural blanks were below detection limits.

Figure 6.2 (following page): Map of Hatchet Bay Cave, Eleuthera, Bahamas. The cave is divided into three levels and the locations of water sampling are approximate. Also shown is the approximate location of water collection and calcite farming. Also included are photographs of the areas which were sampled.

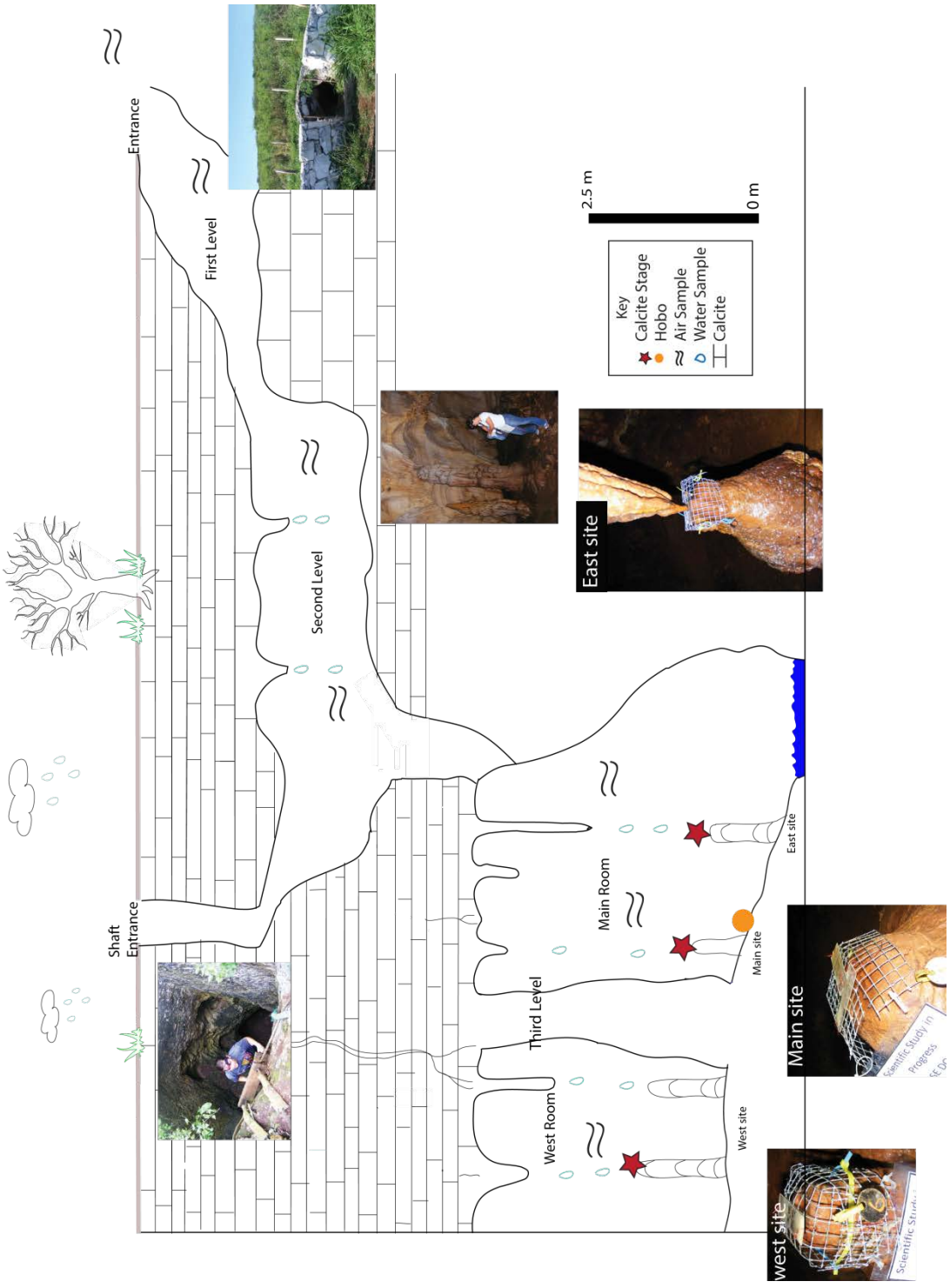
Entrance
First Level
Second Level
Shaft Entrance
Main Room
Third Level
West Room
East site
Main site
West site
2.5 m
0 m
Key
Calcite Stage
Hobo
Air Sample
Water Sample
Calcite
East site
Main site
west site

Calcite:

Standard glass microscope slides were placed on top of currently forming stalagmites. Microscope slides were held in place by wire and were tied down at an angle similar to the methods of Tremaine et al. (2011) and Banner et al. (2007). Prior to installing the slides in the cave, the slides were weighed in the laboratory. Two calcite precipitation sites were set up, one in the main room of the third level (these two will be referred to in the text as east main site (1 slide) and main site locations (2 slides)) and one in the west room (1 slide) (referred to in the text as west site) (Figure 4.2). The microscope slides were left in the cave for 3-5 months.

Slides were brought back to the laboratory, dried in a 40 ºC oven overnight and weighed, slides were not rinsed with DI therefore may be contaminated with sea salts. Sampling of the slide was conducted by removing the calcite using a dental tool. The calcite was then homogenized with a mortar and pestle and stored in Eppendorf vials until analysis. Calcite samples were dissolved in OmniTrace® 4 % HNO_3 to give a concentration of 4 ppm Ca and were analyzed using the ICP-OES.

6.4.2 Ancient samples

Two stalagmite samples (samples AB-DC-09 and AB-DC-12) were collected from a currently submerged cave from Abaco Island, Bahamas (16.5 and 11.9 meters below sea level) (Figure 6.3). A total of 37 U-Th age dates were acquired at the Neptune Isotope Laboratory of the University of Miami utilizing a ThermoFisher-Neptune Plus multi-collection ICP-MS. Details of the U-Th geochronometry technique and propagation of random and systematic uncertainties are discussed in Pourmand et al.

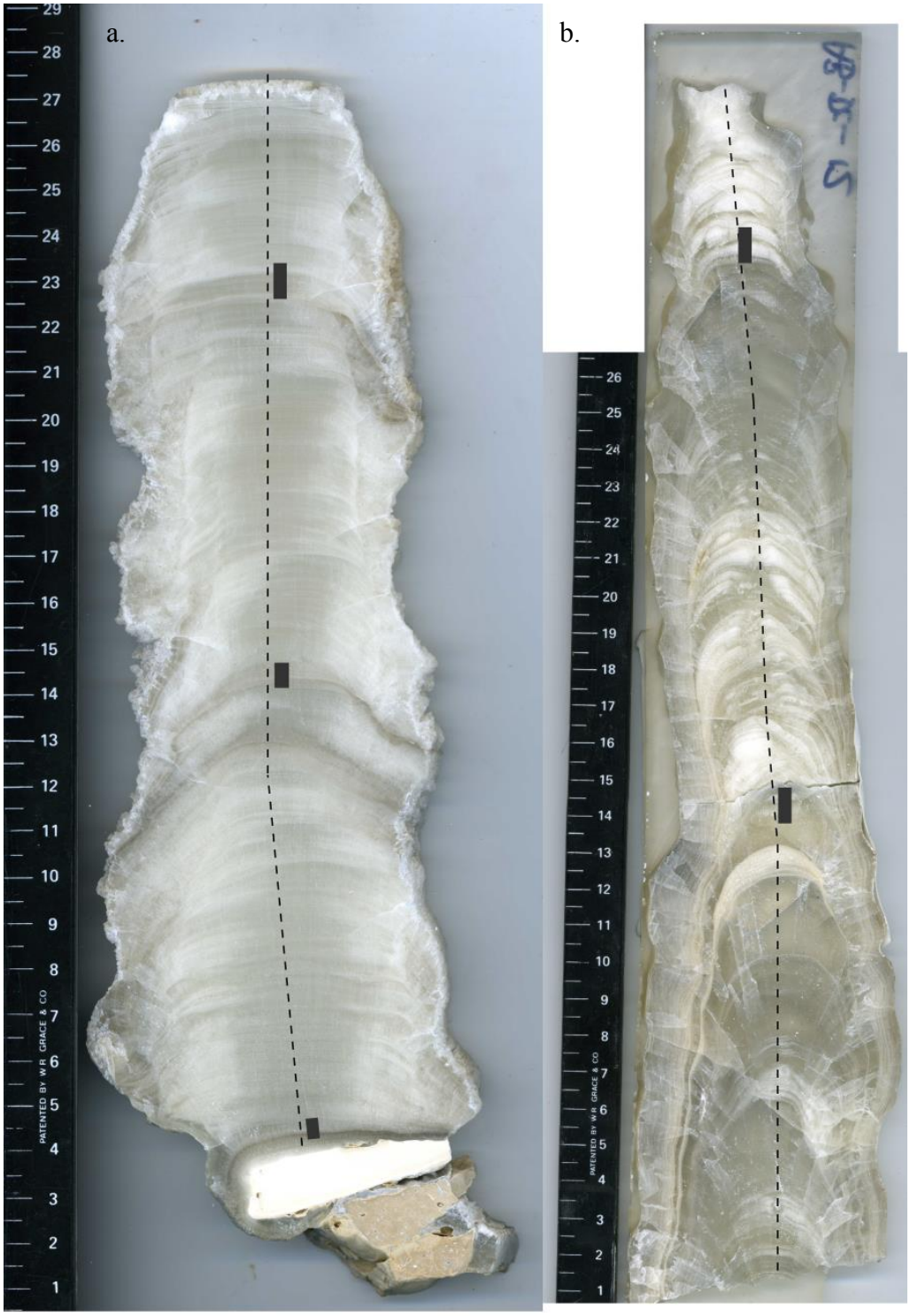

Figure 6.3: Reflected light photos of samples AB-DC-09 (a) and AB-DC-12 (b). For both a and b: Dotted line is the location of low resolution (1000 μm) sampling and black squares are the sampling locations for the high resolution (20 μm) analysis.

(2014b). For all samples, an initial $^{230}Th/^{232}Th$ activity ratio of 3.7 ± 0.6 was used to account for excess (unsupported) ^{230}Th (see Chapter 3). The age models for the stalagmites were determined through linear interpolation between ages and the results are presented in Chapters 3 and 4.

Stalagmite sample AB-DC-09 was sampled every 0.5 mm for trace elements and AB-DC-12 was sampled every 1 mm (Figure 6.3) utilizing a computerized NewWave micromill. Five locations (3 for AB-DC-09 and 2 for AB-DC-12) were additionally sampled at a high resolution (1 sample every 20 μm) (Figure 6.3) utilizing a computerized NewWave micromill. These areas were chosen as the initial $\delta^{18}O$ and $\delta^{13}C$ of the calcite results demonstrated these are intervals of rapid isotopic shifts (Chapter 4). Trace element samples were analyzed on the Varian ICP-OES for trace and minor elements as previously described for calcite samples.

6.5. Results

6.5.1 Modern samples

Waters:

For drip waters collected from Hatchet Bay Cave, an increase in the trace element concentration (in particular Fe) was observed in June 2012 and again in August 2013 (Figure 6.4). The concentration of Fe was lower in the 3rd level west room than the main room (Figure 6.5). The drip waters also demonstrate variability in the Sr/Ca and Mg/Ca values (Figure 6.6) and the $\delta^{18}O$ value of the drip water ($\delta^{18}O_w$) (Figure 6.7). In particular the West room exhibits more negative $\delta^{18}O$ value of the drip water (Figure 6.7) and decreased Sr/Ca and Mg/Ca values (Figure 6.6) when compared to the values observed in the Main room.

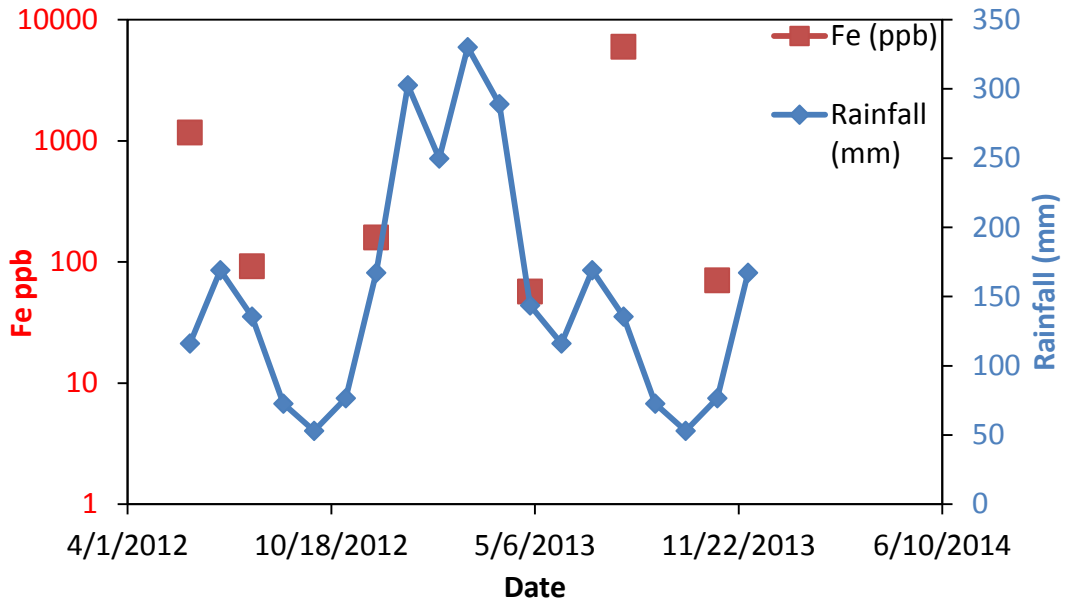

Figure 6.4: Results from the water samples in ppb for Iron (red) for each sampling period. Results have been averaged for all locations for each sampling period. Fe results are in ppb and vertical axis is on a logarithmic scale. The blue line is rainfall (mm) from Baldini et al., (2007).

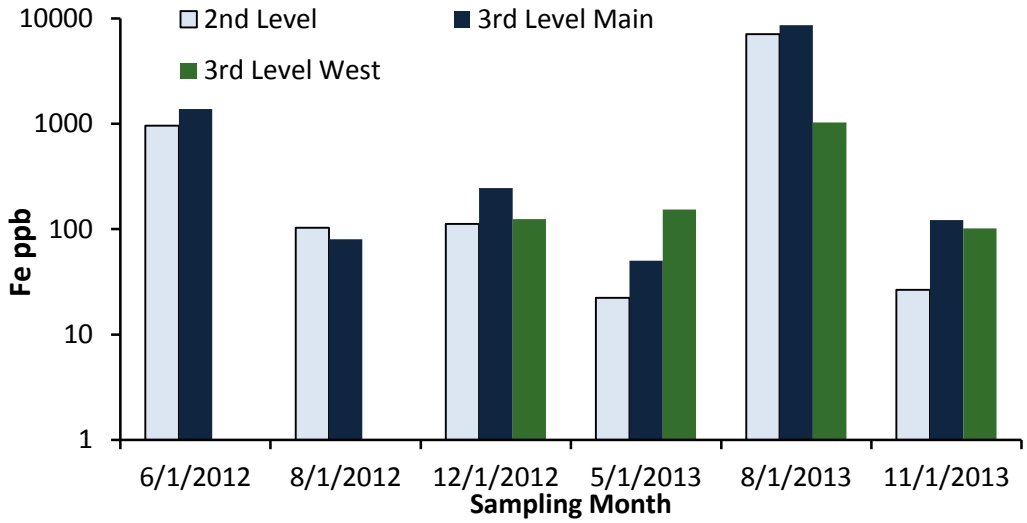

Figure 6.5: Results from the water samples in ppb for Iron for each sampling period shown by location with the cave. Light blue bars represent the Fe results for the second level, dark blue bars for the 3rd level main room and green bars for the 3rd level west room. Results are in ppb and the vertical axis is a logarithmic scale.

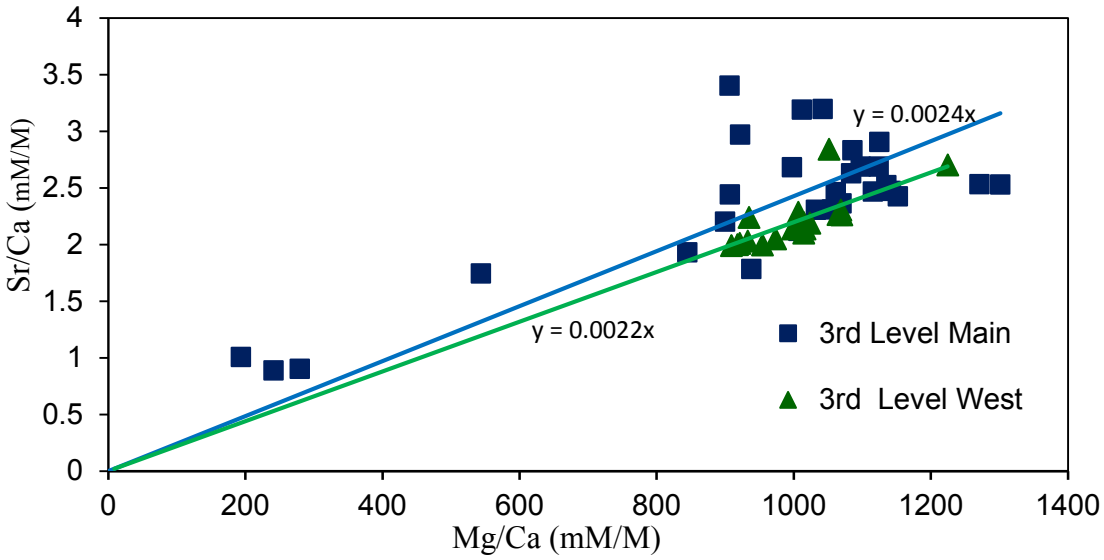

Figure 6.6: Mg/Ca versus Sr/Ca results for drip water samples from the 3rd level main (dark blue) and 3rd level west (green triangles).

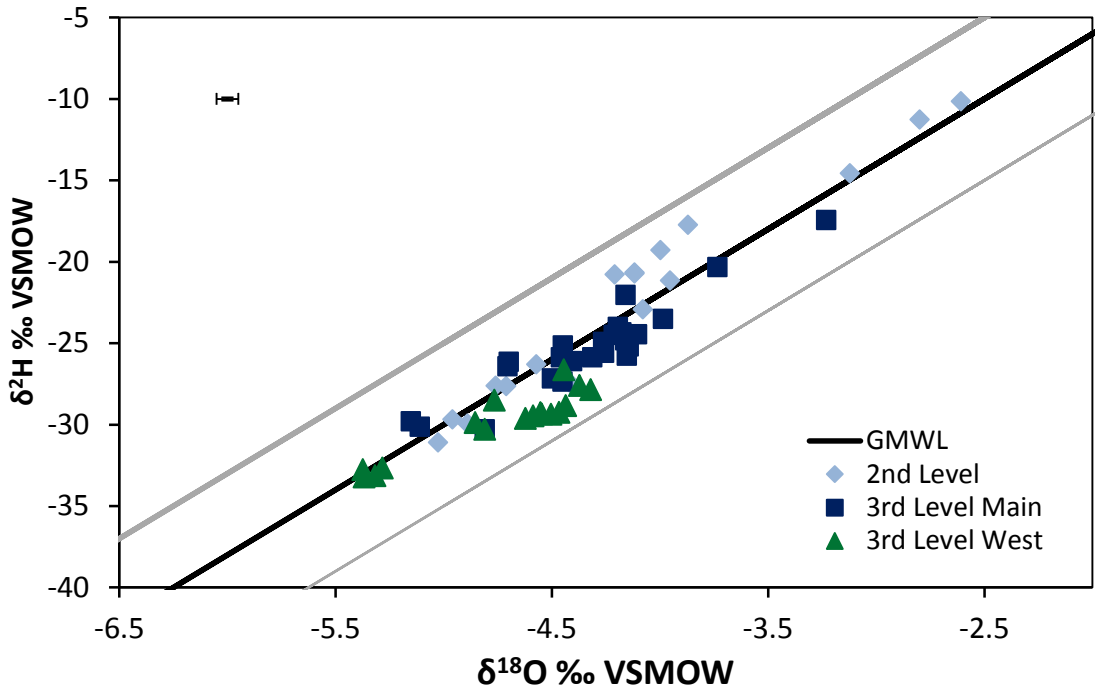

Figure 6.7: $\delta^{18}O_w$ and $\delta^{2}H_w$ for drip water samples from the 2nd level (light blue), 3rd level main (dark blue) and 3rd level west (green triangles). Results are plotted on the GMWL (black) with ± 5 ‰ $\delta^{2}H$ shown in grey. Average errors are shown in the upper left corner in black.

Calcite:

For the precipitated calcite in 2012 and 2013, the slides which were deployed and collected between August and November showed the highest Fe concentrations (Figure 6.8). The calcite precipitated in the main room overall had a higher Fe/Ca ratio, while the west room contained a significantly lower Fe/Ca ratio (Figure 6.9).

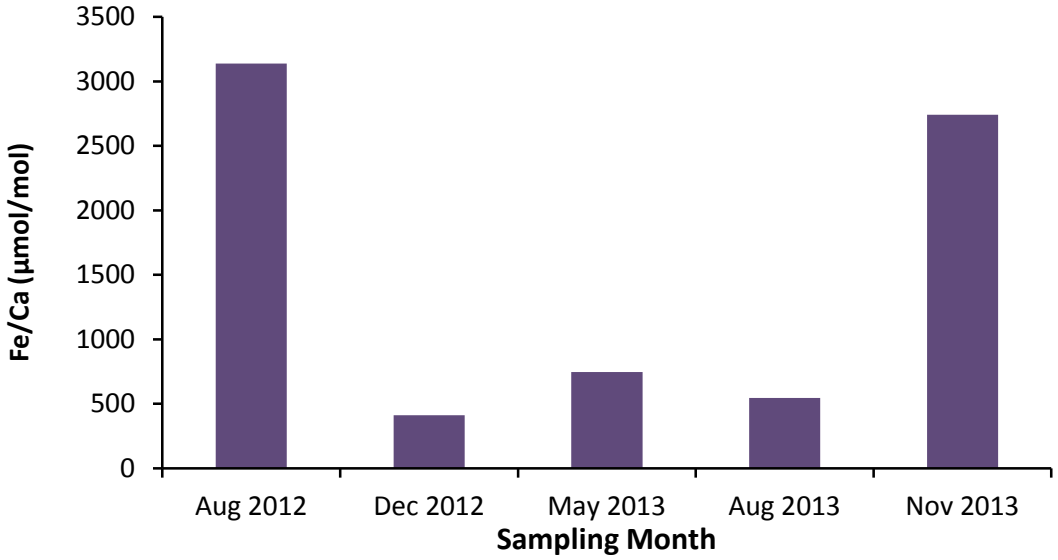

Figure 6.8: Results from the calcite farming precipitation experiment for Iron shown by sampling month. The average of each sampling location for each month is shown as a ratio of Fe/Ca (µM/M).

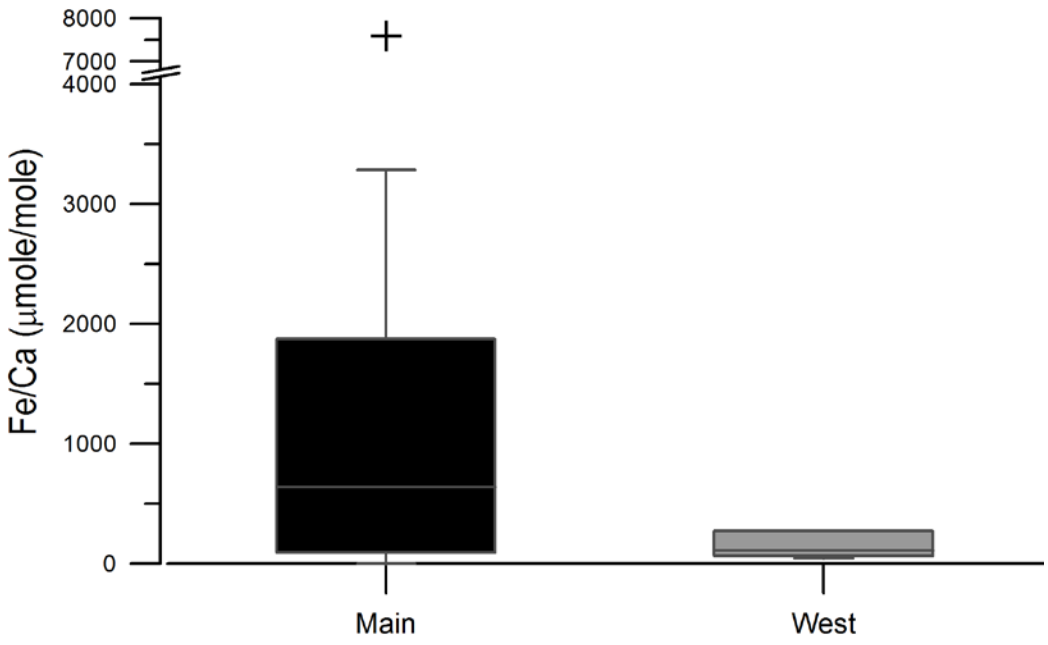

Figure 6.9: Box and whisker plot of the results from the calcite Iron shown by location in the cave. The results include all of the sampling periods. This demonstrates the higher Fe/Ca ratio in the main room when compared to the west room. Results are shown as a ratio of Fe/Ca (µM/M).

6.5.2 Ancient samples

The U-Th age dating of the speleothems demonstrate the stalagmites were formed from 14.2 to 63.5 ka before present with a gap in the record between 31.3 and 35.9 ka. During this time period, neither of the two stalagmite samples was forming (Table 6.1, 6.2, Figure 6.10). Weighted average growth rates are approximately 13 µm/year for sample AB-DC-09 and 11 µm/year for sample AB-DC-12.

The periods which were sampled at high resolution were approximately at 4 cm, 15.3 cm and 22.6 cm from the top for sample AB-DC-09, which correspond to ages 14.9, 24.9 and 31 ka BP. While for DC-12, areas of high resolution were conducted at ~5 cm and 21 cm from the top, corresponding to ages of ~38.8 and 46.4 ka BP. For samples AB-DC-09 and – 12, high Fe/Ca values were found at 15.0±0.2, 31.2±1.1, 38.8±0.2 and

46.0±0.2 ka before present, with highest values during the 15 and 46 ka BP events (Figure 6.10 a). Therefore not all periods which were sampled at a high resolution resulted in increased Fe/Ca values. Additionally it is important to note that the average five point smooth utilized in Figures 6.10 and 6.11 is an average smoothing of ~ 100 years for sample AB-DC-09 and ~ 150 years for sample AB-DC-12. These higher Fe/Ca values corresponded with increased $\delta^{13}C$ and $\delta^{18}O$ values in the carbonate found at 14.9±0.2, 30.9±1, 38.8±0.2, and 48±0.2 ka BP (Figure 6.10 b and c) suggesting a relationship between increased isotopic values of the calcite and Fe/Ca ratios for the 15, 30.9, 38.8 and 47.0 ka events. For the isotopic events at 14.9, 25 and 62.4 ka BP, there is a decline in the growth rate, but for the other events (30.9, 38.8 and 48 ka BP) there does not appear to be any change in growth rate (Figure 6.10 d).

The high resolution results support abrupt increases in Fe/Ca ratios (Figure 6.11 a-d). For the 15 ±0.2 ka BP event, there appears to be two pulses of increased iron, one at 15.0 which occurs with increasing $\delta^{18}O$ values and a second at 14.8±0.2 ka BP associated with a rapid decline in $\delta^{18}O$ value (Figure 6.11 a). For the 31.2 ka BP event, there is elevated Fe/Ca associated with declining $\delta^{18}O$ values. For the 38.8 and 46 ka BP events, the increased Fe/Ca ratio is associated with a decreasing $\delta^{18}O$ and $\delta^{13}C$ values (Figure 6.11 c and d). Also shown is the [$^{232}Th/^{230}Th$] activity ratio which is a good proxy for detrital contribution again demonstrating minimal relationship between [$^{232}Th/^{230}Th$] and increased Fe/Ca.

Sample Id	Distance from Top	^{238}U	(95% CI)	$[^{230}Th/^{238}U]$	(95% CI)	$[^{230}Th/^{232}Th]$	(95% CI)	Uncorr. Age	(95% CI)	$[^{234}U/^{238}U]$ initial	(95% CI)	Corr. Age	(95% CI)
	µm	(ppb)	±	(activity)	±	(activity)	±	(y)	±	(corrected activity)	±	(y)	±
DC-09	18000	201.839	0.125	0.1332	0.0007	57.6	0.96	15394	77	1.013	0.00262	14544	168
	37000	179.526	0.097	0.136	0.0006	54.5	1.54	15882	72	1.005	0.00264	14956	180
	60000	150.938	0.085	0.1552	0.001	47.9	1.11	18573	125	0.992	0.00273	17354	245
	72500	188.15	0.113	0.1545	0.0014	102.5	1.95	18054	174	1.014	0.00252	17501	200
	85000	204.482	0.109	0.1607	0.0009	43.5	0.28	18955	109	1.009	0.00261	17588	260
	110000	211.462	0.125	0.1779	0.0009	79.5	0.56	20925	110	1.021	0.00265	20110	181
	127000	183.408	0.109	0.1876	0.0022	128.6	1.67	22310	282	1.016	0.00255	21775	295
	137000	164.361	0.082	0.1923	0.001	48.3	0.36	23648	123	0.987	0.00252	22141	288
	145000	192.366	0.114	0.221	0.0011	110.9	0.81	26649	127	1.022	0.00258	25921	180
	156000	202.09	0.129	0.2235	0.0011	139.6	0.9	27028	126	1.02	0.00256	26445	161
	178000	204.471	0.15	0.2427	0.001	38.2	0.17	29796	123	1.017	0.00277	27447	431
	222500	202.531	0.127	0.2879	0.0013	19	0.11	36203	169	1.021	0.00264	30526	1008

Table 6.1: ^{230}Th dating results for sample AB-DC-09. Results from both samples are propagated with an initial $^{230}Th/^{232}Th$ activity ratio of 3.7±0.6.

Sample Id	Distance from Top	^{238}U	(95% CI)	[$^{230}Th/^{238}U$]	(95% CI)	[$^{230}Th/^{232}Th$]	(95% CI)	Uncorr. Age	(95% CI)	[$^{234}U/^{238}U$] initial	(95% CI)	Corr. Age	(95 % CI)
	µm	(ppb)	±	(activity)	±	(activity)	±	(y)	±	(corrected activity)	±	(y)	±
DC-12	14000	775.205	0.423	0.2914	0.0012	268.1	1.97	37150	144	1.011	0.00265	36749	157
	53000	260.535	0.167	0.3022	0.0014	490.8	2.85	39247	188	1.001	0.00268	39018	193
	84000	361.556	0.179	0.3204	0.0012	249.3	3.47	42057	161	1.003	0.00266	41580	184
	101000	395.051	0.346	0.3261	0.0014	1266.5	9.08	42500	193	1.012	0.00291	42405	193
	133000	624.802	0.287	0.3309	0.0013	2330.9	58.85	43036	162	1.017	0.00261	42984	161
	167000	301.034	0.189	0.3360	0.0015	792.0	8.45	44288	222	1.008	0.00278	44131	225
	193000	612.423	0.278	0.3395	0.0013	2653.8	73.63	44445	172	1.017	0.00264	44398	172
	215000	330.759	0.200	0.3532	0.0014	646.8	36.61	47030	208	1.010	0.00281	46829	209
	225000	537.128	0.292	0.3648	0.0014	480.2	5.79	48712	205	1.015	0.00285	48434	210
	228000	319.361	0.159	0.3762	0.0015	921.8	18.67	51000	217	1.009	0.00274	50849	217
	235000	224.135	0.121	0.4072	0.0017	1118.1	99.85	56845	275	1.004	0.00297	56710	275
	240000	375.274	0.214	0.4202	0.0022	514.2	3.19	57771	366	1.025	0.00277	57474	366
	256000	209.071	0.104	0.4249	0.0017	393.1	10.64	60592	291	0.997	0.00293	60188	300
	272000	262.337	0.163	0.4445	0.0019	1247.4	60.47	62470	328	1.022	0.00294	62341	327
	288000	338.949	0.155	0.4485	0.0018	1286.3	23.69	63165	300	1.023	0.00285	63038	300
	309000	535.343	0.257	0.4554	0.0018	1108.7	16.66	63539	281	1.036	0.00283	63392	282

Table 6.2: ^{230}Th dating results for sample AB-DC-12. Results from both samples are propagated with an initial $^{230}Th/^{232}Th$ activity ratio of 3.7±0.6.

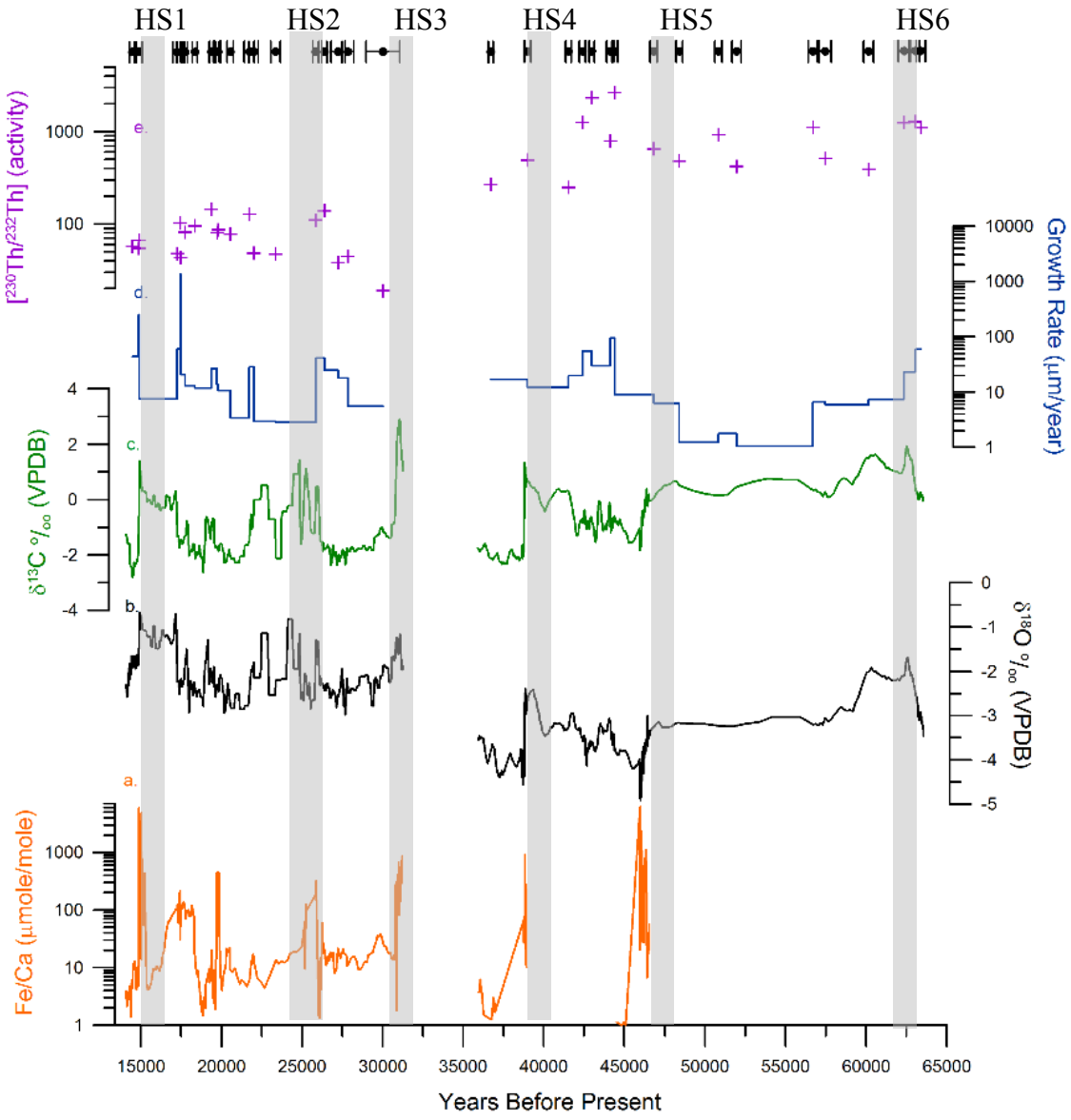

Figure 6.10: Geochemical results for samples AB-DC-09 (from ~14 to 32 ka BP) and AB-DC-12 (from ~36 to 65 ka BP), each sample plotted with its own age model. A) Fe/Ca ratio in orange shown for samples AB-DC-09 and AB-DC-12. Data are both at high and low resolution, with a 5 point running average, plotted on a logarithmic scale. B & C) Black line represents $\delta^{18}O$ values of the carbonate and green line represents $\delta^{13}C$ of the carbonate plotted with a 50 year interpolation forAB-DC-09 and a 5 point running average for sample AB-DC-12. D) Growth rate calculated using the U-Th ages from Table 6.1 shown in blue. E) $^{230}Th/^{232}Th$ activity ratio shown in purple. Grey bars represent the timing of Heinrich stadials (HS) 1-6.

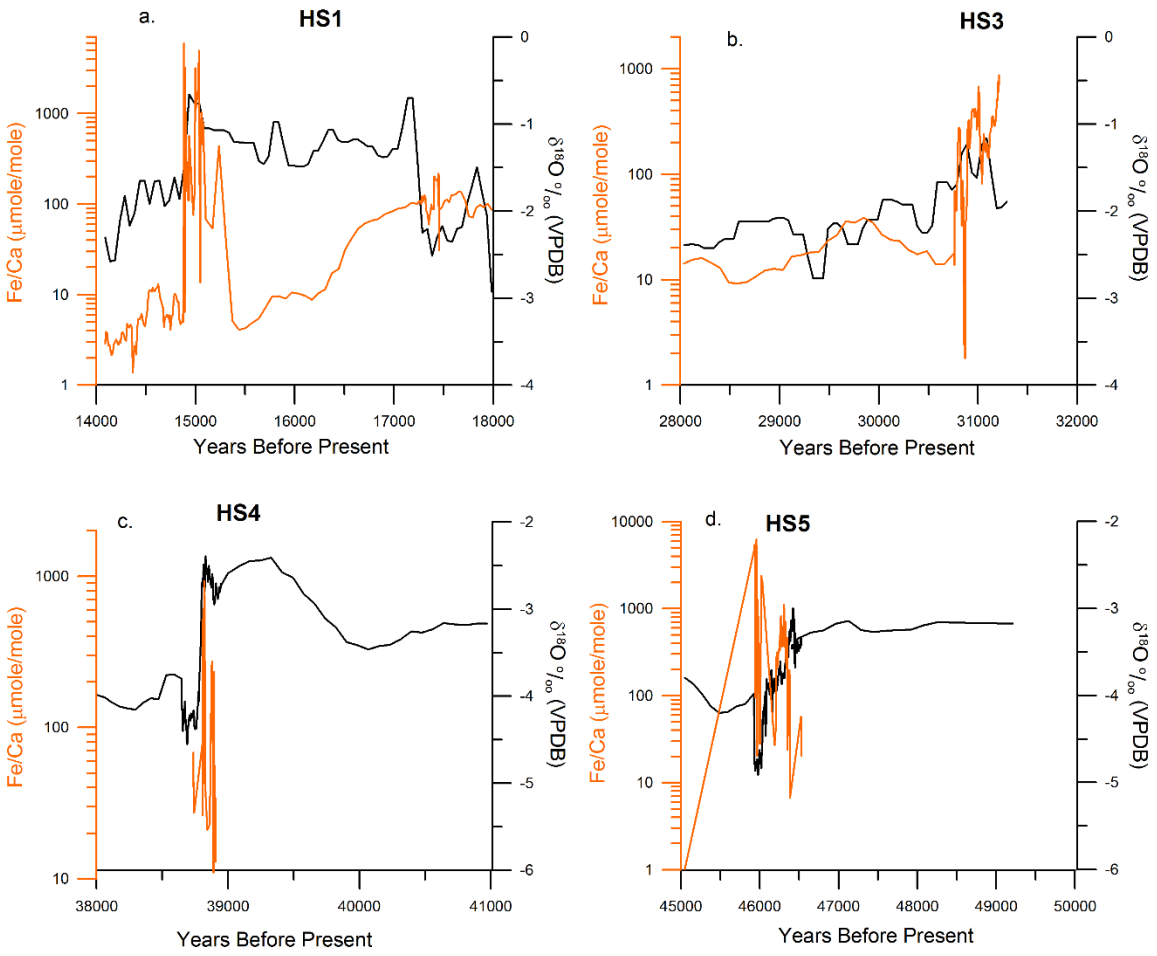

Figure 6.11: Expanded view of $\delta^{18}O$ and Fe/Ca data from Figure 6.8. a) Data from Heinrich stadial 1, showing elevated Fe/Ca from 14.8 to 15.0 ka before present. B) Data from Heinrich stadials 3, demonstrating elevated Fe/Ca from 31.3 to 31.0 ka BP, c) Increased at 38.8 ka BP, associated with Heinrich stadial 4 and d) increase Fe/Ca from 46.3 to 46.0 ka BP associated with Heinrich stadial 5. Both Fe/Ca and $\delta^{18}O$ are plotted with a 5 point running average. Fe is plotted on a logarithmic scale.

6.6. Discussion

6.6.1 Source of Iron

Considering the lack of local sources of iron, the iron must be allochthonous and derived from atmospheric dust deposited on the soil zone (Swart et al., 2014). As already described, the Bahamas annually receives dust from Africa associated with the seasonal

migration of the ITCZ. Once the dust is deposited on the soil surface, to mobilize the Fe in the dust, rainfall is necessary to leach the Fe or to transport colloidally bound Fe. Similar to the dust, rainfall in the Bahamas varies seasonally with the rainy season typically occurring from May to November. These observations are supported by results from a study of calcretes in Caicos Island. Similar to the Bahamas, Caicos Island (located to the south of the Bahamas) is geologically analogous, comprised of relatively pure carbonate with few contaminants. Caicos Island is characterized by red soils up to a meter thick with high levels of iron (~16000 ppm Fe), while the underlying host limestone contains very low concentrations of iron of about 100 ppm Fe (Rossinsky and Wanless, 1992). Considering that there are few local sources of iron in Caicos, the authors suggest the insoluble red calcrete soils on Caicos Island must have originated from aerosols from Africa (Rossinsky and Wanless, 1992). The authors also showed that the surface of the soil is directly affected by aerosol inputs and contains very high Fe concentrations, while Fe is not present 1.5 m into the limestone bedrock, supporting the importance of aerosol input (Rossinsky et al., 1992).

In the Bahamas, an additional source of iron may be recycled Fe from the soil as the soils have been shown to be derived from dust (Muhs et al., 2007). However, the soil layer in the Bahamas is thin in most areas and was also thin in the past (Muhs et al., 2007). The soil is therefore most likely not a significant contributor of Fe. Nonetheless in HBC the soil layer is more developed above this cave and therefore cannot be ruled out as a potential source of iron. The various factors driving aerosol inputs to stalagmites, as described above, are outlined and summarized in Figure 6.12.

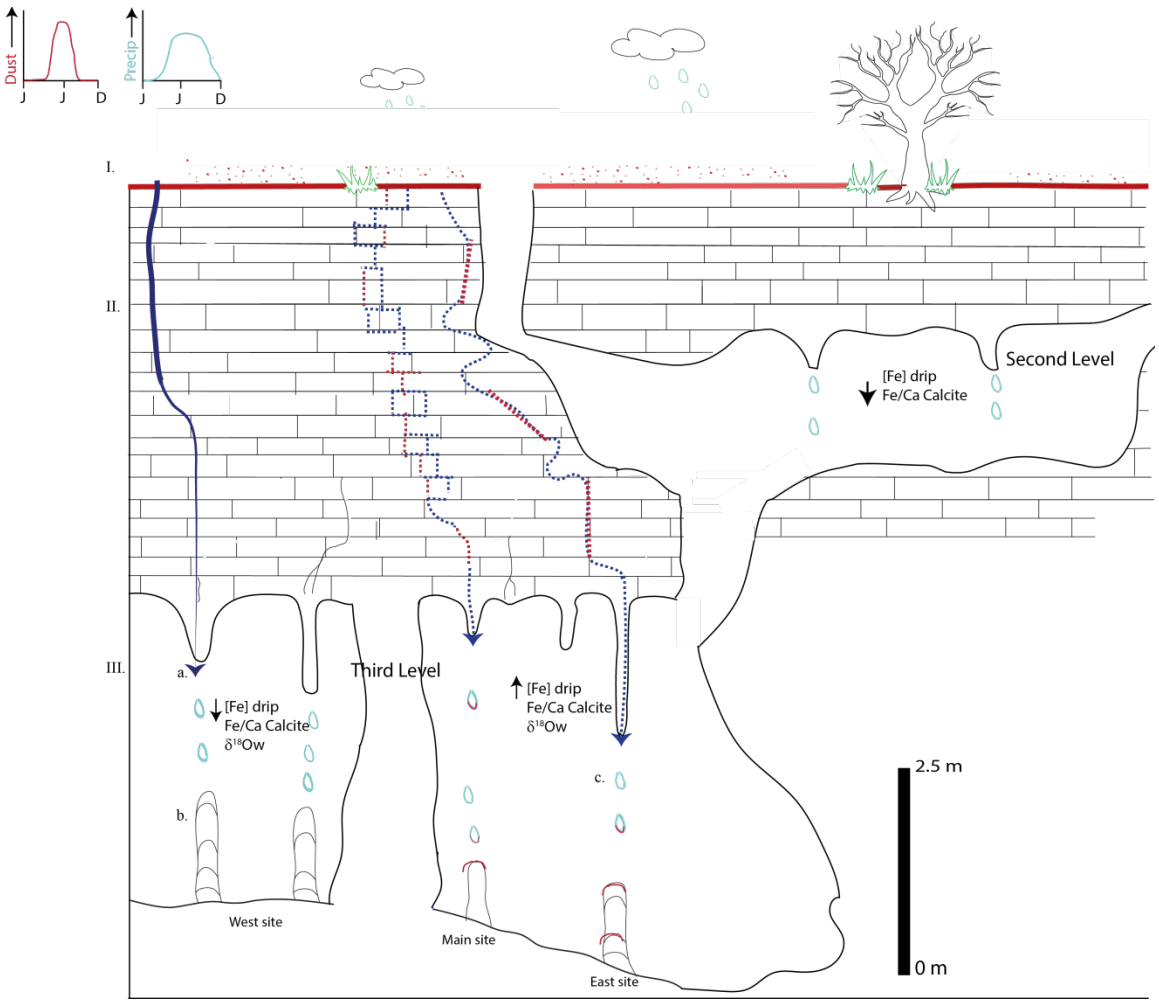

Figure 6.12: Model for the deposition of dust to the precipitation of Fe in the cave. I) Dust is deposited on the soil layer either through rain out and/or the settling of dust on the soil layer. From studies, it has been demonstrated that dust deposition to the Bahamas varies seasonally (Prospero and Lamb, 2003) as does precipitation (Baldini et al., 2007) (annual variations shown here are schematics). II) The rate of percolation of water through the soil zone and into the limestone bedrock varies by site. III) The water from precipitation flows rapidly through the limestone bed rock as shown in (a) leading to a lower residence time of the water in the soil zone or the bedrock, resulting in lower Fe concentrations in the precipitated calcite as shown in (b). Slower flow rates through the soil and bedrock as shown in (c) would lead to greater leaching of Fe into the drip waters and therefore more Fe deposited in the stalagmite (d). This is discussed in the text in section (6.6.2).This model is based on the assumption that the Fe is dissolved or colloidal in the drip water.

6.6.2 Modern samples

Drip waters:

In the modern samples, the highest concentrations of iron found in drip waters were during the wet summer months. The seasonality in the concentration of trace elements in the water is possibly driven both by the changes in dust deposition to the Bahamas (considering the greatest dust deposition in Miami and Barbados is found in June and July (Trapp et al., 2010)) and higher amounts of rainfall from May to November (the rainy season) in the Bahamas (Baldini et al., 2007) (Figure 6.12). Considering the samples were filtered prior to analysis, the water samples represent fine phase particulate and colloidal Fe.

Calcites:

Similar to the water results, the carbonate results demonstrate seasonal variation as well as heterogeneity within the cave. The slides deployed in June of 2012 and collected in August 2012 contain above average Fe/Ca ratios, reflecting the increased Fe observed in the drip waters of June 2012. Similarly, the slides deployed in August 2013 and removed in November of 2013 show an increased Fe/Ca ratio (Figure 6.8) reflecting the observed increase in Fe/Ca of the waters in August of 2013 (Figure 6.5). The periods of increased Fe/Ca (June – August) are coincident with the rainy season and dust deposition to the Bahamas. The rainfall allows for the leaching of Fe or the transport of collodially bounded Fe into the cave which is deposited with the calcite.

There is also observed heterogeneity in the Fe concentration within the cave, with the main room containing higher Fe/Ca ratios than the west room. Trace and minor element variations have also been observed within HBC, particularly for Mg and Sr

concentrations (Chapter 4). This spatial variation has been suggested to be driven by changes in the routing path or the residence time of the water in the overlying bedrock as modifications in the routing path of the water or the residence time may impact the incorporation of trace and minor elements into the drip water (Fairchild and Treble, 2009). In HBC, as demonstrated above and in Chapter 4, the Mg/Ca and Sr/Ca results show higher Mg/Ca and Sr/Ca ratios of the calcite precipitated in the main room compared to the west room (Figure 6.6). This is additionally supported by the results of the isotopic analysis of the drip waters. The west room drip waters on average consist of a $\delta^{18}O_{water}$ value 0.5 ‰ more depleted than the main room $\delta^{18}O_{water}$ value (Figure 6.7). The results from both elemental and isotopic analyses suggest that the waters feeding the main room undergo a longer residence time in the soil zone and the epikarst resulting in increased elemental concentrations. Variations in the residence time would primarily drive the incorporation of Fe leached from the dust, not the collodially bounded Fe.

The incorporation of Fe into the drip waters (hence calcite) may also vary with drip rate and drip path length. Variations in drip rate are primarily driven by residence time, which can potentially influence the incorporation of Fe into drip waters. Future work in HBC should also measure drip rate.

Finally, an additional source of Fe to the calcite may be aerosols. This spatial variability may also be driven by ventilation of the cave. As the cave ventilates, atmospheric air enters the cave which can carry with it aerosols. Additionally, the cave is accessible to the public, who may kick up dust in the cave, and additionally since the cave is ventilated, air flow through the cave can move particulates (Dredge et al., 2013).

One way to address if aerosols within the cave are a major contributor to Fe deposition is through the collection and monitoring of aerosols throughout the cave.

6.6.3 Ancient samples

From the ancient samples, increased Fe/Ca occurs synchronously with the changes in the $\delta^{18}O$ and $\delta^{13}C$ record. Previous studies support that the timing of the increased $\delta^{18}O$ and $\delta^{13}C$ values of the carbonate from both stalagmite samples (AB-DC-09 and -12) correlates well with the timing of Heinrich stadials (see Chapters 3 and 4). The paleoclimate interpretation of the $\delta^{18}O$ and $\delta^{13}C$ record have been previously discussed, but briefly, the geochemical results support the interpretation that increases in the $\delta^{18}O$ of the carbonate associated with Heinrich stadials are primarily driven by a temperature decrease associated with the events. The associated increase in the $\delta^{13}C$ record is thought to be driven by a likely combination of lower temperatures and higher aridity during Heinrich stadials and/or higher ventilation of the cave. The terminations of Heinrich stadials are characterized as periods of enhanced rainfall, higher temperatures and/or less ventilation as supported by lower carbon and oxygen isotopes of the carbonate. Paleoclimate records suggest that the abrupt terminations of Heinrich stadials are driven by resumption of the AMOC, leading to an increase in SSTs in the North Atlantic (McManus et al., 2004), and a northward shift of the ITCZ (Peterson et al., 2000) (Chapters 3 and 4). The paleoclimatic interpretations of the Bahamas records have been developed through isotopic analysis of the fluid inclusions and coupled trace element and stable isotopic analysis of the carbonate and are consistent with this scenario.

The high resolution data presented here demonstrate that the increase in iron is abrupt and occurs near the termination of the Heinrich events, not during the onset. This

was observed during Heinrich stadial 1 (Figure 6.11 a) which shows an increased Fe/Ca associated with the termination of the event at 14.9 ka BP and elevated Fe/Ca ratios persisting until 14.8 ka. Similar results are seen for HS 3 -5. Therefore, considering that the modern data suggest that precipitation amount is important for the leaching of Fe into the drip water; this mechanism is applicable to the past. Heinrich stadials are known to be dusty events (Jullien et al., 2007; McGee et al., 2013; Murphy et al., 2014). However, geochemical results suggest that Heinrich stadials are also dry in the Bahamas and therefore the leaching of soil Fe may not have been significant during the stadial itself. Therefore, the proposed process is 1) Heinrich stadials result in the deposition of dust to the soil layer, 2) the iron is leached out of the dust during increased rainfall events associated with the termination of the Heinrich stadial, and 3) the iron is deposited within the calcite (Baldini et al., 2007; Zhou et al., 2008). This supports both the timing and the rapid nature of the increased Fe/Ca ratio. It is important to note that while stadials may have been drier, there was still rain that could mobilize Fe as stalagmite growth continues during the stadials supports that there was clearly enough rain to supply carbonate precipitation inside the cave.

The growth rate of a speleothem is dependent on the drip rate, temperature, calcite saturation and pCO_2 of the cave (Banner et al., 2007; Oster et al., 2014) and therefore may be a good indicator of environmental conditions at the time of speleothem formation. Hence another possible explanation for the increase in iron associated with Heinrich stadials is a significant decrease in growth rate, allowing for the accumulation of iron on the stalagmite surface (Dredge et al., 2013). When comparing the Fe/Ca record with growth rate, there is minimal evidence of growth rate controlling the deposition of Fe for

either stalagmite (Figure 6.13 & 6.14). While the 25 ka and 62 ka events both demonstrate a decreased growth rate (Figure 6.10 d), these events consist of little to no change in the Fe/Ca ratio of the speleothem calcite (Figure 6.10 a). Therefore growth rate is not a significant driver of the increased Fe/Ca ratio, but rather it is possible the increased iron is driven by an increased supply (e.g. more dust and/or more rainfall).

The [$^{230}Th/^{232}Th$] ratio demonstrates that the ratio is larger for sample AB-DC-12, supporting a decreased detrital component to sample, when compared to sample AB-DC-09 (Figure 6.10 e). Additionally it is important to note that there is not a significant decrease in the [$^{230}Th/^{232}Th$] ratio associated with Heinrich stadials (Figure 6.10 e), with the possible exceptions of Heinrich stadial 1 and 3.

6.6.4 Comparison with other dust records

Numerous studies have suggested that Heinrich stadials are associated with increased dust deposition to Greenland, while the warm interstadials are represented by a reduction of atmospheric detrital dust (Fuhrer et al., 1999; McGee et al., 2010; Ruth et al., 2007). Ruth et al. (2007) demonstrated a relationship between NGRIP dust and China loess deposits, suggesting that dust increases in Greenland are driven by Asian aridity during Heinrich stadials (Figure 6.15 a). NGRIP dust concentration was calculated by Laser particle counter (Ruth et al., 2007). During Heinrich stadials, the Sahel region of Africa was drier and cooler as supported by paleoclimate records (Stager et al., 2011; Tjallingii et al., 2008) which may in turn have created more dust sources (Figure 6.15).

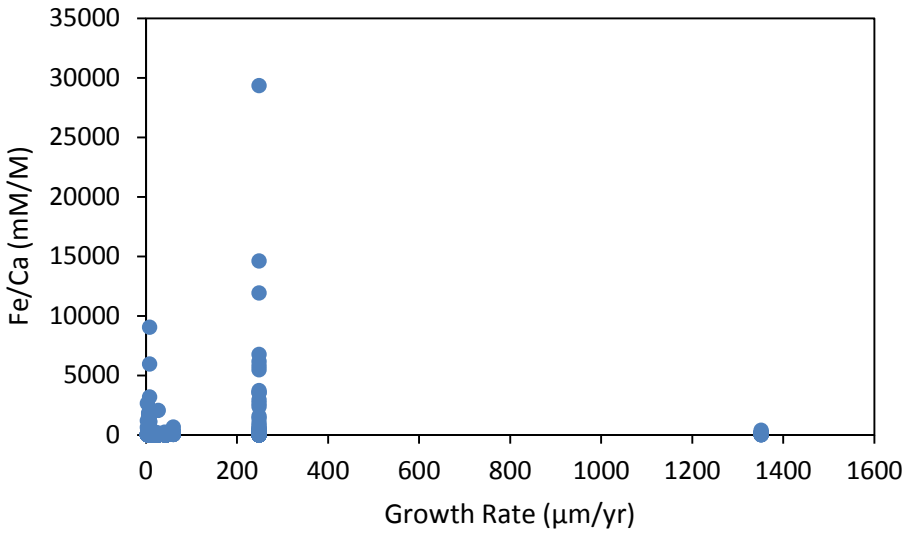

Figure 6.13: Growth rate versus Fe/Ca for sample AB-DC-09 demonstrating minimal relationship between growth rate and Fe/Ca ratio.

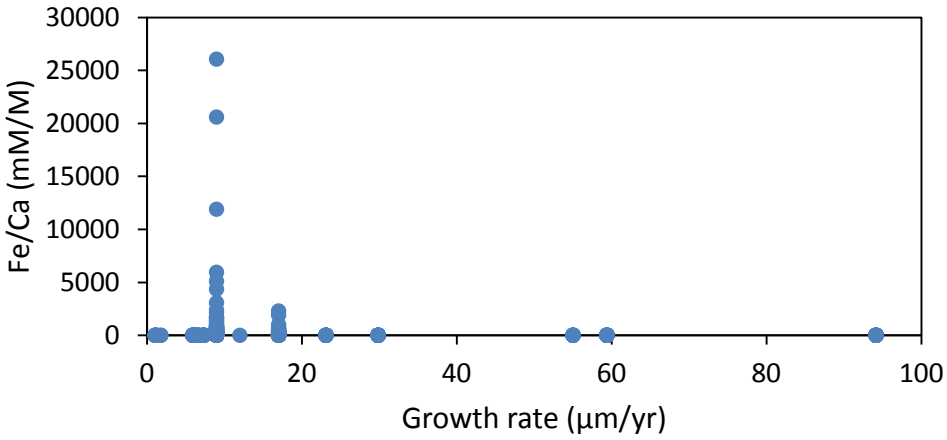

Figure 6.14: Growth rate versus Fe/Ca for sample AB-DC-12 demonstrating minimal relationship between growth rate and Fe/Ca ratio.

There is evidence from modeling studies that the AEJ was intensified during this period, potentially transporting more dust from western Africa to the eastern Atlantic Ocean (Just et al., 2012; Mulitza et al., 2008; Murphy et al., 2014) as increased dust deposition has been observed in the eastern Atlantic associated with Heinrich stadials (Jullien et al.,

2007; McGee et al., 2013; Mulitza et al., 2008). McGee et al. (2013) found a 2.6 factor increase in dust flux off the coast of Africa associated with Heinrich stadial 1 (Figure 6.15 b) and a sediment core from Mulitza et al. (2008) demonstrated increased atmospheric dust and a decrease in the contribution of sediment from the Senegal River during Heinrich stadials (Figure 6.15 c). These records from Africa and Greenland support increased aridity and atmospheric dust associated with Heinrich stadials and a similar timing to the increased Fe observed in the Bahamas (Figure 6.15 e).

The records from Africa and the Bahamas demonstrate variability in the climate and dust flux across Heinrich stadials 1-6. Variability in dust flux deposited on the soil layer above the cave between Heinrich stadials can be driven by changes in the dust source, intensity of the Heinrich event, wind speed and wind direction (McGee et al., 2010; Murphy et al., 2014). While changes in the dust record in the speleothem may also be influenced by changes in the amount of rainfall bringing iron into the cave. In the Bahamas records, Heinrich stadial 1 and 5 are characterized by the highest Fe/Ca ratio while Heinrich stadials 2 and 6 contain the lowest ratios. Tjallingii et al. (2008) also note variability in a humidity index, based on size fractions from a core from off the coast of west Africa and utilizing the relative proportions of each end member, changes in continental humidity and vegetation cover were determined; with Heinrich stadials 2, 3 and 4 having the least amount of change in the humidity index, which may lead to a decrease in the sources of dust. The record from Mulitza et al. (2008) also supports a reduced increase in dust delivery associated with Heinrich stadial 3. Both the Bahamas record and the records from Africa suggest that Heinrich stadial 1 is an extremely arid and a high dust event that appears to have been the strongest Heinrich aridity event in the

Northern Hemisphere tropics (Stager et al., 2011). It further is associated with an almost complete shutdown in the AMOC (McManus et al., 2004). In contrast, some studies suggest that Heinrich stadials 2 and 3 exhibited only a minimal change in the AMOC when compared to the change in AMOC across Heinrich stadials 1 and 4 – 6, possibly impacting the climatic response to these events (Lynch-Stieglitz et al., 2014; McManus et al., 2004). Additionally, the provenance of IRD layers deposited during Heinrich stadials 3 and 6 was different than the IRD sources for other Heinrich stadials of the last 65,000 years (Farmer et al., 2003; Hemming, 2004; Martins et al., 2013). These factors (i.e. AMOC and IRD source) may account for variability in dust across Heinrich stadials. An additional factor which may account for dust variability is the timing of the Heinrich stadials relative to other global climate events. For example, Heinrich stadials 4 and 5 occur during MIS 3, when sea-level was higher than during the other stadials, which may be an important factor for climate response.

6.6.5 Potential sources of dust

As demonstrated above, there is good agreement between evidence for aridity in western Africa, dust deposition to the Atlantic and increases in Fe in Bahamas speleothems during Heinrich stadials 1-6. Africa is known to be a source of dust to the Bahamas today, as supported by the modern day influx of dust from this region to

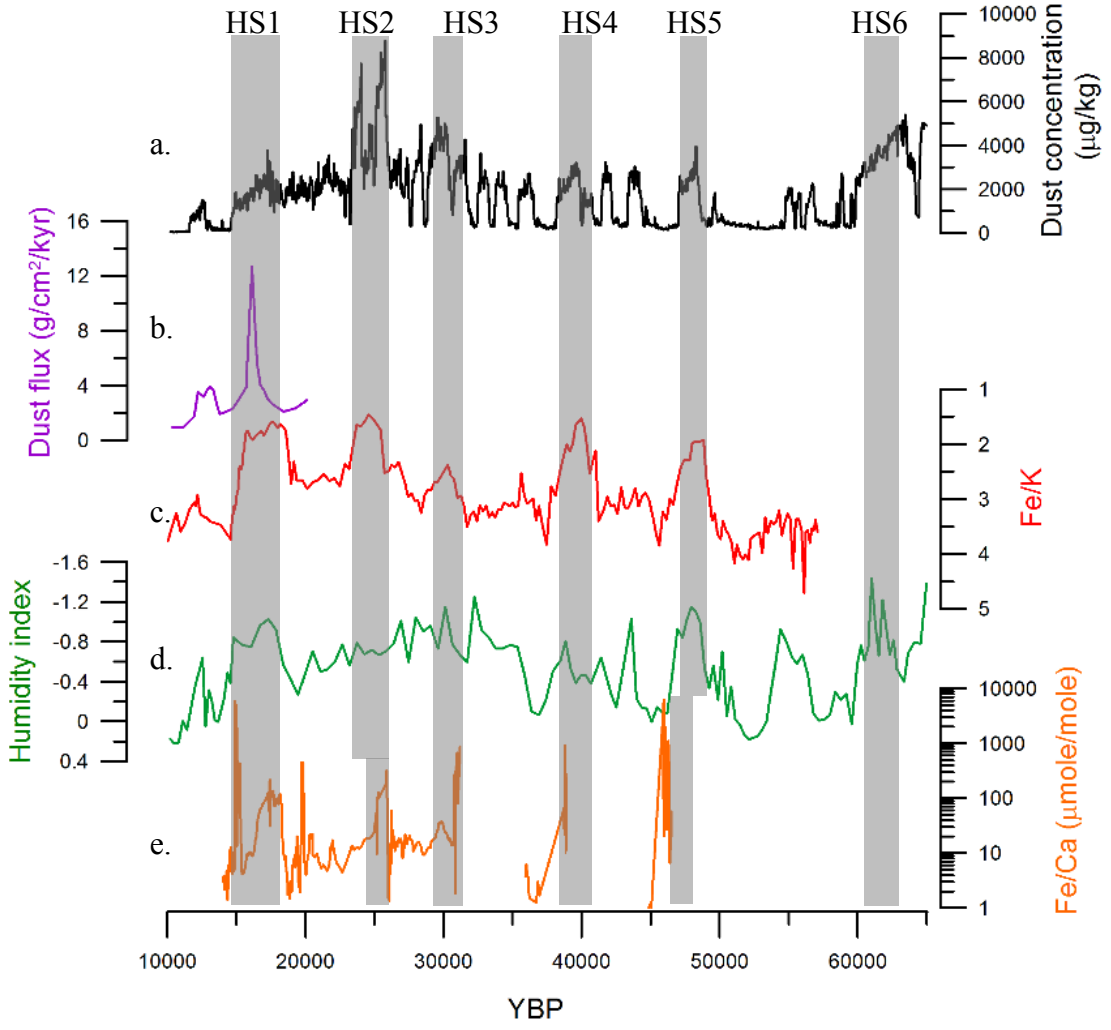

Figure 6.15: Northern Hemisphere records of dust. A) NGRIP record of dust concentration from laser particle results thought to be driven by Asian aridity associated with a reduction in the Asian monsoon. Data from Ruth et al. (2007). B) Dust flux record for off the coast of Western Africa from McGee et al. (2013). C) Core from off the coast of Senegal demonstrates decreases in Fe/K ratios associated with increased atmospheric deposition of dust (Mulitza et al., 2008). D) African continental humidity and vegetation cover were determined from core off the coast of Western Africa (Tjallingii et al., 2008). E) Fe/Ca record of dust from Bahamas speleothems plotted on a logarithmic scale. Grey bars represent the timing of Heinrich stadials (HS) 1-6.

Barbados and Florida and from soil studies (Muhs et al., 2007; Prospero and Lamb, 2003; Prospero et al., 2010). However, one modeling study predicts a southerly shift in the AEJ with consequent reduction in dust transport form Africa to the Bahamas during Heinrich stadials (Murphy et al., 2014) (Figure 6.16 a and b). This model also supports increased North American aridity leading to increased dust deposition to the east coast of North America, the Bahamas and the North Atlantic (Murphy et al., 2014). This suggests that during Heinrich stadials sources of dust to the Bahamas may have instead been the Mississippi River Valley loess deposits. There are several loess deposits in the Mississippi Valley from the LGM (Muhs, 2012) and studies have shown that mass accumulation rates of mid-continent loess during the LGM were an order of magnitude higher than in the Holocene (Bettis et al., 2003). However, it is unknown if these sources were greater during Heinrich stadials.

One tantalizing idea is that by conducting Sr isotopic measurements on the speleothem, a comparison of the Sr isotopic composition from within the Heinrich stadial and outside of the Heinrich stadial would shed light on the provenance of the dust. Studies have effectively determined the provenance of dust by analyzing for a unique geochemical "finger print" (Grousset and Biscaye, 2005). As a feasibility test, the $^{87}Sr/^{86}Sr$ variability has been utilized in speleothem studies for the identification of Sr source and source variability with time (Ayalon et al., 1999; Bar-Matthews et al., 1999; Frumkin and Stein, 2004; Goede et al., 1998; Li et al., 2005; Zhou et al., 2009) and periods of increased aridity (Banner et al., 1996). The $^{87}Sr/^{86}Sr$ isotopic values were measured within the Heinrich stadial and outside the Heinrich stadial of the calcite; however the $^{87}Sr/^{86}Sr$ results were invariant (Appendix E). In addition, the speleothem

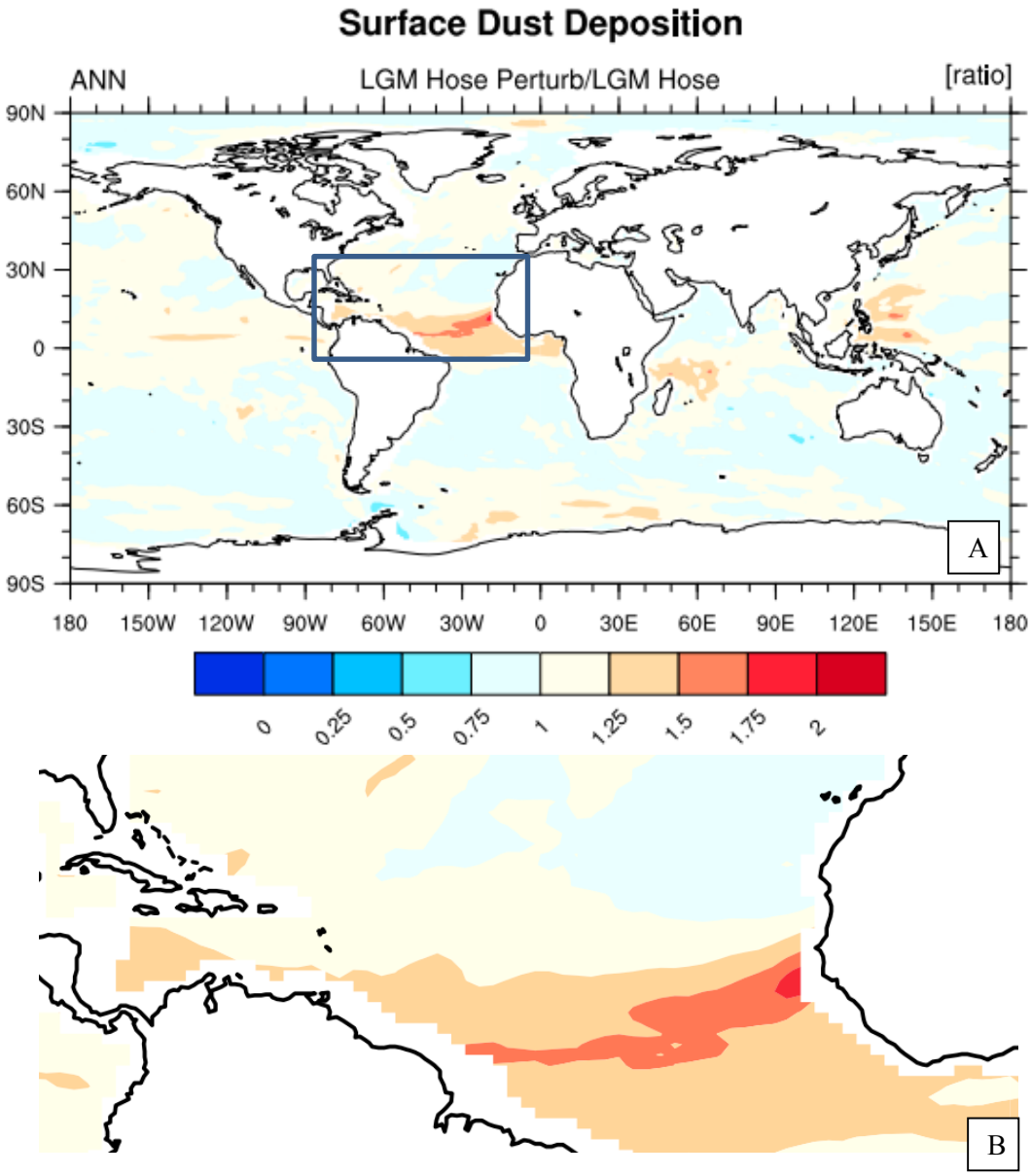

Figure 6.16: a) Modeling results from Murphy et al. (2014) demonstrating the flux of dust to the surface for Heinrich stadials compared to LGM dust flux. B) Close up of Western Africa and the Caribbean. Note the predicted southerly shift of the dust plume thought to be due to a southerly shifted AEJ.

$^{87}Sr/^{86}Sr$ isotopic values (0.70913 ±0.00003 (2σ)) are similar to published values of Bahamas bedrock $^{87}Sr/^{86}Sr$ values as limestones and dolomites from Abaco Island demonstrate an average $^{87}Sr/^{86}Sr$ value of 0.70909± 0.000010 (Vahrenkamp et al., 1991). The Sr isotopes of the stalagmite are representative of the bedrock possibly because the relatively large amount of Sr available in the bedrock. Unfortunately, this does not clarify the source of the increased Fe/Ca of the Bahamas stalagmite. Other potential analyses which can be conducted in the future include Nd and Pb isotopic ratios.

6.6.6 Climatic influence of atmospheric dust

The Bahamian stalagmite records clearly reveal that this isolated platform received significant amounts of dust during Heinrich stadials. Studies have shown that increases in atmospheric aerosols have impacted climate in the modern, therefore during dusty events, dust may have played a critical role in the climate system. Understanding the direct impacts of dust is inherently complicated as dust aerosols may both absorb and scatter incoming and outgoing radiation (Knippertz and Todd, 2012; Maher et al., 2010; Mahowald et al., 2010). Dust may also act as a cloud or ice nucleus, especially if the dust consists of feldspars, which have been shown to be a more effective ice nucleus (Atkinson et al., 2013; Maher et al., 2010). Dust deposition to the surface ocean may increase ocean primary productivity through the delivery of iron to high nitrate, low chlorophyll areas, potentially impacting atmospheric CO_2 concentrations (Maher et al., 2010; Martinez-Garcia et al., 2011; Martinez-Garcia et al., 2014).

During Heinrich stadials, observations and modeling studies support lower SSTs in the Northern Hemisphere (Chiang, 2009; Voelker, 2002; Zhang and Delworth, 2005). From a modeling study of a Heinrich stadial, it was found that atmospheric dust increases

the climate response to the Heinrich state (Murphy et al., 2014). Increased atmospheric dust was demonstrated to increase cooling in the North Atlantic SSTs and amplify aridity in Africa, the Arabian Sea and India (Murphy et al., 2014). The dust-climate feedback on a high-albedo surface, such as ice, is still not well understood (Maher et al., 2010). A study of the radiative effects of mineral dust in the high latitudes during LGM conditions demonstrates increased dust leads to decreased radiative forcings and amplification of surface cooling (Lambert et al., 2013). This is due to dust creating a cooling in the lower troposphere. Recent studies have demonstrated the importance of light absorbing aerosols, primarily black carbon, as significant contributors to warming in the Arctic (Hegg et al., 2010). The deposition of light absorbing aerosols on ice sheets can lead to a reduction of surface albedo and warming of temperatures which is critical if future anthropogenic black carbon emissions increase (Lee et al., 2013). Future work focused on dust variability in the atmosphere in the present and the past is important for the determination of climate-dust feedbacks, impacts on the global climate and predictions for future climate (Lambert et al., 2013; Lee et al., 2013; Mahowald et al., 2010).

6.7 Conclusion

Today the Bahamas seasonally receives dust from Africa. This study demonstrates modern dust delivery to the cave and has shown that in the past, there were increases in the amount of dust delivered to the Bahamas during Heinrich stadials.

To summarize the findings, in the modern, results support temporal and spatial variability in the concentration of Fe within the cave. The temporal variability is thought to be driven both by annual changes in the amount of available dust Fe and the amount of precipitation. The variability between sites within the cave is driven by variations in flow

rates in the epikarst and soil zone as supported by other geochemical tools. The transport of the iron from the dust to the cave is dependent on the amount of precipitation to leach the iron and/or the transport of the colloid-bound Fe.

From the ancient stalagmites, the Fe/Ca ratios are found to increase concurrently with changes in oxygen and carbon isotopes. An increased Fe/Ca ratio is associated with Heinrich stadials and is thought to be driven by the leaching of Fe from the dust. From the high resolution data, the increased Fe/Ca ratios are associated with the Heinrich stadial termination, suggesting that increased Fe/Ca may be the result of an increase in precipitation associated with the end of the Heinrich stadial. The washing of Fe rich waters into the cave leads to an increase of iron at the termination. The increase in dust to the Bahamas across Heinrich stadials is shown to be in good agreement with the timing of other Heinrich stadial dust records from Africa and Greenland. Additionally, variability in dust records between Heinrich stadials may provide insights into the relative strength of each event. This study is the first study to demonstrate increased dust deposition to the Bahamas associated with Heinrich stadials. It supports the view that Heinrich stadials are dusty events; given the importance of dust to the climate system, further studies should consider the climatic feedbacks of atmospheric dust.

Chapter 7

Review of millennial scale climate variability

Summary

In this chapter, an overview of recent paleoclimate data will be utilized to provide a review of the timing and nature of millennial scale climate and driving mechanisms. When possible, the hitherto unpublished Bahamian records will be compared to published data. The discussion of paleoclimate proxies will be followed by a review of the mechanisms driving Dansgaard/Oeschger and Heinrich stadials and the global propagation of these events.

7.1 Background

Global climate variations at the millennial scale are dominated by Dansgaard/Oeschger (D/O) cycles and Heinrich stadial events (Denniston et al., 2007; Fletcher et al., 2010; Jiménez-Moreno et al., 2010; Jouzel et al., 2007; Siddall et al., 2010). Over the last 100,000 years, there have been 25 D/O cycles and 6 Heinrich stadials (Figure 7.1). This chapter will primarily focus on these Heinrich stadials and D/O cycles and the climatic expression in various regions of the world. However a brief review of older events will be included in section 7.4. Several previous studies have reviewed the paleoclimate and mechanisms associated with millennial scale climate (Alley et al., 1999; Chiang, 2009; Clement and Peterson, 2008; Seager and Battisti, 2007; Voelker, 2002), therefore this study will primarily focus on recently published archives. This study is by no means a complete review of paleoclimate reconstructions for millennial scale climate variability; rather the goal is to shed light on questions which remain.

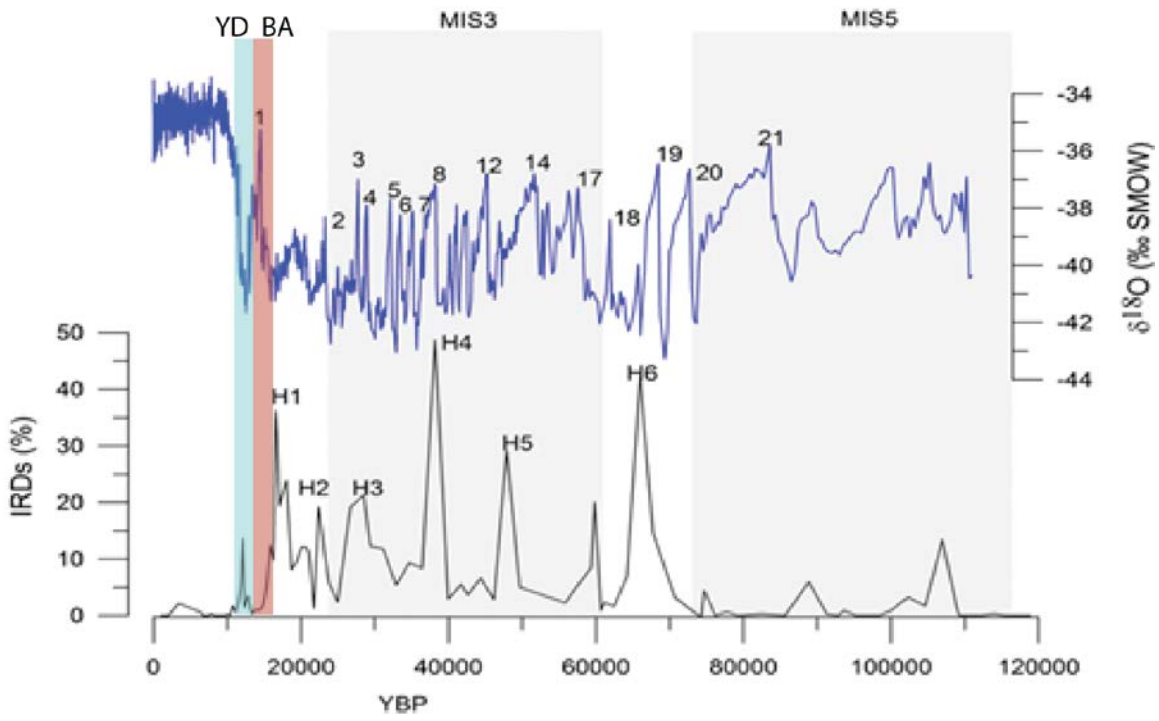

Figure 7.1: High latitude records of millennial scale climate variations. $\delta^{18}O$ of ice core record from GISPII (blue) from Grootes et al. (1993). Numbers represent interstadial (warm) D/O events. Ice rafted debris (IRDs) as represented by the percent of sediment detrital grains larger than 150 µm from ODP site 980 from McManus (1999). Heinrich events are labeled as H1- 6. One issue with using the percent detrital sediment grains is that this index is not sensitive to a change in mean sedimentation rate, which may change with overturning (McManus, 1999). Grey bars represent marine isotope stages 3 and 5. Also shown are the Younger Dryas (YD) and Bolling-Allerod (BA) events.

7.2 Northern Hemisphere Records of Heinrich and D/O Events

7.2.1 High latitudes

The D/O interstadials are best recorded in the Greenland ice cores as periods of warming within a few decades, with temperature shifts up to 10-16 °C (Figure 7.1). This warming is followed by a gradual return to cooler temperatures until the next warming cycle (Capron et al., 2010; Dansgaard et al., 1984; Dansgaard et al., 1993) (Figure 7.1). Although the $\delta^{18}O$ of water in ice cores is utilized as a proxy for temperature, there is

some evidence that seasonal distribution of precipitation and atmospheric processes may cause oxygen isotopes to be driven by other processes (Wolff et al., 2010). Other proxies such as the $\delta^{15}N$ of trapped N_2 can also be utilized to support increased temperature across D/O cycles (Capron et al., 2010; Guillevic et al., 2013). There is additional evidence that D/O events 8 – 10 in eastern Greenland exhibit the greatest temperature increases (Guillevic et al., 2013; Wolff et al., 2010).

In addition to warming, there are several other environmental factors which change in response to millennial scale climate events in the high latitudes. Methane concentrations increase in the ice cores of Greenland during interstadials and decrease during stadial events (Wolff et al., 2010). Records demonstrate nearly synchronous increases of methane in both Greenland and Antarctic ice cores supporting rapid interhemispheric atmospheric response (Blunier and Brook, 2001; Wolff et al., 2010). Ruth et al. (2007) demonstrated a relationship between NGRIP dust and China loess deposits, suggesting that dust increases in Greenland are driven by Asian aridity during Heinrich stadials (HS).

The clearest record of Heinrich stadial (HS) events is in sediment cores from the North Atlantic (Figure 1). Cold (stadial) events are associated with the southerly extension of ice and an increase in freshwater discharge in to the North Atlantic (Broecker et al., 1985; McManus et al., 2004). Heinrich stadials are characterized in the North Atlantic by cold periods, and are recognized in the sedimentary record as eroded terrigenous materials (Ice Rafted Debris IRD) deposited in the North Atlantic by ice

bergs upon melting (Bond et al., 1997; Heinrich, 1988).

Not only are there records of a decrease in temperature and collapse of ice sheets associated with Heinrich stadials, but there is additional evidence in the North Atlantic for changes in oceanic circulation. With the introduction of melt water to the surface of the North Atlantic, decreasing the sea surface salinity of the North Atlantic leads to a reduction of the Atlantic meridional overturning circulation (AMOC) (McManus et al., 2004)(Figure 7.2). This was well supported by McManus et al. (2004) in which $^{231}Pa/^{230}Th$ was utilized as a proxy for the AMOC from a North Atlantic sediment core. As demonstrated in figure 7.2, the shutdown of the AMOC into HS 1 was not abrupt; rather it slowed over about 1,000 years which has implications for the forcing mechanism. Similar results were found off the Iberian margin by Gherardi et al. (2005), however the $^{231}Pa/^{230}Th$ of sediments from the Bermuda Rise may not reflect AMOC reconstructions alone as it was determined that biogenic silica and $^{231}Pa/^{230}Th$ were highly correlated and therefore may reflect an upwelling signal and not a proxy for overturning at this location (Lippold et al., 2009).

As regards the origins of D/O cycles, there are conflicting interpretations from the North Atlantic. There is some evidence from sediment cores of IRDs associated with D/O interstadials, with peak iceberg calving associated with stadials (Broecker et al., 1985; Bond et al., 1997; Menviel et al., 2014). This possibly suggests an associated AMOC variation associated with D/O cycles, driven by iceberg calving (Menviel et al., 2014).

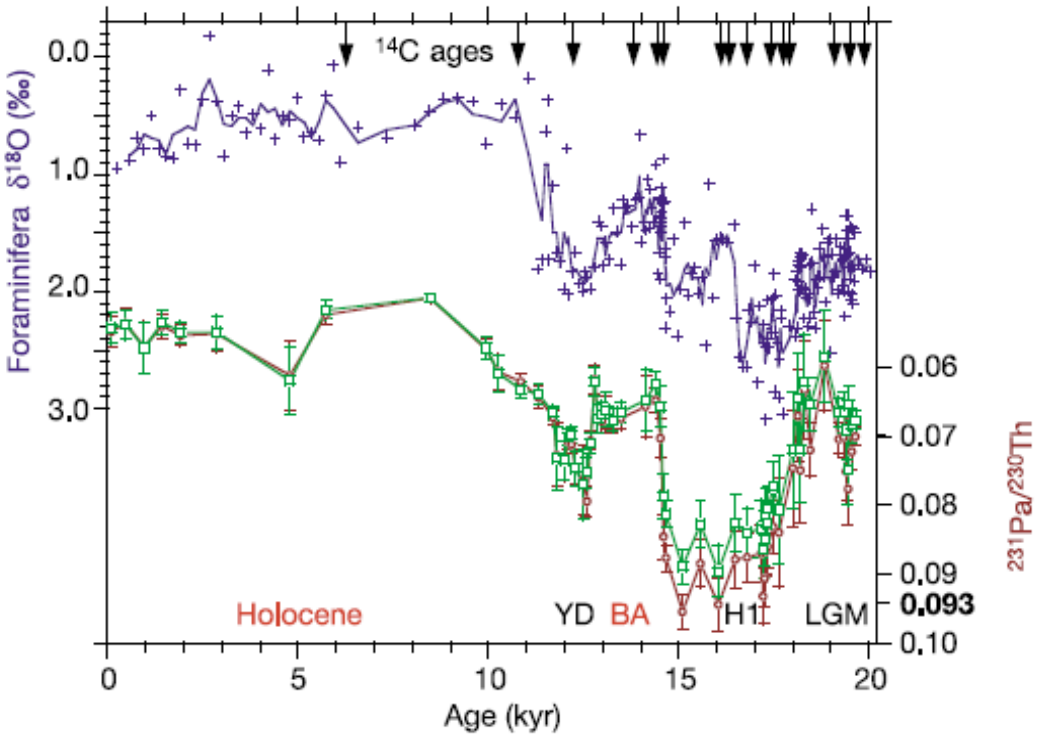

Figure 7.2: North Atlantic AMOC reconstruction from McManus et al. (2004). $\delta^{18}O$ of foraminifera from sediment core OCE326 from Bermuda Rise used to reconstruct the deglacial stratigraphy (blue). This is compared with the sedimentary $^{231}Pa/^{230}Th$ from GGC5 in red and green. The red values are calculated by subtracting the ^{230}Th and ^{231}Pa estimated from the measured ^{238}U activity; the green values are calculated by subtracting the ^{230}Th and ^{231}Pa estimated from the measured ^{232}Th activity. YD indicated Younger Dryas, BA indicates the Bolling Allerod, H1 indicates Heinrich event 1, LGM indicates the Last Glacial Maximum. The highest $^{231}Pa/^{230}Th$ values are reached during H1, supporting a nearly complete shutdown of overturning at this time.

7.2.2 Mid-latitudes

The climate responses across the mid-latitudes for HS are varied, with most records supporting increased aridity and decreased temperatures. Studies from the mid-latitudes include paleoclimate studies in Europe (Couchoud et al., 2009; Genty et al., 2003; Moreno et al., 2010a) and the United States (Asmerom et al., 2010; McGee et al., 2012) to list a few. Overall, Heinrich stadials are associated with a colder Europe and wetter southwestern United States.

Europe:

Several millennial scale studies have been conducted on sediment cores from off the Iberian Margin and cave records from France. The marine records support decreased sea surface temperatures (SSTs) associated with Heinrich stadials (Moreno et al., 2010a) and are supported by terrestrial lake records (Moreno et al., 2010b), speleothem records from France (Genty et al., 2003; Genty et al., 2010) and a lake record from the Balkans (Panagiotopoulos et al., 2014). Sea surface temperature decreases during HS range between 5-10 ºC across the Iberian Margin (Martrat et al., 2007; Patton et al., 2011) and similar results were found in the Alboran Sea (northern Morocco), across the Straits of Gibraltar (Cacho et al., 1999). The decreased SSTs during HS events in this region are thought to be driven by the influx of cold surface water to the Mediterranean, due to a reduction in AMOC.

In contrast to the findings during stadials, the D/O interstadials are periods of increased humidity (Moreno et al., 2010a), up to a 10°C increase in temperature in the Mediterranean (Genty et al., 2010) and a shift to more C_3 plants versus C_4 plants and hence a wetter climate (Fleitmann et al., 2009).

Contrary to the results from Western Europe, a speleothem record from eastern Turkey reveals increased aridity associated with stadials and increased humidity during interstadials (Rowe et al., 2012). This is supported by a lake low stand at 15,000 yr BP also possibly suggesting increased aridity associated with HS 1, however a higher dating resolution is necessary (Landmann and Reimer, 1996). Rowe et al. (2012) proposed that increased aridity during stadials in northeastern Turkey was driven by a reduction in the export of winter moisture from the Mediterranean.

Further to the south several speleothem stable C and O isotopic studies conducted from Soreq Cave and Peqiin Cave (Israel) reflect a decrease in precipitation associated with Heinrich stadials (Bar-Matthews et al., 2003; Bar-Matthews et al., 1997). A more recent, high resolution ion microprobe and confocal laser fluorescent microscope imaging study of a Soreq Cave speleothem supports decreased temperatures, decreased seasonal rainfall and changes in the vegetation type during HS1 (Orland et al., 2012). These changes are thought to be driven by southerly shifted westerlies leading to an overall decreased rainfall (Orland et al., 2012).

United States:

In the United States (US), variability to the response to millennial scale climate events is observed with the west coast of the US exhibiting a decrease in temperatures and an increase in precipitation (Hendy and Kennett, 2000; Oster et al., 2014). In the southwestern United States, modern precipitation is in part driven by the North American monsoon (NAM) however this does not appear to be a significant driver at the millennial scale. Periods of increased precipitation have been observed in records of Heinrich stadials from the southwest of the US (Asmerom et al., 2010; McGee et al., 2012; Wagner et al., 2010) and as far east as Alabama (Lambert, 2010), while interstadials have been shown to be periods of increased aridity (Wagner et al., 2010) (Figure 7.3). However, not all studies agree, with some studies suggesting increased aridity associated HS events in the southwest of the US (Benson et al., 2011). This suggests that western US may not be a significant dust source during stadial events.

Increased precipitation to the west coast of the US is thought to be driven by increased storms associated with a strengthened Aleutian Low (Hendy and Kennett, 2000; Oster et

al., 2014). While the mechanisms driving the climate response in the southwestern United States is primarily attributed to the strengthening of the subtropical jet and storm track (McGee et al., 2012), and southerly shift in the jet stream which may bring increased winter precipitation from the Pacific Ocean (Asmerom et al., 2010; Wagner et al., 2010). Conversely, periods of warming are associated with a weakening Aleutian low, northward storm track and hence reduced precipitation (Wagner et al., 2010).

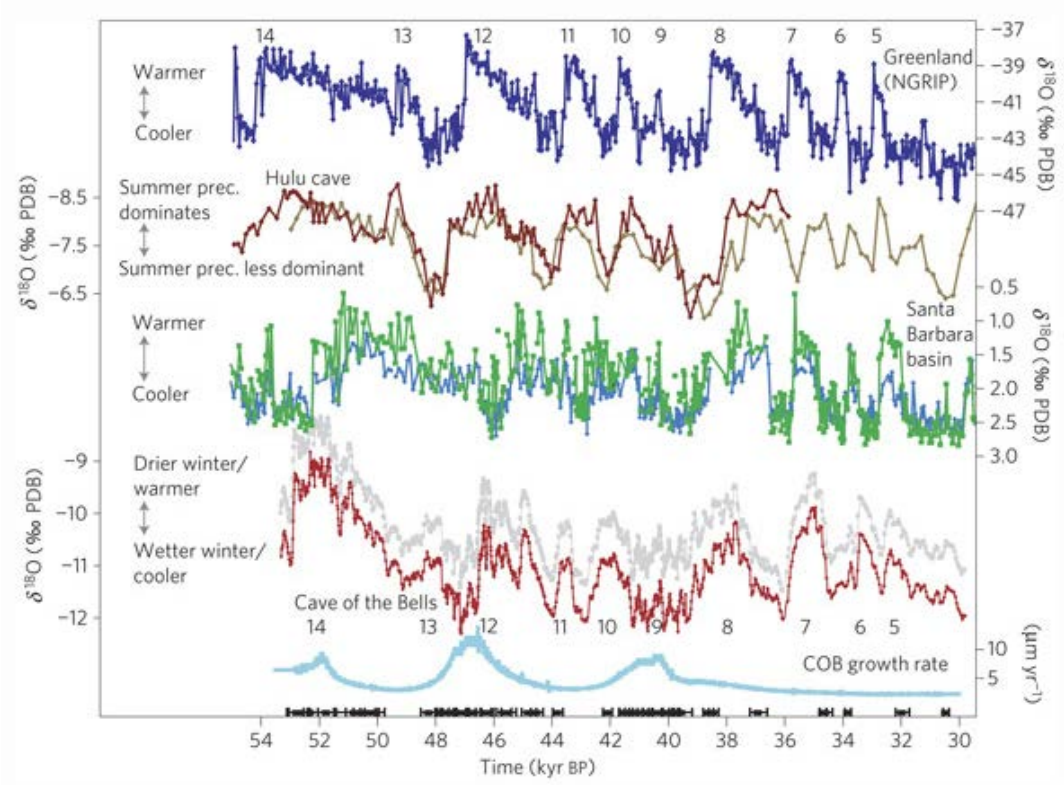

Figure 7.3: Figure from Wagner et al. (2010) demonstrating the relationship between oxygen isotopes from a speleothem from Arizona (red) and Santa Barbra Basin oxygen isotopes (green and blue) (Hendy and Kennett, 2000), Hulu cave oxygen isotopes from China (brown) (Wang et al., 2001) and NGRP ice core oxygen isotopes (dark blue) (Svensson et al., 2008). These records demonstrate the increased aridity in Arizona associated with D/O interstadials and warmer temperatures in Santa Barbara Basin.

7.2.3 Subtropics and tropics

Similar to the findings from the mid-latitudes, many tropical records reflect increased aridity and cooling associated with Heinrich stadials in the Northern Hemisphere. Conversely, D/O interstadial periods are typically associated with a warmer and wetter climate.

Western Atlantic:

Records from Western Atlantic provide evidence for both increased aridity associated with stadials and decreasing temperatures. Decreasing temperature is observed from an alkenone-derived SST record from the Bermuda rise during stadials, with increasing temperatures during interstadials (Sachs and Lehman, 1999). Further south, increased aridity and decreased temperatures are observed during stadials from speleothem records from the Bahamas (this study) and a lake record from Guatemala (Escobar et al., 2012; Hodell et al., 2012). While some records from this region solely suggest increased aridity during stadials, including a record in southwestern Mexico (driven by a reduction in the NAM) and Cariaco Basin (driven by a southerly shifted ITCZ) (Lachniet et al., 2013; Peterson et al., 2000) (Figure 7.4). These observations are also supported by records from the Caribbean Sea, with increased salinity driven by a reduction in the AMOC or a reduction in rainfall (Schmidt et al., 2004). Records from the Straits of Florida support decreased northerly flow during Heinrich stadials due to reduction in AMOC (Lynch-Stieglitz et al., 2014).

Interestingly, not all the D/O cycles are found in the stalagmite geochemistry from the Bahamas and some stalagmites do not exhibit any geochemical change associated with D/O cycles (discussed in Chapter 4). In addition, two stalagmites (AB-DC-14 and AB-

DC-16) were analyzed for $\delta^{13}C$ and $\delta^{18}O$ of the carbonate and did not exhibit any geochemical change associated with Heinrich stadials possibly suggesting that some events are not captured in the speleothem geochemistry (see appendix E).

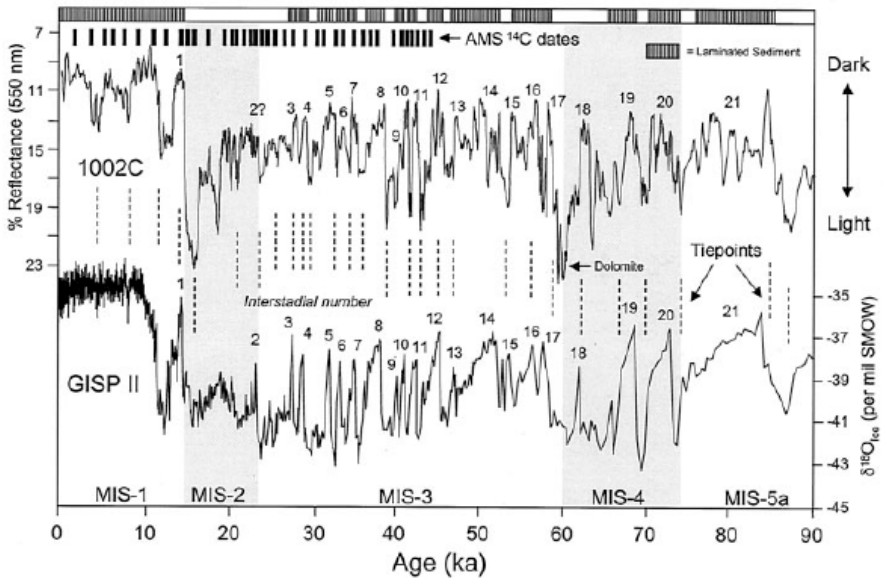

Figure 7.4: Color reflectance of Cariaco Basin sediment core. Darker lamina found during warmer periods and light color sediments found during colder stadials. The Cariaco basin data is compared to $\delta^{18}O$ from GISPII ice core. Numbers represent interstadial D/O events, with marine isotope stages also labeled. Figure from Peterson et al. (2000).

Africa:

In the modern, equatorial eastern Africa is primarily semi-arid; however the ITCZ migrates across this region leading to periods of variable precipitation modulated by the Indian Ocean and the El Nino phenomenon (Tierney et al., 2011). Western sub-Saharan Africa exhibits a more monsoonal like climate driven by the movement of the ITCZ.

In a recent study by Stager et al. (2011) paleoclimate records from Africa and Asia demonstrated that subtropical/tropical Africa and Asia is characterized by decreasing precipitation associated with HS 1 (Figure 7.5). Associated with such increased aridity in

Africa are records of increased atmospheric dust emission from western Africa (See Chapter 6) (McGee et al., 2013; Multiza et al., 2008). Further evidence of increased aridity for Western Africa is present in relic sand dunes and indicates that the Sahel-Sahara boundary reached it most southerly position during HS 1-5 (Collins et al., 2013). Off the coast of West Africa, results from a sediment core supports a reduction in glacial North Atlantic intermediate water during HS 1 (Meckler et al., 2013) possibly driven by the reduction in AMOC.

What are the mechanisms driving the widespread aridity associated with HS 1 in tropical Africa? Stager et al. (2011) proposed that the widespread aridity cannot be solely attributed to the southerly shifted ITCZ, but aridity may be enhanced as a result of reduced SSTs in the Atlantic and in the Indian Ocean. A recent modeling study of the ITCZ demonstrates the mean ITCZ shift during HS1 is likely less than 1 º latitude supporting that the regional response in Africa may not be solely due to a shifted ITCZ, but rather a response to different forcing mechanisms (McGee et al., 2014). One interesting point is that the widespread aridity observed in the paleoclimate records has been difficult to reconstruct in models (Murphy et al., 2014).

Asia:

Climate variation of the subtropical/tropical region of the Asian continent today is dominated by monsoonal systems including both the Indian and Asian monsoons. During HS events, there is significant evidence that the monsoonal systems weakened. Sediment cores from the Arabian Sea exhibit lighter colored, bioturbated intervals during HS 1 through HS 6, while dark organic carbon rich layers were deposited during interstadials. However, the mechanism driving these sedimentological changes is not

clear. Some authors attribute these to changes in the Indian monsoon, with decreasing Indian monsoon during stadials (Schulz et al., 1998; von Rad et al., 1999), while others have suggested that AMOC reduction during HS may be driving the observed productivity changes, as a reduced AMOC leads to a reduction in the productivity of the Arabian Sea (Deplazes et al., 2014). Studies from this location also suggest increased fluvial sediments during interstadials from the Indus River, which in turn increased nutrient availability (Deplazes et al., 2013; Deplazes et al., 2014). Stadial sediments also are characterized by a larger aeolian fraction due to increased aridity and increased northwesterlies (Deplazes et al., 2014; Pourmand et al., 2004).

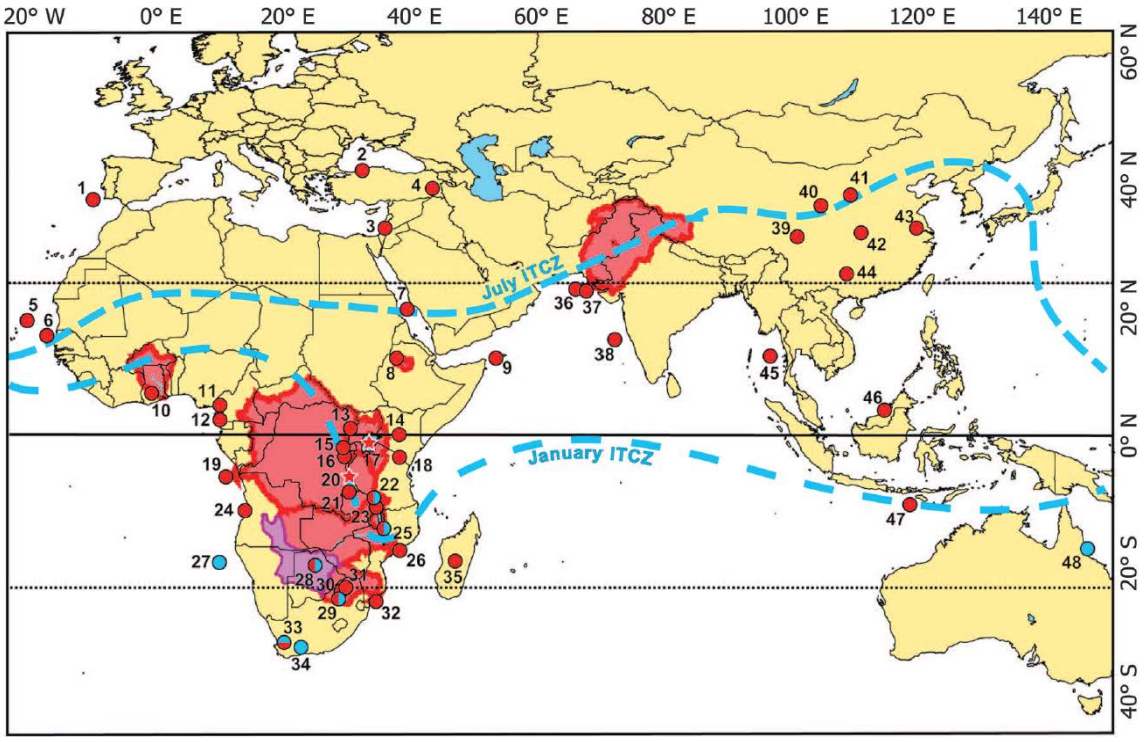

Figure 7.5: Widespread tropical aridity for Africa and Asia associated with Heinrich stadial 1. These records were compiled by Stager et al. (2011) and demonstrate the significant aridity associated with HS1 for this region.

Several studies have been conducted on speleothems from China, as this area is influenced both by the Indian and East Asian monsoons. The southwest of China is characterized as a transition zone between the East Asian Monsoon and Indian Summer Monsoon, while more northerly Hulu and Sanbao Caves are dominated by the East Asian Monsoon (Zhao et al., 2010)(Figure 7.6). Good agreement was found between northern and southern Chinese speleothem records across millennial scale climate events, suggesting both monsoonal systems are responding similarly to these events with a decrease in the monsoons during stadials and an increase during interstadials (Cai et al., 2006; Wang et al., 2001; Zhao et al., 2010). Isotope records from speleothems from China also support changes in the monsoon associated with summer insolation at 65 °N (Wang et al., 2008).

Using an isotope enabled model, Pausata et al. (2011) modeled changes in the $\delta^{18}O$ of precipitation during Heinrich stadials in India and China. Pausata et al. (2011) suggest that during stadials, precipitation changes in Asia are primarily driven by changes in the Indian Summer Monsoon, rather than changes in the East Asian Monsoon and the speleothem records from China reflect these changes. A study analyzing the drivers of Holocene $\delta^{18}O$ increases from speleothems from across China also found the drivers of speleothem $\delta^{18}O$ values to be primarily changes in the summer rainfall source and not a change in the amount of rainfall (Maher and Thompson, 2012).

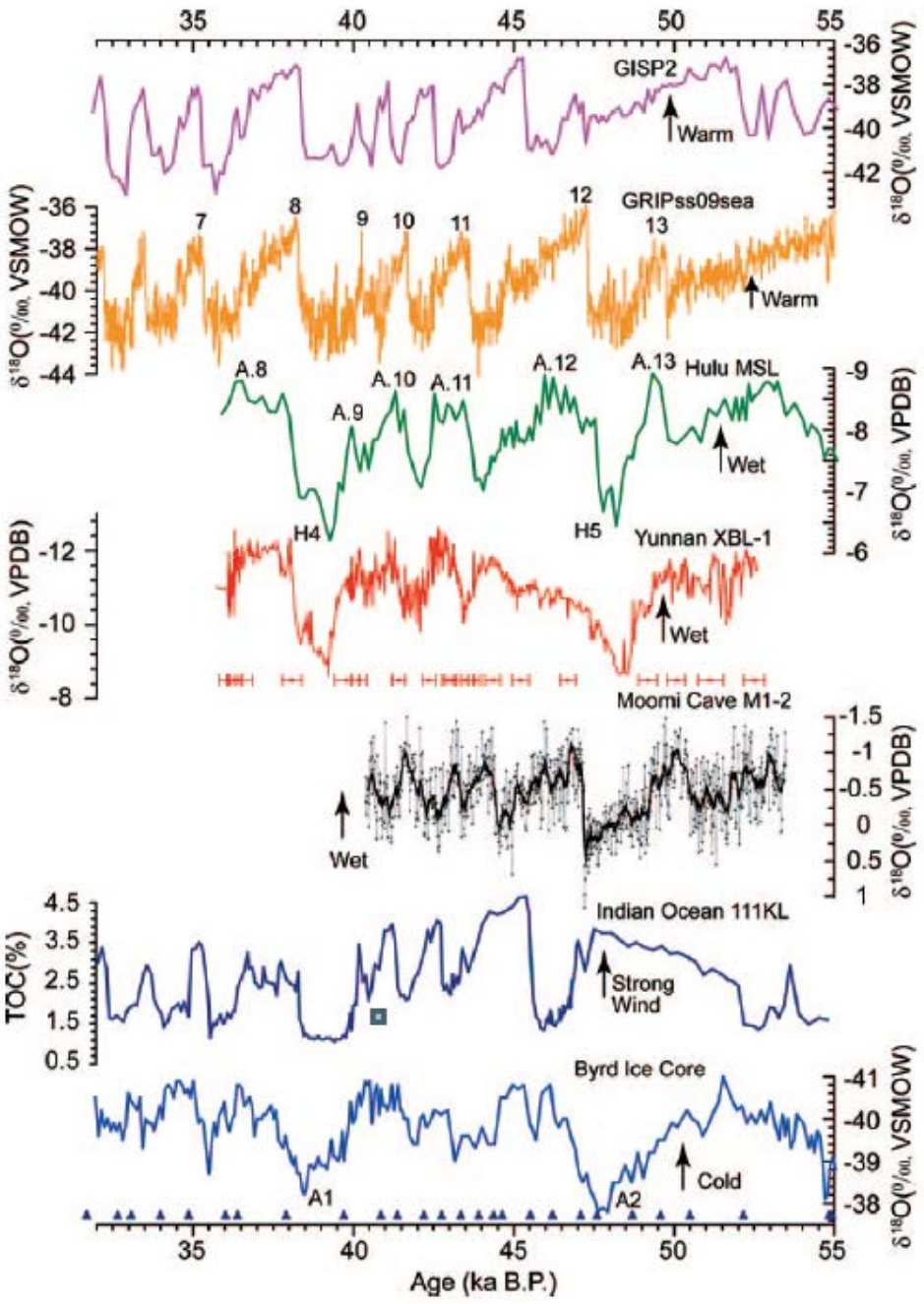

Figure 7.6: Paleoclimate records from China compared to other global climate records. Figure is from Cai et al. (2006). In pink is the GISP2 ice core oxygen isotope record, orange is ice core oxygen isotopes from GRIP plotted using the time scale from Johnsen et al. (2001). Green is the Hulu cave stalagmite record from Wang et al. 2001, and red is a stalagmite oxygen isotope record from Cai et al. 2006 (both from China). Black is oxygen isotope record from the Indian Ocean stalagmite from Socotra Island (Burns et al., 2003). Dark blue is total organic carbon from Indian Ocean sediment core from Schulz et al. (1998) and the lighter blue is oxygen isotopes from Byrd ice core from Antarctica (Blunier and Brook, 2001).

Pacific:

In the Pacific, the ITCZ is situated over northern Borneo year round with minimal annual variation. Several studies have been conducted from speleothems from Borneo and records from this location support a decrease in precipitation associated with HS (Carolin et al., 2013; Partin et al., 2007) and minimal geochemical response across D/O cycles (Carolin et al., 2013). Additionally the records support a precessional (21 ka) insolation forcing (Carolin et al., 2013; Partin et al., 2007).

From the tropical eastern Indian Ocean located to the west of the Borneo records, results from geochemical analysis of foraminifera support drier conditions across HS 1 (Mohtadi et al., 2014). This is supported by longer records from sediment cores from the west coast of Sumatra, Indonesia (Russell et al., 2014), a speleothem record from West Flores, Indonesia (Lewis et al., 2011) and reduced precipitation in the eastern Indian Ocean is supported by increased sea surface salinity from sediment cores (Gibbons et al., 2014). Mechanisms which have been proposed for the resulting climatic response include sea surface cooling driving precipitation decrease, decrease in Indo-Austral Summer Monsoon (IASM) intensity due to ITCZ migration or the changes in ocean fronts (Mohtadi et al., 2014), and a reorganization of Hadley circulation (Gibbons et al., 2014; Mohtadi et al., 2014). These findings are well summarized in Mohtadi et al. (2014) and Denniston et al. (2013b).

7.3 Southern Hemisphere

The climatic response across millennial scale climate events in the Southern Hemisphere is often expressed as periods of increased precipitation and temperatures during stadials, with decreased precipitation during interstadials.

7.3.1 Tropics

The South American summer monsoon (SASM) is primarily driven by seasonal migration in the ITCZ. During the Northern Hemisphere winter, the ITCZ is shifted further south over Brazil, and easterly winds transport moisture across from the Amazon Basin (Kanner et al., 2012). During the Northern Hemisphere summer, the ITCZ shifts further north, bringing rains to northern South America.

Stalagmites from the Peruvian Andes support intensified SASM across Heinrich stadials while D/O interstadials are characterized by a reduction in precipitation amount (Kanner et al., 2012) (Figure 7.7). Several records from Brazil also exhibit similar changes across Heinrich and D/O cycles, supporting good coherence in the climatic response to HS (Cheng et al., 2013; Cruz et al., 2009; Kanner et al., 2012; Mosblech et al., 2012)(Figure 7.7).The increased SASM is primarily thought to be driven by a southward shift in the mean position of the ITCZ, possibly due to the strengthening in Hadley cell circulation and decreased SSTs (Cheng et al., 2013; Cheng et al., 2012).

Studies have demonstrated an anti-phase relationship over the last precession cycle between eastern/northeastern Brazil and western/southern Brazil, contrary to the good agreement during millennial scale climate events (Cheng et al., 2013; Mosblech et al., 2012). Eastern/northeastern Brazil records demonstrate an antiphased relationship with insolation due to high insolation intensifying the SASM leading to increased precipitation in south/west of Brazil and decreased precipitation in the east/north (Cheng et al., 2013).

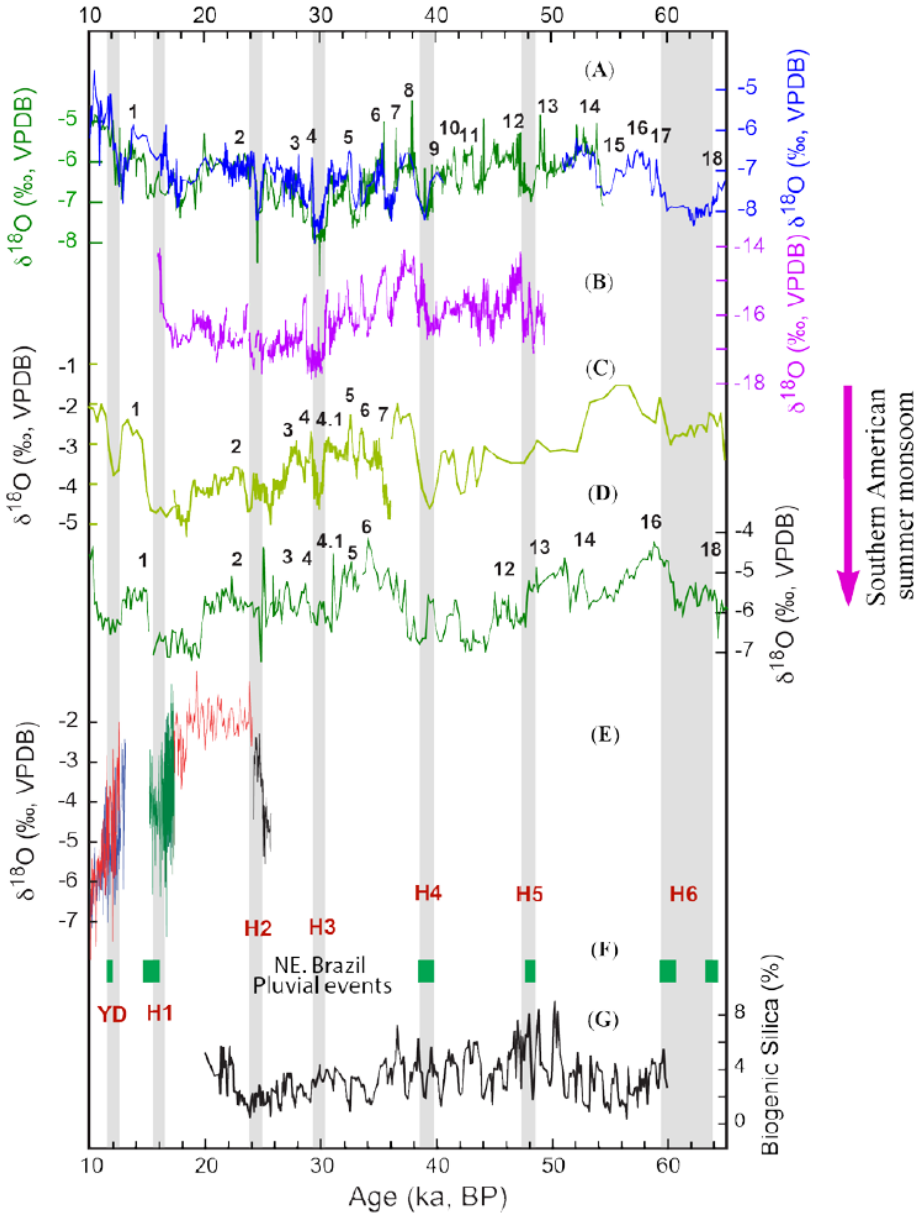

Figure 7.7: Paleoclimate record compilation of the last 65,000 years from South America. This figure is a supplementary figure from Cheng et al. (2013). A) Western Amazon oxygen isotope record from NAR cave and ELC cave, Brazil (Blue and green respectively) from (Cheng et al., 2013). B) Oxygen isotope record from Pacupahuian cave from the Peruvian Andes (Kanner et al., 2012). C) Oxygen isotope records from Southern Brazil Botuverá cave (Wang et al., 2007). D) Santana cave oxygen isotope record from southeastern Brazil (Cruz et al., 2006). E) Rio Grande do Norte cave oxygen isotope record northeastern Brazil (Cruz et al., 2009). F) Northeastern Brazil pluvial records (Wang et al., 2004a). G) Lake Titicaca southern Peru biogenic silica (%) as a proxy for runoff (Fritz et al., 2010). Vertical grey bars are Heinrich stadials and Younger Dryas (YD) and numbers are D/O interstadials events.

Pacific:

In the Southern Hemisphere Pacific, there is evidence for increased Indo-Australian Summer Monsoon (IASM) associated with HS (Ayliffe et al., 2013) from southern Indonesia and from Western Australia (Denniston et al., 2013b) (Figure 7.8). The record from northwestern Australia provides evidence of a weakened IASM during D/O interstadials (Denniston et al., 2013b), however the U-Th dating is not at a resolution which can exactly determine the timing of the D/O interstadials in this record. Further south in Western Australia there is evidence for minimal geochemical changes across HS 2, suggesting that HS 2 was not a significant event (Denniston et al., 2013a). The increased IASM during stadials is thought to be due to a steepening north-south interhemispheric gradient driving a southward shift of the IASM during stadials (Ayliffe et al., 2013) and additionally stadials are thought to exhibit increased tropical cyclone activity (Denniston et al., 2013a).

7.3.2 Mid to high latitudes

Antarctic cores preserve much longer records (to 800,000 years before present) than the Greenland ice cores providing a long record of millennial and orbital scale climate (Jouzel et al., 2007). For every Greenland interstadial, there is a corresponding Antarctic event. Antarctica exhibits cooling during Greenland interstadials and warming during Greenland stadials, however the magnitude of change is much smaller in Antarctica (Blunier and Brook, 2001; Jouzel et al., 2007; Wolff et al., 2010) (Figure 7.9). Additionally the response to millennial scale climate events varies by location on Antarctica, with the Atlantic sector exhibiting a much more rapid temperature rise than those found in the Indian/Pacific ocean sector (Buiron et al., 2012). With the recently

acquired WAIS ice core, results will aid in the understanding of such differences (Buiron et al., 2012).

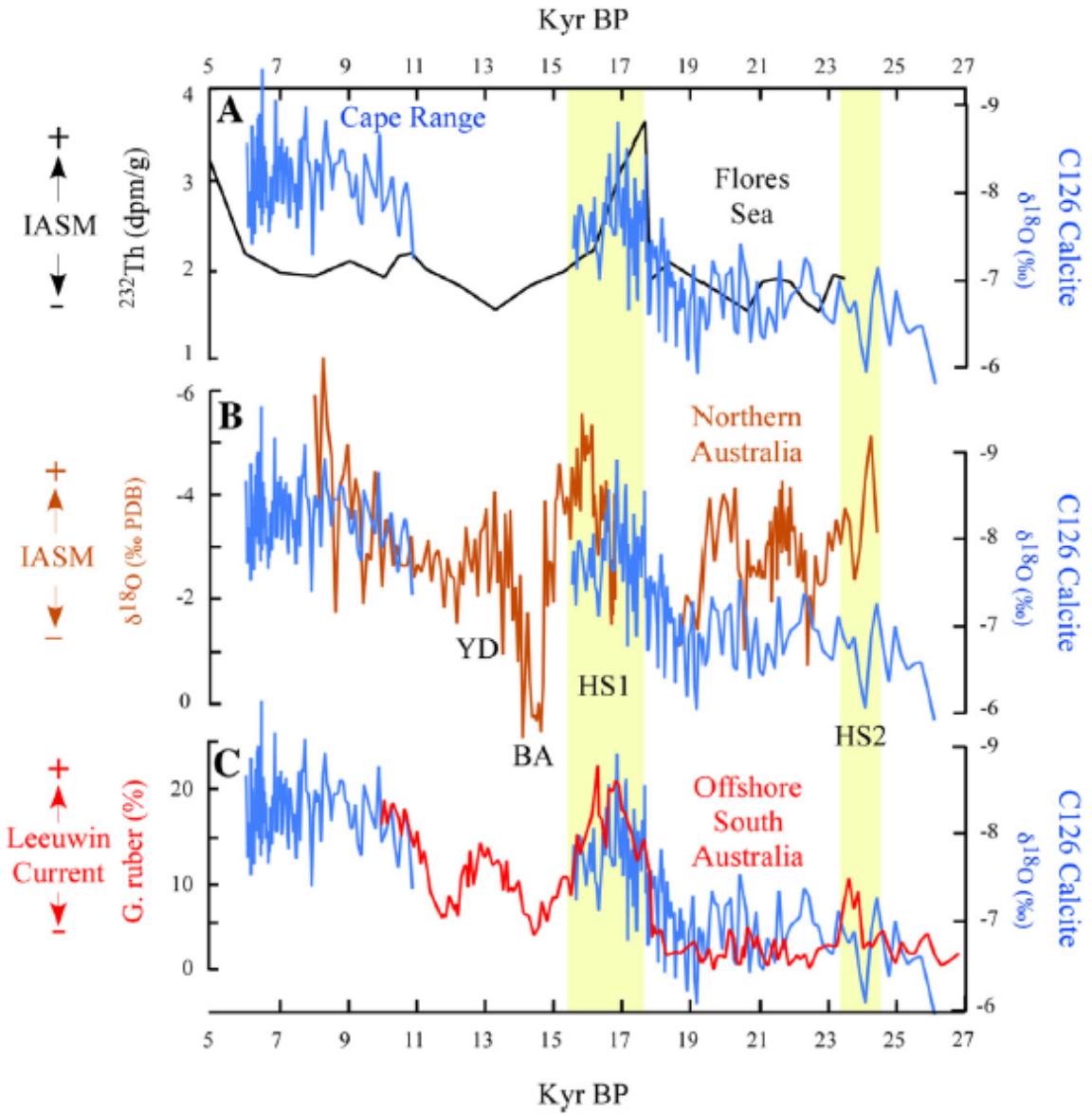

Figure 7.8: comparison of the record from (Denniston et al., 2013a) from coastal Western Australia in blue to records from Flores Sea (black) (a) from (Muller et al., 2012). The Flores Sea record is from a sediment core which supports increased precipitation associated with Heinrich stadial 1 (Muller et al., 2012). (b) Red is a record from Northern Australia (Denniston et al., 2013b) demonstrating an increased IASM associated with Heinrich stadial 1 and 2. Figure (c) red is from (De Deckker et al., 2012) from offshore Western Australia, supports increased Leeuwin Current during Heinrich stadial 1 and 2.

Two sediment cores from the Weddell Sea support eight periods of increased IRD deposition during the past 20 ka BP, derived from Antarctica (Weber et al., 2014). The IRD deposits exhibit a pacing similar to the observations from the North Atlantic, suggesting the Antarctic ice sheet also exhibited similar abrupt ice-sheet instability (Weber et al., 2014).

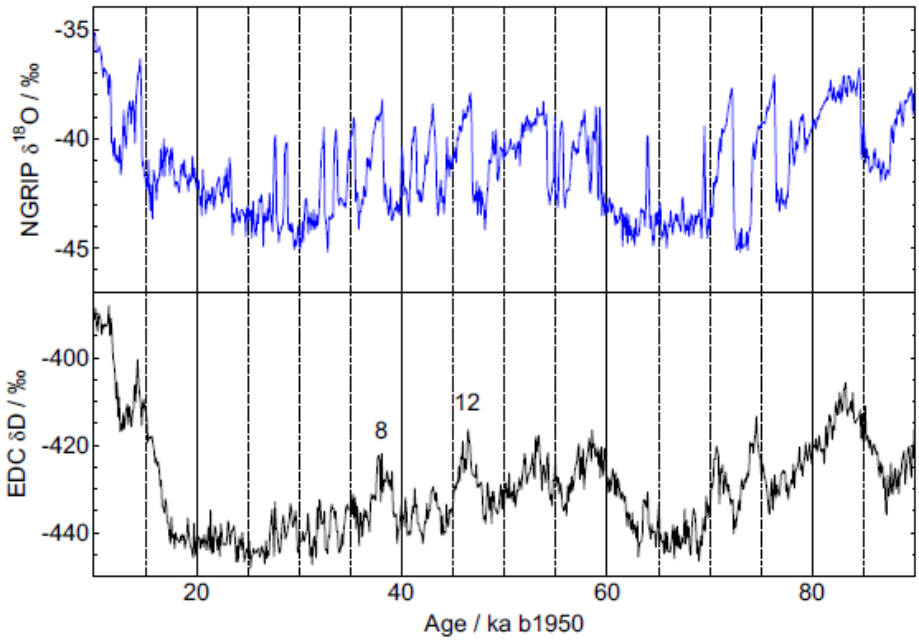

Figure 7.9: Oxygen isotopes from NGRIP ice core (Greenland) compared with Deuterium isotopes from Epica Dome C. The numbers indicate D/O cycle 8 and 12 which are two very large interstadials in the ice core records. This figure from Wolff et al. (2010) demonstrates the good agreement in the timing of events between the two hemispheres.

7.4 Evidence of Heinrich Stadials beyond Last 100,000 Years

Evidence of sub-orbital millennial scale climate variability has been identified well beyond the last 100,000 years and has been demonstrated to be a pervasive feature of the climate state over longer periods of times (Johnsen et al., 2001; Jouzel et al., 2007; McManus, 1999; Weirauch et al., 2008). Sedimentary records demonstrate that climate instability is the norm rather than the exception in both high latitude and low latitude

records (Gibson and Peterson, 2014; McManus, 1999). McManus (1999) demonstrated fewer IRDs during interglacial periods in the North Atlantic and those IRDs are associated with benthic $\delta^{18}O$ values greater than +3.5 ‰, suggesting that a minimum amount of ice is required. A molybdenum record from Cariaco basin (proxy for anoxic conditions) also supports that millennial scale climate variations are persistent over the last 600,000 years, although this record does not suggest a minimum ice sheet size is required (Gibson and Peterson, 2014). This record suggests that either a non-Laurentide ice sheet melt water source or glacial sea-ice extent may drive millennial scale climate variations, however questions still remain about the forcing mechanisms, particularly during periods of minimal ice sheet volume (Gibson and Peterson, 2014). Potentially, developing records from the subtropical Bahamas may aid in the understanding of millennial scale climate variations during older glacial periods, in particular if older samples forming from above water caves can be acquired, these samples may provide information on millennial scale climate variations in the subtropical Atlantic during interglacials.

Two older stalagmite samples from the Bahamas have been analyzed. One sample, AB-DC-07 was dated at 367,880 yr BP (Figures 7.10 and 7.11). Only one age date was acquired and more are necessary, however preliminary C and O isotopes suggest possible millennial scale variations (Figure 7.10). Sample AB-DC-08 was dated at 231,660, 249,470 and 258,820 yr BP and may support increases in C and O isotopes associated with the IRD deposit at 241,000 yr BP (Figure 7.11). Future work focusing on establishing a reliable age model for these samples may be of interest.

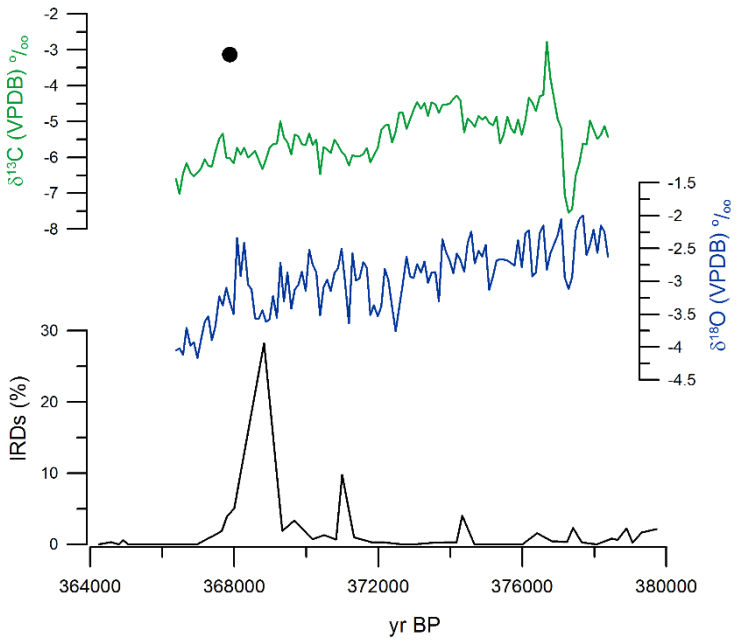

Figure 7.10: Sample AB-DC-07 collected from Abaco Island Bahamas was found to be forming from 366 to 378 ka BP assuming a 10 µm/yr growth rate. One U-Th age has been acquired from Anton Eisenhaur at GEOMAR. Age was calculated assuming a $^{230}Th/^{232}Th$ activity ratio of 0.6 ± 0.2. Shown in black are results from (McManus, 1999) demonstrating increased IRD deposits at 368,000 yr BP.

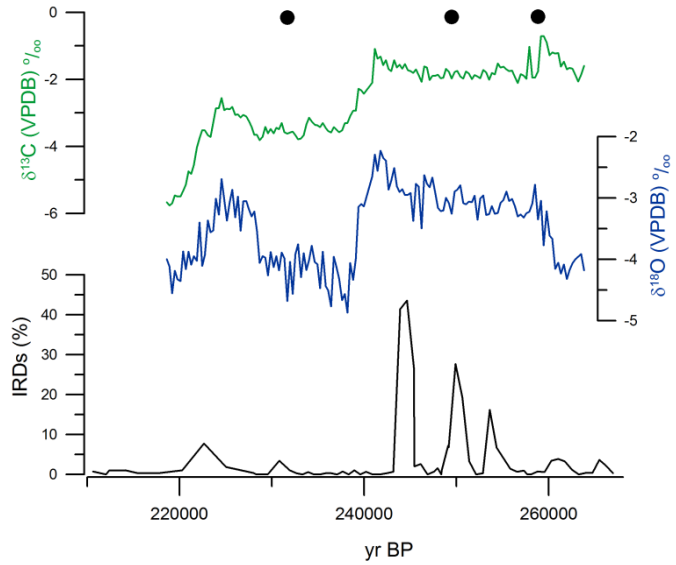

Figure 7.11: Sample AB-DC-08 collected from Abaco Island Bahamas was found to be forming from 218 to 264 ka BP using three U-Th ages acquired from Anton Eisenhaur at GEOMAR. Ages were calculated assuming a $^{230}Th/^{232}Th$ activity ratio of 0.6 ± 0.2. The black line are results from (McManus, 1999) demonstrating increased IRD deposits from 240,000 yr BP to 255,000 yr BP.

7.5 Forcing of Millennial Scale Climate

Critical to understanding subtropical climate during Heinrich events and Bond cycles is the forcing mechanisms of these events. Several forcing mechanisms have been proposed including, but not limited to: freshwater forcing, tropical forcing and sea-ice feedback forcing. These mechanisms are well reviewed in papers such as Clement and Peterson (2008), Hemming (2004), Chiang (2009), Seager and Battisti (2007), and Overpeck and Cole (2006). The mechanisms driving D/O cycles and the global propagation are still not well understood (Clement and Peterson, 2008; Timmermann et al., 2003).

7.5.1 Freshwater forcing

The forcing mechanism of millennial scale climate must be 1) abrupt and 2) enable a global scale climate response (Clement and Peterson, 2008). The freshwater forcing mechanism invokes a decrease in the AMOC as a driver for the observed climate. The reduction or shut down of the AMOC is thought to lead to the formation of the "bipolar seesaw" or the antiphased relationship between the North Atlantic and Antarctic climate (Blunier and Brook, 2001; Overpeck and Cole, 2006). This antiphased relationship is seen across Heinrich stadials and D/O cycles between the Antarctic and the Greenland ice core records. AMOC resumes once salinities in the North Atlantic are restored by a decrease in the freshwater influx. Many models have been built using the freshwater forcing mechanism and agree reasonably well with the observed paleoclimate response across Heinrich stadials with the major exception being the tropics (Menviel et al., 2011; Vellinga and Wood, 2002; Zhang and Delworth, 2005).

The freshwater forcing mechanism relies on the buildup and subsequent melting of the ice sheets as a driver for reduction in AMOC. There have been several theories proposed for the mechanisms driving the ice sheet dynamics, including the binge-purge model, geothermal heating (Macayeal, 1993), insolation driven ice sheet dynamics (Bond et al., 2001) and others, however uncertainties still remain. The binge-purge model suggests that large ice sheets buildup gradually (binge phase) until it reaches a phase of destabilization.

D/O cycles and the evidence for IRDs:

There is some recent evidence that all D/O stadials between 30-50 ka BP are associated with IRD deposits in the North Atlantic (Menviel et al., 2014). Records support that iceberg calving occurred during interstadials and peaked during stadial periods (Menviel et al., 2014). It has been suggested that therefore the forcing for D/O cycles is very similar to the forcing mechanisms of Heinrich stadials (Menviel et al., 2014).

7.5.2 Tropical ocean/atmosphere forcing

The antiphased relationship between the AMOC and the southern hemisphere supports the global importance of the AMOC in climate modulation. Change of the thermohaline circulation is the current favorite explanation for abrupt climate change. However, this mechanism does not explain all of the observed paleoclimate variability. Seager and Battisti (2007) argue that the degree of winter cooling must be caused by a change in the atmospheric heat transport potentially driven by wind changing the movement of water northward. This change would lead to a southward extension of the

ice sheets and an increased aridity in the tropics (Seager and Battisti, 2007). However, it is still unclear how such a change in the wind field would occur.

The tropics may serve as a critical point in the global propagation of these events because the tropics act as a barrier between the two hemispheres. As demonstrated by El Nino Southern Oscillation events, the tropics can play a very large role in the global climate (Cane and Clement, 1999). Mechanisms that have been proposed for AMOC and tropical climate are outlined in Clement and Peterson, 2008.

Tropical dust:

As suggested previously, tropical paleoclimate records support increased aridity during HS, a feature which is not resolved in many models of these events (Murphy et al., 2014). One potential source of this offset is the impacts of dust on climate. From a modeling study of a Heinrich stadial, it was found that dust increases the climate response to the Heinrich stadials and increased atmospheric dust was demonstrated to increase cooling in the North Atlantic SSTs and amplify aridity in Africa, the Arabian Sea and India (Murphy et al., 2014). Future studies should consider aerosol-sea ice feedbacks in the North Atlantic for HS, however studies have demonstrated, models have difficulty capturing accurate dust emissions, based on modern analysis of dust as well as paleo dust measurements (Evan et al., 2014; Lambert et al., 2013; Lee et al., 2013; Mahowald et al., 2010; Murphy et al., 2014; Pourmand et al., 2014a).

7.5.3 Sea-ice forcing

The D/O cycles are associated with an increased accumulation for the Greenland ice sheet, difficult to explain based on the mechanisms discussed thus far (Li et al., 2010). It has been proposed that D/O cycles may be driven by a different forcing mechanism

which accounts for this increase in accumulation (Li et al., 2010). For D/O cycles (interstadials), there is minimal evidence for changes in overturning, therefore it has been proposed that sea ice changes may be an important mechanism driving climate responses (Petersen et al., 2013). This mechanism supports the changes in accumulation as well as the saw-tooth pattern of the oxygen isotopes of Greenland across D/O events (Petersen et al., 2013). This hypothesis is supported by evidence of IRD deposits associated with D/O events in particular during interstadials and modeling studies suggest D/O events are forced both by ice-sheet and AMOC variations (Menviel et al., 2014).

7.6 Summary and Conclusion

This chapter has provided an overview of the recent paleoclimate studies on millennial scale climate variability and the driving mechanisms of these events. To summarize, there are several global scale changes associated with millennial scale climate variations, including in the Northern Hemisphere, decreased SSTs, increased aridity in many locations (in particular in the tropics), reduction of the IASM, Asian monsoons and NAM, while interstadials are often expressed as periods of rapid warming (in particular in Greenland) and SST increase, and increased rainfall. Contrary, in the Southern Hemisphere stadials are characterized by increased SASM and IASM which are thought to be driven by increased SSTs and a southerly shifted ITCZ. Future research efforts on millennial scale climate events which would be of importance includes continued research on the NAM during these events, continued research on millennial scale climate variation during interglacial periods and paleoclimate research to continue to quantify dust emissions during Heinrich stadials for the production of reliable dust models.

References

Affek, H., Barmatthews, M., Ayalon, A., Matthews, A., and Eiler, J., 2008, Glacial/interglacial temperature variations in Soreq cave speleothems as recorded by 'clumped isotope' thermometry: Geochimica et Cosmochimica Acta, v. 72, no. 22, p. 5351-5360.

Affek, H. P., 2013, Clumped Isotopic Equilibrium and the Rate of Isotope Exchange between CO_2 and Water: American Journal of Science, v. 313, no. 4, p. 309-325.

Affek, H. P., and Eiler, J. M., 2006, Abundance of mass 47 CO_2 in urban air, car exhaust, and human breath: Geochimica Et Cosmochimica Acta, v. 70, no. 1, p. 1-12.

Alley, R. B., Clark, P. U., Keigwin, L. D., and Webb, R. S., 1999, Making sense of millennial-scale climate change, Mechanisms of Global Climate Change at Millennial Time Scales, Volume Geophysical Monograph 112, American Geophyisical Union.

Arienzo, M. M., Swart, P. K., and Vonhof, H. B., 2013, Measurement of $\delta^{18}O$ and $\delta^{2}H$ values of fluid inclusion water in speleothems using cavity ring-down spectroscopy compared with isotope ratio mass spectrometry: Rapid Communications in Mass Spectrometry, v. 27, no. 23, p. 2616-2624.

Asmerom, Y., Polyak, V. J., and Burns, S. J., 2010, Variable winter moisture in the southwestern United States linked to rapid glacial climate shifts: Nature Geoscience, v. 3, no. 2, p. 114-117.

Atkinson, J. D., Murray, B. J., Woodhouse, M. T., Whale, T. F., Baustian, K. J., Carslaw, K. S., Dobbie, S., O'Sullivan, D., and Malkin, T. L., 2013, The importance of feldspar for ice nucleation by mineral dust in mixed-phase clouds: Nature, v. 498, no. 7454, p. 355-358.

Ayalon, A., Bar-Matthews, M., and Kaufman, A., 1999, Petrography, strontium, barium and uranium concentrations, and strontium and uranium isotope ratios in speleothems as palaeoclimatic proxies: Soreq Cave, Israel: The Holocene, v. 9, no. 6, p. 715-722.

Ayliffe, L. K., Gagan, M. K., Zhao, J. X., Drysdale, R. N., Hellstrom, J. C., Hantoro, W. S., Griffiths, M. L., Scott-Gagan, H., St Pierre, E., Cowley, J. A., and Suwargadi, B. W., 2013, Rapid interhemispheric climate links via the Australasian monsoon during the last deglaciation: Nat Commun, v. 4, p. 2908.

Baker, A., and Bradley, C., 2010, Modern stalagmite δ18O: Instrumental calibration and forward modelling: Global and Planetary Change, v. 71, no. 3-4, p. 201-206.

Baldini, J. U. L., McDermott, F., Baldini, L. M., Ottley, C. J., Linge, K. L., Clipson, N., and Jarvis, K. E., 2012, Identifying short-term and seasonal trends in cave drip water trace element concentrations based on a daily-scale automatically collected drip water dataset: Chemical Geology, v. 330, p. 1-16.

Baldini, L. M., Walker, S. E., Railsback, L. B., Baldini, J. U. L., and Crowe, D. E., 2007, Isotopic ecology of the modern land snail Cerion, San Salvador, Bahamas: Preliminary advances toward establishing a low-latitude island paleoenvironmental proxy: Palaios, v. 22, no. 2, p. 174-187.

Banner, J. L., Guilfoyle, A., James, E. W., Stern, L. A., and Musgrove, M., 2007, Seasonal variations in modern speleothem calcite growth in Central Texas, U.S.A: Journal of Sedimentary Research, v. 77, no. 8, p. 615-622.

Banner, J. L., Musgrove, M. L., Asmerom, Y., Edwards, R. L., and Hoff, J. A., 1996, High-resolution temporal record of Holocene ground-water chemistry: Tracing links between climate and hydrology: Geology, v. 24, no. 11, p. 1049-1053.

Bar-Matthews, M., Ayalon, A., Gilmour, M., Matthews, A., and Hawkesworth, C. J., 2003, Sea-land oxygen isotopic relationships from planktonic foraminifera and speleothems in the Eastern Mediterranean region and their implication for paleorainfall during interglacial intervals: Geochimica Et Cosmochimica Acta, v. 67, no. 17, p. 3181-3199.

Bar-Matthews, M., Ayalon, A., and Kaufman, A., 1997, Late Quaternary paleoclimate in the eastern Mediterranean region from stable isotope analysis of speleothems at Soreq Cave, Israel: Quaternary Research, v. 47, no. 2, p. 155-168.

Bar-Matthews, M., Ayalon, A., Kaufman, A., and Wasserburg, G. J., 1999, The Eastern Mediterranean paleoclimate as a reflection of regional events: Soreq cave, Israel: Earth and Planetary Science Letters, v. 166, no. 1-2, p. 85-95.

Beck, J. W., Edwards, R. L., Ito, E., Taylor, F. W., Recy, J., Rougerie, F., Joannot, P., and Henin, C., 1992, Sea-surface temperature from coral skeletal strontium calcium ratios: Science, v. 257, no. 5070, p. 644-647.

Benson, L. V., Lund, S. P., Smoot, J. P., Rhode, D. E., Spencer, R. J., Verosub, K. L., Louderback, L. A., Johnson, C. A., Rye, R. O., and Negrini, R. M., 2011, The rise and fall of Lake Bonneville between 45 and 10.5 ka: Quaternary International, v. 235, p. 57-69.

Bettis, E. A., Muhs, D. R., Roberts, H. M., and Wintle, A. G., 2003, Last Glacial loess in the conterminous USA: Quaternary Science Reviews, v. 22, no. 18-19, p. 1907-1946.

Bigeleisen, J., and Mayer, M. G., 1947, Calculation of equilibrium constants for isotopic exchange reactions: Journal of Chemical Physics, v. 15, no. 5, p. 261-267.

Blunier, T., and Brook, E. J., 2001, Timing of millennial-scale climate change in Antarctica and Greenland during the last glacial period: Science, v. 291, no. 5501, p. 109-112.

Bond, G., Broecker, W., Johnsen, S., Mcmanus, J., Labeyrie, L., Jouzel, J., and Bonani, G., 1993, Correlations between climate records from North-Atlantic sediments and Greenland ice: Nature, v. 365, no. 6442, p. 143-147.

Bond, G., Heinrich, H., Broecker, W., Labeyrie, L., Mcmanus, J., Andrews, J., Huon, S., Jantschik, R., Clasen, S., Simet, C., Tedesco, K., Klas, M., Bonani, G., and Ivy, S., 1992, Evidence for massive discharges of icebergs into the North-Atlantic Ocean during the Last Glacial Period: Nature, v. 360, no. 6401, p. 245-249.

Bond, G., Kromer, B., Beer, J., Muscheler, R., Evans, M. N., Showers, W., Hoffmann, S., Lotti-Bond, R., Hajdas, I., and Bonani, G., 2001, Persistent solar influence on north Atlantic climate during the Holocene: Science, v. 294, no. 5549, p. 2130-2136.

Bond, G., Showers, W., Cheseby, M., Lotti, R., Almasi, P., deMenocal, P., Priore, P., Cullen, H., Hajdas, I., and Bonani, G., 1997, A pervasive millennial-scale cycle in North Atlantic Holocene and glacial climates: Science, v. 278, no. 5341, p. 1257-1266.

Bourdon, B., Turner, S., Henderson, G. M., and Lundstrom, C. C., 2003, Introduction to U-series geochemistry, *in* Bourdon, B., ed., Reviews in Mineralogy and Geochemistry: Uranium-series Geochemistry, Volume 52: Washington, DC, Mineralogical Society of America.

Brand, W. A., Geilmann, H., Crosson, E. R., and Rella, C. W., 2009, Cavity ring-down spectroscopy versus high-temperature conversion isotope ratio mass spectrometry; a case study on δ^2H and $\delta^{18}O$ of pure water samples and alcohol/water mixtures: Rapid Communications in Mass Spectrometry, v. 23, no. 12, p. 1879-1884.

Broecker, W. S., 1994, Massive iceberg discharges as triggers for global climate change: Nature, v. 372, no. 6505, p. 421-424.

Broecker, W. S., Peteet, D. M., and Rind, D., 1985, Does the ocean-atmosphere system have more than one stable mode of operation: Nature, v. 315, no. 6014, p. 21-26.

Buiron, D., Stenni, B., Chappellaz, J., Landais, A., Baumgartner, M., Bonazza, M., Capron, E., Frezzotti, M., Kageyama, M., Lemieux-Dudon, B., Masson-Delmotte, V., Parrenin, F., Schilt, A., Selmo, E., Severi, M., Swingedouw, D., and Udisti, R., 2012, Regional imprints of millennial variability during the MIS 3 period around Antarctica: Quaternary Science Reviews, v. 48, p. 99-112.

Burns, S. J., Fleitmann, D., Matter, A., Kramers, J., and Al-Subbary, A. A., 2003, Indian Ocean climate and an absolute chronology over Dansgaard/Oeschger events 9 to 13: Science, v. 301, no. 5638, p. 1365-1367.

Cacho, I., Grimalt, J. O., Pelejero, C., Canals, M., Sierro, F. J., Flores, J. A., and Shackleton, N., 1999, Dansgaard-Oeschger and Heinrich event imprints in Alboran Sea paleotemperatures: Paleoceanography, v. 14, no. 6, p. 698-705.

Cai, Y., An, Z., Cheng, H., Edwards, R. L., Kelly, M. J., Liu, W., Wang, X., and Shen, C.-C., 2006, High-resolution absolute-dated Indian Monsoon record between 53 and 36 ka from Xiaobailong Cave, southwestern China: Geology, v. 34, no. 8, p. 621.

Came, R. E., Eiler, J. M., Veizer, J., Azmy, K., Brand, U., and Weidman, C. R., 2007, Coupling of surface temperatures and atmospheric CO_2 concentrations during the Palaeozoic era: Nature, v. 449, no. 7159, p. 198-U193.

Capron, E., Landais, A., Chappellaz, J., Schilt, A., Buiron, D., Dahl-Jensen, D., Johnsen, S. J., Jouzel, J., Lemieux-Dudon, B., Loulergue, L., Leuenberger, M., Masson-Delmotte, V., Meyer, H., Oerter, H., and Stenni, B., 2010, Millennial and sub-millennial scale climatic variations recorded in polar ice cores over the last glacial period: Climate of the Past, v. 6, no. 3, p. 345-365.

Carolin, S. A., Cobb, K. M., Adkins, J. F., Clark, B., Conroy, J. L., Lejau, S., Malang, J., and Tuen, A. A., 2013, Varied response of western Pacific hydrology to climate forcings over the last glacial period: Science, v. 340, no. 6140, p. 1564-1566.

Cheng, H., Sinha, A., Cruz, F. W., Wang, X., Edwards, R. L., d'Horta, F. M., Ribas, C. C., Vuille, M., Stott, L. D., and Auler, A. S., 2013, Climate change patterns in Amazonia and biodiversity: Nat Commun, v. 4, p. 1411.

Cheng, H., Sinha, A., Wang, X. F., Cruz, F. W., and Edwards, R. L., 2012, The Global Paleomonsoon as seen through speleothem records from Asia and the Americas: Climate Dynamics, v. 39, no. 5, p. 1045-1062.

Chiang, J. C. H., 2009, The tropics in paleoclimate: Annual Review of Earth and Planetary Sciences, v. 37, no. 1, p. 263-297.

Christoforou, C. S., Salmon, L. G., and Cass, G. R., 1994, Deposition of atmospheric particles within the Buddhist Cave Temples at Yungang, China: Atmospheric Environment, v. 28, no. 12, p. 2081-2091.

Cisneros, C. J., Caballero, E., Vera, J. A., and Andreo, B., 2011, An optimized thermal extraction system for preparation of water from fluid inclusions in speleothems: Geologica Acta, v. 9, no. 2, p. 9.

Clement, A. C., and Cane, M. A., 1999, A role for the tropical pacific coupled ocean-atmosphere system on Milankovitch and millennial timescales, *in* Clark, P. U., Webb, R. S., and Keigwin, L. D., eds., Mechanisms of Global Climate Change at Millennial Time Scales, Volume 112: Washington, D.C., AGU, p. 363-371.

Clement, A. C., and Peterson, L. C., 2008, Mechanisms of abrupt climate change of the last glacial period: Reviews of Geophysics, v. 46, no. 4.

Collins, J. A., Govin, A., Mulitza, S., Heslop, D., Zabel, M., Hartmann, J., Rohl, U., and Wefer, G., 2013, Abrupt shifts of the Sahara-Sahel boundary during Heinrich stadials: Climate of the Past, v. 9, no. 3, p. 1181-1191.

Coplen, T. B., 2007, Calibration of the calcite-water oxygen-isotope geothermometer at Devils Hole, Nevada, a natural laboratory: Geochimica Et Cosmochimica Acta, v. 71, no. 16, p. 3948-3957.

Couchoud, I., Genty, D., Hoffmann, D., Drysdale, R., and Blamart, D., 2009, Millennial-scale climate variability during the Last Interglacial recorded in a speleothem from south-western France: Quaternary Science Reviews, v. 28, no. 27-28, p. 3263-3274.

Craig, H., 1961, Isotopic variations in meteoric waters: Science, v. 133, no. 3465, p. 1702-1703.

-, 1965, The measurement of oxygen isotope paleotemperatures, *in* Tongiorgi, E., ed., Stable Isotopes in Oceanographic Studies and Paleotemperatures: Pisa, Italy, Consiglio Nazionale delle Ricerche, Laboratorio de Geologia Nucleare, p. 161-182.

Cruz, F., Burns, S., Jercinovic, M., Karmann, I., Sharp, W., and Vuille, M., 2007, Evidence of rainfall variations in Southern Brazil from trace element ratios (Mg/Ca and Sr/Ca) in a Late Pleistocene stalagmite: Geochimica et Cosmochimica Acta, v. 71, no. 9, p. 2250-2263.

Cruz, F. W., Burns, S. J., Karmann, I., Sharp, W. D., Vuille, M., and Ferrari, J. A., 2006, A stalagmite record of changes in atmospheric circulation and soil processes in the Brazilian subtropics during the Late Pleistocene: Quaternary Science Reviews, v. 25, no. 21-22, p. 2749-2761.

Cruz, F. W., Karmann, I., Magdaleno, G. B., Coichev, N., and Viana, O., 2005, Influence of hydrological and climatic parameters on spatial-temporal variability of fluorescence intensity and DOC of karst percolation waters in the Santana Cave System, Southeastern Brazil: Journal of Hydrology, v. 302, no. 1-4, p. 1-12.

Cruz, F. W., Vuille, M., Burns, S. J., Wang, X., Cheng, H., Werner, M., Edwards, R. L., Karmann, I., Auler, A. S., and Nguyen, H., 2009, Orbitally driven east-west antiphasing of South American precipitation: Nature Geoscience, v. 2, no. 3, p. 210-214.

Daëron, M., Guo, W., Eiler, J., Genty, D., Blamart, D., Boch, R., Drysdale, R., Maire, R., Wainer, K., and Zanchetta, G., 2011, $^{13}C^{18}O$ clumping in speleothems: Observations from natural caves and precipitation experiments: Geochimica et Cosmochimica Acta, v. 75, no. 12, p. 3303-3317.

Dallai, L., Lucchini, R., and Sharp, Z. D., 2004, Techniques for stable isotope analysis of fluid and gaseous inclusions, *in* de Groot, P. A., ed., Handbook of stable isotope analytical techniques: Amsterdam, Elsevier, p. v.

Dansgaard, W., 1964, Stable isotopes in precipitation: Tellus, v. 16, no. 4, p. 436-468.

Dansgaard, W., Johnsen, S. J., Clausen, H. B., Dahl-Jensen, D., Gundestrup, N., Hammer, C. U., and Oeschger, H., 1984, North Atlantic climatic oscillations revealed by deep Greenland ice cores, Climate Processes and Climate Sensitivity, Volume 29, AGU, p. 10.

Dansgaard, W., Johnsen, S. J., Clausen, H. B., Dahljensen, D., Gundestrup, N. S., Hammer, C. U., Hvidberg, C. S., Steffensen, J. P., Sveinbjornsdottir, A. E., Jouzel, J., and Bond, G., 1993, Evidence for general instability of past climate from a 250-Kyr ice-core record: Nature, v. 364, no. 6434, p. 218-220.

De Deckker, P., Moros, M., Perner, K., and Jansen, E., 2012, Influence of the tropics and southern westerlies on glacial interhemispheric asymmetry: Nature Geoscience, v. 5, no. 4, p. 266-269.

Dennis, K. J., 2011, Clumped isotope paleothermometry and its application to Earth's history [PhD: Harvard University].

Dennis, K. J., Affek, H. P., Passey, B. H., Schrag, D. P., and Eiler, J. M., 2011, Defining an absolute reference frame for 'clumped' isotope studies of CO_2: Geochimica et Cosmochimica Acta, v. 75, no. 22, p. 7117-7131.

Dennis, K. J., and Schrag, D. P., 2010, Clumped isotope thermometry of carbonatites as an indicator of diagenetic alteration: Geochimica et Cosmochimica Acta, v. 74, no. 14, p. 4110-4122.

Dennis, P. F., Rowe, P. J., and Atkinson, T. C., 2001, The recovery and isotopic measurement of water from fluid inclusions in speleothems: Geochimica et Cosmochimica Acta, v. 65, no. 6, p. 871-884.

Denniston, R. F., Asmerom, Y., Lachniet, M., Polyak, V. J., Hope, P., An, N., Rodzinyak, K., and Humphreys, W. F., 2013a, A Last Glacial Maximum through middle Holocene stalagmite record of coastal Western Australia climate: Quaternary Science Reviews, v. 77, p. 101-112.

Denniston, R. F., Asmerom, Y., Polyak, V., Dorale, J. A., Carpenter, S. J., Trodick, C., Hoye, B., and González, L. A., 2007, Synchronous millennial-scale climatic changes in the Great Basin and the North Atlantic during the last interglacial: Geology, v. 35, no. 7, p. 619.

Denniston, R. F., Wyrwoll, K.-H., Asmerom, Y., Polyak, V. J., Humphreys, W. F., Cugley, J., Woods, D., LaPointe, Z., Peota, J., and Greaves, E., 2013b, North Atlantic forcing of millennial-scale Indo-Australian monsoon dynamics during the Last Glacial period: Quaternary Science Reviews, v. 72, p. 159-168.

Deplazes, G., Luckge, A., Peterson, L. C., Timmermann, A., Hamann, Y., Hughen, K. A., Rohl, U., Laj, C., Cane, M. A., Sigman, D. M., and Haug, G. H., 2013, Links between tropical rainfall and North Atlantic climate during the last glacial period: Nature Geoscience, v. 6, no. 3, p. 213-217.

Deplazes, G., Lückge, A., Stuut, J.-B. W., Pätzold, J., Kuhlmann, H., Husson, D., Fant, M., and Haug, G. H., 2014, Weakening and strengthening of the Indian monsoon during Heinrich events and Dansgaard-Oeschger oscillations: Paleoceanography, v. 29, no. 2, p. 99-114.

Donders, T. H., Boer, H. J., Finsinger, W., Grimm, E. C., Dekker, S. C., Reichart, G. J., and Wagner-Cremer, F., 2009, Impact of the Atlantic Warm Pool on precipitation and temperature in Florida during North Atlantic cold spells: Climate Dynamics, v. 36, no. 1-2, p. 109-118.

Doner, H. A., and Hoskins, W. M., 1925, Coprecipitation of radium and barium sulphates: Journal of the American Chemical Society.

Dorale, J. A., and Liu, Z. H., 2009, Limitations of Hendy Test criteria in judging the paleoclimatic suitability of speleothems and the need for replication: Journal of Cave and Karst Studies, v. 71, no. 1, p. 73-80.

Dredge, J., Fairchild, I. J., Harrison, R. M., Faernandez-Cortes, A., Sanchez-Moral, S., Jurado, V., Gunn, J., Smith, A., Spotl, C., Mattey, D., Wynn, P. M., and Grassineau, N., 2013, Cave aerosols: distribution and contirbuton to speleothem geochemistry: Quaternary Science Reviews, no. 63, p. 23-41.

Dublyansky, Y. V., and Spotl, C., 2009, Hydrogen and oxygen isotopes of water from inclusions in minerals: design of a new crushing system and on-line continuous-flow isotope ratio mass spectrometric analysis: Rapid Communincations in Mass Spectrometry, v. 23, no. 17, p. 2605-2613.

Edwards, R. L., Gallup, C. D., and Cheng, H., 2003, U-series dating of marine and lacustrine carbonates, *in* Bourdon, B., ed., Reviews in Mineralogy and Geochemistry: Uranium Series Geochemistry, Volume 52: Washington, DC, Mineralogical Society of America.

Eiler, J. M., 2007, "Clumped-isotope" geochemistry—The study of naturally-occurring, multiply-substituted isotopologues: Earth and Planetary Science Letters, v. 262, no. 3-4, p. 309-327.

-, 2011, Paleoclimate reconstruction using carbonate clumped isotope thermometry: Quaternary Science Reviews, v. 30, no. 25-26, p. 3575-3588.

Epstein, S., Buchsbaum, R., Lowenstam, H. A., and Urey, H. C., 1953, Revised carbonate-water isotopic temperature scale: Geological Society of America Bulletin, v. 64, no. 11, p. 1315-1325.

Escobar, J., Hodell, D. A., Brenner, M., Curtis, J. H., Gilli, A., Mueller, A. D., Anselmetti, F. S., Ariztegui, D., Grzesik, D. A., Perez, L., Schwalb, A., and Guilderson, T. P., 2012, A similar to 43-ka record of paleoenvironmental change in the Central American lowlands inferred from stable isotopes of lacustrine ostracods: Quaternary Science Reviews, v. 37, p. 92-104.

Evan, A. T., Flamant, C., Fiedler, S., and Doherty, O., 2014, An analysis of aeolian dust in climate models: Geophysical Research Letters, v. 41, no. 16, p. 5996-6001.

Evan, A. T., Foltz, G. R., Zhang, D. X., and Vimont, D. J., 2011, Influence of African dust on ocean-atmosphere variability in the tropical Atlantic: Nature Geoscience, v. 4, no. 11, p. 762-765.

Evan, A. T., Vimont, D. J., Heidinger, A. K., Kossin, J. P., and Bennartz, R., 2009, The role of aerosols in the evolution of tropical North Atlantic Ocean temperature anomalies: Science, v. 324, no. 5928, p. 778-781.

Fairchild, I. J., Borsato, A., Tooth, A. F., Frisia, S., Hawkesworth, C. J., Huang, Y. M., McDermott, F., and Spiro, B., 2000, Controls on trace element (Sr-Mg) compositions of carbonate cave waters: implications for speleothem climatic records: Chemical Geology, v. 166, no. 3-4, p. 255-269.

Fairchild, I. J., Smith, C. L., Baker, A., Fuller, L., Spötl, C., Mattey, D., McDermott, F., and E.I.M.F, 2006, Modification and preservation of environmental signals in speleothems: Earth-Science Reviews, v. 75, no. 1-4, p. 105-153.

Fairchild, I. J., and Treble, P. C., 2009, Trace elements in speleothems as recorders of environmental change: Quaternary Science Reviews, v. 28, no. 5-6, p. 449-468.

Farmer, G. L., Barber, D., and Andrews, J., 2003, Provenance of Late Quaternary ice-proximal sediments in the North Atlantic: Nd, Sr and Pb isotopic evidence: Earth and Planetary Science Letters, v. 209, no. 1-2, p. 227-243.

Feng, W. M., Banner, J. L., Guilfoyle, A. L., Musgrove, M., and James, E. W., 2012, Oxygen isotopic fractionation between drip water and speleothem calcite: A 10-year monitoring study, central Texas, USA: Chemical Geology, v. 304, p. 53-67.

Feng, W. M., Casteel, R. C., Banner, J. L., and Heinze-Fry, A., 2014, Oxygen isotope variations in rainfall, drip-water and speleothem calcite from a well-ventilated cave in Texas, USA: Assessing a new speleothem temperature proxy: Geochimica Et Cosmochimica Acta, v. 127, p. 233-250.

Fernandez, A., Tang, J. W., and Rosenheim, B. E., 2014, Siderite 'clumped' isotope thermometry: A new paleoclimate proxy for humid continental environments: Geochimica Et Cosmochimica Acta, v. 126, p. 411-421.

Ferry, J. M., Passey, B. H., Vasconcelos, C., and Eiler, J. M., 2011, Formation of dolomite at 40-80 C in the Latemar carbonate buildup, Dolomites, Italy, from clumped isotope thermometry: Geology, v. 39, no. 6, p. 571-574.

Fleitmann, D., Burns, S. J., Neff, U., Mangini, A., and Matter, A., 2003, Changing moisture sources over the last 330,000 years in Northern Oman from fluid-inclusion evidence in speleothems: Quaternary Research, v. 60, no. 2, p. 223-232.

Fleitmann, D., Cheng, H., Badertscher, S., Edwards, R. L., Mudelsee, M., Gokturk, O. M., Fankhauser, A., Pickering, R., Raible, C. C., Matter, A., Kramers, J., and Tuysuz, O., 2009, Timing and climatic impact of Greenland interstadials recorded in stalagmites from northern Turkey: Geophysical Research Letters, v. 36.

Fletcher, W. J., Sánchez Goñi, M. F., Allen, J. R. M., Cheddadi, R., Combourieu-Nebout, N., Huntley, B., Lawson, I., Londeix, L., Magri, D., Margari, V., Müller, U. C., Naughton, F., Novenko, E., Roucoux, K., and Tzedakis, P. C., 2010, Millennial-scale variability during the last glacial in vegetation records from Europe: Quaternary Science Reviews, v. 29, no. 21-22, p. 2839-2864.

Fohlmeister, J., Scholz, D., Kromer, B., and Mangini, A., 2011, Modelling carbon isotopes of carbonates in cave drip water: Geochimica Et Cosmochimica Acta, v. 75, no. 18, p. 5219-5228.

Friedman, I., and O'Neil, J. R., 1977, Compilation of stable isotope fractionation factors of geochemical interest: Geolog. Surv. Prof. Paper, v. 440-KK, p. 11.

Fritz, S. C., Baker, P. A., Ekdahl, E., Seltzer, G. O., and Stevens, L. R., 2010, Millennial-scale climate variability during the Last Glacial period in the tropical Andes: Quaternary Science Reviews, v. 29, no. 7-8, p. 1017-1024.

Frumkin, A., and Stein, M., 2004, The Sahara–East Mediterranean dust and climate connection revealed by strontium and uranium isotopes in a Jerusalem speleothem: Earth and Planetary Science Letters, v. 217, no. 3-4, p. 451-464.

Fuhrer, K., Wolff, E. W., and Johnsen, S. J., 1999, Timescales for dust variability in the Greenland Ice Core Project (GRIP) ice core in the last 100,000 years: Journal of Geophysical Research-Atmospheres, v. 104, no. D24, p. 31043-31052.

Gat, J. R., 1996, Oxygen and hydrogen isotopes in the hydrologic cycle: Annual Review of Earth and Planetary Sciences, v. 24, p. 225-262.

Genty, D., Blamart, D., Ouahdi, R., Gilmour, M., Baker, A., Jouzel, J., and Van-Exter, S., 2003, Precise dating of Dansgaard-Oeschger climate oscillations in western Europe from stalagmite data: Nature, v. 421, no. 6925, p. 833-837.

Genty, D., Combourieu-Nebout, N., Peyron, O., Blamart, D., Wainer, K., Mansuri, F., Ghaleb, B., Isabello, L., Dormoy, I., von Grafenstein, U., Bonelli, S., Landais, A., and Brauer, A., 2010, Isotopic characterization of rapid climatic events during OIS3 and OIS4 in Villars Cave stalagmites (SW-France) and correlation with Atlantic and Mediterranean pollen records: Quaternary Science Reviews, v. 29, no. 19-20, p. 2799-2820.

Genty, D., Labuhn, I., Hoffmann, G., Danis, P. A., Mestre, O., Bourges, F., Wainer, K., Massault, M., Exter, S. V., Regnier, E., Orengo, P., Farlourd, S., and Minster, B., 2014, Rainfall and cave water isotopic relationships in two South-France sites: Geochimica et Cosmochimica Acta, v. 131, p. 3233-3343.

Gherardi, J. M., Labeyrie, L., McManus, J. F., Francois, R., Skinner, L. C., and Cortijo, E., 2005, Evidence from the Northeastern Atlantic basin for variability in the rate of the meridional overturning circulation through the last deglaciation: Earth and Planetary Science Letters, v. 240, no. 3-4, p. 710-723.

Ghosh, P., Adkins, J., Affek, H., Balta, B., Guo, W., Schauble, E., Schrag, D., and Eiler, J., 2006, $^{13}C–^{18}O$ bonds in carbonate minerals: A new kind of paleothermometer: Geochimica et Cosmochimica Acta, v. 70, no. 6, p. 1439-1456.

Gibbons, F. T., Oppo, D. W., Mohtadi, M., Rosenthal, Y., Cheng, J., Liu, Z., and Linsley, B. K., 2014, Deglacial $\delta^{18}O$ and hydrologic variability in the tropical Pacific and Indian Oceans: Earth and Planetary Science Letters, v. 387, p. 240-251.

Gibson, K. A., and Peterson, L. C., 2014, A 0.6 million year record of millennial-scale climate variability in the tropics: Geophysical Research Letters, v. 41, no. 3, p. 2013GL058846.

Goede, A., McCulloch, M., McDermott, F., and Hawkesworth, C., 1998, Aeolian contribution to strontium and strontium isotope variations in a Tasmanian speleothem: Chemical Geology, v. 149, no. 1-2, p. 37-50.

Goldstein, R. H., 1986, Reequilibration of fluid inclusions in low-temperature calcium-carbonate cement: Geology, v. 14, no. 9, p. 792-795.

-, 2001, Fluid inclusions in sedimentary and diagenetic systems: Lithos, v. 55, no. 1–4, p. 159-193.

Gordon, D., Smart, P. L., Ford, D. C., Andrews, J. N., Atkinson, T. C., Rowe, P. J., and Christopher, N. S. J., 1989, Dating of Late Pleistocene interglacial and interstadial periods in the United-Kingdom from speleothem growth frequency: Quaternary Research, v. 31, no. 1, p. 14-26.

Griffiths, M. L., Drysdale, R. N., Vonhof, H. B., Gagan, M. K., Zhao, J.-x., Ayliffe, L. K., Hantoro, W. S., Hellstrom, J. C., Cartwright, I., and Frisia, S., 2010, Younger Dryas–Holocene temperature and rainfall history of southern Indonesia from δ18O in speleothem calcite and fluid inclusions: Earth and Planetary Science Letters, v. 295, no. 1-2, p. 30-36.

Grimm, E. C., Watts, W. A., Jacobson Jr, G. L., Hansen, B. C. S., Almquist, H. R., and Dieffenbacher-Krall, A. C., 2006, Evidence for warm wet Heinrich events in Florida: Quaternary Science Reviews, v. 25, no. 17-18, p. 2197-2211.

Grootes, P. M., Stuiver, M., White, J. W. C., Johnsen, S., and Jouzel, J., 1993, Comparison of oxygen isotope records from the GISP2 and GRIP Greenland ice cores: Nature, v. 366, no. 6455, p. 552-554.

Grousset, F. E., and Biscaye, P. E., 2005, Tracing dust sources and transport patterns using Sr, Nd and Pb isotopes: Chemical Geology, v. 222, no. 3-4, p. 149-167.

Guillevic, M., Bazin, L., Landais, A., Kindler, P., Orsi, A., Masson-Delmotte, V., Blunier, T., Buchardt, S. L., Capron, E., Leuenberger, M., Martinerie, P., Prié, F., and Vinther, B. M., 2013, Spatial gradients of temperature, accumulation and $\delta^{18}O$ ice in Greenland over a series of Dansgaard Oeschger events: Climate of the Past, v. 9, no. 3, p. 1029-1051.

Guo, W., 2008, Carbonate clumped isotope thermometry: Application to carbonaceous chondrites & effects of kinetic isotope fractionation [Ph. D. : California Institute of Technology].

Guo, W., Mosenfelder, J. L., Goddard, W. A., III, and Eiler, J. M., 2009, Isotopic fractionations associated with phosphoric acid digestion of carbonate minerals: Insights from the first principles theoretical modeling and clumped isotope measurements: Geochimica et Cosmochimica Acta, v. 73, p. 7203-7225.

Hagen, S., and Keigwin, L. D., 2002, Sea-surface temperature variability and deep water reorganisation in the subtropical North Atlantic during Isotope Stage 2-4: Marine Geology, v. 189, no. 1-2, p. 145-162.

Harmon, R. S., Schwarcz, H. P., and Oneil, J. R., 1979, D-H Ratios in speleothem fluid inclusions - Guide to variations in the isotopic composition of meteoric precipitation: Earth and Planetary Science Letters, v. 42, no. 2, p. 254-266.

Hegg, D. A., Warren, S. G., Grenfell, T. C., Doherty, S. J., and Clarke, A. D., 2010, Sources of light-absorbing aerosol in arctic snow and their seasonal variation: Atmospheric Chemistry and Physics, v. 10, no. 22, p. 10923-10938.

Heinrich, H., 1988, Origin and consequences of cyclic ice rafting in the Northeast Atlantic-Ocean during the past 130,000 Years: Quaternary Research, v. 29, no. 2, p. 142-152.

Hemming, S. R., 2004, Heinrich events: Massive Late Pleistocene detritus layers of the North Atlantic and their global climate imprint: Reviews of Geophysics, v. 42, no. 1.

Hendy, C. H., 1971, The isotopic geochemistry of speleothems—I. The calculation of the effects of different modes of formation on the isotopic composition of speleothems and their applicability as palaeoclimatic indicators: Geochimica et Cosmochimica Acta, v. 35, no. 8, p. 801-824.

Hendy, I. L., and Kennett, J. P., 2000, Dansgaard-Oeschger cycles and the California Current System: Planktonic foraminiferal response to rapid climate change in Santa Barbara Basin, Ocean Drilling Program hole 893A: Paleoceanography, v. 15, no. 1, p. 30-42.

Henkes, G. A., Passey, B. H., Wanamaker, A. D., Grossman, E. L., Ambrose, W. G., and Carroll, M. L., 2013, Carbonate clumped isotope compositions of modern marine mollusk and brachiopod shells: Geochimica Et Cosmochimica Acta, v. 106, p. 307-325.

Hill, P. S., Tripati, A. K., and Schauble, E. A., 2014, Theoretical constraints on the effects of pH, salinity, and temperature on clumped isotope signatures of dissolved inorganic carbon species and precipitating carbonate minerals: Geochimica Et Cosmochimica Acta, v. 125, p. 610-652.

Hodell, D. A., Brenner, M. K., and Curtis, J. H., 2000, Climate change in the northern American tropics and subtropics since the last ice age: Implications for environment and culture, *in* Lentz, D. L., ed., An Imperfect Balance : Landscape Transformations in the Pre-Columbian Americas: New York, Columbia University Press, p. 547 p.

Hodell, D. A., Turchyn, A. V., Wiseman, C. J., Escobar, J., Curtis, J. H., Brenner, M., Gilli, A., Mueller, A. D., Anselmetti, F., Ariztegui, D., and Brown, E. T., 2012, Late Glacial temperature and precipitation changes in the lowland Neotropics by tandem measurement of $\delta^{18}O$ in biogenic carbonate and gypsum hydration water: Geochimica et Cosmochimica Acta, v. 77, p. 352-368.

Hough, B. G., Fan, M., and Passey, B., 2014, Calibration of the clumped isotope geothermometer in soil carbonate in Wyoming and Nebraska, USA: Implications for paleoelevation and paleoclimate reconstruction: Earth and Planetary Science Letters, v. 391, p. 110-120.

Huang, Y. M., and Fairchild, I. J., 2001, Partitioning of Sr^{2+} and Mg^{2+} into calcite under karst-analogue experimental conditions: Geochimica Et Cosmochimica Acta, v. 65, no. 1, p. 47-62.

Huntington, K. W., Eiler, J. M., Affek, H. P., Guo, W., Bonifacie, M., Yeung, L. Y., Thiagarajan, N., Passey, B., Tripati, A., Daeron, M., and Came, R., 2009, Methods and limitations of 'clumped' CO_2 isotope (Δ_{47}) analysis by gas-source isotope ratio mass spectrometry: J Mass Spectrom, v. 44, no. 9, p. 1318-1329.

Jiménez-Moreno, G., Anderson, R. S., Desprat, S., Grigg, L. D., Grimm, E. C., Heusser, L. E., Jacobs, B. F., López-Martínez, C., Whitlock, C. L., and Willard, D. A., 2010, Millennial-scale variability during the last glacial in vegetation records from North America: Quaternary Science Reviews, v. 29, no. 21-22, p. 2865-2881.

Jochum, K. P., Wilson, S. A., Abouchami, W., Amini, M., Chmeleff, J., Eisenhauer, A., Hegner, E., Iaccheri, L. M., Kieffer, B., Krause, J., McDonough, W. F., Mertz-Kraus, R., Raczek, I., Rudnick, R. L., Scholz, D., Steinhoefel, G., Stoll, B., Stracke, A., Tonarini, S., Weis, D., Weis, U., and Woodhead, J. D., 2011, GSD-1G and MPI-DING reference glasses for in situ and bulk isotopic determination: Geostandards and Geoanalytical Research, v. 35, no. 2, p. 193-226.

Johnsen, S. J., DahlJensen, D., Gundestrup, N., Steffensen, J. P., Clausen, H. B., Miller, H., Masson-Delmotte, V., Sveinbjornsdottir, A. E., and White, J., 2001, Oxygen isotope and palaeotemperature records from six Greenland ice-core stations: Camp Century, Dye-3, GRIP, GISP2, Renland and NorthGRIP: Journal of Quaternary Science, v. 16, no. 4, p. 299-307.

Johnson, L. R., Sharp, Z. D., Galewsky, J., Strong, M., Van Pelt, A. D., Dong, F., and Noone, D., 2011, Hydrogen isotope correction for laser instrument measurement bias at low water vapor concentration using conventional isotope analyses: application to measurements from Mauna Loa Observatory, Hawaii: Rapid Communications in Mass Spectrometry, v. 25, no. 5, p. 608-616.

Jouzel, J., Masson-Delmotte, V., Cattani, O., Dreyfus, G., Falourd, S., Hoffmann, G., Minster, B., Nouet, J., Barnola, J. M., Chappellaz, J., Fischer, H., Gallet, J. C., Johnsen, S., Leuenberger, M., Loulergue, L., Luethi, D., Oerter, H., Parrenin, F., Raisbeck, G., Raynaud, D., Schilt, A., Schwander, J., Selmo, E., Souchez, R., Spahni, R., Stauffer, B., Steffensen, J. P., Stenni, B., Stocker, T. F., Tison, J. L., Werner, M., and Wolff, E. W., 2007, Orbital and millennial Antarctic climate variability over the past 800,000 years: Science, v. 317, no. 5839, p. 793-796.

Jullien, E., Grousset, F., Malaizé, B., Duprat, J., Sanchez-Goni, M. F., Eynaud, F., Charlier, K., Schneider, R., Bory, A., Bout, V., and Flores, J. A., 2007, Low-latitude “dusty events” vs. high-latitude “icy Heinrich events”: Quaternary Research, v. 68, no. 3, p. 379-386.

Just, J., Heslop, D., von Dobeneck, T., Bickert, T., Dekkers, M. J., Frederichs, T., Meyer, I., and Zabel, M., 2012, Multiproxy characterization and budgeting of terrigenous end-members at the NW African continental margin: Geochemistry Geophysics Geosystems, v. 13.

Kaldi, J., and Gidman, J., 1982, Early diagenetic dolomite cements - Examples from the Permian Lower Magnesian limestone of England and the Pleistocene carbonates of the Bahamas: Journal of Sedimentary Petrology, v. 52, no. 4, p. 1073-1085.

Kanner, L. C., Burns, S. J., Cheng, H., and Edwards, R. L., 2012, High-latitude forcing of the South American summer monsoon during the Last Glacial: Science, v. 335, no. 6068, p. 570-573.

Keeling C., 1958, The concentration and isotopic abundances of atmospheric carbon dioxide in rural areas. Geochimica Et Cosmochimica Acta, v. 13, p. 322–334.

Keigwin, L. D., and Jones, G. A., 1994, Western North-Atlantic evidence for millennial-scale changes in ocean circulation and climate: Journal of Geophysical Research-Oceans, v. 99, no. C6, p. 12397-12410.

Kieber, R. J., Williams, K., Willey, J. D., Skrabal, S., and Avery, G. B., 2001, Iron speciation in coastal rainwater: concentration and deposition to seawater: Marine Chemistry, v. 73, no. 2, p. 83-95.

Kim, S. T., and O'Neil, J. R., 1997, Equilibrium and nonequilibrium oxygen isotope effects in synthetic carbonates: Geochimica et Cosmochimica Acta, v. 61, no. 16, p. 3461-3475.

Kluge, T., and Affek, H. P., 2012, Quantifying kinetic fractionation in Bunker Cave speleothems using Δ47: Quaternary Science Reviews, v. 49, p. 82-94.

Kluge, T., Affek, H. P., Marx, T., Aeschbach-Hertig, W., Riechelmann, D. F. C., Scholz, D., Riechelmann, S., Immenhauser, A., Richter, D. K., Fohlmeister, J., Wackerbarth, A., Mangini, A., and Spötl, C., 2012, Reconstruction of drip-water $\delta^{18}O$ based on calcite oxygen and clumped isotopes of speleothems from Bunker Cave (Germany): Climate of the Past Discussions, v. 8, no. 4, p. 2853-2892.

Kluge, T., Affek, H. P., Zhang, Y. G., Dublyansky, Y., Spotl, C., Immenhauser, A., and Richter, D. K., 2014, Clumped isotope thermometry of cryogenic cave carbonates: Geochimica Et Cosmochimica Acta, v. 126, p. 541-554.

Knippertz, P., and Todd, M. C., 2012, Mineral dust aerosols over the Sahara: meteorological controls on emission and transport and implications for modeling: Reviews of Geophysics, v. 50.

Kowalczk, A. J., and Froelich, P. N., 2010, Cave air ventilation and CO_2 outgassing by radon-222 modeling: How fast do caves breathe?: Earth and Planetary Science Letters, v. 289, no. 1-2, p. 209-219.

Kumar, A., Abouchami, W., Galer, S. J. G., Garrison, V. H., Williams, E., and Andreae, M. O., 2014, A radiogenic isotope tracer study of transatlantic dust transport from Africa to the Caribbean: Atmospheric Environment, v. 82, p. 130-143.

Lachniet, 2004, A 1500-year El Niño/Southern Oscillation and rainfall history for the Isthmus of Panama from speleothem calcite: Journal of Geophysical Research, v. 109, no. D20.

-, 2009, Climatic and environmental controls on speleothem oxygen-isotope values: Quaternary Science Reviews, v. 28, no. 5-6, p. 412-432.

Lachniet, M. S., Asmerom, Y., Bernal, J. P., Polyak, V. J., and Vazquez-Selem, L., 2013, Orbital pacing and ocean circulation-induced collapses of the Mesoamerican monsoon over the past 22,000 y: Proceedings of the National Academy of Sciences of the United States of America, v. 110, no. 23, p. 9255-9260.

Lambert, F., Kug, J. S., Park, R. J., Mahowald, N., Winckler, G., Abe-Ouchi, A., O'ishi, R., Takemura, T., and Lee, J. H., 2013, The role of mineral-dust aerosols in polar temperature amplification: Nature Climate Change, v. 3, no. 5, p. 487-491.

Lambert, W. J., 2010, High Resolution, U/Th Dated (32,000 to 11,000 Years), Oxygen and Carbon Isotope Proxy Climate Records from a Stalagmite in DeSoto Caverns, Alabama, USA [PhD: University of Alabama].

Lambert, W. J., and Aharon, P., 2011, Controls on dissolved inorganic carbon and $\delta^{13}C$ in cave waters from DeSoto Caverns: Implications for speleothem $\delta^{13}C$ assessments: Geochimica et Cosmochimica Acta, v. 75, no. 3, p. 753-768.

Landmann, G., and Reimer, A., 1996, Climatically induced lake level changes at Lake Van, Turkey, during the Pleistocene/Holocene transition: Global Biogiochemical Cycles, v. 10, no. 4, p. 797-808.

Lecuyer, C., and Oneil, J. R., 1994, Stable isotope compositions of fluid inclusions in biogenic carbonates: Bulletin De La Societe Geologique De France, v. 165, no. 6, p. 573-581.

Lee, Y. H., Lamarque, J. F., Flanner, M. G., Jiao, C., Shindell, D. T., Berntsen, T., Bisiaux, M. M., Cao, J., Collins, W. J., Curran, M., Edwards, R., Faluvegi, G., Ghan, S., Horowitz, L. W., McConnell, J. R., Ming, J., Myhre, G., Nagashima, T., Naik, V., Rumbold, S. T., Skeie, R. B., Sudo, K., Takemura, T., Thevenon, F., Xu, B., and Yoon, J. H., 2013, Evaluation of preindustrial to present-day black carbon and its albedo forcing from Atmospheric Chemistry and Climate Model Intercomparison Project (ACCMIP): Atmospheric Chemistry and Physics, v. 13, no. 5, p. 2607-2634.

Lewis, S. C., Gagan, M. K., Ayliffe, L. K., Zhao, J.-x., Hantoro, W. S., Treble, P. C., Hellstrom, J. C., LeGrande, A. N., Kelley, M., Schmidt, G. A., and Suwargadi, B. W., 2011, High-resolution stalagmite reconstructions of Australian–Indonesian monsoon rainfall variability during Heinrich stadial 3 and Greenland interstadial 4: Earth and Planetary Science Letters, v. 303, no. 1-2, p. 133-142.

Li, C., Battisti, D. S., and Bitz, C. M., 2010, Can North Atlantic sea ice anomalies account for Dansgaard-Oeschger climate signals: Journal of climate, v. 23, p. 5457-5475.

Li, H.-C., Ku, T.-L., You, C.-F., Cheng, H., Edwards, R. L., Ma, Z.-B., Tsai, W.-s., and Li, M.-D., 2005, $^{87}Sr/^{86}Sr$ and Sr/Ca in speleothems for paleoclimate reconstruction in Central China between 70 and 280 kyr ago: Geochimica et Cosmochimica Acta, v. 69, no. 16, p. 3933-3947.

Lippold, J., Grützner, J., Winter, D., Lahaye, Y., Mangini, A., and Christl, M., 2009, Does sedimentary $^{231}Pa/^{230}Th$ from the Bermuda Rise monitor past Atlantic Meridional Overturning Circulation?: Geophysical Research Letters, v. 36, no. 12.

Lisiecki, L. E., 2005, A Pliocene-Pleistocene stack of 57 globally distributed benthic $\delta^{18}O$ records: Paleoceanography, v. 20, no. 1.

Lorens, R. B., 1981, Sr, Cd, Mn and Co distribution coefficients in calcite as a function of calcite precipitation rate: Geochimica Et Cosmochimica Acta, v. 45, no. 4, p. 553-561.

Lynch-Stieglitz, J., Schmidt, M. W., Henry, L. G., Curry, W. B., Skinner, L. C., Mulitza, S., Zhang, R., and Chang, P., 2014, Muted change in Atlantic overturning circulation over some glacial-aged Heinrich events: Nature Geoscience.

Macayeal, D. R., 1993, A low-order model of the Heinrich event cycle: Paleoceanography, v. 8, no. 6, p. 767-773.

Magana, V., Amador, J. A., and Medina, S., 1999, The midsummer drought over Mexico and Central America: Journal of Climate, v. 12, no. 6, p. 1577-1588.

Maher, B. A., Prospero, J. M., Mackie, D., Gaiero, D., Hesse, P. P., and Balkanski, Y., 2010, Global connections between aeolian dust, climate and ocean biogeochemistry at the present day and at the last glacial maximum: Earth-Science Reviews, v. 99, no. 1-2, p. 61-97.

Maher, B. A., and Thompson, R., 2012, Oxygen isotopes from Chinese caves: records not of monsoon rainfall but of circulation regime: Journal of Quaternary Science, v. 27, no. 6, p. 615-624.

Mahowald, N. M., Kloster, S., Engelstaedter, S., Moore, J. K., Mukhopadhyay, S., McConnell, J. R., Albani, S., Doney, S. C., Bhattacharya, A., Curran, M. A. J., Flanner, M. G., Hoffman, F. M., Lawrence, D. M., Lindsay, K., Mayewski, P. A., Neff, J., Rothenberg, D., Thomas, E., Thornton, P. E., and Zender, C. S., 2010, Observed 20th century desert dust variability: impact on climate and biogeochemistry: Atmospheric Chemistry and Physics, v. 10, no. 22, p. 10875-10893.

Mahowald, N. M., Muhs, D. R., Levis, S., Rasch, P. J., Yoshioka, M., Zender, C. S., and Luo, C., 2006, Change in atmospheric mineral aerosols in response to climate: Last glacial period, preindustrial, modern, and doubled carbon dioxide climates: Journal of Geophysical Research-Atmospheres, v. 111, no. D10.

Martinez-Garcia, A., Rosell-Mele, A., Jaccard, S. L., Geibert, W., Sigman, D. M., and Haug, G. H., 2011, Southern Ocean dust-climate coupling over the past four million years: Nature, v. 476, no. 7360, p. 312-315.

Martinez-Garcia, A., Sigman, D. M., Ren, H., Anderson, R. F., Straub, M., Hodell, D. A., Jaccard, S. L., Eglinton, T. I., and Haug, G. H., 2014, Iron fertilization of the Subantarctic Ocean during the last ice age: Science, v. 343, no. 6177, p. 1347-1350.

Martins, V. A., Santos, J. F., Mackensen, A., Dias, J. A., Ribeiro, S., Moreno, J. C., Soares, A. M., Frontalini, F., Rey, D., and Rocha, F., 2013, The sources of the glacial IRD in the NW Iberian Continental Margin over the last 40 ka: Quaternary International, v. 318, p. 128-138.

Martrat, B., Grimalt, J. O., Shackleton, N. J., de Abreu, L., Hutterli, M. A., and Stocker, T. F., 2007, Four climate cycles of recurring deep and surface water destabilizations on the Iberian margin: Science, v. 317, no. 5837, p. 502-507.

Mattey, D., Lowry, D., Duffet, J., Fisher, R., Hodge, E., and Frisia, S., 2008, A 53 year seasonally resolved oxygen and carbon isotope record from a modem Gibraltar speleothem: Reconstructed drip water and relationship to local precipitation: Earth and Planetary Science Letters, v. 269, no. 1-2, p. 80-95.

Matthews, A., Ayalon, A., and Bar-Matthews, M., 2000, D/H ratios of fluid inclusions of Soreq cave (Israel) speleothems as a guide to the Eastern Mediterranean Meteoric Line relationships in the last 120 ky: Chemical Geology, v. 166, no. 3-4, p. 183-191.

McDermott, F., 2004, Palaeo-climate reconstruction from stable isotope variations in speleothems: a review: Quaternary Science Reviews, v. 23, no. 7-8, p. 901-918.

McGee, D., Broecker, W. S., and Winckler, G., 2010, Gustiness: The driver of glacial dustiness?: Quaternary Science Reviews, v. 29, no. 17-18, p. 2340-2350.

McGee, D., deMenocal, P. B., Winckler, G., Stuut, J. B. W., and Bradtmiller, L. I., 2013, The magnitude, timing and abruptness of changes in North African dust deposition over the last 20,000 yr: Earth and Planetary Science Letters, v. 371, p. 163-176.

McGee, D., Donohoe, A., Marshall, J., and Ferreira, D., 2014, Changes in ITCZ location and cross-equatorial heat transport at the Last Glacial Maximum, Heinrich Stadial 1, and the mid-Holocene: Earth and Planetary Science Letters, v. 390, p. 69-79.

McGee, D., Quade, J., Edwards, R. L., Broecker, W. S., Cheng, H., Reiners, P. W., and Evenson, N., 2012, Lacustrine cave carbonates: Novel archives of paleohydrologic change in the Bonneville Basin (Utah, USA): Earth and Planetary Science Letters, v. 351, p. 182-194.

McManus, J. F., 1999, A 0.5 million year record of millennial scale climate variability in the North Atlantic: Science, v. 283, no. 5404, p. 971-975.

McManus, J. F., Francois, R., Gherardi, J. M., Keigwin, L. D., and Brown-Leger, S., 2004, Collapse and rapid resumption of Atlantic meridional circulation linked to deglacial climate changes: Nature, v. 428, no. 6985, p. 834-837.

Meckler, A. N., Sigman, D. M., Gibson, K. A., Francois, R., Martinez-Garcia, A., Jaccard, S. L., Rohl, U., Peterson, L. C., Tiedemann, R., and Haug, G. H., 2013, Deglacial pulses of deep-ocean silicate into the subtropical North Atlantic Ocean: Nature, v. 495, no. 7442, p. 495.

Menviel, L., Timmermann, A., Friedrich, T., and England, M. H., 2014, Hindcasting the continuum of Dansgaard–Oeschger variability: mechanisms, patterns and timing: Climate of the Past, v. 10, no. 1, p. 63-77.

Menviel, L., Timmermann, A., Timm, O. E., and Mouchet, A., 2011, Deconstructing the Last Glacial termination: the role of millennial and orbital-scale forcings: Quaternary Science Reviews, v. 30, no. 9-10, p. 1155-1172.

Meyer, M. C., Spotl, C., Mangini, A., and Tessadri, R., 2012, Speleothem deposition at the glaciation threshold - An attempt to constrain the age and paleoenvironmental significance of a detrital-rich flowstone sequence from Entrische Kirche Cave (Austria): Palaeogeography Palaeoclimatology Palaeoecology, v. 319, p. 93-106.

Mickler, P. J., Banner, J. L., Stern, L., Asmerom, Y., Edwards, R. L., and Ito, E., 2004, Stable isotope variations in modern tropical speleothems: Evaluating equilibrium vs. kinetic isotope effects: Geochimica Et Cosmochimica Acta, v. 68, no. 21, p. 4381-4393.

Mickler, P. J., Stern, L. A., and Banner, J. L., 2006, Large kinetic isotope effects in modern speleothems: Geological Society of America Bulletin, v. 118, no. 1-2, p. 65-81.

Mohtadi, M., Prange, M., Oppo, D. W., De Pol-Holz, R., Merkel, U., Zhang, X., Steinke, S., and Luckge, A., 2014, North Atlantic forcing of tropical Indian Ocean climate: Nature, v. 509, no. 7498, p. 76-80.

Moore, C. E., 1989, Carbonate diagenesis and porosity, New York, NY, Elsevier, Developments in Sedimentology.

Moreno, A., Stoll, H., Jiménez-Sánchez, M., Cacho, I., Valero-Garcés, B., Ito, E., and Edwards, R. L., 2010a, A speleothem record of glacial (25–11.6 kyr BP) rapid climatic changes from northern Iberian Peninsula: Global and Planetary Change, v. 71, no. 3-4, p. 218-231.

Moreno, A., Valero-Garces, B. L., Jimenez-Sanchez, M., Dominguez-Cuesta, M. J., Mata, M. P., Navas, A., Gonzalez-Samperiz, P., Stoll, H., Farias, P., Morellon, M., Corella, J. P., and Rico, M., 2010b, The last deglaciation in the Picos de Europa National Park (Cantabrian Mountains, northern Spain): Journal of Quaternary Science, v. 25, no. 7, p. 1076-1091.

Mosblech, N. A. S., Bush, M. B., Gosling, W. D., Hodell, D., Thomas, L., van Calsteren, P., Correa-Metrio, A., Valencia, B. G., Curtis, J., and van Woesik, R., 2012, North Atlantic forcing of Amazonian precipitation during the last ice age: Nature Geoscience, v. 5, no. 11, p. 817-820.

Mühlinghaus, C., Scholz, D., and Mangini, A., 2009, Modelling fractionation of stable isotopes in stalagmites: Geochimica et Cosmochimica Acta, v. 73, no. 24, p. 7275-7289.

Muhs, D. R., 2012, The geologic records of dust in the Quaternary: Aeolian Research.

Muhs, D. R., Budahn, J. R., Prospero, J. M., and Carey, S. N., 2007, Geochemical evidence for African dust inputs to soils of western Atlantic islands: Barbados, the Bahamas, and Florida: Journal of Geophysical Research, v. 112, no. F2.

Mulitza, S., Prange, M., Stuut, J.-B., Zabel, M., von Dobeneck, T., Itambi, A. C., Nizou, J., Schulz, M., and Wefer, G., 2008, Sahel megadroughts triggered by glacial slowdowns of Atlantic meridional overturning: Paleoceanography, v. 23, no. 4.

Muller, J., McManus, J. F., Oppo, D. W., and Francois, R., 2012, Strengthening of the Northeast Monsoon over the Flores Sea, Indonesia, at the time of Heinrich event 1: Geology, v. 40, no. 7, p. 635-638.

Munksgaard, N. C., Wurster, C. M., and Bird, M. I., 2011, Continuous analysis of $\delta^{18}O$ and δD values of water by diffusion sampling cavity ring-down spectrometry: a novel sampling device for unattended field monitoring of precipitation, ground and surface waters: Rapid Communications in Mass Spectrometry, v. 25, no. 24, p. 3706-3712.

Murphy, L. N., Clement, A. C., Albani, S., Mahowald, N. M., Swart, P. K., and Arienzo, M. M., 2014, Simulated changes in atmospheric dust in response to a Heinrich stadial: Paleoceanography, v. 29, no. 1, p. 30-43.

Murray, S. T., Arienzo, M. M., and Swart, P. K., Submitted, Applications of the clumped isotopic method to the study of dolomitization in the Bahamas: Implications for the interpretation of clumped isotopes in dolomites: Geochimica et Cosmochimica Acta.

Mylroie, J. E., and Mylroie, J. R., 2009, Caves of the Bahamas, Guidebook for Excursion No. 82, 15th International Congress of Speleology: Huntsville, Alabama, National Speleological Society, p. 76

O'Neil, J. R., Clayton, R. N., and Mayeda, T. K., 1969, Oxygen isotope fractionation in divalent metal carbonates: Journal of Chemical Physics, v. 51, no. 12, p. 5547-&.

Orland, I. J., Bar-Matthews, M., Ayalon, A., Matthews, A., Kozdon, R., Ushikubo, T., and Valley, J. W., 2012, Seasonal resolution of Eastern Mediterranean climate change since 34 ka from a Soreq Cave speleothem: Geochimica et Cosmochimica Acta, v. 89, p. 240-255.

Oster, J. L., Montañez, I. P., Guilderson, T. P., Sharp, W. D., and Banner, J. L., 2010, Modeling speleothem $\delta^{13}C$ variability in a central Sierra Nevada cave using ^{14}C and $^{87}Sr/^{86}Sr$: Geochimica et Cosmochimica Acta, v. 74, no. 18, p. 5228-5242.

Oster, J. L., Montañez, I. P., Mertz-Kraus, R., Sharp, W. D., Stock, G. M., Spero, H. J., Tinsley, J., and Zachos, J. C., 2014, Millennial-scale variations in western Sierra Nevada precipitation during the last glacial cycle MIS 4/3 transition: Quaternary Research.

Overpeck, J. T., and Cole, J. E., 2006, Abrupt change in Earth's climate system: Annual Review of Environment and Resources, v. 31, no. 1, p. 1-31.

Panagiotopoulos, K., Bohm, A., Leng, M. J., Wagner, B., and Schabitz, F., 2014, Climate variability over the last 92 ka in SW Balkans from analysis of sediments from Lake Prespa: Climate of the Past, v. 10, no. 2, p. 643-660.

Partin, J. W., Cobb, K. M., Adkins, J. F., Clark, B., and Fernandez, D. P., 2007, Millennial-scale trends in west Pacific warm pool hydrology since the Last Glacial Maximum: Nature, v. 449, no. 7161, p. 452-455.

Partin, J. W., Cobb, K. M., Adkins, J. F., Tuen, A. A., and Clark, B., 2013, Trace metal and carbon isotopic variations in cave dripwater and stalagmite geochemistry from northern Borneo: Geochemistry Geophysics Geosystems, v. 14, no. 9, p. 3567-3585.

Passey, B. H., and Henkes, G. A., 2012, Carbonate clumped isotope bond reordering and geospeedometry: Earth and Planetary Science Letters, v. 351, p. 223-236.

Passey, B. H., Levin, N. E., Cerling, T. E., Brown, F. H., and Eiler, J. M., 2010, High-temperature environments of human evolution in East Africa based on bond ordering in paleosol carbonates: Proceedings of the National Academy of Sciences of the United States of America, v. 107, no. 25, p. 11245-11249.

Patton, G. M., Martin, P. A., Voelker, A., and Salgueiro, E., 2011, Multiproxy comparison of oceanographic temperature during Heinrich Events in the eastern subtropical Atlantic: Earth and Planetary Science Letters, v. 310, no. 1-2, p. 45-58.

Pausata, F. S. R., Battisti, D. S., Nisancioglu, K. H., and Bitz, C. M., 2011, Chinese stalagmite $\delta^{18}O$ controlled by changes in the Indian monsoon during a simulated Heinrich event: Nature Geoscience, v. 4, no. 7, p. 474-480.

Perrette, Y., Delannoy, J. J., Desmet, M., Lignier, V., and Destombes, J. L., 2005, Speleothem organic matter content imaging. The use of a Fluorescence Index to characterise the maximum emission wavelength: Chemical Geology, v. 214, no. 3-4, p. 193-208.

Petersen, S. V., Schrag, D., and Clark, P. U., 2013, A new mechanism for Dansgaard-Oeschger cycels: Paleoceanography, v. 28, p. 24-30.

Peterson, L. C., Haug, G. H., Hughen, K. A., and Rohl, U., 2000, Rapid changes in the hydrologic cycle of the tropical Atlantic during the last glacial: Science, v. 290, no. 5498, p. 1947-1951.

Pourmand, A., Marcantonio, F., and Schulz, H., 2004, Variations in productivity and eolian fluxes in the northeastern Arabian Sea during the past 110 ka: Earth and Planetary Science Letters, v. 221, no. 1-4, p. 39-54.

Pourmand, A., Prospero, J. M., and Sharfi, A., 2014a, Geochemical fingerprinting of trans-Atlantic African dust based on radiogenic Sr-Nd-Hf isotopes and rare earth element anomalies: Geology, v. 42, no. 8, p. 675-678.

Pourmand, A., Tissot, F. L. H., Arienzo, M. M., and Sharifi, A., 2014b, Introducing a comprehensive data reduction and uncertainty propagation algorithm for U-Th geochronometry with extraction chromatography and isotope dilution MC-ICP-MS: Geostandards and Geoanalytical Research, v. 38, no. 2, p. 129-148.

Price, R. M., Swart, P. K., and Willoughby, H. E., 2008, Seasonal and spatial variation in the stable isotopic composition ($\delta^{18}O$ and δD) of precipitation in south Florida: Journal of Hydrology, v. 358, no. 3-4, p. 193-205.

Prospero, J. M., and Lamb, P. J., 2003, African droughts and dust transport to the Caribbean: climate change implications: Science, v. 302, no. 5647, p. 1024-1027.

Prospero, J. M., Landing, W. M., and Schulz, M., 2010, African dust deposition to Florida: Temporal and spatial variability and comparisons to models: Jornal of Geophysical Research, v. 115.

Pye, K., and Johnson, R., 1988, Stratigraphy, geochemistry and thermoluminescence ages of lower Mississippi Valley loess: Earth Surface Processes and Landforms, v. 13, p. 103-124.

Reid, E. A., 2003, Characterization of African dust transported to Puerto Rico by individual particle and size segregated bulk analysis: Journal of Geophysical Research, v. 108, no. D19.

Richards, D. A., and Dorale, J. A., 2003, Uranium-series chronology and environmental applications of speleothems, *in* Bourdon, B., ed., Reviews in Mineralogy and Geophysics: Uranium-series Geochemistry, Volume 52: Washington, DC, Mineralogical Society of America.

Richards, D. A., Smart, P. L., and Edwards, R. L., 1994, Maximum sea levels for the Last Glacial Period from U-series ages of submerged speleothems: Nature, v. 367, no. 6461, p. 357-360.

Richter, D. K., Gotte, T., Niggemann, S., and Wurth, G., 2004, REE^{3+} and Mn^{2+} activated cathodoluminescence in lateglacial and Holocene stalagmites of central Europe: evidence for climatic processes?: Holocene, v. 14, no. 5, p. 759-767.

Riechelmann, D. F. C., Deininger, M., Scholz, D., Riechelmann, S., Schroder-Ritzrau, A., Spotl, C., Richter, D. K., Mangini, A., and Immenhauser, A., 2013, Disequilibrium carbon and oxygen isotope fractionation in recent cave calcite: Comparison of cave precipitates and model data: Geochimica Et Cosmochimica Acta, v. 103, p. 232-244.

Riechelmann, D. F. C., Schroder-Ritzrau, A., Scholz, D., Fohlmeister, J., Spotl, C., Richter, D. K., and Mangini, A., 2011, Monitoring Bunker Cave (NW Germany): A prerequisite to interpret geochemical proxy data of speleothems from this site: Journal of Hydrology, v. 409, no. 3-4, p. 682-695.

Romanek, C. S., Grossman, E. L., and Morse, J. W., 1992, Carbon isotopic fractionation in synthetic aragonite and calcite - effects of temperature and precipitation rate: Geochimica Et Cosmochimica Acta, v. 56, no. 1, p. 419-430.

Rossinsky, V., and Wanless, H. R., 1992, Topographic and vegetative controls on calcrete formation, Turks and Caicos Islands, British West Indies: Journal of Sedimentary Petrology, v. 62, no. 1, p. 84-98.

Rossinsky, V., Wanless, H. R., and Swart, P. K., 1992, Penetrative calcretes and their stratigraphic implications: Geology, v. 20, no. 4, p. 331-334.

Rowe, P. J., Mason, J. E., Andrews, J. E., Marca, A. D., Thomas, L., van Calsteren, P., Jex, C. N., Vonhof, H. B., and Al-Omari, S., 2012, Speleothem isotopic evidence of winter rainfall variability in northeast Turkey between 77 and 6 ka: Quaternary Science Reviews, v. 45, p. 60-72.

Rubinson, M., and Clayton, R. N., 1969, Carbon-13 fractionation between aragonite and calcite: Geochimica et Cosmochimica Acta, v. 33, no. 8, p. 997-1002.

Russell, J. M., Vogel, H., Konecky, B. L., Bijaksana, S., Huang, Y. S., Melles, M., Wattrus, N., Costa, K., and King, J. W., 2014, Glacial forcing of central Indonesian hydroclimate since 60,000 y BP: Proceedings of the National Academy of Sciences of the United States of America, v. 111, no. 14, p. 5100-5105.

Ruth, U., Bigler, M., Rothlisberger, R., Siggaard-Andersen, M. L., Kipfstuhl, S., Goto-Azuma, K., Hansson, M. E., Johnsen, S. J., Lu, H. Y., and Steffensen, J. P., 2007, Ice core evidence for a very tight link between North Atlantic and east Asian glacial climate: Geophysical Research Letters, v. 34, no. 3.

Sachs, J. P., and Lehman, S. J., 1999, Subtropical North Atlantic temperatures 60,000 to 30,000 years ago: Science, v. 286, no. 5440, p. 756-759.

Schauble, E. A., Ghosh, P., and Eiler, J. M., 2006, Preferential formation of C-13-O-18 bonds in carbonate minerals, estimated using first-principles lattice dynamics: Geochimica Et Cosmochimica Acta, v. 70, no. 10, p. 2510-2529.

Schmidt, M., Maseyk, K., Lett, C., Biron, P., Richard, P., Bariac, T., and Seibt, U., 2012, Reducing and correcting for contamination of ecosystem water stable isotopes measured by isotope ratio infrared spectroscopy: Rapid Communications in Mass Spectrometry, v. 26, no. 2, p. 141-153.

Schmidt, M. W., Spero, H. J., and Lea, D. W., 2004, Links between salinity variation in the Caribbean and North Atlantic thermohaline circulation: Nature, v. 428, no. 6979, p. 160-163.

Schulz, H., Von Rad, U., and Erlenkeuser, H., 1998, Correlation between Arabian Sea and Greenland climate oscillations of the past 110,000 years: Nature, v. 393.

Schwarcz, H. P., Harmon, R. S., Thompson, P., and Ford, D. C., 1976, Stable isotope studies of fluid inclusions in speleothems and their paleoclimatic significance: Geochimica et Cosmochimica Acta, v. 40, no. 6, p. 657-665.

Seager, R., and Battisti, D., 2007, Challenges to our understanding of the general circulation: Abrupt climate change, *in* T., S., and Sobel, A. H., eds., The Global Circulation of the Atmosphere: Princeton, N. J., Princeton Univ. Press, p. 331–371.

Sharp, Z. D., Atudorei, V., and Durakiewicz, T., 2001, A rapid method for determination of hydrogen and oxygen isotope ratios from water and hydrous minerals: Chemical Geology, v. 178, no. 1-4, p. 197-210.

Shepherd, T. J., 1977, Fluid inclusion study of gold-uranium ores: Philosophical Transactions of the Royal Society a-Mathematical Physical and Engineering Sciences, v. 286, no. 1336, p. 549.

Siddall, M., Rohling, E. J., Blunier, T., and Spahni, R., 2010, Patterns of millennial variability over the last 500 ka: Climate of the Past, v. 6, no. 3, p. 295-303.

Sima, A., Kageyama, M., Rousseau, D. D., Ramstein, G., Balkanski, Y., Antoine, P., and Hatte, C., 2013, Modeling dust emission response to North Atlantic millennial-scale climate variations from the perspective of East European MIS 3 loess deposits: Climate of the Past, v. 9, no. 4, p. 1385-1402.

Sinha, A., Cannariato, K. G., Stott, L. D., Cheng, H., Edwards, R. L., Yadava, M. G., Ramesh, R., and Singh, I. B., 2007, A 900-year (600 to 1500 A. D.) record of the Indian summer monsoon precipitation from the core monsoon zone of India: Geophysical Research Letters, v. 34, no. 16.

Spotl, C., Fairchild, I. J., and Tooth, A. F., 2005, Cave air control on dripwater geochemistry, Obir Caves (Austria): Implications for speleothem deposition in dynamically ventilated caves: Geochimica et Cosmochimica Acta, v. 69, no. 10, p. 2451-2468.

Stager, J. C., Ryves, D. B., Chase, B. M., and Pausata, F. S., 2011, Catastrophic drought in the Afro-Asian monsoon region during Heinrich event 1: Science, v. 331, no. 6022, p. 1299-1302.

Svensson, A., Andersen, K. K., Bigler, M., Clausen, H. B., Dahl-Jensen, D., Davies, S. M., Johnsen, S. J., Muscheler, R., Parrenin, F., Rasmussen, S. O., Roethlisberger, R., Seierstad, I., Steffensen, J. P., and Vinther, B. M., 2008, A 60 000 year Greenland stratigraphic ice core chronology: Climate of the Past, v. 4, no. 1, p. 47-57.

Swart, P., Oehlert, A., Mackenzie, G., Eberli, G., and Reijmer, J., 2014, The fertilization of the Bahamas by Saharan dust: A trigger for carbonate precipitation?: Geology.

Swart, P. K., Burns, S. J., and Leder, J. J., 1991, Fractionation of the stable isotopes of oxygen and carbon in carbon-dioxide during the reaction of calcite with phosphoric acid as a function of temperature and technique: Chemical Geology, v. 86, no. 2, p. 89-96.

Swart, P. K., Cantrell, D. L., Murray, S. T., and Arienzo, M. M., In Prep, Dolomitization in the Ghawar field: An update based on the clumped isotope technique: Geochimica et Cosmochimica Acta.

Tang, J., Dietzel, M., Fernandez, A., Tripati, A. K., and Rosenheim, B. E., 2014, Evaluation of kinetic effects on clumped isotope fractionation (Δ47) during inorganic calcite precipitation: Geochimica et Cosmochimica Acta, v. 134, p. 120-136.

Thiagarajan, N., Adkins, J., and Eiler, J., 2011, Carbonate clumped isotope thermometry of deep-sea corals and implications for vital effects: Geochimica et Cosmochimica Acta, v. 75, no. 16, p. 4416-4425.

Tierney, J. E., Russell, J. M., Sinninghe Damste, J. S., Huang, Y., and Verschuren, D., 2011, Late Quaternary behavior of the East African monsoon and the importance of the Congo Air Boundary: Quaternary Science Reviews, v. 30, p. 798-807.

Timmermann, A., Gildor, H., Schulz, M., and Tziperman, E., 2003, Coherent resonant millennial-scale climate oscillations triggered by massive meltwater pulses: Journal of Climate, v. 16, no. 15, p. 2569-2585.

Tjallingii, R., Claussen, M., Stuut, J.-B. W., Fohlmeister, J., Jahn, A., Bickert, T., Lamy, F., and Röhl, U., 2008, Coherent high- and low-latitude control of the northwest African hydrological balance: Nature Geoscience, v. 1, no. 10, p. 670-675.

Tooth, A. F., and Fairchild, I. J., 2003, Soil and karst aquifer hydrological controls on the geochemical evolution of speleothem-forming drip waters, Crag Cave, southwest Ireland: Journal of Hydrology, v. 273, no. 1-4, p. 51-68.

Trapp, J. M., Millero, F. J., and Prospero, J. M., 2010, Temporal variability of the elemental composition of African dust measured in trade wind aerosols at Barbados and Miami: Marine Chemistry, v. 120, no. 1-4, p. 71-82.

Tremaine, D. M., and Froelich, P. N., 2013, Speleothem trace element signatures: A hydrologic geochemical study of modern cave dripwaters and farmed calcite: Geochimica Et Cosmochimica Acta, v. 121, p. 522-545.

Tremaine, D. M., Froelich, P. N., and Wang, Y., 2011, Speleothem calcite farmed in situ: Modern calibration of $\delta^{18}O$ and $\delta^{13}C$ paleoclimate proxies in a continuously-monitored natural cave system: Geochimica et Cosmochimica Acta, v. 75, no. 17, p. 4929-4950.

Tripati, A. K., Eagle, R. A., Thiagarajan, N., Gagnon, A. C., Bauch, H., Halloran, P. R., and Eiler, J. M., 2010, ^{13}C–^{18}O isotope signatures and 'clumped isotope' thermometry in foraminifera and coccoliths: Geochimica et Cosmochimica Acta, v. 74, no. 20, p. 5697-5717.

Urey, H. C., 1947, The thermodynamic properties of isotopic substances: Journal of the Chemical Society, no. May, p. 562-581.

Vahrenkamp, V. C., Swart, P. K., and Ruiz, J., 1991, Episodic dolomitization of Late Cenozoic carbonates in the Bahamas - Evidence from strontium isotopes: Journal of Sedimentary Petrology, v. 61, no. 6, p. 1002-1014.

van Breukelen, M. R., Vonhof, H. B., Hellstrom, J. C., Wester, W. C. G., and Kroon, D., 2008, Fossil dripwater in stalagmites reveals Holocene temperature and rainfall variation in Amazonia: Earth and Planetary Science Letters, v. 275, no. 1-2, p. 54-60.

Vellinga, M., and Wood, R. A., 2002, Global climatic impacts of a collapse of the Atlantic thermohaline circulation: Climatic Change, v. 54, no. 3, p. 251-267.

Verheyden, S., Keppens, E., Fairchild, I., McDermott, F., and Weis, D., 2000, Mg, Sr and Sr isotope geochemistry of a Belgian Holocene speleothem: implications for paleoclimate reconstructions: Chemical Geology, v. 169, no. 1-2, p. 131-144.

Verheyden, V., 2004, Trace elements in speleothems: A short review of the state of the art: International Journal of Speleology, v. 33, p. 6.

Voelker, A. H. L., 2002, Global distribution of centennial-scale records for Marine Isotope Stage (MIS) 3: a database: Quaternary Science Reviews, v. 21, no. 10, p. 1185-1212.

von Rad, U., Schulz, H., Riech, V., den Dulk, M., Berner, U., and Sirocko, F., 1999, Multiple monsoon-controlled breakdown of oxygen-minimum conditions during the past 30,000 years documented in laminated sediments off pakistan: Palaeogeography, Palaeoclimatology, Palaeoecology, v. 152, p. 129-161.

Vonhof, H. B., van Breukelen, M. R., Postma, O., Rowe, P. J., Atkinson, T. C., and Kroon, D., 2006, A continuous-flow crushing device for on-line delta2H analysis of fluid inclusion water in speleothems: Rapid Communications in Mass Spectrometry, v. 20, no. 17, p. 2553-2558.

Wagner, J. D. M., Cole, J. E., Beck, J. W., Patchett, P. J., Henderson, G. M., and Barnett, H. R., 2010, Moisture variability in the southwestern United States linked to abrupt glacial climate change: Nature Geoscience, v. 3, no. 2, p. 110-113.

Wainer, K., Genty, D., Blamart, D., Daëron, M., Bar-Matthews, M., Vonhof, H., Dublyansky, Y., Pons-Branchu, E., Thomas, L., van Calsteren, P., Quinif, Y., and Caillon, N., 2011, Speleothem record of the last 180 ka in Villars cave (SW France): Investigation of a large $\delta^{18}O$ shift between MIS6 and MIS5: Quaternary Science Reviews, v. 30, no. 1-2, p. 130-146.

Wang, Auler, A. S., Edwards, R. L., Cheng, H., Cristalli, P. S., Smart, P. L., Richards, D. A., and Shen, C. C., 2004a, Wet periods in northeastern Brazil over the past 210 kyr linked to distant climate anomalies: Nature, v. 432, no. 7018, p. 740-743.

Wang, X., Auler, A. S., Edwards, R. L., Cheng, H., Ito, E., Wang, Y., Kong, X., and Solheid, M., 2007, Millennial-scale precipitation changes in southern Brazil over the past 90,000 years: Geophysical Research Letters, v. 34, no. 23.

Wang, Y., Cheng, H., Edwards, R. L., Kong, X., Shao, X., Chen, S., Wu, J., Jiang, X., Wang, X., and An, Z., 2008, Millennial- and orbital-scale changes in the East Asian monsoon over the past 224,000 years: Nature, v. 451, no. 7182, p. 1090-1093.

Wang, Y. J., Cheng, H., Edwards, R. L., An, Z. S., Wu, J. Y., Shen, C. C., and Dorale, J. A., 2001, A high-resolution absolute-dated late Pleistocene Monsoon record from Hulu Cave, China: Science, v. 294, no. 5550, p. 2345-2348.

Wang, Z. G., Schauble, E. A., and Eiler, J. M., 2004b, Equilibrium thermodynamics of multiply substituted isotopologues of molecular gases: Geochimica Et Cosmochimica Acta, v. 68, no. 23, p. 4779-4797.

Weber, M. E., Clark, P. U., Kuhn, G., Timmermann, A., Sprenk, D., Gladstone, R., Zhang, X., Lohmann, G., Menviel, L., Chikamoto, M. O., Friedrich, T., and Ohlwein, C., 2014, Millennial-scale variability in Antarctic ice-sheet discharge during the last deglaciation: Nature, v. 510, no. 7503, p. 134.

Weirauch, D., Billups, K., and Martin, P., 2008, Evolution of millennial-scale climate variability during the mid-Pleistocene: Paleoceanography, v. 23, no. 3, p. PA3216.

West, A. G., Goldsmith, G. R., Brooks, P. D., and Dawson, T. E., 2010, Discrepancies between isotope ratio infrared spectroscopy and isotope ratio mass spectrometry for the stable isotope analysis of plant and soil waters: Rapid Communications in Mass Spectrometry, v. 24, no. 14, p. 1948-1954.

West, A. G., Goldsmith, G. R., Matimati, I., and Dawson, T. E., 2011, Spectral analysis software improves confidence in plant and soil water stable isotope analyses performed by isotope ratio infrared spectroscopy (IRIS): Rapid Communications in Mass Spectrometry, v. 25, no. 16, p. 2268-2274.

White, W. B., 1976, Cave minerals and speleothems, *in* Ford, T. D., ed., The Science of Speleology: London, Academic Press, p. 267-327.

Wolff, E. W., Chappellaz, J., Blunier, T., Rasmussen, S. O., and Svensson, A., 2010, Millennial-scale variability during the last glacial: The ice core record: Quaternary Science Reviews, v. 29, no. 21-22, p. 2828-2838.

Wong, C. I., Banner, J. L., and Musgrove, M., 2011, Seasonal dripwater Mg/Ca and Sr/Ca variations driven by cave ventilation: Implications for and modeling of speleothem paleoclimate records: Geochimica Et Cosmochimica Acta, v. 75, no. 12, p. 3514-3529.

Yanes, Y., and Romanek, C. S., 2013, Quaternary interglacial environmental stability in San Salvador Island (Bahamas): A land snail isotopic approach: Palaeogeography Palaeoclimatology Palaeoecology, v. 369, p. 28-40.

Yoshioka, M., Mahowald, N. M., Conley, A. J., Collins, W. D., Fillmore, D. W., Zender, C. S., and Coleman, D. B., 2007, Impact of desert dust radiative forcing on Sahel precipitation: Relative importance of dust compared to sea surface temperature variations, vegetation changes, and greenhouse gas warming: Journal of Climate, v. 20, no. 8, p. 1445-1467.

Zaarur, S., Affek, H. P., and Brandon, M. T., 2013, A revised calibration of the clumped isotope thermometer: Earth and Planetary Science Letters, v. 382, p. 47-57.

Zaarur, S., Olack, G., and Affek, H. P., 2011, Paleo-environmental implication of clumped isotopes in land snail shells: Geochimica et Cosmochimica Acta, v. 75, no. 22, p. 6859-6869.

Zhang, R., and Delworth, T. L., 2005, Simulated tropical response to a substantial weakening of the Atlantic thermohaline circulation: Journal of Climate, v. 18, no. 12, p. 1853-1860.

Zhao, K., Wang, Y., Edwards, R. L., Cheng, H., and Liu, D., 2010, High-resolution stalagmite $\delta^{18}O$ records of Asian monsoon changes in central and southern China spanning the MIS 3/2 transition: Earth and Planetary Science Letters, v. 298, no. 1-2, p. 191-198.

Zhou, H., Chi, B., Lawrence, M., Zhao, J., Yan, J., Greig, A., and Feng, Y., 2008, High-resolution and precisely dated record of weathering and hydrological dynamics recorded by manganese and rare-earth elements in a stalagmite from Central China: Quaternary Research, v. 69, no. 3, p. 438-446.

Zhou, H., Feng, Y.-x., Zhao, J.-x., Shen, C.-C., You, C.-F., and Lin, Y., 2009, Deglacial variations of Sr and $^{87}Sr/^{86}Sr$ ratio recorded by a stalagmite from Central China and their association with past climate and environment: Chemical Geology, v. 268, no. 3-4, p. 233-247.

APPENDIX A

U-Th dating of Bahamas speleothems at the NIL

Below follows a list of samples and the results from ^{230}Th dating. These samples are all from the Bahamas and were all propagated with the initial ^{230}Th/^{232}Th value of 0.6 ±0.2, which represents the average crustal value.

Table A.1 (following page): Results from ^{230}Th dating of samples which are not presented in Chapters 1-7 from samples which were analyzed at the Neptune Isotope Laboratory, Miami, FL.

Sample Name	**dc02-2**	**dc02-3**	**dc02-4**	**dc02-5**	**dc02-5**	**dc03-2**	**dc03-3**	**dc03-4**
Sample location (cm from top)	0.9	8.5	10.8	13.1	12.5	4.8	10.8	17.3
Age CORRECTED	16584.07	19817.65	20865.03	14735.28	22435.01	15553.48	16716.45	22580.52
± (95% CI)	87.56324	81.01513	95.16033	65.94255	382.393	89.32837	102.9513	574.1513
Activity ratio 234U/238U initial	1.02396	1.022367	1.026914	1.02232	1.010146	1.025806	1.022877	1.029137
± (95% CI)	0.002647	0.002562	0.002641	0.002538	0.00246	0.002503	0.003604	0.002648
Age UNCORRECTED	16730.15	19876.18	20925.23	14782.48	23565.4	15745.1	16857.67	24245.38
± (95% CI)	73.74563	77.80245	93.18077	63.76408	98.63549	64.33252	91.22727	211.553
[238U] sample from MC	296.3009	266.0862	326.9085	328.5952	258.5363	355.1504	349.3238	380.8452
± (95% CI)	0.181118	0.159872	0.196664	0.206831	0.124605	0.206513	0.238406	0.233784
Activity Ratio 230/232Th from MC	63.8676	186.0787	189.8251	175.4296	11.28651	45.88423	66.43142	7.894044
± (95% CI)	0.852817	1.816595	0.946052	1.11965	0.056245	0.385826	0.473885	0.06654
Activity Ratio 230Th/238U from MC	0.145373	0.17003	0.178936	0.129375	0.196016	0.137667	0.146246	0.204736
± (95% CI)	0.000673	0.000723	0.000818	0.000604	0.000883	0.000618	0.000714	0.001671
Initial 230/232Th activity ratio	0.6	0.6	0.6	0.6	0.6	0.6	0.6	0.6
± (2Stdev)	0.2	0.2	0.2	0.2	0.2	0.2	0.2	0.2

Sample Name	**dc03-5**	**dc03-6**	**dc03-7**	**dc03-15cm**	**dc05-5.1**	**dc05-0.2**	**dc05-4**
Sample location (cm from top)	8000	13.8	17.8	15	5.1	0.2	4.7
Age CORRECTED	14839.13	15183.87	15756.93	15452.26	18385.54	15041.84	14823.38
± (95% CI)	66.58032	62.31176	68.35129	51.39398	195.298	112.4006	97.49437
Activity ratio 234U/238U initial	1.022048	1.01155	1.019289	1.01967	1.013058	1.007636	1.00489
± (95% CI)	0.002439	0.002529	0.002397	0.002526	0.002575	0.002444	0.002492
Age UNCORRECTED	14924.66	15265.38	15804.06	15477.86	18530.5	15342.64	14884.52
± (95% CI)	60.60394	56.60762	66.83471	51.06552	190.1065	53.94589	95.97227
[238U] sample from MC	566.6857	349.7033	389.3268	358.7275	304.1965	335.2952	298.7335
± (95% CI)	0.260281	0.161298	0.184524	0.188898	0.185268	0.158606	0.152538
Activity Ratio 230/232Th from MC	97.74625	104.8963	187.0052	337.8824	70.74647	28.58991	136.5694
± (95% CI)	0.900508	1.697674	4.082334	3.581503	3.432085	0.178061	3.148813
Activity Ratio 230Th/238U from MC	0.130505	0.131941	0.137283	0.134696	0.158062	0.13206	0.128034
± (95% CI)	0.00058	0.000548	0.000634	0.000526	0.00152	0.000529	0.000828
Initial 230/232Th activity ratio	0.6	0.6	0.6	0.6	0.6	0.6	0.6
± (2Stdev)	0.2	0.2	0.2	0.2	0.2	0.2	0.2

Sample Name	dc05-3	dc05-3cm	dc11-1	dc13-1	dc16-1	dc16-2	dc16-3
Sample location (cm from top)	3	3	38.1	16.2	103	6.03	19.9
Age CORRECTED	21451	14422.72	140423.6	52629.58	28662.97	15461.28	15604.54
± (95% CI)	269.3009	61.09142	1364.422	283.7874	161.05	99.9728	66.84124
Activity ratio 234U/238U initial	1.022201	1.008775	1.033367	1.015855	1.007514	1.009554	1.003772
± (95% CI)	0.00273	0.002436	0.003629	0.002786	0.0026	0.002518	0.002476
Age UNCORRECTED	22205.15	14495.86	140452.7	52662.63	28801.72	15483.95	15633.11
± (95% CI)	98.8779	56.32941	1365.363	283.068	154.955	99.72376	66.41775
[238U] sample from MC	234.2365	278.6228	282.4661	176.1576	342.022	352.6139	433.4549
± (95% CI)	0.159721	0.12854	0.181081	0.107718	0.197614	0.219898	0.204171
Activity Ratio 230/232Th from MC	16.05689	111.5517	1614.365	757.2033	109.7123	382.0028	305.6376
± (95% CI)	0.079647	0.553053	12.01406	16.78501	0.744011	3.386422	6.398784
Activity Ratio 230Th/238U from MC	0.187969	0.125384	0.742803	0.388221	0.233508	0.133435	0.133879
± (95% CI)	0.000851	0.000551	0.003647	0.001799	0.001198	0.000862	0.000609
Initial 230/232Th activity ratio	0.6	0.6	0.6	0.6	0.6	0.6	0.6
± (2Stdev)	0.2	0.2	0.2	0.2	0.2	0.2	0.2

Sample Name	**dc16-4**	**dc16-5**	**dc16-6**	**dc16-7**	**dc16-8**	**hbc02-1**	**hbc04-1**
Sample location (cm from top)	40.2	49.5	60.5	70.5	84.2	49.8	8.89
Age CORRECTED	17164.62	18574.89	19386.8	21531.17	22808.42	54780.52	50180.07
± (95% CI)	65.93536	67.74371	77.81069	96.49976	112.1688	336.3089	776.8564
Activity ratio 234U/238U initial	1.00456	1.012736	1.003301	1.008978	1.005888	1.041021	0.970886
± (95% CI)	0.002441	0.002443	0.002441	0.002459	0.002501	0.002992	0.00314
Age UNCORRECTED	17209.16	18600.82	19413.88	21548.54	22923.22	55016.93	52179.38
± (95% CI)	64.55316	66.85597	77.04716	96.76672	106.8439	325.5247	395.8804
[238U] sample from MC	374.9951	452.4962	302.9372	367.6634	322.7952	63.67839	27.61215
± (95% CI)	0.169057	0.218338	0.138883	0.171735	0.15092	0.039401	0.018784
Activity Ratio 230/232Th from MC	214.3073	395.5017	394.3562	675.7478	108.2816	109.3689	12.59842
± (95% CI)	2.292412	11.03496	14.40563	20.74765	1.095514	0.639281	0.086171
Activity Ratio 230Th/238U from MC	0.146453	0.158564	0.163407	0.180641	0.190431	0.410733	0.369597
± (95% CI)	0.000625	0.000637	0.000716	0.000839	0.000904	0.002066	0.002265
Initial 230/232Th activity ratio	0.6	0.6	0.6	0.6	0.6	0.6	0.6
± (2Stdev)	0.2	0.2	0.2	0.2	0.2	0.2	0.2

Sample Name	**hiw01-1**	**rc01-1**	**rc02-1**	**rc05-1**	**kb03-1**	**kb04-1**
Sample location (cm from top)	2.5	13.75	22.4	79	21.6	4.2
Age CORRECTED	44955.4	14319.98	58682.2	34314.25	14652.3	15090.69
± (95% CI)	373.4271	179.2481	412.8213	371.1514	72.34122	104.509
Activity ratio 234U/238U initial	1.021101	1.082048	1.018226	1.074931	1.033198	1.041112
± (95% CI)	0.002774	0.00271	0.002847	0.002952	0.003377	0.002617
Age UNCORRECTED	45548.43	14358.56	58855.54	34371.68	14733.35	15239.26
± (95% CI)	323.9113	177.9126	408.4609	370.6424	66.50342	91.03338
[238U] sample from MC	374.3235	211.6801	114.7779	135.4045	367.6253	391.9998
± (95% CI)	0.242745	0.131458	0.071101	0.081826	0.250789	0.25402
Activity Ratio 230/232Th from MC	37.68319	209.1717	157.3033	307.124	102.2626	57.50537
± (95% CI)	0.249085	2.93612	1.760754	4.650939	0.49821	0.363664
Activity Ratio 230Th/238U from MC	0.347797	0.133117	0.423604	0.28927	0.130319	0.135494
± (95% CI)	0.002119	0.001583	0.002374	0.00271	0.000562	0.000814
Initial 230/232Th activity ratio	0.6	0.6	0.6	0.6	0.6	0.6
± (2Stdev)	0.2	0.2	0.2	0.2	0.2	0.2

APPENDIX B

The Miami Device

Provided in Appendix B is an overview of the water standards used for calibration of the Miami Device and the various alternative designs which were tested for the Miami Device. The final design of the Miami Device is similar to the design of the Picarro vaporizer unit; therefore we compared results of the Miami Device to results from the Picarro vaporizer unit. Finally, we have provided data which demonstrates the long term stability of a sample introduced through the Miami Device. We allowed a sample to be continually measured for 700 seconds to demonstrate variability in the water concentration and oxygen and hydrogen isotopes over time.

Water Standards

In order to correct to VSMOW scale, four standard waters were analyzed which have been previously calibrated to the VSMOW-GISP-SLAP scale. For the 100 cm^3 volume, 0.5 μL of each water standard was injected twice at the beginning of each day (Supplementary Table 1). Supplementary table 1 demonstrates the average for each standard over a period of approximately a month. Also shown is the oxygen and hydrogen isotope value after correction to VSMOW scale. The average external standard deviation for the injections was ±0.4‰ for $\delta^{18}O$ and ±1.1‰ for $\delta^{2}H$.

Design of the Miami Device

In the development of the Miami Device, a series of alternative designs were tested (Figure B.1). The original design is primarily based on the design of the Amsterdam Device (Vonhof et al., 2006) with a cold trap to freeze out the water (Figure

B.1a) rather than the final design which does not utilize a trap, but instead a large volume reservoir. However, issues were encountered when utilizing a water trap.

For the original design of the Miami Device (Figure B.1a), the method for sample extraction included freezing the water into the trap utilizing either liquid nitrogen or a methanol /liquid nitrogen trap (temperature at -70 to -90 °C). The water was allowed to freeze for on average 5 minutes after injection or crush to ensure all of the water froze down while the nitrogen carrier gas was flowing to the L2130-i Picarro. After 5 minutes, valve 4 and 5 were closed and the trap was heated for 5 minutes, at which point valve 5 is opened and the water was released to the Picarro CRDS instrument for analysis (Figure B.1a). We conducted tests at various time intervals (2 to 10 minutes) for both freezing and heating and found similar results.

The set up in supplementary figure 1a was not utilized because (1) the system had large blanks which we believed resulted from freezing water which was in the carrier gas, (2) the CRDS instrument experienced large pressure increases which we believe is the result of the condensation of N_2 when liquid nitrogen was used. In order to reduce the blank, we inserted a water trap before valve 1 to trap any water from the carrier gas (Figure B.1 b), but this was not found to make any significant difference. The large pressure increases resulted in inconsistent data because the CRDS cavity is sensitive to pressure changes. To reduce the pressure effect, we increased the volume of the line between the cold trap and the Picarro by utilizing 3/8" outer diameter tubing to reduce the pressure to the Picarro, (Figure B.1 c) however this did not significantly reduce the pressure and the resulting oxygen and hydrogen isotope values were unstable, as shown in Figure B.2.

As stated in the text, the final design was based on aspects of the Amsterdam Device and the Picarro vaporizer unit. The implementation of the volume reservoir reduced the pressure effects and eliminated the blank issues, as observed with the original designs. Figure B.3 compares data between the vaporizer introductory system and the Miami Device. The resulting oxygen and hydrogen isotope values and water concentration from the Miami Device and the Picarro vaporizer unit demonstrate minimal difference between the two introductory systems. The change in the water concentration, $\delta^{18}O$ and $\delta^{2}H$ values over 300 seconds is similar for both introductory systems. This system works well because all of the water from the injection or crush is transferred to the reservoir and the reservoir provides a stable signal to the instrument for analysis.

Sample variation with time

When averaging data, data was averaged 2 minutes after the crushed or injected sample was introduced, up to 1 minute before the sample was flushed away, as described in the text. Tests were conducted to determine how the water concentration, $\delta^{18}O$ and $\delta^{2}H$ values change over time. To conduct this test, the sample was expanded into the volume reservoir and the sample was pumped away after 700 seconds. Figure B.4 demonstrates the resulting oxygen and hydrogen isotopes as well as water concentration over 700 seconds. Table B.2 demonstrates the change in oxygen and hydrogen isotope values and water concentration over various integration periods, demonstrating minimal difference between integrating over 250 seconds compared with 650 seconds. This validates the stability of the system when conducting measurements.

Table B.1: Reproducibility test for 4 standard waters utilizing the 100 cm^3 volume. Each standard was injected (0.5 μL) twice per day and the average of the two injections is shown. The average $\delta^{18}O$ and $\delta^{2}H$ data have not been corrected to VSMOW. Also shown is the average corrected to VSMOW and the reported value for the standard.

Date analyzed	Standard water	$\delta^{18}O$ (‰)	$\delta^{2}H$ (‰)
1/18/2013	LS4	-1.4	-12.6
1/21/2013	LS4	-0.5	-13.2
1/22/2013	LS4	-0.7	-11.6
1/24/2013	LS4	-1.5	-14.2
1/28/2013	LS4	-1.8	-14.5
1/30/2013	LS4	-1.6	-16.3
1/31/2013	LS4	-1.7	-14.8
2/10/2013	LS4	-1.4	-12.4
2/14/2013	LS4	-2.0	-14.5
	Average	-1.4	-13.8
	Standard deviation	0.5	1.4
Average Corrected to VSMOW		-2.9	-19.2
	Reported Value	-2.9	-16.0
1/18/2013	LS	0.4	-1.8
1/21/2013	LS	0.9	-1.1
1/22/2013	LS	0.6	-1.3
1/24/2013	LS	0.1	-2.4
1/28/2013	LS	0.2	-1.7
1/30/2013	LS	0.3	-0.7
1/31/2013	LS	0.4	-2.1
2/4/2013	LS	0.3	-1.9
2/10/2013	LS	0.0	-1.4
	Average	0.3	-1.6
	Standard deviation	0.3	0.5
Average Corrected to VSMOW		-1.1	-4.0
	Reported Value	-1.1	-5.3

1/24/2013	LS3	-8.4	-56.4
1/28/2013	LS3	-8.5	-56.7
1/30/2013	LS3	-7.9	-53.3
2/4/2013	LS3	-8.0	-53.7
2/10/2013	LS3	-9.1	-55.1
2/14/2013	LS3	-8.4	-56.3
	Average	-8.4	-55.2
	Standard deviation	0.4	1.5
Average Corrected to VSMOW		-10.3	-70.8
	Reported Value	-9.9	-71.6
1/16/2013	LS2	4.9	18.0
1/18/2013	LS2	5.1	18.7
1/24/2013	LS2	4.2	16.4
1/30/2013	LS2	4.8	18.7
1/31/2013	LS2	4.6	17.4
2/10/2013	LS2	3.9	16.7
	Average	4.6	17.6
	Standard deviation	0.5	1.0
Average Corrected to VSMOW		3.4	19.9
	Reported Value	3.7	19.2

Figure B.1 (following page): Various alternative designs of the Miami Device. a) Schematic of original extraction line design with a cold trap to freeze out water rather than the current design which implements the volume reservoir. The sample method was the same, with the exception that the water was frozen in the trap utilizing either liquid nitrogen or a methanol /liquid nitrogen trap (temperature at -70 to -90 °C). The water was allowed to freeze for on average 5 minutes after injection to ensure all of the water froze down while nitrogen carrier gas was flowing to the Picarro. After 5 minutes, valve 4 and 5 were closed and the trap was heated for another 5 minutes, at which point valve 5 was opened. b) The second design implemented a cold trap prior to valve one in order to eliminate any water in the carrier gas. c) The volume of the line between the cold trap and the Picarro CRDS instrument was increased by utilizing 3/8" outer diameter tubing to reduce the pressure reaching the Picarro, however this did not significantly reduce the pressure to the CRDS instrument.

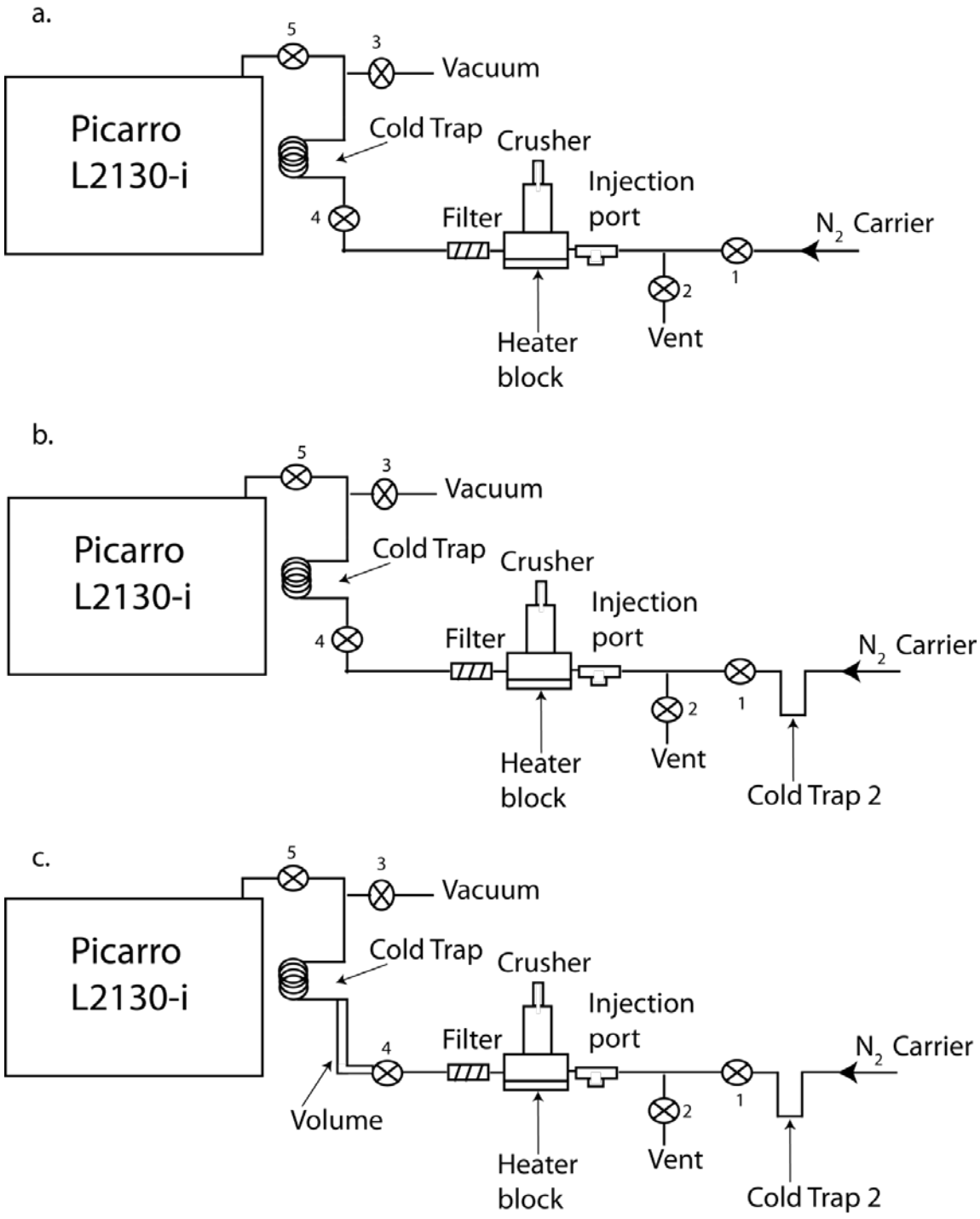
a.
Picarro
L2130-i
5
3
Vacuum
Cold Trap
Crusher
Injection
port
4
Filter
N2 Carrier
2
1
Heater
block
Vent
b.
Picarro
L2130-i
5
3
Vacuum
Cold Trap
Crusher
Injection
port
4
Filter
N2 Carrier
2
1
Heater
block
Vent
Cold Trap 2
c.
Picarro
L2130-i
5
3
Vacuum
Cold Trap
Crusher
Injection
port
4
Filter
N2 Carrier
Volume
2
1
Heater
block
Vent
Cold Trap 2

Figure B.2: Results for a standard water injection utilizing the set up depicted in Figure B.1c a) Oxygen and hydrogen isotope values (machine scale) for an injection with the resulting water concentration. b) Close up of the water concentration, $\delta^{18}O$ and $\delta^{2}H$ data from the dashed square in a. The sharp decline in water concentration from 200 to 400 seconds is due to the large pulse of water from the trap and the decline in the $\delta^{2}H$ signal and the increase in the $\delta^{18}O$ signal is also due to the pulse of water coming off of the trap.

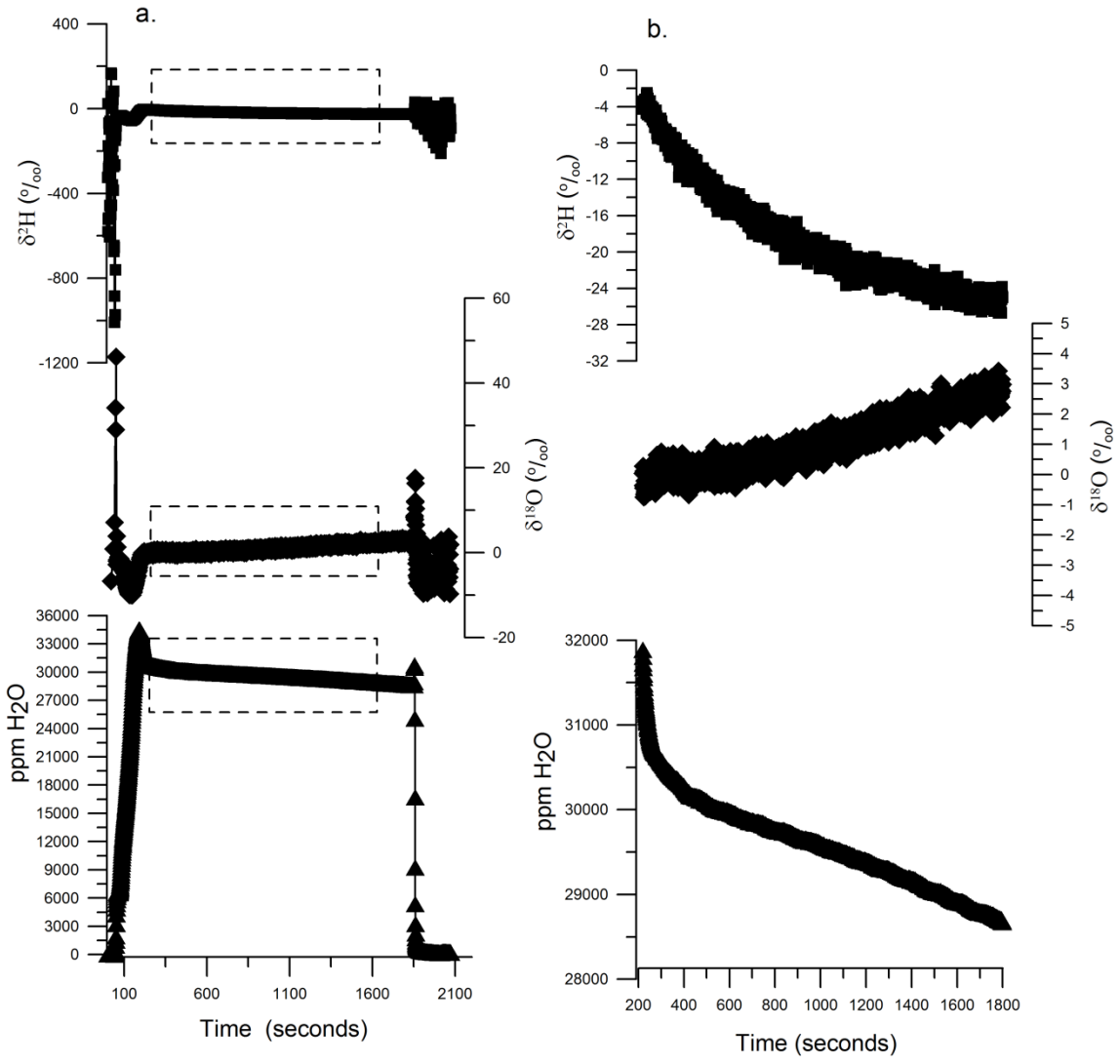

Figure B.3: Comparison between the resultant ppm of H_2O, $\delta^{18}O$ and $\delta^{2}H$ values (machine scale) using a) the Miami Device and b) the Picarro vaporizer unit. There is minimal difference between the two. For a 300 second integration (represented by the dashed rectangles), there was a maximum rise in the water concentration in (a) of approximately 1,600 ppm, while for the data acquired using the vaporizer unit (b) the rise is about 1,400 ppm. For oxygen isotopes the standard deviation of $\delta^{18}O$ values over 300 seconds was 0.3 ‰ for both the Miami Device (a) and the vaporizer unit (b). For $\delta^{2}H$ the standard deviation over 300 seconds was 0.9 ‰ for both introductory systems.

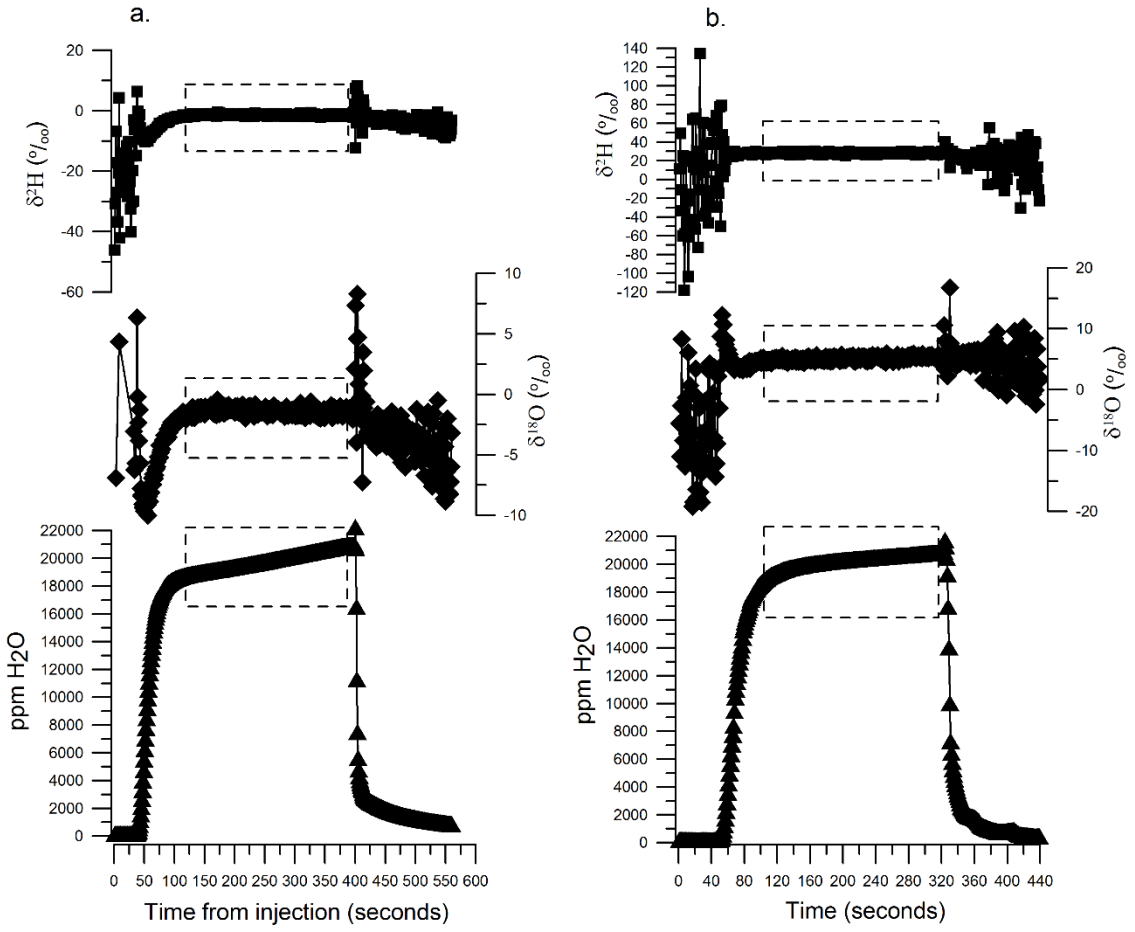

Figure B.4: The resultant ppm H_2O, $\delta^{18}O$ and $\delta^{2}H$ values (machine scale) over 700 seconds. The dashed rectangles represent the data which were averaged in supplementary table 2.

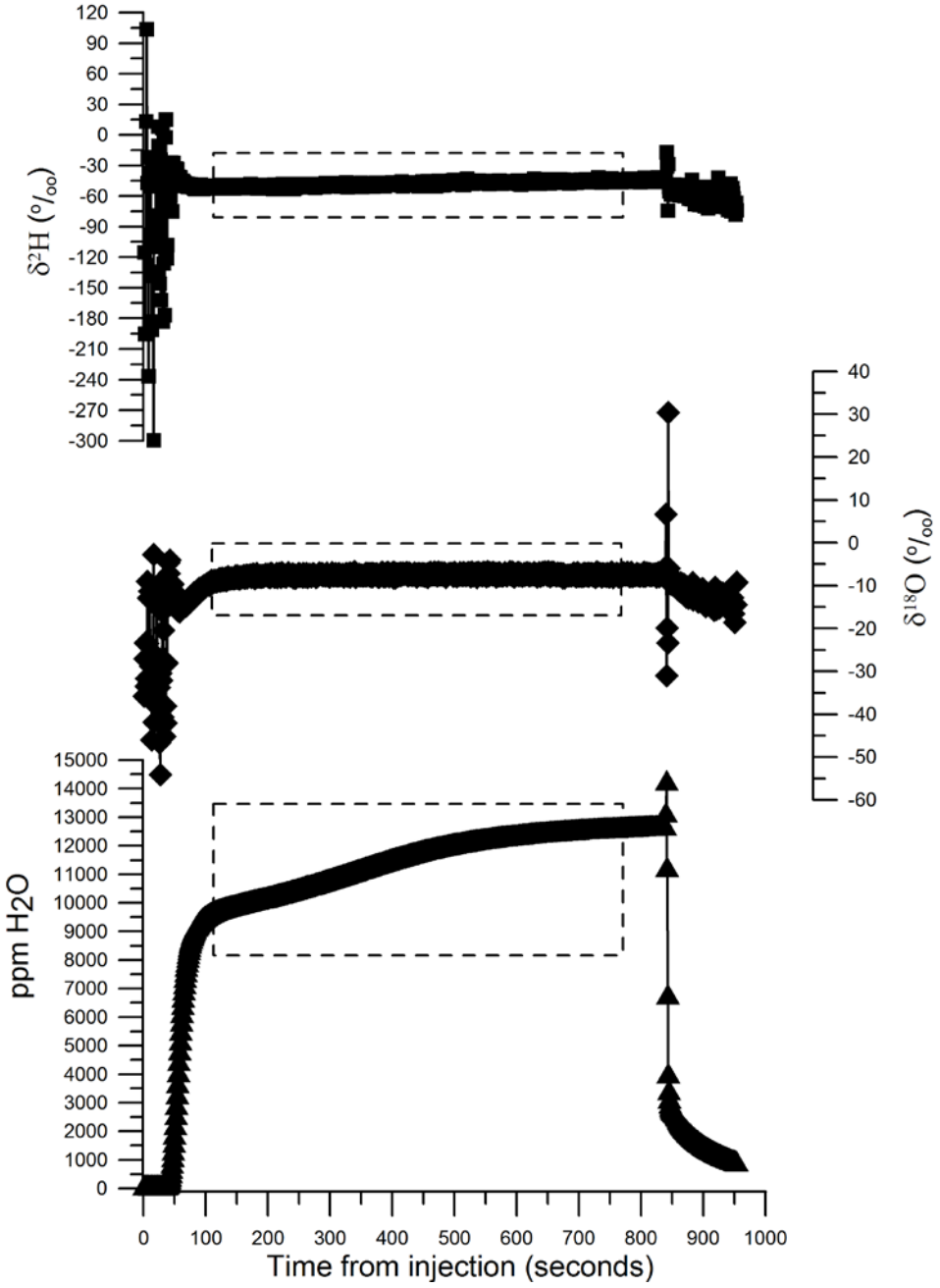

Table B.2: Average ppm H_2O, $\delta^{18}O$ and $\delta^{2}H$ values (machine scale) from supplementary figure 4 over different time intervals (represented in supplementary figure 4 by the rectangles). There is minimal difference between 250 second integration compared with integration over 650 seconds for $\delta^{18}O$ values with higher variability for $\delta^{2}H$ results.

	ppm H_2O	$\delta^{18}O$ (‰)	$\delta^{2}H$ (‰)
Average over 250 seconds	10758.7	-7.6	-49.6
SD over 250 seconds	473.9	0.3	1.4
Average over 350 seconds	11079.3	-7.5	-48.9
SD over 350 seconds	652.6	0.3	1.7
Average over 450 seconds	11346.3	-7.5	-48.4
SD over 450 seconds	763.9	0.3	1.9
Average over 550 seconds	11558.0	-7.5	-47.9
SD over 550 seconds	824.8	0.3	2.1
Average over 650 seconds	11725.8	-7.5	-47.4
SD over 650 seconds	855.1	0.3	2.3
Average	*11293.6*	*-7.5*	*-48.4*
SD	*384.6*	*0.0*	*0.9*

APPENDIX C

Overview of the U-Th dating mechanisms for sample AB-DC-09

Provided in the supplementary material is an overview of results from the modern samples collected from Eleuthera, Bahamas which were used to calculate initial, unsupported (230Th/232Th) ratio. The modern samples were also analyzed for oxygen isotopes and were utilized to demonstrate that minimal kinetic fractionation occurs in the modern. Also provided is an overview of some of the potential sources of error in the development of the age model for sample AB-DC-09.

Modern samples: Determination of initial (230Th/232Th) ratio from modern (zero age) cave calcites

To determine the initial (230Th/232Th) ratio, modern calcite was collected from a cave with actively forming stalagmites in Eleuthera, Bahamas (Figure 1). Modern cave deposits were collected by placing standard glass microscope slides on top of currently forming stalagmites similar to the methods of Tremaine et al. (2011) and Banner et al. (2007). The slides were left in the cave for 3-5 months, then brought back to the laboratory and dried at 40 °C for 24 hours. The calcite was scraped off the slides, and 145-185 mg of calcite was weighed and dissolved for U-Th separation using the methods presented in the text and outlined in Pourmand et al. (2014). The samples were spiked prior to analysis in the Neptune Isotope Laboratory of the University of Miami - RSMAS utilizing a ThermoFisher-Neptune Plus multi-collection ICP-MS to determine Th concentrations. Considering that these are modern precipitates, the entire 230 Th contribution (after spike correction) can be attributed to unsupported Th from the

epikarst, rather than the decay of uranium equilibrium series. Therefore, the mass-bias corrected 230Th/232Th ratio in these modern samples can be used to calculate the unsupported (detrital) activity ratio by assuming a zero-age for these samples (Supplementary Table 1).

Determination of the initial (230Th/232Th) ratio

As described in the text, the sample ages were corrected for contribution of initial, unsupported 230Th using an initial (230Th/232Th) ratio of 3.7 ±0.6. This initial (230Th/232Th) ratio falls in the range of values for the Bahamas, and additionally results in good agreement with previously published records. Provided below is an assessment of potential sources of error to the age model for sample AB-DC-09.

We have chosen to utilize a single (230Th/232Th) ratio for the propagation of ages for the sample, which is a reasonable assumption given that this ratio cannot be realistically determined for every interval at which an age determination was made. Nevertheless we acknowledge the possibility that the detrital activity ratio may have changed with time. Two of the ages located ~5 cm from the top resulted in age reversals. These ages were younger than the previous ages. This is thought be due to a reduction in the initial 230Th/232Th component during this time period, leading to ages which appear to be younger. This is demonstrated in supplementary figure 1. If the age model is propagated with a much greater (230Th/232Th) ratio, the older ages become younger, resulting in a significant age reversal. Here we utilize an activity ratio of 7.8±0.6 to demonstrate this (supplementary figure 1). No reversal is observed when the ages are propagated with lower activity ratios. We conclude that the two samples located ~5 cm from the top are younger than would be expected due to a reduced initial (230Th/232Th) ratio at this

period. Considering the disagreement between these two ages and the surrounding ages, we do not consider these ages as part of the age model. Similarly, one U-Th age at 11 cm from the top was older than the previous ages, possibly suggesting an increased the initial 230Th/232Th component at this time period as shown in supplementary figure 2. Supplementary figure 2 demonstrates that with increasing 230Th/232Th activity ratio, propagated ages become younger. Considering the good agreement between surrounding ages, we discount this age and do not include it in the final age model.

We further assess the contribution of variable initial, unsupported 230Th by a sensitivity test whereby the resultant age models propagated at various initial (230Th/232Th) ratios. Supplementary figure 2 demonstrates the carbon isotopic record with varying initial Th activity ratios (0.6, 2.2, 3.4 and 3.7) to demonstrate the effect of the initial Th values on the age model and the timing of the isotopic shifts. As is demonstrated in supplementary figure 2, when propagated at a higher activity ratio, the oldest ages become younger. This causes the timing of Heinrich stadial 3 to become unreasonable younger in comparison to other records from the region. However, we would like to note that the timing of the isotopic shifts for Heinrich stadial 1 and 2 do not significantly change when propagating at 2.2 or 3.7 (supplementary Table 2). Therefore the initial value chosen most significantly impacts the timing of Heinrich stadial 3, but neither the younger two events.

Modern samples: Oxygen isotopes

Not only was the modern calcite analyzed for Th concentrations, additionally, the oxygen isotopes of the drip waters and the calcites were measured. The temperature of the cave was measured every 2 hours using a HOBO U23 Pro v2 Temperature/Relative

Humidity Data Logger from Onset. Predicted δ18Oc values were calculated using the equation from Tremaine et al. (2011) using the results from the drip water oxygen isotope measurements (annual average = -4.8 ± 0.05 ‰ VSMOW) and the temperature (23.2±0.2 °C). When compared to the measured δ18Oc values, an average offset of 0.3 ‰ was found for the location from which these samples were collected from. We therefore conclude that these samples were precipitated very close to equilibrium. As cave studies have shown that cave drip water has δ18O values similar to local precipitation (Yonge et al., 1985).

Table C.1: The results from the analysis of the modern cave deposits from the Bahamas. The samples were collected from an actively forming cave in Eleuthera, Bahamas.

Sample ID	Th-232 ug/g	Th-230 ug/g	Detrital [Th-230/Th-232]* dpm/dpm
Slide 1	0.2654	2.07E-06	1.46
Slide 3	0.0095	1.35E-07	2.66
Slide 10	0.0117	1.48E-07	2.37
		Average	*2.16*
		SD	*0.6*

*Activity ratios are calculated assuming a zero age

Table C.2: Timing of the isotopic shifts based on various initial Th values as shown in supplementary Figure 2. Results demonstrate that with decreasing initial Th value, ages become older with the timing of Heinrich stadial 3 being impacted the most by changing initial Th value.

	Timing of even (ka BP)		
Initial Th value	HS1	HS2	HS3
3.7	14.9	24.8	30.9
3.4	15	25	31
2.2	16	25.3	34.4
0.6	16.5	25.8	37.8

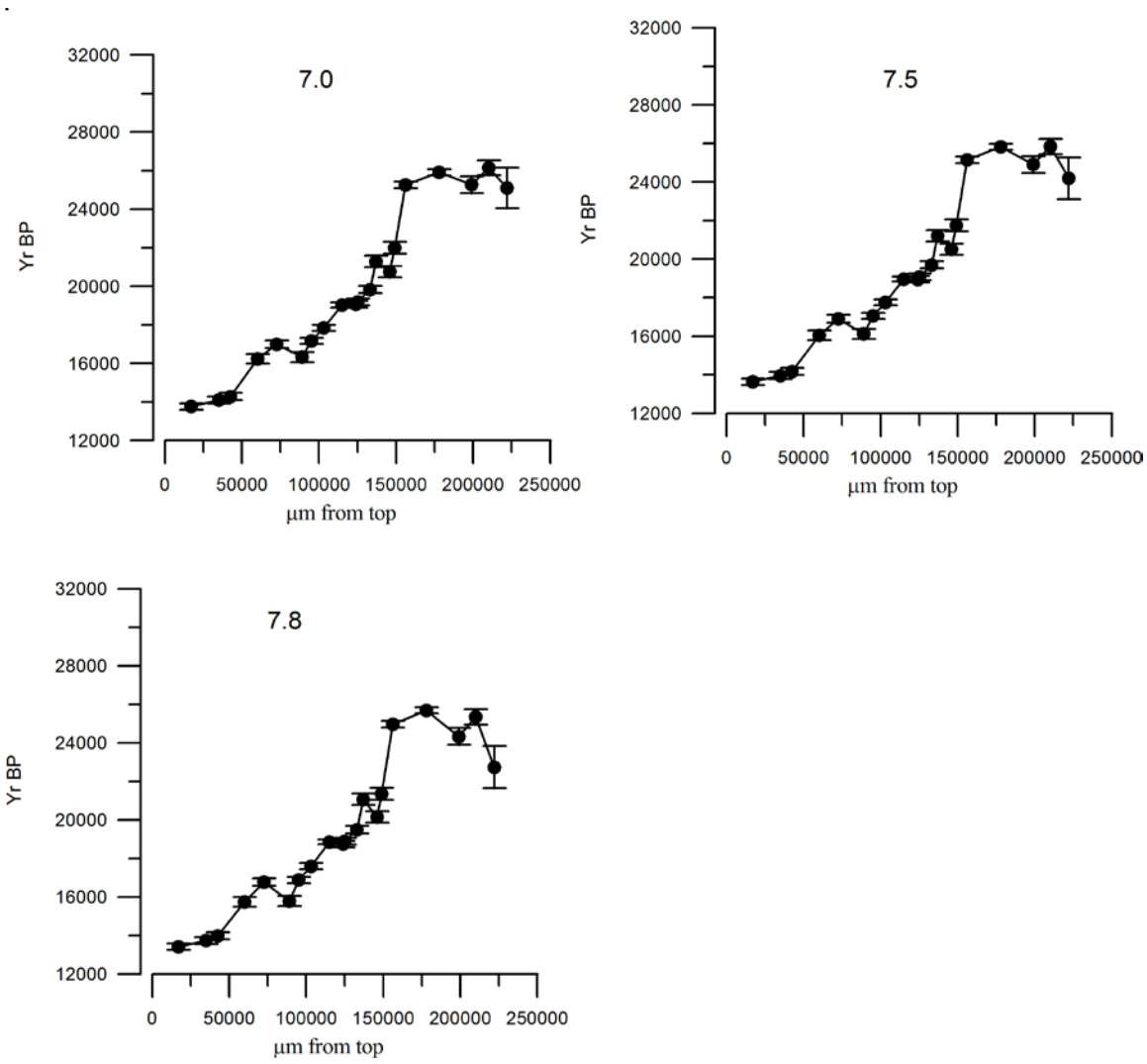

Figure C.1: Propagation of the age model with an 230Th/232Th activity ratio of 7, 7.5 and 7.8 ±0.6. This demonstrates the impact on the ages when propagating with a much greater 230Th/232Th activity ratio. With increasing initial, the bottom of the stalagmite yields ages which are younger than those to the top of the stalagmite.

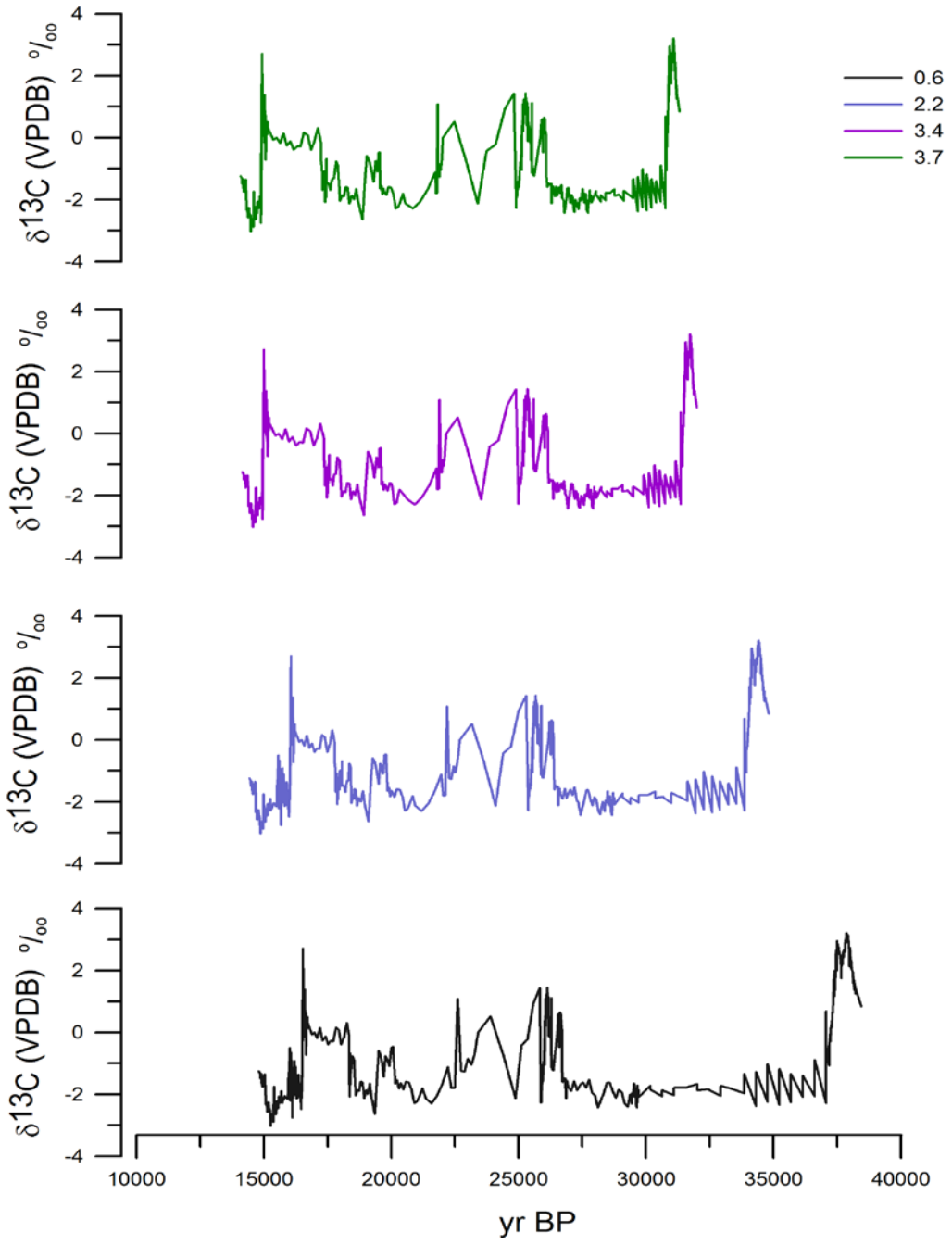

Figure C.2: The carbon isotopic record plotted with various initial 230Th/232Th activity ratios. The age models were propagated at 0.6 (black), 2.2 (blue), 3.4 (purple) and 3.7 (green) 230Th/232Th activity ratio. Overall the timing of Heinrich stadial 3 is the most impacted. Note the carbon isotopic record has not undergone the 50 year interpolation as is shown in the main text.

APPENDIX D

Provided in Appendix D is the results from air and water analysis from the HBC monitoring, followed by a description of the extraction line for the preparation of samples for clumped isotope analysis, followed by the heated and water equilibrated gas results, the long term reproducibility of the Carrara marble standard, the results of samples which were not included in the text of chapter 5 and the data used in the compilation Figure 5.18.

Results from cave monitoring at HBC

Table D.1: A) $\delta^{13}C_{CO2}$ of air results relative to VPDB (‰).

Sample Location	δ13C AIR (VPDB) ‰
6/2/12 HBC outside	-9.7
6/2/12 HBC 3rd Level 1	-11.6
6/2/12 HBC 3rd Level 2	-11.3
6/2/12 HBC west room	-12.2
6/4/12 HBC 1 Level	-11.9
6/4/12 HBC 2 Level -1	-11.1
6/4/12 HBC 2 Level -2	-10.7
6/4/12 HBC 3 Level	-15.9
6/4/12 HBC WEST ROOM	-15.4
8/21/12 Outside	-8.2
8/21/12 Outside	-55.8
8/21/12 1st Level	-8.9
8/21/12 1st Level	-8.0
8/21/12 2nd Level -1	-9.2
8/21/12 2nd Level -1	-8.0
8/21/12 2nd Level-2	-9.1
8/21/12 2nd Level-2	-7.7
8/21/12 3rd Level -	-9.2
8/21/12 3rd Level-	-7.9
8/21/12 3rd Level West-	-11.8
8/21/12 3rd Level West-	-9.2

HBC 12/11/12 Outside -	-18.6
HBC 12/11/12 1st Level -	-10.6
HBC 12/11/12 2nd Level -1	-8.3
HBC 12/11/12 2nd Level -2	-12.3
HBC 12/11/12 2nd Level l-2	-9.3
HBC 12/11/12 3rd Level -	-10.0
HBC 12/11/12 3rd Level -2	-12.6
HBC 12/11/12 3rd Level - 2	-12.0
HBC 12/11/12 3rd Level far-	-10.6
HBC 12/11/12 3rd Level far-	-12.6
5/1/2013 outside cave	
5/1/2013 1st Level	-8.9
5/1/2013 2ndLevel by 1st Level	-6.8
5/1/2013 2nd Level by mid	
5/1/2013 2nd Level by 3rd Level	-6.5
5/1/2013 3rd Level by ladder	-5.4
5/1/2013 3rd Level Main	-4.5
5/1/2013 3rd Levelnear 2	-6.1
5/1/2013 3rd Level west	-6.5
5/1/2013 above 3rd Level West	
5/1/2013 HBC 3rd Level 2	
5/1/2013 HBC 3rd Level 2	-8.4
5/1/2013 HBC 3rd Level West 1	-10.2
5/1/2013 HBC 3rd Levelnear 2	-8.7
5/1/2013 HBC 3rd Level 2	
5/1/2013 HBC 3rd Level West 2	-11.8
5/1/2013 HBC 3rd Level West 1	-13.7
8/6/2013 OUTSIDE CAVE	-7.9
8/6/2013 1RST Level	-8.4
8/6/2013 2ND Level BY FIRST FLOOR	-9.2
8/6/2013 2ND Level MID	-9.6
8/6/2013 2ND Level BY 3RD FLOOR	-8.9
8/6/2013 3RD Level	-10.0
8/6/2013 3RD Level 2	-9.6
8/6/2013 3RD Level West	-11.6
8/7/20132ND Level MID	-9.0
8/7/20133RD Level	-10.6

8/7/20133RD Level West	-9.1
outside cave 11/21/2013	-9.4
1st Level 11/21/2013	-13.4
1st Level by ladder 11/21/2013	-8.4
2nd Level by 1st 11/21/2013	-7.1
2nd Level mid 1 11/21/2013	-12.6
2nd Level mid 2 11/21/2013	-12.3
2nd Level mid 3 11/21/2013	-13.0
3rd Level by ladder 1 11/21/2013	-8.7
3rd Level ladder 2 11/21/2013	-12.2
3RD Level 11/21/2013	-8.7
3rd Level near mud room 11/21/2013	-9.8
3rd Level West 11/21/2013	-13.3
3rd Level West 2 11/21/2013	-13.8

Table D.1: B) CO_2 concentration (ppm) from HBC

Location date	[CO2] ppm
outside cave 11/21/2013	517.4949
HBC 12/11/12 Outside	582.5152
8/6/2013 OUTSIDE CAVE	435.2595
outside cave 11/21/2013	517.4949
8/6/2013 OUTSIDE CAVE	435.2595
1st level by ladder 11/21/2013	603.2793
1st level 11/21/2013	677.0985
8/6/2013 1RST level	433.8399
HBC 12/11/12 1st level	381.7503
2nd level by 1st 11/21/2013	176.2839
HBC 12/11/12 2nd Fl-1 level	358.9998
2nd levelmid 1 11/21/2013	658.086
2nd level mid 2 11/21/2013	609.3633
2nd levelmid 3 11/21/2013	578.0814
8/6/2013 2ND level MID	450.2667
8/7/20132ND level MID	436.4763
8/6/2013 2ND FLOOR BY 3RD level	444.7911
8/6/2013 2ND FLOOR BY FIRST level	468.2652
HBC 12/11/12 2nd level-2	355.0949
HBC 12/11/12 2ndlevel 2	441.428

3rd level by ladder 1 11/21/2013	440.9886
3rd level by ladder 2 11/21/2013	545.1771
8/6/2013 3RD level main	492.3984
8/6/2013 3RD level main	498.9387
3rd level main 11/21/2013	485.706
8/7/20133RD level main	521.3481
HBC 12/11/12 3rd level main- 2	436.2497
HBC 12/11/12 3rd level main-2	451.0206
HBC 12/11/12 3rd levelmain	372.6671
3RD level west 11/21/2013	437.6424
3rd level west 11/21/2013	666.1473
3rd level west 2 11/21/2013	642.4197
8/6/2013 3RD level west	570.6792
8/7/20133RD level west	458.5815
HBC 12/11/12 3rd level west	495.7576
HBC 12/11/12 3rd level west	405.2649

Table D.2:A) Sr, Ca, Mg, Fe concentrations

Date collected	ID	Ca	Fe	Mg	Sr
		ppm	ppb	ppm	ppm
6/2/2012	2nd Level drip	1.79354	1.15606	0.437912	0.007272
6/2/2012	3rd Level Drip 2	4.33137	25.5768	0.624953	0.008408
6/2/2012	3rd Level Drip 3	9.43244	2.05447	1.57776	0.01861
8/21/2012	2nd Level Drip	0.675939	0.537779	0.177959	0.003396
8/21/2012	2 Level fl drip 2	0.640321	1.52573	0.166482	0.003062
8/21/2012	2nd Level drip 3	0.579177			0.00183
8/21/2012	3rd Level west room				
8/21/2012	3rd Level drip	1.25132	0.466134	0.407297	0.004773
8/21/2012	3rd Level drip 4	0.739121			0.003443
8/21/2012	3rd Level	2.39666	1.14023	1.34595	0.009345
12/11/2012	HBC 2nd 1	0.790804	0.480294	0.120638	0.00265
12/11/2012	HBC 2nd 2	0.623532	1.03719	0.227007	0.00356
12/11/2012	HBC 2nd 3	0.365772	1.26749	0.124754	0.00138
12/11/2012	HBC 2nd 4	1.03831	1.32924	0.27187	0.004725
12/11/2012	HBC 2nd 5	8.11358	0.984906		0.047166
12/11/2012	2nd 7	0.826334	1.62324	0.143563	0.003373

12/11/2012	HBC 3rd Level West 1	2.14704	0.570163	1.25126	0.009628
12/11/2012	HBC 3rd Level West 2	2.44131	1.91824	1.48595	0.011412
12/11/2012	HBC 3rd Level 1	0.60043	1.19141	0.374708	0.004197
12/11/2012	HBC 3rd Level 2	1.57894	0.739818	0.850473	0.007605
12/11/2012	HBC 3rd Level 3	1.73386	3.03546	0.200492	0.003814
12/11/2012	HBC 3rd Level 4	1.7177	4.84415		0.006772
5/1/2013	2nd fl	0.645008	0.222884	0.254392	0.00254
5/1/2013	HBC 3rd Level 1	1.91653	0.351921	1.24336	0.011014
5/1/2013	HBC 3rd Level 2				
5/1/2013	3rd fl near stage 8	0.876632	0.300236	0.595703	0.004838
5/1/2013	3rd fl mud room	2.31349	0.84831	1.53962	0.010592
5/1/2013	HBC 3rd Level West 1	2.6086	0.401615	1.58459	0.011985
5/1/2013	HBC 3rd Level West 2				
5/1/2013	HBC 3rd Level West 3	2.8401	2.68225	1.62327	0.012399
8/6/2013	HBC 2nd 1	1.16728	17.0356	0.246752	0.004128
8/6/2013	HBC 2nd 2	1.4871	150.746	0.645135	0.008933
8/6/2013	HBC 2nd 3	1.32128	84.6662	0.417187	0.006486
8/6/2013	HBC 2nd 4	1.41932	84.884	0.420204	0.006603
8/6/2013	HBC 2nd 5	1.09314	17.7423	0.254513	0.004554
8/6/2013	HBC 2nd 6				
8/6/2013	3rd FL Main 1	2.88088	84.9245	1.8307	0.01552
8/6/2013	3rd FL Main 2	2.44664	167.466	1.47475	0.011345
8/6/2013	3rd FL Main 3	1.93025	162.864	1.04777	0.010311
8/6/2013	3rd FL Main 4	2.60993	3.97104	1.61358	0.013171
8/6/2013	3rd FL Main 5	1.28243	11.8357	0.842939	0.007537
8/6/2013	HBC 3rd Level West 1	3.80283	14.1296	2.09007	0.016632
8/6/2013	HBC 3rd Level West 2	3.58177	14.0606	2.00054	0.015895
8/6/2013	HBC 3rd Level West 3	3.30466	3.25754	1.97489	0.015456
8/6/2013	HBC 3rd Level West 4	3.96447	5.83269	2.18722	0.017427
8/6/2013	HBC 3rd Level West 5	3.82176	14.291	2.07997	0.01664
11/21/2013	2nd fl 1	0.978275	0.129658	0.386143	0.005886
11/21/2013	2nd fl 2	0.747408	0.078609	0.28364	0.003951
11/21/2013	2nd fl 3	2.08551	0.625428	0.692697	0.011902
11/21/2013	2nd fl 4	1.06842	0.286015	0.355851	0.006212
11/21/2013	2nd fl 5	0.744487	0.209525	0.25517	0.004019
11/21/2013	3rd fl Near 1 stage 8	1.69821		1.14286	0.009986
11/21/2013	3rd FL Main 2	0.730079	0.107232	0.402868	0.004744
11/21/2013	3rd FL Main 3	0.915639	0.164336	0.496756	0.006812

11/21/2013	3rd FL Main 4	1.5341	0.896502	1.04867	0.0083
11/21/2013	3rd FL Main 5	2.67771	0.341416	2.0865	0.014808
11/21/2013	3rd FL Main 6	1.98214	0.863804	1.36726	0.010517
11/21/2013	3rd FL Main 7	1.8398	0.071312	1.19571	0.0114
11/21/2013	3rd FL Main 8	1.30878	0.768036	0.79296	0.009135
11/21/2013	3rd FL Main 9	2.30306	0.60739	1.47483	0.011908
11/21/2013	3rd fl Main 10 stage 11	2.0881	0.273899	1.24717	0.012244
11/21/2013	3rd fl Main 11	2.68919	0.069551	2.04636	0.014895
11/21/2013	3rd fl Main 12 stage 4	2.32302	0.112393	1.46809	0.011733
11/21/2013	3rd fl Main 13 stage 11	1.65039	0.337736	1.10251	0.008902
11/21/2013	3rd fl Main 15	1.59193	1.64523	1.07211	0.010116
11/21/2013	3rd fl Main 16	4.88354	10.777	2.46993	0.020628
11/21/2013	HBC 3rd Level West 1	2.832395	0.085373	1.812855	0.014263
11/21/2013	HBC 3rd Level West 2	2.966515	0.061276	1.89106	0.014695
11/21/2013	HBC 3rd Level West 3	2.897595	0.290907	1.76002	0.013894
11/21/2013	HBC 3rd Level West 4	3.44612	0.865279	2.11208	0.016501
11/21/2013	HBC 3rd Level West 5	2.53614	0.196662	1.4197	0.01242
11/21/2013	HBC 3rd Level West 6	1.89597	0.943537	1.39023	0.011203
11/21/2013	HBC 3rd Level West 7	3.2012	5.97452	2.01566	0.019889
11/21/2013	HBC 3rd Level West 8	2.89601	0.172938	1.85592	0.014328
11/21/2013	HBC 3rd Level West 8	2.3987	0.549486	1.44568	0.011987

Table D.2:B) Water Sr/Ca, Mg/Ca, $\delta^{18}O$, $\delta^{13}C$DIC from HBC monitoring.

Date collected	ID	Sr/Ca	Mg/Ca		δ18O	δ2H	δ13C DIC
		mM/M	mM/M				
6/2/2012	2nd Level drip	1.9	407.7				
6/2/2012	3rd Level Drip 2	0.9	241.0				1.7
6/2/2012	3rd Level Drip 3	0.9	279.3		-2.9	-19.6	2.6
8/21/2012	2nd Level Drip	2.3	439.7		-1.2	-5.5	-6.8
8/21/2012	2 Level fl drip 2	2.2	434.2		-4.9	-29.9	-6.7
8/21/2012	2nd Level drip 3	1.4			-2.6	-10.2	
8/21/2012	3rd Level west room				-4.8	-30.3	
8/21/2012	3rd Level drip	1.7	543.6		-4.5	-27.2	-7.9
8/21/2012	3rd Level drip 4	2.1					-8.7
8/21/2012	3rd Level	1.8	937.9				-10.0

12/11/2012	HBC 2nd 1	1.5	254.8		-4.7	-27.6	-9.2
12/11/2012	HBC 2nd 2	2.6	608.0		-5.0	-29.7	-10.0
12/11/2012	HBC 2nd 3	1.7	569.6		-4.8	-27.6	-7.4
12/11/2012	HBC 2nd 4	2.1	437.3		-4.0	-21.2	-8.5
12/11/2012	HBC 2nd 5				-4.6	-26.3	-8.1
12/11/2012	2nd 7	1.9	290.1				
12/11/2012	HBC 3rd Level West 1	2.1	973.2		-4.8	-28.5	
12/11/2012	HBC 3rd Level West 2	2.1	1016.5		-4.9	-29.9	-10.3
12/11/2012	HBC 3rd Level 1	3.2	1042.2		-4.5	-25.9	-9.5
12/11/2012	HBC 3rd Level 2	2.2	899.5		-4.2	-24.0	
12/11/2012	HBC 3rd Level 3	1.0	193.1				-9.8
12/11/2012	HBC 3rd Level 4						-10.2
5/1/2013	2nd fl	1.8	658.7		-3.0	-16.5	
5/1/2013	HBC 3rd Level 1	2.6	1083.4		-4.7	-26.1	-13.1
5/1/2013	HBC 3rd Level 2						-9.8
5/1/2013	3rd fl near stage 8	2.5	1134.8		-4.2	-22.0	-9.2
5/1/2013	3rd fl mud room	2.1	1111.4		-4.5	-25.1	-10.2
5/1/2013	HBC 3rd Level West 1	2.1	1014.4		-5.0	-28.0	-10.5
5/1/2013	HBC 3rd Level West 2						-14.0
5/1/2013	HBC 3rd Level West 3	2.0	954.5		-4.9	-27.6	-9.2
8/6/2013	HBC 2nd 1	1.6	353.0		-3.9	-17.7	
8/6/2013	HBC 2nd 2	2.7	724.5		-4.0	-19.3	-5.0
8/6/2013	HBC 2nd 3	2.2	527.3		-4.2	-20.8	-18.6
8/6/2013	HBC 2nd 4	2.1	494.4		-4.1	-20.7	-8.8
8/6/2013	HBC 2nd 5	1.9	388.8		-4.1	-20.7	
8/6/2013	HBC 2nd 6				-2.8	-11.3	
8/6/2013	3rd Level Main 1	2.5	1061.2		-5.1	-30.1	-11.2
8/6/2013	3rd level Main 2	2.1	1006.6		-4.7	-26.4	-10.5
8/6/2013	3rd Level Main 3	2.4	906.5		-5.2	-29.8	-11.5
8/6/2013	3rd Level Main 4	2.3	1032.5		-3.7	-20.3	-5.8
8/6/2013	3rd Level Main 5	2.7	1097.7		-3.2	-17.4	
8/6/2013	HBC 3rd Level West 1	2.0	917.8		-5.4	-32.8	-10.7
8/6/2013	HBC 3rd Level West 2	2.0	932.8		-5.4	-33.2	-11.7
8/6/2013	HBC 3rd Level West 3	2.1	998.0		-4.4	-26.6	
8/6/2013	HBC 3rd Level West 4	2.0	921.3		-5.3	-32.7	
8/6/2013	HBC 3rd Level West 5	2.0	908.9		-5.3	-33.1	-12.4
11/21/2013	2nd Level 1	2.8	659.2		-4.2	-25.0	-1.1
11/21/2013	2nd Level 2	2.4	633.8		-5.0	-31.1	-8.7

11/21/2013	2nd Level 3	2.6	554.7		-4.4	-27.4	-7.6
11/21/2013	2nd Level 4	2.7	556.2		-4.1	-22.9	-8.6
11/21/2013	2nd Level 5	2.5	572.4		-3.1	-14.6	-5.9
11/21/2013	3rd Level Near 1 stage 8	2.7	1123.9		-4.5	-27.4	-9.5
11/21/2013	3rd Level Main 2	3.0	921.5		-4.4	-26.1	-9.9
11/21/2013	3rd Level Main 3	3.4	906.0				-8.4
11/21/2013	3rd Level Main 4	2.5	1141.6		-4.2	-24.5	-10.3
11/21/2013	3rd Level Main 5	2.5	1301.3		-4.2	-25.8	-11.3
11/21/2013	3rd Level Main 6	2.4	1151.9		-4.1	-24.4	-10.8
11/21/2013	3rd Level Main 7	2.8	1085.4		-4.2	-24.8	-10.0
11/21/2013	3rd Level Main 8	3.2	1011.8		-4.0	-23.5	-8.0
11/21/2013	3rd Level Main 9	2.4	1069.4		-4.3	-25.6	-10.9
11/21/2013	3rd Level Main 10 stage 11	2.7	997.4		-4.3	-24.9	-11.5
11/21/2013	3rd Level Main 11	2.5	1270.8		-4.1	-25.2	-12.7
11/21/2013	3rd Level Main 12 stage 4	2.3	1055.4		-4.3	-25.9	-10.9
11/21/2013	3rd Level Main 13 stage 11	2.5	1115.6		-4.2	-24.3	-9.9
11/21/2013	3rd Level Main 15	2.9	1124.7				
11/21/2013	3rd Level Main 16	1.9	844.6				-8.2
11/21/2013	HBC 3rd Level West 1	2.3	1068.9		-4.5	-29.2	-9.0
11/21/2013	HBC 3rd Level West 2	2.3	1064.6		-4.5	-29.4	-9.0
11/21/2013	HBC 3rd Level West 3	2.2	1014.4		-4.4	-28.8	-8.2
11/21/2013	HBC 3rd Level West 4	2.2	1023.5		-4.4	-27.6	-9.3
11/21/2013	HBC 3rd Level West 5	2.2	934.8		-4.6	-29.6	-10.5
11/21/2013	HBC 3rd Level West 6	2.7	1224.5		-4.6	-29.3	-11.3
11/21/2013	HBC 3rd Level West 7	2.8	1051.5		-4.6	-29.5	-9.2
11/21/2013	HBC 3rd Level West 8	2.3	1070.2		-4.3	-27.8	-8.7
11/21/2013	HBC 3rd Level West 8	2.3	1006.5		-4.5	-29.3	-8.6

Table D.3: Water pH, Alkalinity and Cl- results from HBC monitoring.

Date collected	**ID**	**pH**	**Alkalinity**	**Cl-**
			Mmoles/L	**ppm**
6/2/2012	2nd Level drip			
6/2/2012	3rd Level Drip 2			
6/2/2012	3rd Level Drip 3	7.3	1.2	
8/21/2012	2nd Level Drip	7.2	0.6	

8/21/2012	2 Level fl drip 2	8.4	2.8	
8/21/2012	2nd Level drip 3			
8/21/2012	3rd Level west room	8.2	5.1	
8/21/2012	3rd Level drip	8.3	6.0	
8/21/2012	3rd Level drip 4			
8/21/2012	3rd Level			
12/11/2012	HBC 2nd 1	7.8	3.9	542.6293
12/11/2012	HBC 2nd 2	8.2	4.6	546.2212
12/11/2012	HBC 2nd 3			
12/11/2012	HBC 2nd 4			
12/11/2012	HBC 2nd 5			
12/11/2012	2nd 7			
12/11/2012	HBC 3rd Level West 1	7.8	4.3	
12/11/2012	HBC 3rd Level West 2		3.3	2048.887
12/11/2012	HBC 3rd Level 1			813.006
12/11/2012	HBC 3rd Level 2			
12/11/2012	HBC 3rd Level 3			
12/11/2012	HBC 3rd Level 4			
5/1/2013	2nd fl			
5/1/2013	HBC 3rd Level 1	8.2	4.9	2755.056
5/1/2013	HBC 3rd Level 2			813.006
5/1/2013	3rd Level near stage 8	7.9	4.7	1767.785
5/1/2013	3rd Level mud room			
5/1/2013	HBC 3rd Level West 1	8.1	3.7	
5/1/2013	HBC 3rd Level West 2			
5/1/2013	HBC 3rd Level West 3			
8/6/2013	HBC 2nd 1	8.1	5.5	470.0044
8/6/2013	HBC 2nd 2	7.3	2.2	
8/6/2013	HBC 2nd 3	6.8	4.2	
8/6/2013	HBC 2nd 4	7.9	5.3	
8/6/2013	HBC 2nd 5	7.8	4.7	
8/6/2013	HBC 2nd 6			
8/6/2013	3rd Level Main 1	7.9	4.1	2811.369
8/6/2013	3rd Level Main 2	8.0	5.5	2148.309
8/6/2013	3rd Level Main 3	8.0	5.3	
8/6/2013	3rd Level Main 4	7.8	3.1	
8/6/2013	3rd Level Main 5			
8/6/2013	HBC 3rd Level West 1	7.6	3.7	3055.505

8/6/2013	HBC 3rd Level West 2	7.8	3.5	3036.815
8/6/2013	HBC 3rd Level West 3	7.8	1.9	
8/6/2013	HBC 3rd Level West 4	8.3	3.7	
8/6/2013	HBC 3rd Level West 5	7.8	4.0	3074.442
11/21/2013	2nd Level 1	7.9	4.7	634.4709
11/21/2013	2nd Level l 2	8.3	2.2	376.0226
11/21/2013	2nd Level 3	8.0	1.9	594.3647
11/21/2013	2nd Level 4			607.627
11/21/2013	2nd Level 5			
11/21/2013	3rd Level Near 1 stage 8	8.1	4.0	1608.824
11/21/2013	3rd Level Main 2	7.9	3.6	743.383
11/21/2013	3rd Level Main 3	7.7	2.9	1107.954
11/21/2013	3rd Level Main 4	8.4	4.7	1777.778
11/21/2013	3rd Level Main 5	8.4	5.5	3227.354
11/21/2013	3rd Level Main 6	8.4	4.0	2051.573
11/21/2013	3rd Level Main 7	8.2	2.5	1949.731
11/21/2013	3rd Level Main 8	7.9	3.7	
11/21/2013	3rd Level Main 9			2377.915
11/21/2013	3rd Level Main 10 stage 11			2266.227
11/21/2013	3rd Level l Main 11			3333.38
11/21/2013	3rd Level Main 12 stage 4			2396.019
11/21/2013	3rd Level Main 13 stage 11			
11/21/2013	3rd Level Main 15			
11/21/2013	3rd Level Main 16			
11/21/2013	HBC 3rd Level West 1	7.8	4.4	2936.728
11/21/2013	HBC 3rd Level West 2	7.5	4.3	3377.554
11/21/2013	HBC 3rd Level West 3	8.0	2.8	2955.777
11/21/2013	HBC 3rd Level West 4	7.5	4.6	2872.603
11/21/2013	HBC 3rd Level West 5	8.4	3.8	
11/21/2013	HBC 3rd Level West 6			1938.66
11/21/2013	HBC 3rd Level West 7	8.3	3.8	
11/21/2013	HBC 3rd Level West 8			2814.758
11/21/2013	HBC 3rd Level West 8			

Table D.4: Slides Sr/Ca, Mg/Ca, Fe/Ca and Sr/Mg ratios and $\delta^{13}C$ and $\delta^{18}O$ of the carbonate.

Slide #	Location	Sr/Ca	Mg/Ca	Fe/Ca	Sr/Mg	δ13C	δ18O

		mM/M	mM/M	uM/M		‰ VPDB	‰ VPDB
3	East Main	0.37	28.85	135.39	0.01	-8.90	-4.23
4	Main	0.33	35.27	511.23	0.01	-10.27	-4.90
6	West	0.26	21.58	170.00	0.01	-10.94	-5.19
8	Main	0.42	41.75	56.72	0.01	-7.31	-3.34
9	Main	0.46	39.83	1076.43	0.01	-8.41	-3.85
10	East Main	0.50	29.40	2143.00	0.02	-11.33	-5.38
11	West	0.30	24.78	43.32	0.01	-11.08	-5.32
12	Main	0.44	43.73	2849.45	0.01	-6.00	-3.05
13	East Main	0.43	30.12	124.90	0.01	-7.89	-3.95
14	West	0.28	22.40	263.97	0.01	-10.99	-5.10
15	Main	0.53	33.91	1475.53	0.02	-10.04	-4.39
16	Main	0.48	35.63	86.59	0.01	-9.25	-3.97
17	East Main	0.41	29.85	-98.97	0.01	-8.67	-4.24
18	West	0.29	24.88	129.64	0.01	-10.00	-4.62
19	Main	0.57	32.78	4563.94	0.02	-10.17	-4.32
20	Main	0.51	37.06	2234.61	0.01	-8.58	-3.72
21	East Main	0.37	27.17	86.06	0.01	-10.31	-5.07
22	West	0.27	22.37	69.11	0.01	-11.50	-5.49

Table D.5: XRD results for select slides from HBC. Results are shown with the slide number and the location of peaks within the results. The results are followed by photos.

Slide #9			
	Pos. [°2Th.]	**Area [cts*°2Th.]**	**Id**
	23.2248	2.15	2ndary
	29.5964	22.82	LMC

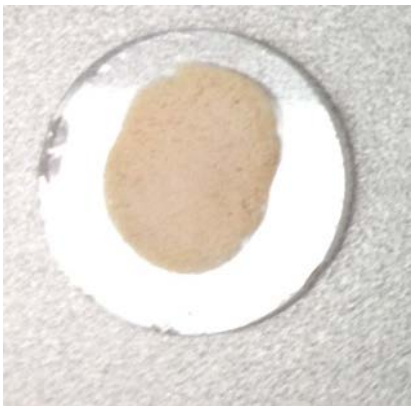

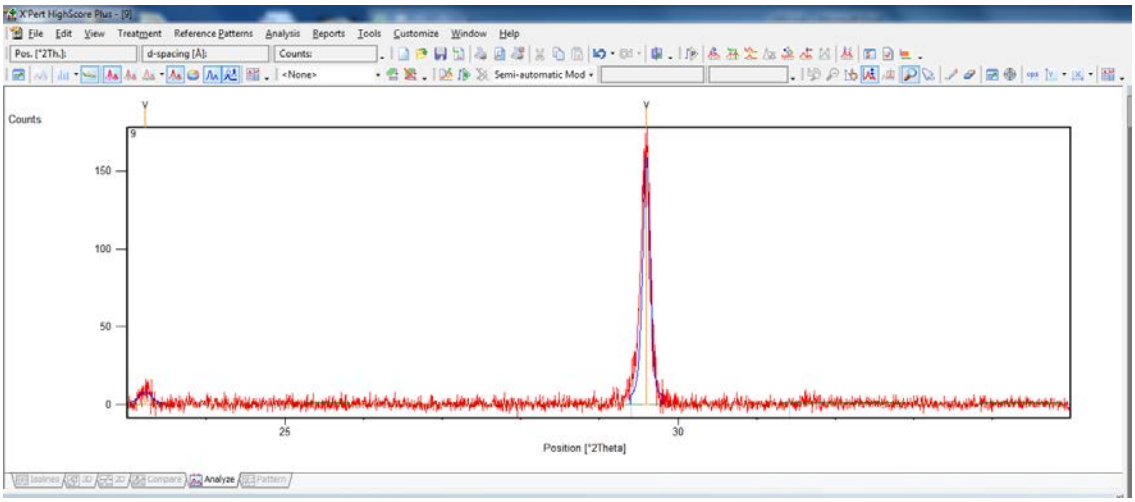

Slide #14			
	Pos. [°2Th.]	Area [cts*°2Th.]	Id
	23.2088	1.53	2ndary
	29.577	24.59	LMC

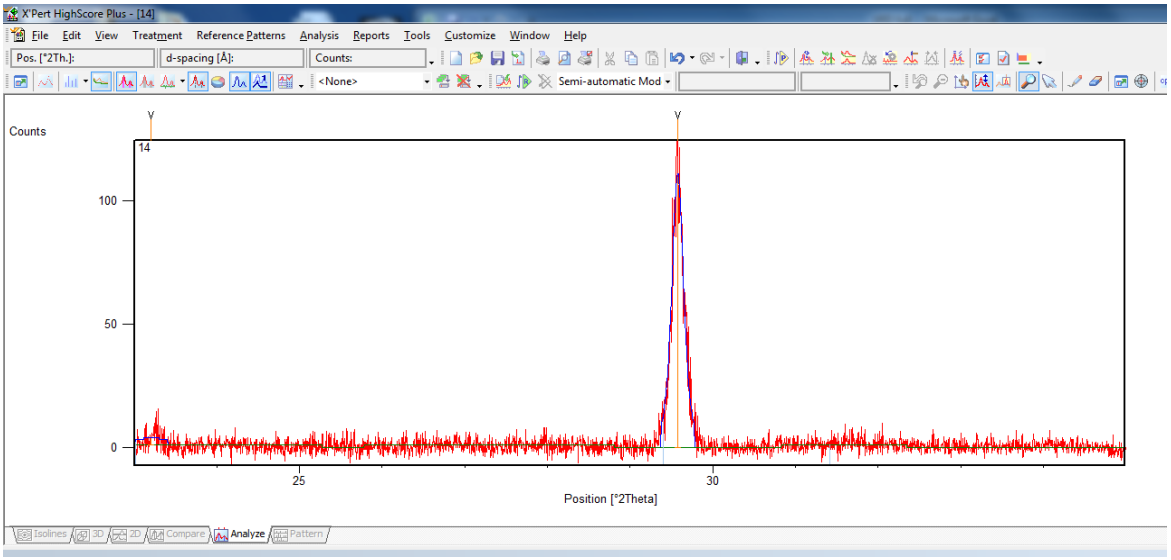

Slide #15			
	Pos. [°2Th.]	**Area [cts*°2Th.]**	**Id**
	23.1562	1.68	2ndary
	29.5434	20.19	LMC

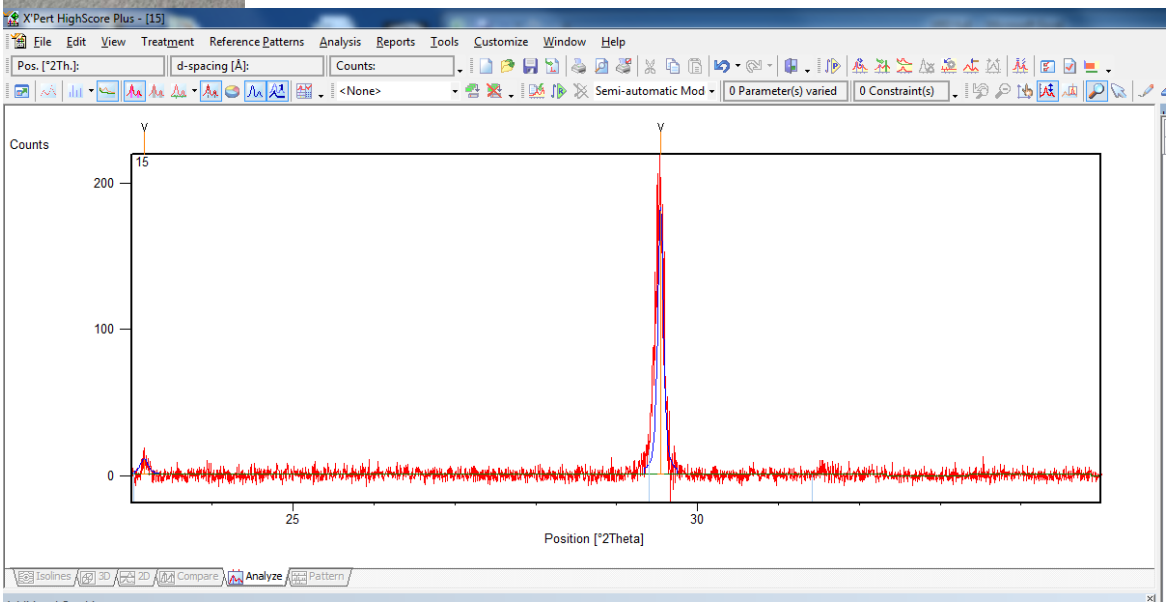

Slide #17			
	Pos. [°2Th.]	**Area [cts*°2Th.]**	**Id**
	23.1373	1.6	2ndary
	29.5274	26.23	LMC
	31.5986	1.07	2ndary

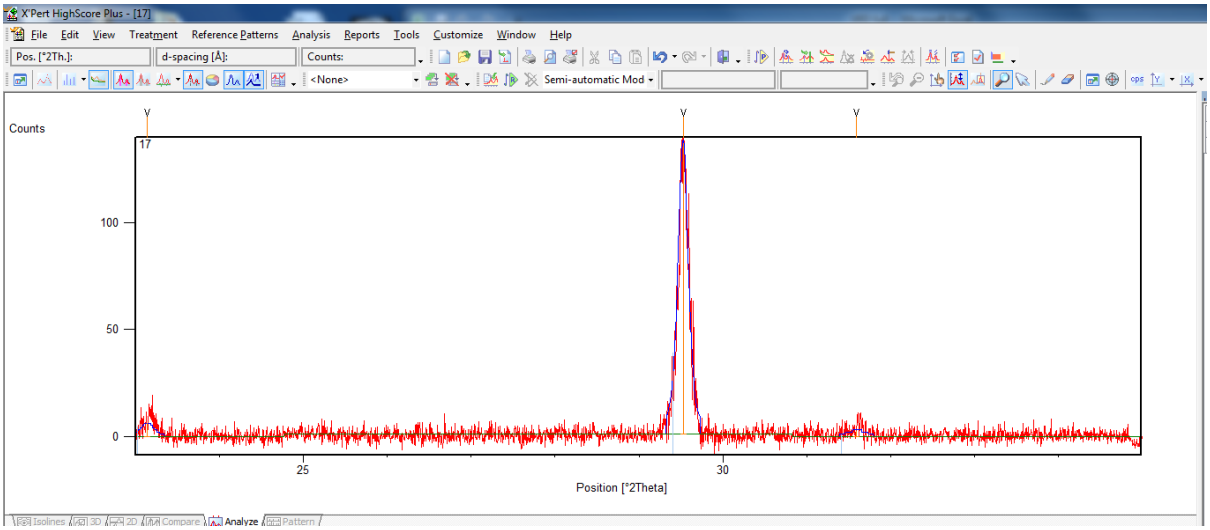

Slide #10			
	Pos. [°2Th.]	**Area [cts*°2Th.]**	**Id**
	23.1643	5.63	calcite 2ndary
	29.515	105.65	LMC
	36.1006	8.76	calcite 2ndary
	39.5603	17.55	calcite 2ndary
	43.3294	13.42	calcite 2ndary
	47.2664	8.99	flourite?
	47.6624	22.83	calcite 2ndary
	48.6793	20.13	calcite 2ndary
	56.7574	3.77	Halite ?
	57.5871	11.54	calcite 2ndary
	60.8741	7.04	Talc ?
	64.8929	7.6	Mica ?

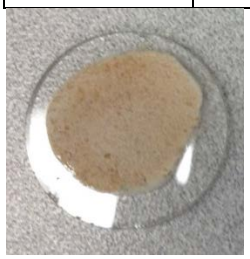

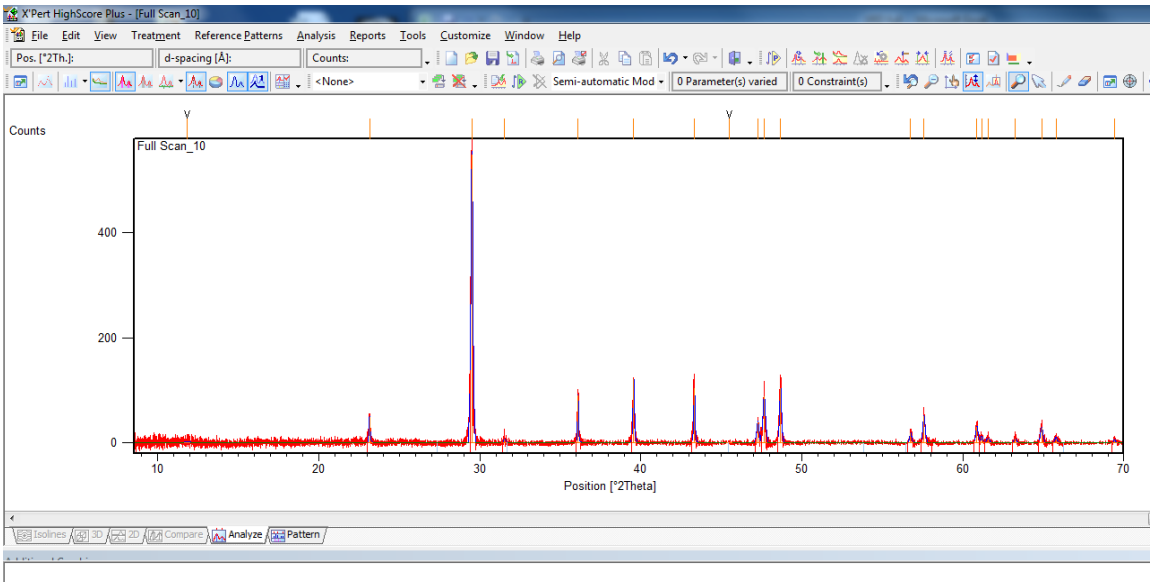

Slide #18			
	Pos. [°2Th.]	**Area [cts*°2Th.]**	**Id**
	23.1821	3.92	2ndary
	29.5135	61.22	LMC
	31.5666	3.23	2ndary
	36.1252	12.88	2ndary
	39.562	13.84	2ndary
	43.3447	22.24	2ndary
	47.32	3.94	flourite?
	47.7157	15.77	2ndary
	48.7051	17.64	2ndary
	56.7735	2.14	Halite ?
	57.6387	9.25	2ndary
	60.9233	4.32	Talc ?
	64.9344	4.89	Mica ?
	65.9095	4.24	?

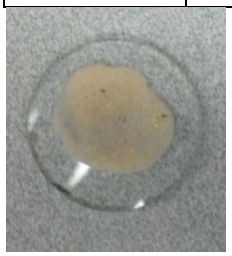

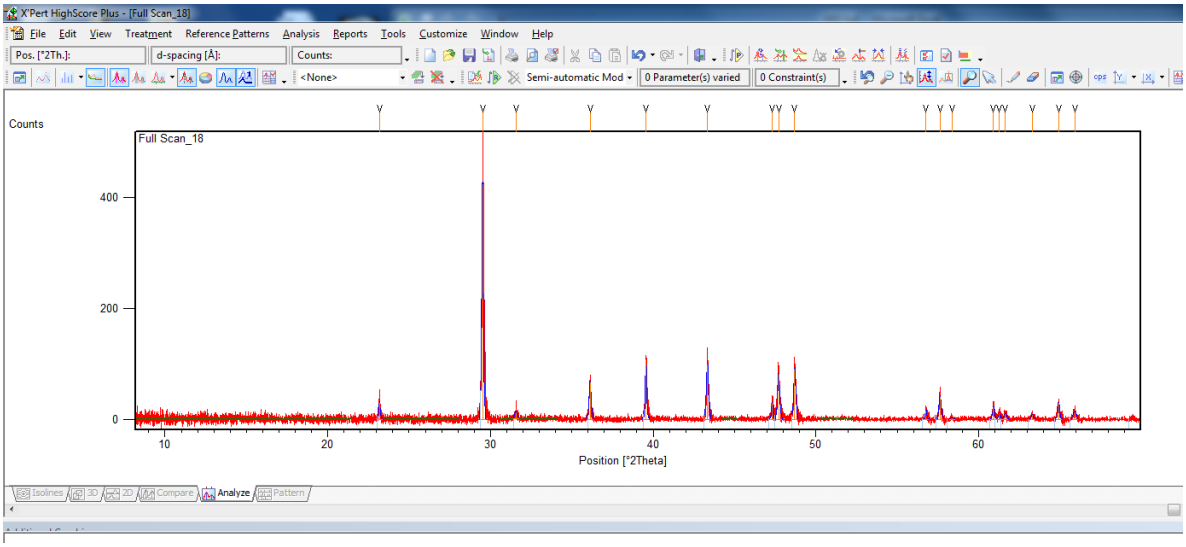

Slide #19			
	Pos. [°2Th.]	Area [cts*°2Th.]	Id
	23.2412	3.61	2ndary
	29.5588	89.27	LMC
	36.1839	17.57	2ndary
	39.6328	14.27	2ndary
	43.4364	6.45	2ndary
	47.4034	4.57	flourite?
	47.6959	20.56	2ndary
	48.7653	12.03	2ndary
	56.868	4.73	Halite ?
	60.98	4.09	Talc ?
	64.9943	4.95	Mica ?
	65.935	3.26	?

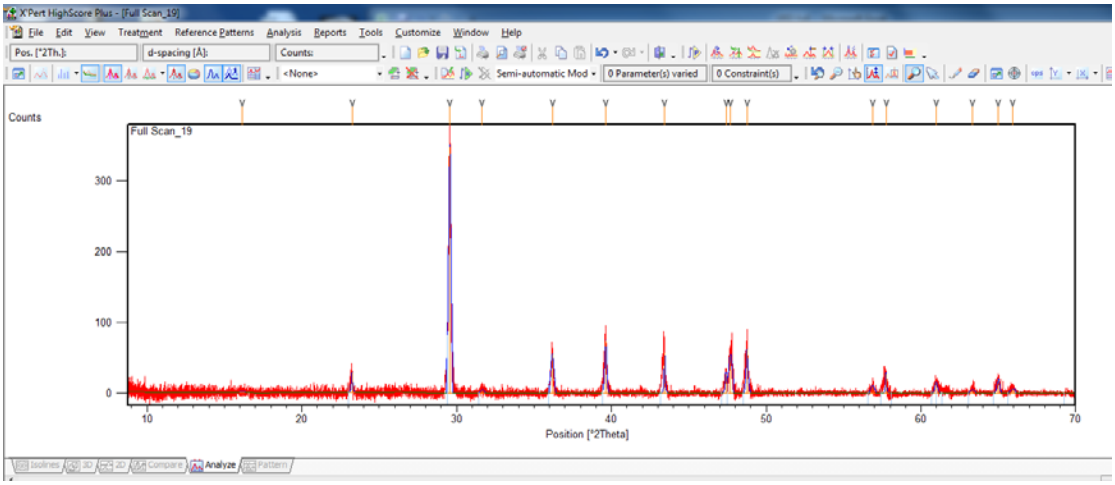

Slide #22			
	Pos. [°2Th.]	Area [cts*°2Th.]	Id
	23.3818	2.36	2ndary
	29.7438	21.27	LMC
	31.7476	2.24	2ndary
	36.2999	9.57	2ndary
	39.7777	18.32	2ndary
	43.4835	16.05	2ndary
	47.4559	4.18	flourite?
	47.8993	13.21	2ndary
	48.8651	17.7	2ndary
	56.9757	2.97	Halite ?
	57.8101	5.52	2ndary
	61.0341	4.11	Talc ?
	65.0905	5.73	Mica ?
	66.0085	4.01	?

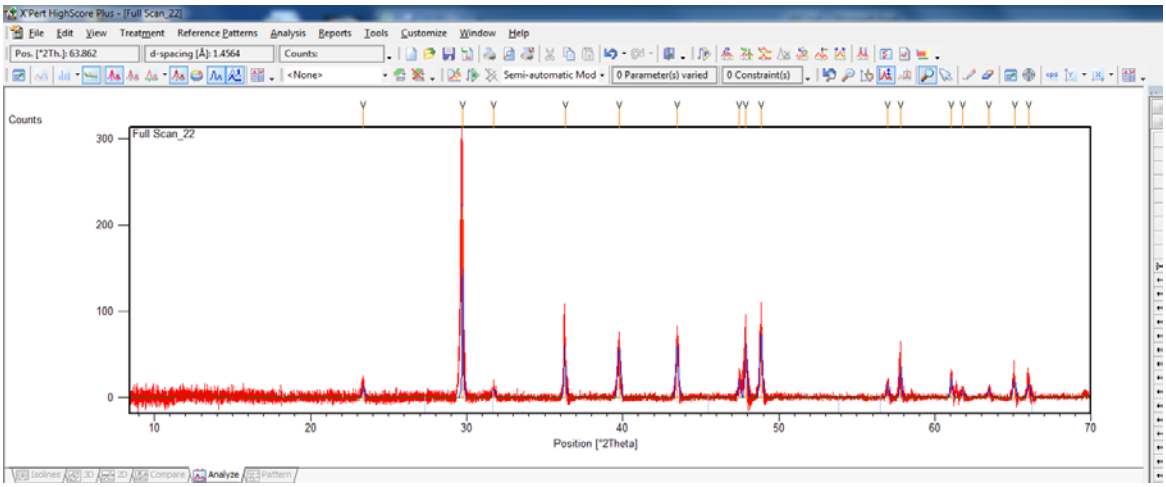

Sample preparation for clumped isotopes

Below follows an outline of sampling for clumped isotopes. Samples for clumped isotopes are reacted in the modified Fairbanks device using the common acid bath method (Figure D.1). The samples are cryogenically frozen in the first trap during reaction, which takes approximately 30 minutes. Sample in trap one is then heated between -90 to -70 ºC using a methanol/liquid nitrogen slush. The amount of CO_2 gas which is released is monitored on a capacitance manometer (MKS 220). The CO_2 is then frozen into trap two, using liquid nitrogen. The remaining non-condensables are removed using a turbo molecular pump using the methanol slush to protect the sample CO_2 gas. The sample is then sealed off from the turbo molecular pump and the liquid nitrogen is removed to release the CO_2 gas. The sample is transferred to trap three via the Porapak (Type Q 50-80 mesh packing material). The Porapak is held between -30 to -20 ºC, and this transfer takes approximately 45 minutes. While the sample is being transferred through the Porapak, trap 1 is heated and evacuated. Once ~99.99% of all CO_2 has transferred through the Porapak, the sample is sealed off from the Porapak and again a methanol trap replaces the liquid nitrogen on trap three. The sample is then transferred to

the cold finger, and again the CO_2 pressure is measured on a capacitance manometer to ensure proper sample yield. The CO_2 gas is then transferred to a sample vial using liquid nitrogen, the CO_2 gas is sealed and transferred to the MAT 253. Upon completion of a sample, the entire line is pumped to background pressure using the Penning gauge to monitor the pressure. The line and Porapak are heated to 200 ºC using insulated nichrome wire for at least 30 minutes. Additionally provided throughout the line are a suite of thermocouple gauges to monitor the movement of CO_2 throughout the entire system.

Water equilibrated and heated gases preparation

Water equilibrated and heated gases are composed of three CO_2 gases, with a suite of $\delta^{13}C$ and $\delta^{18}O$ values. These gases are stored in sealed bulbs (2000 cm^3) at atmospheric pressure attached to the extraction line (Figure D.1). All gases were precleaned through a H_2O removal trap and all non-condensable gases were evacuated.

For the water equilibrated gases, 500 μL of in house ultrapure water was frozen into a Pyrex tube and evacuated using the extraction line. The water was heated and frozen several times to ensure no residual CO_2 was in the Pyrex tube. An aliquot of the tank gas was then frozen into the evacuated Pyrex tube. The tube was sealed and placed in either a 25.0°C ± 1.0°C or 50.0°C ± 1.0°C, temperature controlled, water bath for at least 120 hours. The tubes were then removed from the baths, the water was frozen using a methanol slush held at -90 to -70 °C. Prior to breaking the tube, the tube was evacuated and then broken to release the equilibrated CO_2. The CO_2 gas was then purified using the methods outlined above for a sample and then analyzed on the MAT-253.

The heated gases also utilize the same CO_2 tank gases as the water equilibrated gases. However, the CO_2 is purified first, using the same method as for the samples.

Contrary to the samples, the CO_2 for the heated gases are frozen into a quartz tube and flame sealed. This is followed by heating at 1000 °C in the furnace for over two hours. The tube is quenched and transferred to the MAT-253 mass spectrometer where the tube is cracked and the gas released into the IRMS.

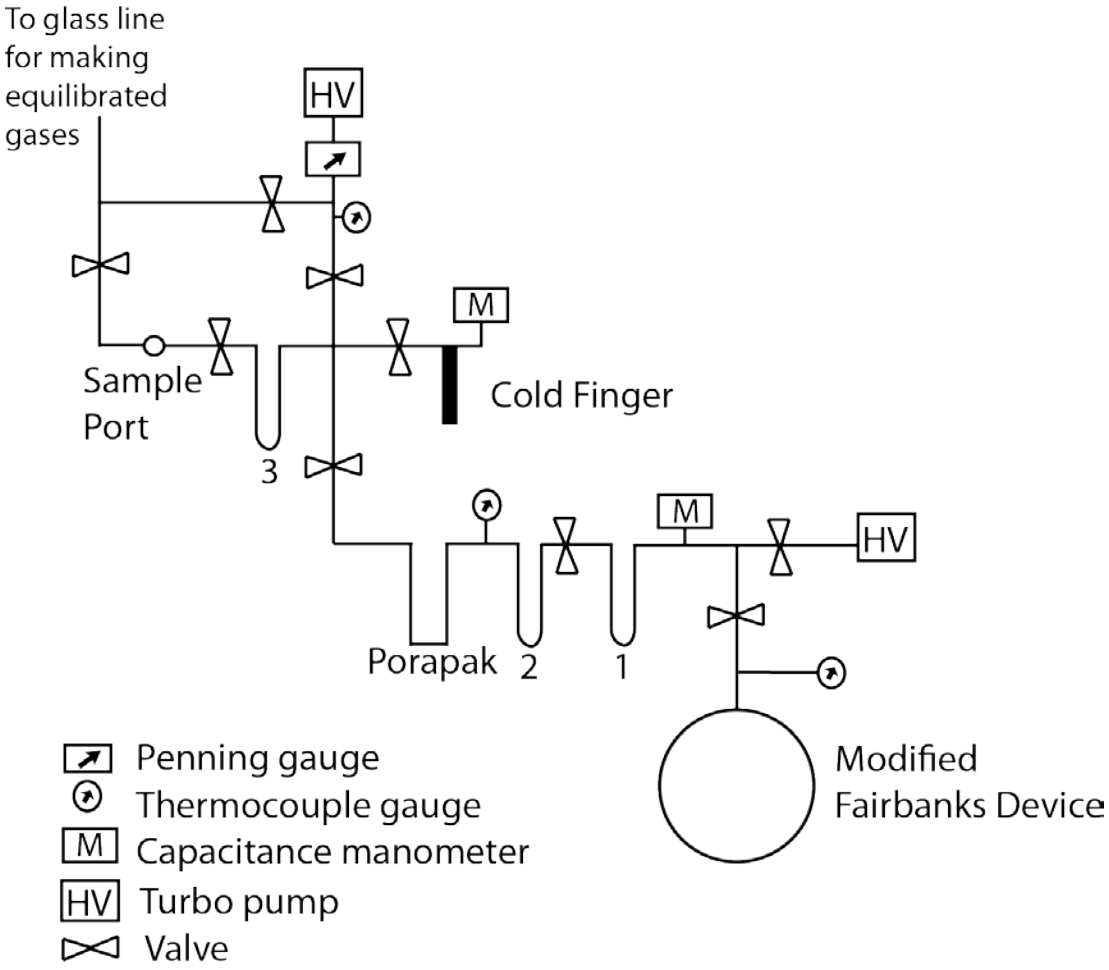

Figure D.1: Extraction line for sample preparation. The line is made up of 3/8" o.d. stainless steel tubing, with the exception of the area between trap 2, the modified Fairbanks device and the high vacuum which is comprised of 1/4" o.d. stainless steel tubing. All valves are Swagelok valves (SS-6BK) which are able to be heated. Evacuation from atmosphere is through a dedicated roughing line (Edwards E2M2). Samples are loaded into the modified Fairbanks device, evacuated through the roughing line, and then pumped further using the Turbo molecular pumps (Balzer TPU 170 and Edwards 50EX). Overnight the samples are evacuated to < 0.001 mbar.

Table D.6: Long term averages for Carrara Marble in-house standard.

	Carrara May, 11 2012 to March 6, 2014
$\delta^{13}C$ VPDB ‰	1.84
s.d.	0.18
$\delta^{18}O$ VPDB ‰	-1.70
s.d.	0.15
$\delta^{47}CO_2$ WG ‰	16.93
s.e.	0.04
$\delta^{48}CO_2$ WG ‰	32.807
s.e.	0.130
$\Delta_{47}CO_2$ WG ‰	-0.084
s.e.	0.007
$\Delta_{48}CO_2$ WG ‰	8.091
s.e.	0.117
$\Delta_{47}CO_2$ RF ‰*	0.287
s.e.	0.003
$\Delta_{47}CO_2$ RF ‰**	0.379
s.e.	0.003
Temp. Ghosh	134.89
s.e.	1.67

* Results in Reference frame (RF) but not corrected for acid fractionation

** Results in Reference frame (RF) AND corrected for acid fractionation

Table D.7: Data for samples shown similar to the data utilized in Tremaine et al., 2011

Study: Tremaine 2011 Location: Lucky Room, Florida		**Study: Feng et al. 2014 Location: WC-1, Texas**		**Study: Feng et al. 2012 Location: NBCT, Texas**	
Temp	**1000ln(α)**	**Temp**	**1000ln(α)**	**Temp**	**1000ln(α)**
19.2	30.26	26.5	29.27	22.3	29.3
19.7	30.68	22.6	29.36	22.3	28.7
19.5	29.93	19.6	30.34	21.4	29.2
21.5	30.12	17.2	31.21	20.5	29.2
21.5	30.53	17.8	31.21	20.8	29.4
20.5	30.60	21.1	30.82	22.1	29
19.5	29.92	21.9	29.95		
18.5	30.58	19.1	29.27		
19.2	30.36	25.3	28.68		
16	31.29	24.6	28.39		
21	30.31	21.3	28.68		
20	30.23	20	29.75		
20	29.79	17.3	30.14		
18	30.69	11.5	31.30		
18	30.62	24.8	29.75		
21	29.72				
19.2	30.19				
19.2	30.32				
19.2	30.23				
12	31.99				
19.2	30.45				

Study: Feng et al. 2012 Location: NBWS, Texas		**Study: Riechelmann et al. 2013 Location: Bunker Cave, Germany**		**Study: Griffiths et al. 2010 Location: Liang Luar Cave, Indonesia**	
Temp	**1000ln(α)**	**Temp**	**1000ln(α)**	**Temp**	**1000ln(α)**
22.6	29.5	10.8	31.95	25	29.196
19.6	29.5	10.4	32.66		
18.7	29.5				
20.6	29.2				
21.2	29.3				
18.6	30				
18.5	29				

Study: Van Bruekelen et al. 2008
Location: Cueva del Tigre Perdido, Peru

Temp	1000ln(α)
22	29.689

Study: Sinha et al. 2007

Location: Dandak Cave, India

Temp	1000ln(α)
25	29.711

Study: Coplen et al. 2007
Location: Devils Hole, Nevada

Temp	1000ln(α)
33.7	28.09

Study: Mickler et al. 2004

Location: Harrison's Cave, Barbados

Temp	1000ln(α)
26.6	29.49
26.6	29.892
26.6	29.691
26.6	29.289
26.6	29.088
26.6	28.385

APPENDIX E

Fingerprinting dust to the Bahamas

$^{87}Sr/^{86}Sr$ isotope results

Utilizing the ThermoFisher Neptune Plus laser ablation ICP-MS at the Neptune Laboratory at the University of Miami, the provenance of the dust could be determined. Sr isotopes were measured to determine if the Heinrich layers within the speleothem contained a different isotopic ratio than the non Heinrich layers. The average Sr isotope ratio was 0.70913 ±0.00003 (2σ) for both Heinrich and non Heinrich layers. These results were normalized to MACS-3 with an $^{87}Sr/^{86}Sr$ value of 0.70755 (Jochum et al., 2011). The results demonstrate no significant change in the $^{87}Sr/^{86}Sr$ value associated with Heinrich layers. Strontium isotopic studies which were conducted on the limestones and dolomites from Abaco Island, Bahamas demonstrate an average $^{87}Sr/^{86}Sr$ value of 0.70909± 0.000010 for the samples from the upper 28 meters of the core (for this study, the authors measured NBS 987 with $^{87}Sr/^{86}Sr = 0.710250 \pm 0.000005$) (Vahrenkamp et al., 1991). These values are within error of each other; suggesting the $^{87}Sr/^{86}Sr$ of the speleothem was reflective of the bedrock.

APPENDIX F

Additional Bahamas samples

Provided in Appendix F is the samples which were analyzed from the Bahamas which did not exhibit significant isotopic changes associated with Heinrich events. Two stalagmites (AB-DC-14 and AB-DC-16) were analyzed for carbon and oxygen isotopes of the carbonate and did not exhibit any change in $\delta^{13}C$ and $\delta^{18}O$ values associated with Heinrich stadials (Figure F.1). Both samples AB-DC-16 and AB-DC-14 exhibit variability in the carbon and oxygen isotopes, however there is not a clear climatic driver of the isotopic variability. This suggests these samples may have undergone post-depositional alteration, which may have resulted in changes in the isotopic records. Therefore care must be taken when selecting speleothems for sampling.

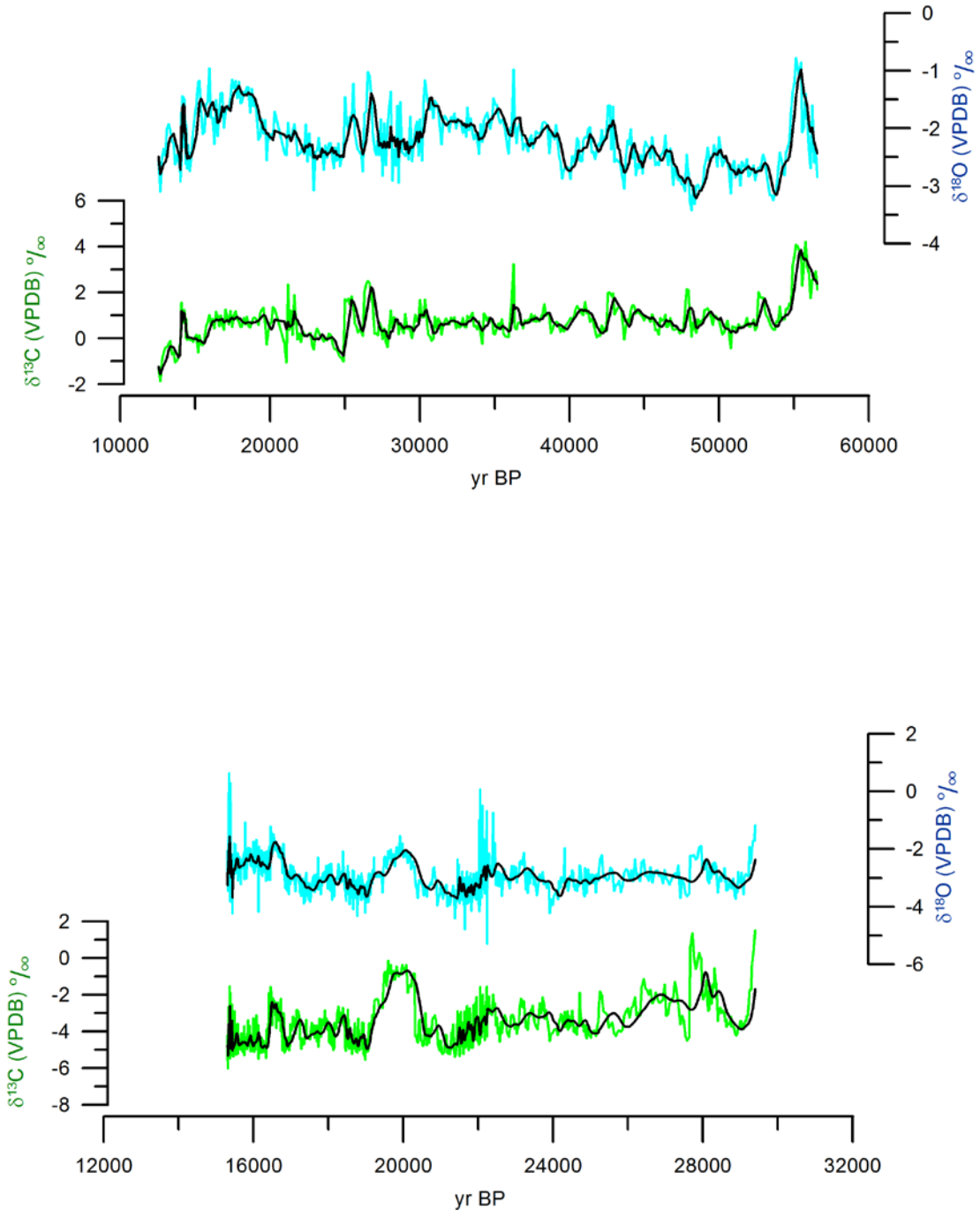

Figure F.1: Oxygen (blue) and carbon (green) isotopes from AB-DC-14 (top) and AB-DC-16 (bottom). Sample AB-DC-14 was forming from 12.5 to 56.5 ka BP from 2 U-Th ages acquired at the NIL. Sample AB-DC-14 is plotted with a 5 point running average in black. Sample AB-DC-16 was forming from 15.0 to 29.3 ka BP (determined from 11 U-Th ages) and is plotted with a 10 point running average in black.